# High Temperature Polymer Electrolyte Membrane Fuel Cells:

## Characterization, Modeling and Materials

Marta Ferreira da Silva Boaventura


**Dissertation presented for the degree of**

Doctor in Chemical and Biological Engineering

**by**

Porto University

**Supervisor**

Professor Adélio Miguel Magalhães Mendes

**LEPAE – Laboratory for Processes, Environment and Energy Engineering**

Chemical Engineering Department

Faculty of Engineering of Porto University


# Acknowledgments

I am thankful to the Portuguese Foundation for Science and Technology for my PhD grant (reference SFRH/BD/28187/2006) and for the financial support through projects PTDC/EQU-EQU/70574/2006 and PTDC/EQU-EQU/104217/2008. I also would like to thank DAAD/CRUP for the financial support (A-6/05) for my first internship at Technical Institute of German Aerospacial Center.

I would like to thank Professor Adélio Mendes for proposing this PhD theme; for his teachings, supervision and support.

My gratitude to LEPAE and DEQ for the support provided to develop my work. A special thanks to my lab mates for the friendship and for the help on solving small "big" problems. I thank Doctor Lúcia Brandão, for providing the SWNH carbon support, and Professor José Sousa, for all the help in the simulation. D. Fátima is acknowledged for the help in the paper work. Thank you to Guida for translating the abstract to French.

I am grateful to Doctor Susana Nunes for receiving me at GKSS, research institute, Geesthacht, for almost 6 months. My appreciation goes to the group "Membranes for Energy" of the Polymer Institute for the support, especially to Doctor Mariela Ponce, with whom I have learnt so much. I would like to thank to all the friends I have meet at the guest house and Geesthacht that made this journey unforgettable.

I am obliged to Doctor Andreas Friedrich for receiving me three times at Technical Institute of German Aerospacial Center (DLR). My gratitude to Alexander Bauder for teaching me how to produce electrodes with DLR dry spray technology and Mr. Heinz Sander for the technical help while developing the high temperature segmented cell.

I appreciate all that made me feel welcome and for letting me be part of the “Rocket Scientists”.

Thanks to the “coffee group” and to the “DEQ mates” for all the laughs and good moments, every day. Many many thanks to my dear friends for the affection, advisements and for listen to me.

I want to express my gratitude to Natália, Rui and Cininha for the support, generosity, and protection.

I want to thank my lovely family, my parents, Anselmo and Laurinda, my brother, Hugo, and my sisters, Sofia and Raquel, for the unconditional support and continuous encouragement during this long journey.

Finally, I want to give a special thank you to Ricardo for the incredible support, comprehension and for standing by my side when I needed. Thank you for never failing on me.

# Abstract

This thesis studies high temperature polymer electrolyte membrane fuel cells (PEMFC) – 120 °C - 200 °C. The interest in the high temperature PEMFC compared to the most commonly studied low temperature PEMFC is related to: 1) improved electrochemical kinetics, 2) simplified water management, 3) simplified cooling system and heat recovery and 4) increased carbon monoxide tolerance.

It is aimed to get an insight on high temperature PEMFC systems. Therefore, high temperature membrane electrode assemblies (MEAs) based in phosphoric acid doped polybenzimidazole (PBI) membranes, a commercial Celtec® - P1000 and an in-house MEA, were studied and a phenomenological model was developed to simulate the high temperature PEMFC behavior.

The phenomena involved in the activation process of Celtec® - P1000 and in-house prepared MEA were investigated at 160 °C. The ohmic resistance decreased and the catalytic activity increased during the activation procedure, for both MEAs. The in-house MEA was also activated at different temperatures (120 °C – 160 °C) and relative humidities (up to 5.0 %). The water had an enhanced effect on ohmic resistance during the PEMFC operation, however, an excess of water has a detrimental effect on the cathode resistance due to phosphoric acid leaching. Moreover, the effect of using hydrogen containing carbon monoxide, as fuel, on the performance of Celtec® - P1000 MEA was studied at 160 °C and 180 °C. A special interest was attributed to the changes in current density distribution. A spatially heterogeneous poisoning was observed when a metal-segmented flow field and current collector were used at the anode side.

Mathematical models are usually used to simulate the behavior of fuel cells and allow a better understanding of the phenomena occurring within the fuel cell. A dynamic one-dimensional isothermal phenomenological model was developed in order to capture the steady-state and the impedance spectra of two fuel cells

operated at 160 °C, one equipped with an in-house assembled MEA and the other with Celtec® - P1000 MEA. To obtain the impedance spectra, a small voltage perturbation was imposed to the simulator, over a wide range of frequencies, and both the current density amplitude and the phase were obtained. The phenomenological model captured the steady-state behavior for both fuel cell systems. Additionally, the Nyquist were fairly well predicted.

A major challenge for high temperature PEMFC development is the search for new materials. It was also aimed to study new materials for high temperature systems.

A non-conventional carbon support, single-wall carbon nanohorns (SWNH), was used for electrocatalyst preparation. The performance of electrodes based on platinum supported on single-wall carbon nanohorns and supported on carbon black was compared, using a phosphoric acid doped PBI membrane. Contrarily to what was expected, a similar peak power density was obtained for both carbon supports. The higher hydrophobic character of the SWNH carbon support originated a MEA with higher ohmic resistance. Moreover, the SWNH-based anode and cathode electrodes presented lower and similar charge transfer resistances, respectively, when compared to the conventional carbon support. Furthermore, two PEM, sulfonated poly (oxadiazole-triazole) copolymer and sulfonated polytriazole membranes, were prepared and characterized. The phosphoric acid doped sulfonated polytriazole was also evaluated in a fuel cell set-up at 120 °C and 2.5 % relative humidity and compared to phosphoric acid doped polybenzimidazole membrane. An initial similar performance was observed for both MEAs, however, after 7 hours of operation the performance of the sulfonated polytriazole membrane started to decrease due to severe phosphoric acid leaching.

# Sumário

A presente tese foca o estudo de células de combustível de electrólito de membrana polimérica com alimentação de hidrogénio (PEMFC) de temperatura elevada. Relativamente às células que operam a baixa temperatura, as PEMFC de temperatura elevada apresentam vantagens como: 1) melhoria da cinética de reacção electroquímica, 2) simplificação da gestão de água, 3) uso de sistemas de arrefecimento simplificados e possibilidade de recuperação de calor e 4) aumento da tolerância do catalisador ao monóxido de carbono.

Esta tese tem como objectivo aprofundar os conhecimentos relativos aos sistemas de PEMFC de temperatura elevada. Assim, foram estudados conjuntos membrana/ eléctrodos (MEAs) de temperatura elevada baseados em membranas de polibenzimidazole dopadas com ácido fosfórico (PBI/$H_3PO_4$), um comercial, Celtec® - P1000, e um montado no LEPAE. Adicionalmente, foi desenvolvido um modelo fenomenológico para simular o comportamento das PEMFC de temperatura elevada.

O processo de activação das duas MEAs de PBI / $H_3PO_4$ foi estudado a 160 °C. O processo de activação originou um decréscimo da resistência óhmica, assim como um aumento da actividade catalítica durante a activação das duas MEAs. A MEA montada no LEPAE foi também activada a diferentes temperaturas (entre 120 °C e 160 °C) e humidades relativas (entre 1,0 % e 5,0 %). A presença de água teve um efeito benéfico, baixando a resistência óhmica; no entanto, verificou-se que um excesso de água pode originar uma perda de ácido fosfórico no cátodo, levando desta forma a um aumento da resistência à transferência de carga. O envenenamento do catalisador de platina devido ao uso de hidrogénio contaminado com monóxido de carbono (até 3,0 %) foi estudado com base na MEA Celtec® - P1000. A diminuição do pico de potência e o efeito nos espectros de impedância foram quantificados e foi dada especial atenção às variações da distribuição espacial da densidade de corrente. Foi possível observar um envenenamento heterogéneo do

catalisador de platina no ânodo com recurso a um prato bipolar e colectores de corrente segmentados.

Os modelos matemáticos são geralmente usados para simular o desempenho de células de combustível e permitem a compreensão de fenómenos que ocorrem durante a operação. Foi desenvolvido um modelo fenomenológico, uni-dimensional e isotérmico, de forma a prever o comportamento em estado estacionário e em regime transiente de duas células de combustível equipadas com a MEA Celtec® - P1000 e a MEA montada no LEPAE. Para obter os espectros de impedância, foi imposta ao simulador uma pequena perturbação, sob a forma de uma onda sinusoidal de voltagem, e a amplitude da densidade de corrente e a fase foram registadas. O modelo fenomenológico simulou correctamente as curvas de polarização para os dois sistemas de PEMFC de temperatura elevada. Adicionalmente, os diagramas de Nyquist foram qualitativamente previstos.

A síntese e modificação de materiais são essenciais para o desenvolvimento de PEMFC de temperatura elevada. Desta forma, também era pretendido estudar novos materiais para aplicação em sistemas de temperatura elevada.

Foi usado na preparação de electrocatalisadores um suporte de carvão não convencional, denominado nano-cones de parede simples. O desempenho de eléctrodos contendo platina suportada em nano-cones foi comparado com eléctrodos em que a platina foi suportada em negro de fumo, usando uma membrana de PBI/$H_3PO_4$. Contrariamente ao esperado, foram obtidos picos de densidade de corrente similares. O carácter mais hidrofóbico do suporte de nano-cones originou uma resistência óhmica mais elevada da respectiva MEA. Além disso, a resistência à transferência de carga dos eléctrodos com suporte de nano-cones apresentou um menor valor para o ânodo e um valor semelhante para o cátodo, quando comparado com os eléctrodos preparados com suporte de negro de fumo. Adicionalmente, foram preparadas membranas de permuta protónica a partir de copolímero de poli (oxadiazole-triazole) sulfonado e politriazole sulfonado. As membranas de permuta protónica foram caracterizadas e as membranas preparadas

a partir de politriazole sulfonado dopado com ácido fosfórico foram também testadas numa instalação experimental de células de combustível, a 120 °C e 2,5 % de humidade relativa, e comparadas com membranas de polibenzimidazole dopadas com ácido fosfórico, nas mesmas condições experimentais. Inicialmente o desempenho revelou-se semelhante para as duas membranas; no entanto, após 7 h de operação, foi obervado um decréscimo no desempenho da MEA preparada com politriazole devido a perdas de ácido fosfórico da MEA.

# Sommaire

Cette thèse constitue une contribution à l'étude des piles à combustible à membrane électrolyte polymère (PEMFC) à haute température – 120 °C - 200 °C. Ces piles présent des avantages sur les plus connues piles à basse température: 1) meilleur cinétique de la réaction électrochimique, 2) gestion d'eau pour plus facile, 3) systèmes de refroidissement simplifiés et possibilité de récupérer la chaleur, et 4) réduction de la sensibilité à l'empoisonnement au monoxyde de carbone.

Ce travail a comme objectif d'augmenter les connaissances relatives aux systèmes de PEMFC à haute température. Donc, assemblages membrane-électrode (MEA) à haute température avec membranes à base de polybenzimidazole (PBI) dopé par l'acide phosphorique, une commerciale, Celtec® – P1000 et une MEA développée dans LEPAE, ont été testées; et un modèle phénoménologique a été développé pour simuler le fonctionnement de les PEMFC à haute température.

Le procédé de l'activation des MEA à base de PBI / $H_3PO_4$ a été étudié à 160 °C. La résistance ohmique a diminué et l'activité catalytique a augmenté au cours du procédé de l'activation des deux MEA. La dernière MEA (développée dans LEPAE) a été aussi activée sur températures (entre 120 °C et 160 °C) et humidités relatives (entre 1,0 % et 5,0 %) différentes. La présence de l'eau a montré un effet positif à la réduction de la résistance ohmique; toutefois, l'humidité excessive peut augmenter la résistance de la cathode, parce que l'acide phosphorique est perdu. L'empoisonnement du catalyseur du platine en raison de l'utilisation de l'hydrogène contaminé au monoxyde de carbone a été étudié pour la membrane Celtec® - P1000. La diminution de la puissance maximale et l'effet dans les spectres d'impédances on été quantifiés. Une attention particulière a été attribuée à des variations dans la répartition spatiale de la densité de courant. Il a été observé l'empoisonnement hétérogène du catalyseur du platine avec le recours d'une plaque bipolaire et un collecteur de courant à l'anode.

Les modèles mathématiques sont généralement utilisés pour simuler le fonctionnement des piles à combustible et ils permettent la compréhension des phénomènes au cours de l'opération. Un modèle phénoménologique, unidimensionnel et à température constante, a été développé pour prévoir la performance à l'état stationnaire et l'état transitoire des deux piles à combustible à 160 °C, la Celtec® - P1000 et la MEA développée dans LEPAE. Une perturbation sinusoïdale de la tension a été imposée au simulateur, dans un intervalle large de fréquences, et les réponses (amplitude de la de courant et phase) ont été mesurées. Le modèle phénoménologique simule les courbes de polarisation pour les deux systèmes de PEMFC à haute température. D'autre part, les diagrammes de Nyquist ont été prévus qualitativement.

La recherche des nouveaux matériaux est très importante pour le développement de PEMFC à haute température. Donc, son application aux systèmes à haute température a été aussi étudiée. Un support non-conventionnel au carbone, nanocornets de carbone mono-feuillet (SWNH), a été utilisé à la préparation des catalyseurs. La performance des électrodes du platine sur un support des nanocornets de carbone a été comparée aux électrodes du platine sur un support de noir de carbone. Les puissances maximales obtenues pour les deux systèmes ont été très similaires. Le support des nanocornets est plus hydrophobe que le support de noir de carbone, donc, la MEA à base des nanocornets a montré une résistance ohmique supérieure. D'autre part, la résistance de transfert de charge à l'anode avec nanocornets a été inférieur que la résistance à l'anode avec noir de carbone. Les cathodes sur les deux supports de carbone ont montré des résistances de transfert de charge similaires. Dans cette étude, deux membranes d'échange de protons, copolymère au poli (oxadiazole-triazole) sulfonaté et politriazole sulfonaté, ont été aussi préparées et caractérisées. Les membranes à base de politriazole sulfonaté dopé par l'acide phosphorique ont été testées à une installation expérimentale à piles à combustible, sur la température de 120 °C et l'humidité relative de 2,5 %. Ces membranes on été comparées avec les membranes à base de polibenzimidazole dopé par l'acide phosphorique, sur les mêmes conditions de fonctionnement. Il a été

observé une performance similaire au début de l'opération, pour les deux membranes. Cependant, après les premières 7 h de fonctionnement, il a été observé une diminution de la performance à la MEA à base de politriazole parce que l'acide phosphorique est perdu.

# Contents

# List of Figure Captions

# List of Table Captions

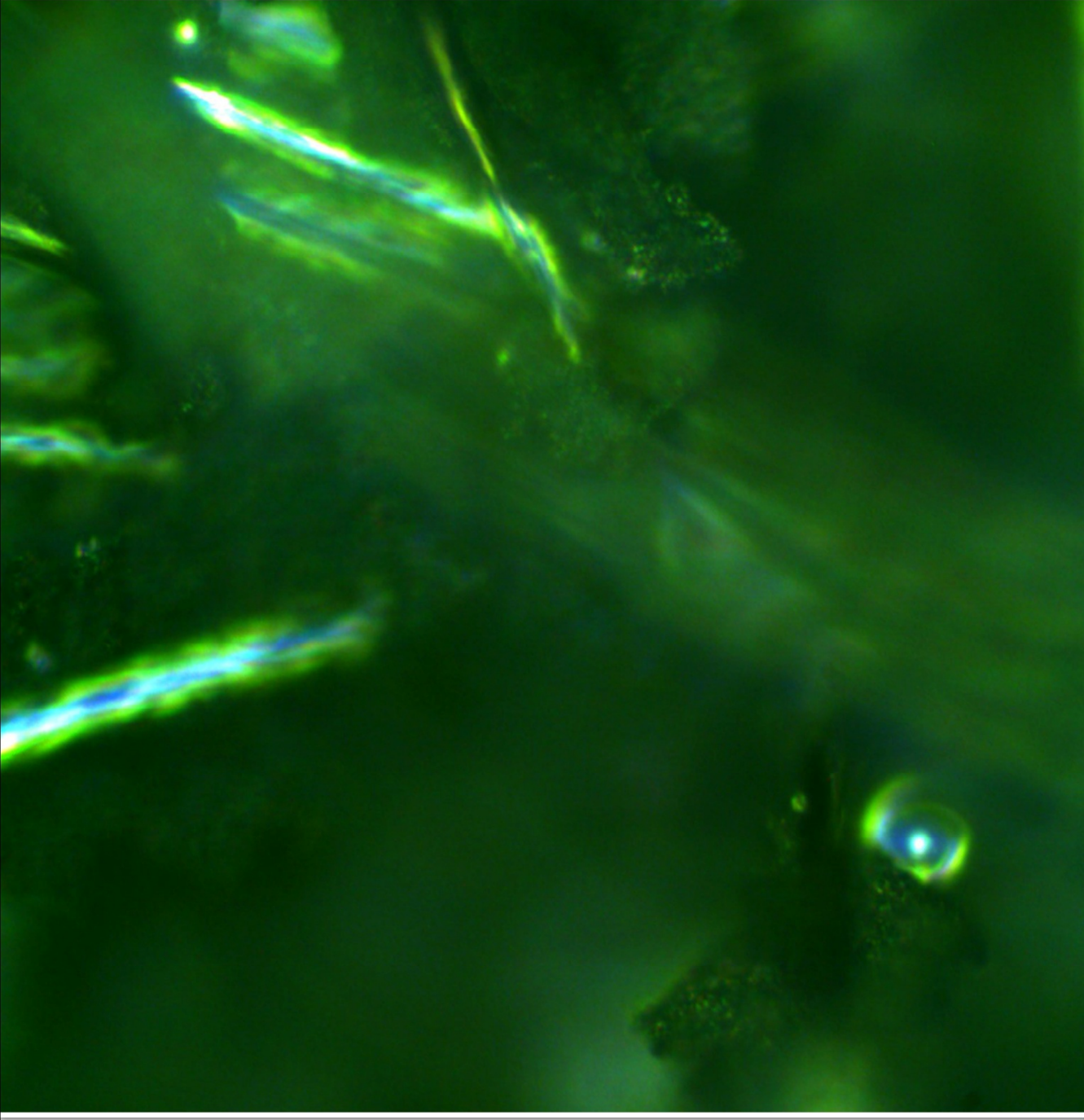

# Part I Introduction

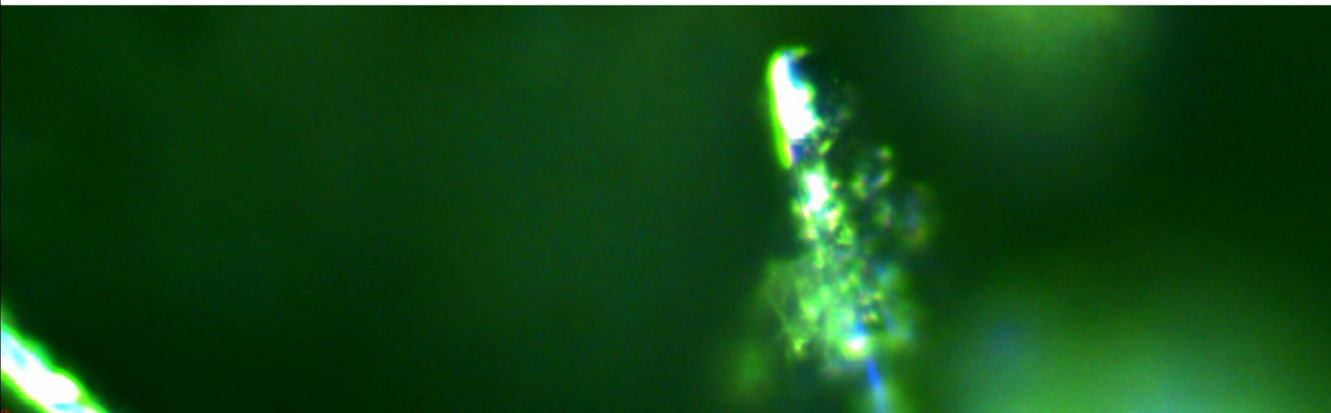

Microscopic view of gas diffusion layer

of Celtec® - P1000 MEA

# Chapter 1 Introduction

## 1.1 Energy

*Energy sustainability is a dynamic harmony between the equitable availability of energy- intensive goods and services to all people and the preservation of the earth for future generations [1].*

Presently the world depends heavily on fossil fuels, such as coal, oil and natural gas, as a source of energy (for heating, mechanical power and electricity generation). Fossil fuels represented in 2002 more than 75 % of the world's primary energy while traditional biomass (such firewood) accounted for 11 % and new forms of renewable energy accounted for less than 2.5 % [2]. If the so called "modern biomass" contribution (such as organic wastes) is not taken into account, the other sources of renewable energy, such as solar, wind, geothermal and waves / tidals, represented 0.55 % of world's primary energy use in 2006 [3], which is a very disappointing mark.

In the European Union (EU) the oil contribution for the primary energy pie is 45.7 %, from which 80 % is imported [4]. The liability of oil supply is a very important issue, especially in the transportation sector. Even though no shortage is expected in the nearest future, it is certain that a shortage of oil supply will happen, some said, around 40 years from now [2]. Other fossil fuel are more abundant and the coal should last for more 150 years [4] or 250 years [5] depending on the studies.

Additionally, there are concerns regarding the negative effects to the environment of using fossil fuels. Shortly, carbon dioxide ($CO_2$) and nitrous oxide ($N_2O$) are formed during combustion of fossil fuels whereas methane ($CH_4$) is emitted during production and transport of natural gas, coal and oil; all these are greenhouse gases. Carbon dioxide produced from fossil fuel represented 56.6 % of anthropogenic greenhouse gases emitted in 2004, in $CO_2$-equivalent basis [6]. Of special relevance is the transport sector: the released contaminants includes carbon monoxide (a health

hazard), nitrogen oxides (NO and $NO_2$ that react with water forming nitric acid) and non-burnt hydrocarbons that react with nitrogen oxides in the presence of sunlight to form ozone [5].

The increasing demand of energy for electricity production and for transportation lead the European Union to define emissions targets. The European Commission and the European Parliament intend to reduce the transport emissions to 120 $g_{CO2}\cdot km^{-1}$ by 2012 and 95 $g_{CO2}\cdot km^{-1}$ by 2020. These values represent a decrease of 1.4 and 1.7 times regarding the average emissions of new sold cars in 2004 [7]. Going further, the EU members agreed to use at least 20 % of all proposes energy from renewable sources and to include at least 10 % of energy from renewable sources for transportation by 2020 [8]. Several challenges are ahead: unlike fossil fuels, most renewable energy sources lack storage capability. Biofuels and electricity are known options. Electricity can be stored in a physical form, like thermal and kinetics energy (among others), or as chemicals, in rechargeable batteries [5]. Furthermore, energy can also be stored in chemical form in compounds such as hydrogen, methanol or methane.

## 1.2 The hydrogen energy economy

*Hydrogen is only as green as its energy source [7].*

Hydrogen, as electricity, is not an energy source but an energy carrier, produced from another source, either non-renewable or renewable. After production, both are environmentally friendly along the path of energy conversion. Unlike electricity, though, hydrogen can store and transport energy in large amounts [9].

Hydrogen can be produced from natural gas and naphtha by steam reforming, and from coal by gasification [5; 10]. It looks environmentally self-defeating to produce hydrogen from fossil fuel (and 90 % of world-wide production of hydrogen still relying on fossil fuels [5]) since carbon dioxide is produced along with hydrogen. The hope relies on $CO_2$ underground sequestration technology (involving capture and

storage of large amounts of $CO_2$), which is a very expensive and challenging approach [5; 11-12].

Hydrogen can also be produced by water splitting using electrical energy (through electrolysis), thermal energy (through thermochemical cycles), and solar energy (photoelectrolysis, biophotololysis and thermolysis) [5; 11; 13]. However, producing hydrogen by electrolysis is, at least, four times more expensive than generating hydrogen from natural gas and twice as much when coal is chosen as source [12].

Alternatively, high temperature pyrolysis of hydrocarbons and biomass can originate hydrogen and clean solid carbon black [11]. Still, a huge amount of land is required if one takes into account the amount of hydrogen necessary to replace fossil fuels.

Finally, hydrogen can be generated from intermittent renewable resources, as solar, wind and waves. Obviously, hydrogen produced from electrolysis or renewable resources is desirable, since it becomes truly sustainable, renewable and clean. To support a hydrogen energy economy, a massive volume of hydrogen is needed; the short term ambition is the clean production of hydrogen from the fossil fuels and the clean use of hydrogen, assuring a transition period.

Nonetheless, hydrogen is difficult to transport and store. The development of viable hydrogen storage and delivery infrastructures is still undergoing. Hydrogen can be stored as compressed hydrogen, liquid hydrogen or in metal hydrides [5; 14-15] The most common and efficient storage technology in use for storing hydrogen is at high-pressure, up to 700 bar, in tanks [15], with an energy density of 4.4 $MJ \cdot L^{-1}$ [14]. These tanks do not provide, though, a satisfactory range for a vehicle. To increase the range (up to 500 km) the pressure must be increased causing an increase in tank weight and cost; on the other hand, for transport and portable applications both the volume and weight must be minimized. Liquid hydrogen seems attractive since its density is 850 times greater than of the gaseous form [5], and the energy density can reach 8.4 $MJ \cdot L^{-1}$ [14]. However, 30 % of the hydrogen energy content is wasted in the liquefaction process [5; 15]. Additionally, liquid hydrogen cannot be stored for long periods due to boil-off rate. A third option is the use of metal hydrides; some metals and alloys can continually absorb and release hydrogen via the formation of unstable hydrides. Heat must be removed during the hydrogen intake and provided during the

release. The hydrides can achieve a high energy density, 6.7 $MJ \cdot L^{-1}$, but present a low gravimetric storage at ambient temperature [5]

## 1.3 Fuel cells

*Fuel cells have emerged as tantalizing alternatives to combustion engines due to their potential to reduce the environmental impact and geopolitical consequences of the use of fossil fuels [16].*

### 1.3.1 Definition

Fuel cells are electrochemical devices that convert chemical energy of a fuel into thermal and electrical energy. Electricity is produced as long as the fuel and oxidant are supplied. A fuel cell consists of an electrolyte sandwiched between an anode, were the fuel is supplied, and a cathode, were the oxidant is supplied - Figure 1.1. Typical reactants of fuel cells are hydrogen and oxygen. The electrolyte is a barrier to gas diffusion, avoiding direct combustion. At the anode, the hydrogen reacts catalytically originating electrons and ions. The ions migrate through the electrolyte while electrons flow through the external circuit. At the cathode, oxygen is supplied and reacts catalytically with electrons and ions, originating water.

The efficient delivery of the reactants is achieved using porous electrodes. Since the generation of current is proportional to the electrochemical reactions rate, catalysts are used to increase the speed and efficiency of reactions.

### 1.3.2 Fuel Cell Types

Fuel cells are classified according to the nature of the electrolyte, which defines the temperature range of the fuel cell and the anode fuel - Figure 1.2.

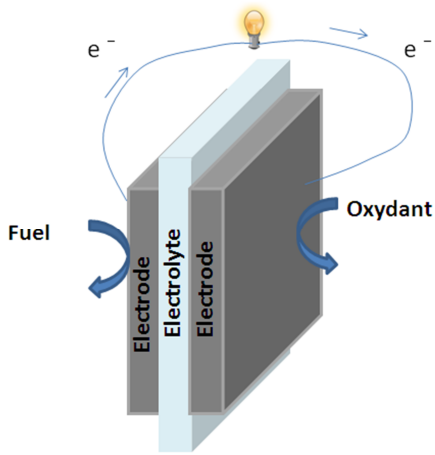


**Figure 1.1** Simplified fuel cell scheme.

Molten carbonate fuel cells (MCFC) use a molten mixture of alkali carbonates, like lithium carbonate and potassium carbonate, as electrolyte. The electrolyte is immobilized in a porous and chemically inert ceramic matrix ($LiAlO_2$) and both anode and cathode electrodes are nickel-based. A $CO_2$ recycling process must be added to MCFC systems since $CO_2$ is produced at the anode and consumed at the cathode electrode. Moreover, the electrolyte is corrosive and mobile, requiring the use of expensive materials and resistant layers [17].

Solid oxide fuel cells (SOFC) use a ceramic electrolyte, like yttria-stabilized zirconia, which is an oxygen ion conductor. The operation temperature can reach 1000 °C leading to thermal stress of materials and longer start-up times.

No precious metal catalyst is needed for both MCFC and SOFC since anode and cathode porous materials have high catalytic activity. As a consequence of high temperature operation for both fuel cell types, hydrogen, coal derived fuel gases or natural gas can be used as fuels. The produced heat can be employed into cogeneration schemes, yielding excellent efficiencies. The electrical efficiency varies between 50-60 % whereas with heat recovery the efficiency can reach 90 % [17-18]. Both fuel cell types reach a power range of megawatts [10] and can be used in combined heat and power (CHP) applications and as auxiliary power units for vehicles.

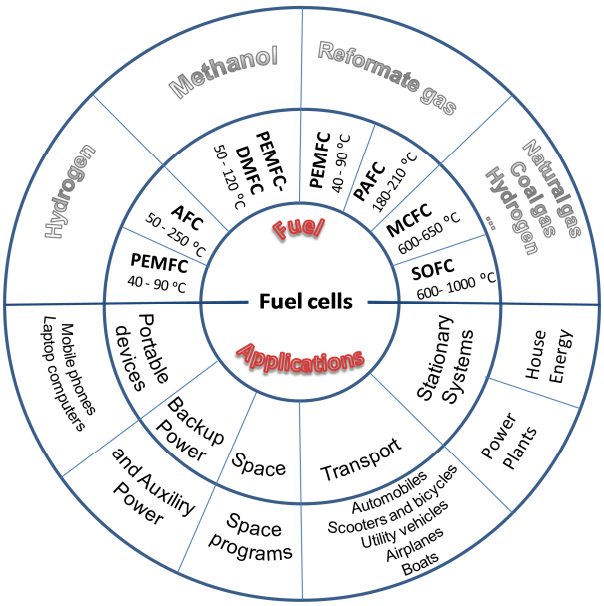


PAFC: Phosphoric Acid Fuel Cell
MCFC: Molten Carbonate Fuel Cell
SOFC: Solid Oxide Fuel Cell
AFC: Alkaline Fuel Cell
DMFC: Direct Methanol Fuel Cell
PEMFC: Polymer Exchange Membrane Fuel Cell

**Figure 1.2** Fuel cell types and applications (adapted from [19]).

Alkaline Fuel Cells (AFC) use aqueous potassium hydroxide as electrolyte, retained in a solid matrix. Either platinum or non precious metal catalysts can be used at the electrodes and, depending on the potassium hydroxide concentration, the operation temperature can vary between 50 °C and 250 °C. At the anode and cathode, pure hydrogen and pure oxygen must be used, since atmospheric levels of carbon dioxide are not tolerated by the electrolyte [18]. Potassium hydroxide reacts with carbon dioxide forming non conducting alkali carbonates. AFC can achieve a very high efficiency (70 %) but seems to be economically viable only for Space applications, despite the low costs of materials and electrolyte.

Phosphoric acid fuel cells (PAFC) use liquid phosphoric acid as electrolyte, usually contained in a SiC matrix. At operation temperature (between 180 °C and 210 °C), heat recovery is possible with the efficiency increasing from 40 % (without heat recovery) to 70 % [18]. A platinum catalyst is needed and, therefore, PAFC are

susceptible to carbon monoxide and sulphur poisoning. Furthermore, an electrolyte make up is required during operation since it gradually evaporates.

Both PAFC and AFC are the most mature fuel cell technologies, with AFC being developed since the 1950's and PAFC being the leading one in the early 1990's [16]. PAFC are semi-commercial and available for stationary electrical applications (*UTC Fuel cells*) while AFC were used in the NASA Space Program (Apollo and Space Shuttle) [20].

Polymer electrolyte membrane fuel cells (PEMFC) use a thin (20-200 μm) solid polymer membrane as electrolyte. PEMFC usually operates at temperatures below 90 °C and a catalyst, like platinum supported on carbon, is used. A more detailed description of PEMFC is given in the next section.

All fuel cell types, using hydrogen or generating it electrochemically from other fuels, are sketched in Figure 1.3.

Compared to traditional systems, fuel cells are advantageous in various ways. Fuel cells are mostly constituted by solid parts and have very few moving parts. For that reason, they are potentially more reliable and have a longer operating life and lower maintenance costs than an equivalent coal power station or internal combustion engine. Moreover, less noise is produced and low emissions make them a clean technology [17-18; 20-21]. With fuel cell systems the independent scaling between power - determined by the fuel cell size - and the capacity from the fuel reservoir is possible [18]. Besides, fuel cells can be built in a wide range of sizes, producing from watts to megawatts of power, thus embracing a vast range of possible applications - Figure 1.2.

Fuel cell systems have higher energy conversion efficiency when compared to an internal combustion engine or coal fired power station [17; 21]. Depending on the fuel cell type it is possible to use pure hydrogen, reformate hydrogen or even primary fuels like natural gas or methanol. The fuel cell electrodes do not undergo chemical changes, contrasting to batteries. Batteries have a limited amount of fuel and oxidant, which are depleted with use, and must suffer a time consuming recharge [17; 20].

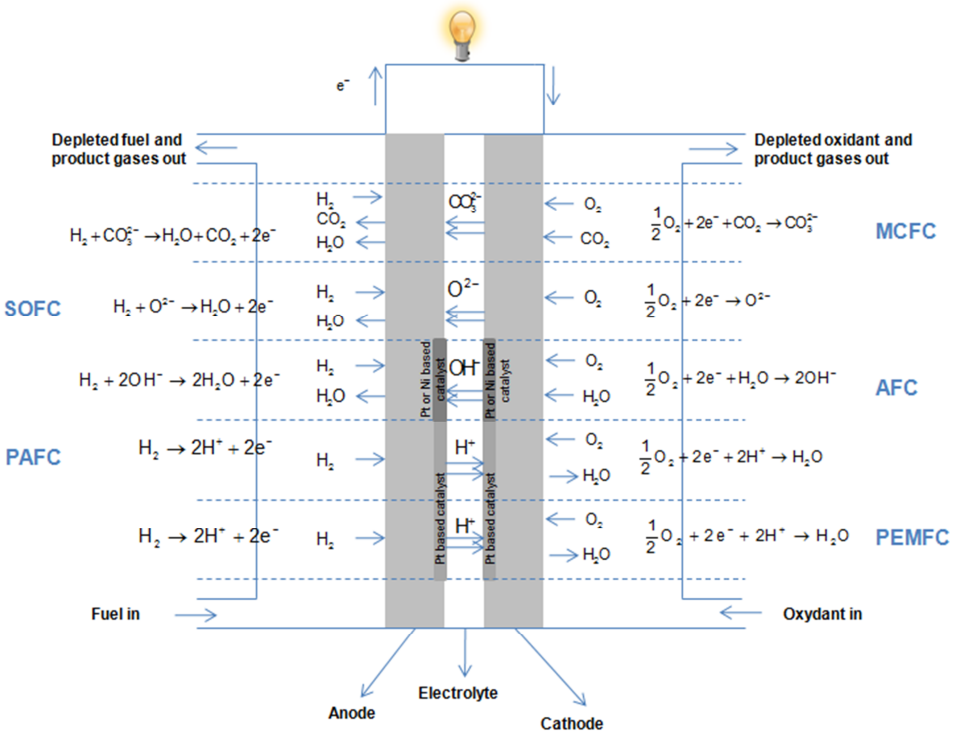


**Figure 1.3** Types of fuel cells and the respective reactions (adapted from [20]).

Taking into account all these advantages it is fair to wonder why these devices are not commercially available. Fuel cells are still expensive for most applications. Furthermore, improvements are necessary in power density (produced power per unit volume or per unit mass), durability and reliability.

### 1.3.3 Polymer electrolyte fuel cells (PEMFC)

About 90 % of research and development of fuel cell involves PEMFC [20]; they are simple and viable devices that have a quick start-up.

The polymer electrolyte must be an ionic conductor, impermeable to gases, electronically resistive and chemically and mechanically stable [16; 22]. The most widely used electrolyte in PEMFC is Nafion®. It has a backbone structure similar to

Teflon, providing chemical and mechanical stability, and sulfonic acid side groups that provide charge sites for proton transport - Figure 1.4.

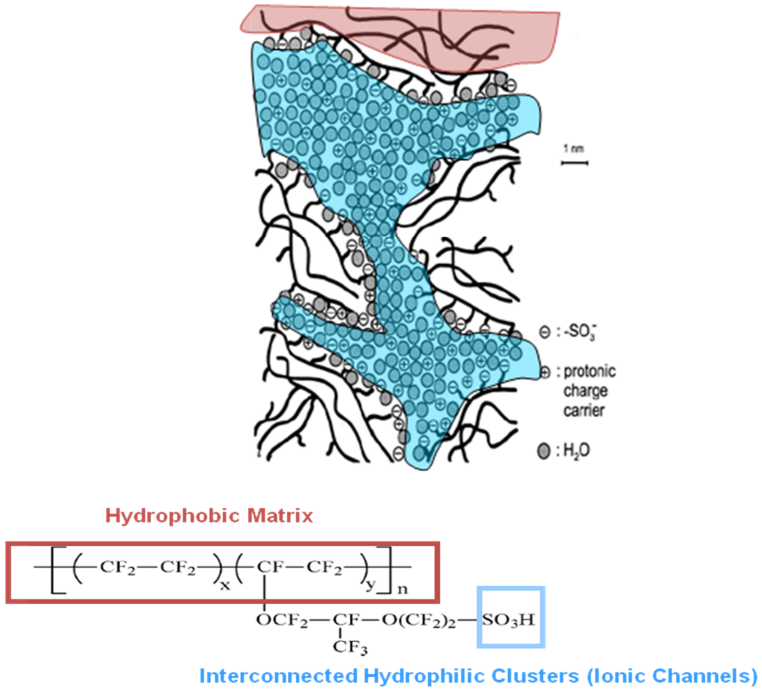


**Figure 1.4** Schematic microscopic view (adapted from [23]) and the chemical structure of Nafion®.

The proton transport through the electrolyte membrane occurs by the so-called "grotthuss" and by the so-called "vehicular" mechanisms. In the "grotthuss" mechanism the proton transport includes a rapid intermolecular proton transfer in a chain of hydrogen bonds, and a subsequent reorientation of the dipoles in order to produce a configuration which allows the next polarization event [24]. For the Nafion® membrane, however, the "vehicular" mechanism is dominant. When water is present, protons in the interconnected hydrophilic channels form hydronium complexes and detach from the sulfonic acid side groups [18; 22]. The hydronium complexes, rather than simple protons, are transported across the membrane from the anode to the cathode, in the aqueous phase.

To ensure membrane hydration, and therefore conductivity, inlet gases at the anode and cathode are fed well humidified, with relative humidity close to 100 %; also,

during the operation of the fuel cell, water is produced at cathode due to electrochemical reaction. This way, water is transported through the membrane by electro-osmotic drag (migrates with protons from the anode to the cathode), and back diffusion (water that is not bonded move in the opposite direction). Water management has a significant impact on fuel cell performance and is one of the key issues for the system design [25-30]. The dependency of water presence for proton transport in Nafion® and related polymers restricts the PEMFC operation to low temperatures (< 90 °C).

The electrolyte membrane is placed between the anode and the cathode electrodes and these three elements are often referred to as membrane electrode assembly (MEA). The MEA, on the other hand, is placed sandwiched by bipolar plates - Figure 1.5.

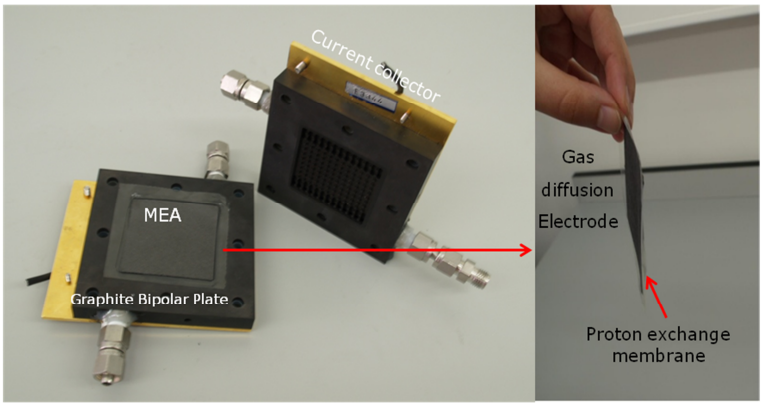


**Figure 1.5** Single cell (Electrochem FC25-01SP/DM) with a graphite bipolar plate and membrane electrode assembly.

The bipolar plates highly contribute for the fuel cell volume and are usually made of graphite composites or metal-based and contain channels. The design includes the cross section shape, distribution channel pattern, and plate and channels dimensions. The bipolar plates have several functions, i) distribute the fuel and oxidant uniformly over the respective electrode surface, ii) collect current and offer an electrical conductive medium, iii) facilitate water and heat management and iv) prevent

leakage of gases. They must have high mechanical strength, be impermeable to gases and resistant to corrosion. Last but not least, bipolar plates must be produced from cheap materials [31-33].

Each electrode has a porous diffusive layer (usually carbon cloth or carbon fiber paper). It must be an optimal electron conductor in order to transports electrons to and from the catalyst layer, ensure that reactants diffuse to the catalyst layer and assist in the water management of the fuel cell. The diffusion layer is wet-proofed with a PTFE coating to ensure that the pores of the diffusion layer do not flood with liquid water [34-35].

Between the membrane and the diffusion layer lays the catalyst layer, where the half redox reaction take place. When pure hydrogen and oxygen/air are used as fuel/oxidant, the catalyst is usually based in platinum supported in carbon, in order to increase the electrochemical active surface area [36]. Catalyst load have been reduced from 4 $mg_{Pt} \cdot cm^{-2}$ to ca. 0.4 $mg_{Pt} \cdot cm^{-2}$ in the past decades, as a result of an optimized dispersion of catalyst nanoparticles [16]. Because there are three kinds of species that participate on the electrochemical reactions (gases, protons and electrons) the electrochemical reactions take place on the portion of the catalyst where the three meet - Figure 1.6 (b). At the anode, the hydrogen is catalytically reacted, splitting into electrons and protons, and oxygen is supplied to the cathode. The electrons flow through the external circuit, producing DC power, and protons permeate the electrolyte, which provides a pathway towards the cathode side. At the cathode side, electrons, protons and oxygen react, originating water.

A scanning electron microscopy of membrane electrode assembly can be seen in Figure 1.6 (c).

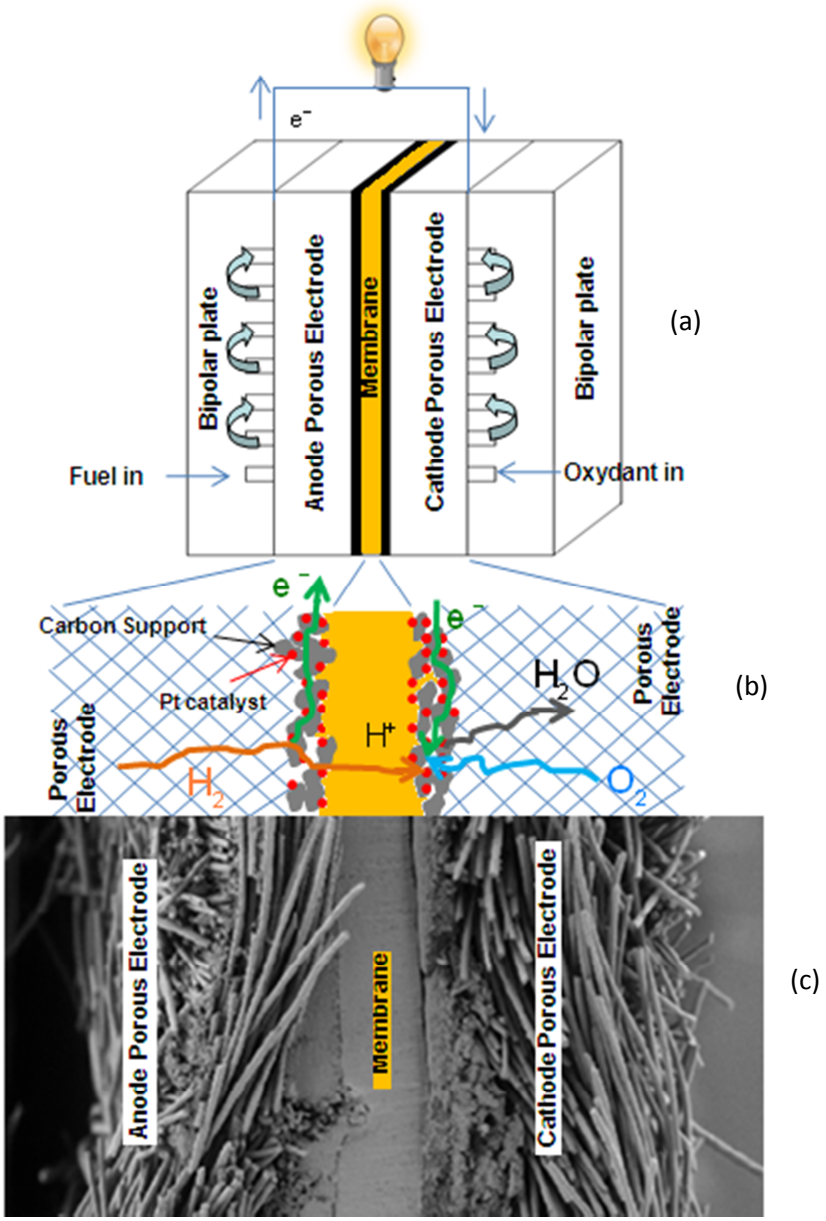


**Figure 1.6** Cross section of a fuel cell (a), the basic principle of operation in PEMFC (b) and scanning electron microscopy of membrane electrode assembly (c).

PEMFC shows the highest power density of all fuel cell types and reaches an efficiency of 60 %. They can be used for small-scale stationary power generation, portable applications and are the favorite for the transport applications [37-38].

Since the 90's, several car companies developed hydrogen fuel cell vehicles (HFCV). Recent developments were addressed by Ford Motor Company [39], GM [40], DaimlerAG/Mercedes-Benz [41], Hyundai [42] and Toyota [43]. There are still several techno-economical challenges to be addressed concerning the fuel cell cold weather operation, hydrogen storage (driving range limits), fuel supply infrastructures and cost and availability of materials. The increase on reliability and durability is an important research topic as mentioned above. Finally, HFCV are expected to be affordable, functional, attractive, and safe in order to gain the consumers approval. Frenette and Forthoffer [39] suggested that without major technologic breakthroughs, the actual predictions of 2010-2035 for HFCV major market penetration are quite optimistic.

Besides gas fuels like hydrogen and reformate gas, liquid fuels, such as methanol and ethanol, can be used. Direct methanol fuel cells (DMFC) are a PEMFC that directly oxidizes methanol (actually electrooxidizes) to obtain electrons and protons. The reaction mechanism includes several steps resulting in a slow oxidation kinetics. Some of the reaction paths lead to the formation of carbon monoxide. Additionally, carbon dioxide is produced as a by-product at the anode side. Moreover, methanol can easily permeate from the anode to the cathode decreasing the fuel cell performance [16; 22; 38]. PtRu alloy is used at the DMFC anode since ruthenium can electro-oxidize the CO adsorbed onto the Pt catalyst, providing CO tolerance. For low power portable applications, DMFC are the most promising candidates to replace batteries [38; 44].

### 1.3.4 PEMFC characterization

The standard electrochemical technique for fuel cell characterization is the polarization curve, also called the I-V curve. It is obtained by recording the fuel cell voltage as a function of the current density, in steady-state conditions. A typical voltage-current density curve for a PEMFC is represented in Figure 1.7. The I-V curve is a result of performance losses [45]: at low current densities, the fuel cell voltage decreases sharply due to kinetic losses associated to oxygen reduction reaction (ORR)

and hydrogen oxidation reaction (HOR). At intermediate current densities the voltage loss caused by proton transport becomes significant while the activation overvoltage remains fairly constant. At high current densities the mass transfer resistance becomes significant due to transport limitations through the gas diffusion layer and catalyst layer. In this region the fuel cell voltage decreases sharply.

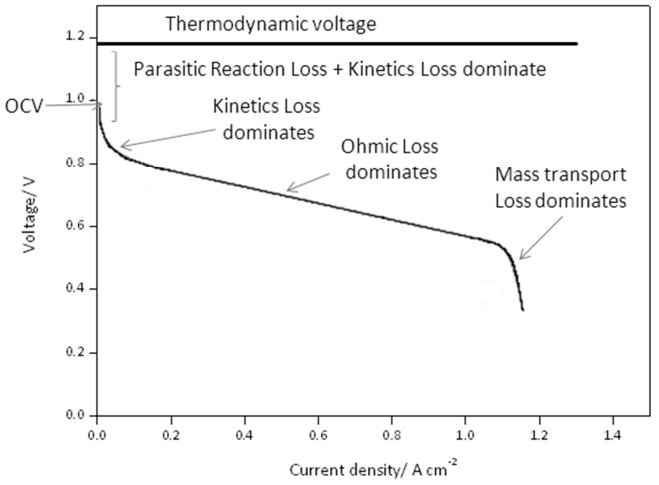


**Figure 1.7** Voltage-current density curve and sources of voltage loss.

The steady-state characterization, however, does not provide detailed information concerning the influence of different processes occurring during fuel cell operation. Other electrochemical techniques such electrochemical impedance spectroscopy (EIS), current interrupt measurements and cyclic voltammetry (CV), are often used for fuel cell characterization [45-46].

EIS is a time resolving technique that allows differentiating the contributions of each fuel cell process, such as mass transport in the gas diffusion electrodes, charge transport in the polymer electrolyte membrane and interfaces and electrochemical reaction kinetics [46]. EIS is a helpful technique for diagnosing problems within the components and for fuel cell optimization.

In this technique, a sinusoidal wave of low amplitude ($V_0$) is applied in voltage as a perturbation signal to the fuel cell voltage ($V_{cell}$) over a wide range of frequencies (usually from 100 kHz to 100 mHz):

$$V(t) = V_{cell} + V_0 \sin(\omega t) \tag{1.1}$$

where $V(t)$ is the voltage for instant time $t$ and $\omega$ is the radial frequency. The relationship between radial frequency and frequency ($f$) is given by $\omega = 2\pi f$ .

The perturbation is usually very small, normally 5 mV or 10 mV, so the response of the cell can be considered pseudo-linear, Figure 1.8. The system response is a sinusoidal current density with the same frequency, with amplitude $J_0$ and phase shifted by $\varphi$:

$$J(t) = j_{cell} + J_0 \sin(\omega t + \varphi) \tag{1.2}$$

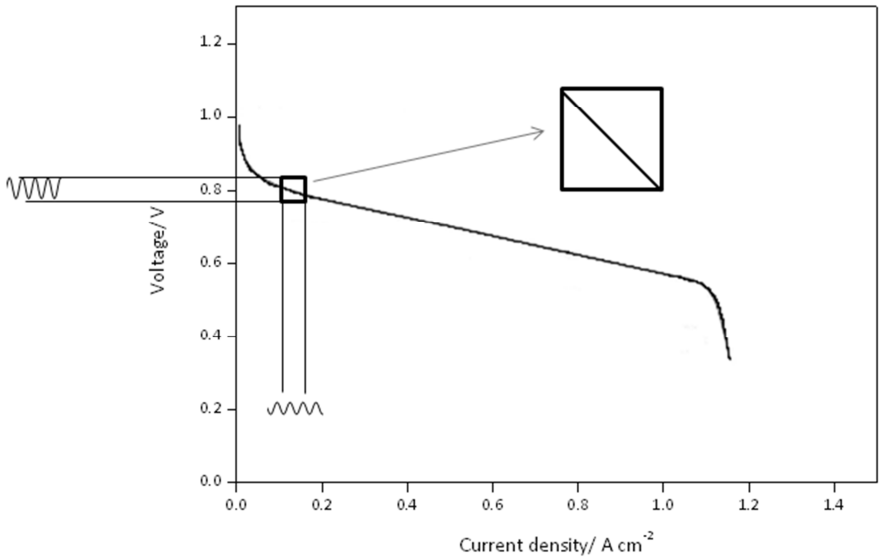


**Figure 1.8** Sinusoidal voltage perturbation and correspondent sinusoidal response in a pseudo-linear location of the I-V curve (adapted from [18]).

The impedance of the system ($Z$) can be obtained from [18]:

$$Z = \frac{V_0 sin(\omega t)}{J_0 sin(\omega t + \varphi)} = Z_0 \frac{sin(\omega t)}{sin(\omega t + \varphi)} \quad (1.3)$$

where $Z_0$ is the impedance magnitude.

It is possible to express the impedance as a complex function, in terms of real ($Z'$) and imaginary ($Z''$) components:

$$Z = \frac{V_0 e^{j\omega t}}{J_0 e^{j\omega t - j\varphi}} = Z_0 \exp(j\varphi) = Z_0 (\cos\varphi + j \sin\varphi) \quad (1.4)$$

where $j = \sqrt{-1}$. The real component of the impedance is $Z' = Z_0(\cos\varphi)$ and the imaginary component of the impedance is $Z'' = Z_0(\sin\varphi)$.

The typical outputs of an EIS experiment are the Nyquist and Bode plots. The Nyquist plot shows the imaginary versus the real parts of the impedance while in the Bode plot it is shown the impedance magnitude and phase shift as a function of frequency.

## 1.4 High temperature polymer electrolyte fuel cells (HT-PEMFC)

*The development of high temperature specific PEMFC designs is of key importance to mitigate issues of membrane dehydration and MEA degradation [47].*

The Nafion® membrane has very high proton conductivity in fully humidified conditions, 0.1 S·cm$^{-1}$ at 30 °C and 0.2 S·cm$^{-1}$ at 80 °C [47], and a lifetime of over 60 000 hours at 80 °C [22]. However, the proton conductivity of the Nafion® membrane decreases to 1.4×10$^{-4}$ S·cm$^{-1}$ when relative humidity decreases to 34 % at 30 °C. At temperatures below 90 °C, there is a dual-phase water system that carries the risk of starvation at the anode, dehydration of the membrane and flooding at the cathode, hindering the oxygen in the gas diffusion layer. Auxiliary components are needed for the hydrogen humidification in the fuel cell system. The constant changes

in the water content in the membrane may result in swelling and shrinkage and, ultimately, on the mechanical deterioration of the membrane and the membrane/catalyst interface. Water management is then a delicate issue. Operating a fuel cell at temperature above 100 °C may mitigate water management problems since only a single phase of water is involved [47-50].

A PEMFC produces heat that has to be removed, via a cooling system, in order to maintain the working temperature. Temperature distribution would affect the water management, the rates of electrochemical reactions and the gas and water transport. Operating at temperatures higher than 100 °C has the advantage of generating larger driving force for more efficient cooling. A simplified cooler system can then be used and the overall system efficiency can be significantly increased with waste heat recovery.

The temperature increase has a beneficial effect on the electrochemical kinetics at both electrodes, which is especially important for the cathode side (exchange current density for the oxygen reduction reaction is much smaller than for the hydrogen oxidation reaction). Nonetheless, the overall thermodynamic drive force (reversible fuel cell voltage) decreases with increasing temperature [47].

Carbon monoxide traces at the hydrogen feed strongly affect the PEMFC performance at temperatures below 90 °C due to strong adsorption on platinum electrocatalysts and, consequently, pure hydrogen or purified reformate gas (with CO concentration < 10 ppm) are usually used at the anode. The carbon monoxide adsorption in platinum is associated to negative entropy and therefore disfavored at higher temperatures [47; 51-53].

All of these factors have caused extensive research related to alternative HT-PEMFC materials, especially polymer electrolyte membranes.

### 1.4.1 High temperature polymer electrolyte membranes

The design of proton conducting membranes for high temperature operation represents a tremendous challenge. The membranes for high temperature PEMFC

currently under development can be classified into membranes that use water as proton carrier and anhydrous membranes [47-49; 54-57]. These two approaches are discussed below.

#### *1.4.1.1 Membranes that use water as proton carrier - inorganic/organic composite membranes*

The first approach to obtain a conducting membrane for high temperature operation is to increase water retention at temperatures near and above its boiling point, thus maintaining the proton conductivity. The most studied membranes are the inorganic/organic composite membranes. They consist on an ionomer matrix in which inorganic or inorganic-organic solid particles (usually nano-size) are dispersed.

The inorganic fillers can be proton conductive (such heteropolyacids, zirconium phosphates and phosphonates) or hygroscopic metal oxides (like silica, alumina, and zirconia) [49]. The composite membranes are expected to increase proton conduction, water retention capability and mechanical properties, and suppress the fuel crossover, when compared to the un-modified polymer in the same operational conditions.

The composite membrane can be produced by 1) adding solid particles to the ionomer solution followed by casting, 2) impregnation of membranes with solutions of inorganic precursors or 3) in situ sol–gel reaction to produce a metal oxide [47].

Since Watanabe and co-workers [58] suggested the use of compounds such as silica and titania to prepare Nafion® composite membranes, several works have been published regarding the use of composite Nafion® membranes for high temperature and low relative humidity (RH) operation. Some of the most recent works on Nafion® composite membranes (since 2008) are highlighted in Table 1.1. Commonly to all these composite membranes, the water uptake ability is higher when compared to the plain polymer membrane.

Non-perfluorosulfonated polymers can also be used as ionomer matrix for inorganic/organic composite membranes. For instance, sulfonated

polyetheretherketone (SPEEK) membranes were prepared with titania nanosheets [59], $SiO_2$ [60] and with solid proton conductors developed from heteropolyacids loaded onto mesoporous molecular sieve MCM-41 [61] and sulfonated polysulfone was investigated with titanium dioxide ($TiO_2$) nanoparticles [62].

**Table 1.1** Nafion® composite membranes.

| Reference | Modifiers | *Remarks* |
|---|---|---|
| [63] | $SiO_2$ and $ZrO_2$ nanoparticles | *Proton conductivity of $10^{-2}$ S·cm$^{-1}$ at 100 °C / 0 % RH for Nafion®–5 wt. % $ZrO_2$.* |
| [64] | Zr nanoparticles | *Enhanced water retention ability at 100 °C.* |
| [65] | $TiO_2$ | *Higher performance at 110 °C / moderate humidification in a $H_2$ / $O_2$ fuel cell.* |
| [66] | Titanate nanotubes (TNT) | *Proton conductivity of $3.4\times10^{-1}$ S·cm$^{-1}$ at 100 °C / 0 % RH for Nafion® - 5 wt. % TNT ($2.5\times10^{-3}$ S·cm$^{-1}$ for plain polymer).* |
| [67] | Sulfated $ZrO_2$ | *Current density of 0.93 A·cm$^{-2}$ at 0.6 V and at 70 °C / 30 % RH for Nafion® - 5 wt. % $ZrO_2$ (0.20 A·cm$^{-2}$ for plain polymer) in a $H_2$ / Air fuel cell.* |
| [68] | Phospho-silicate | *Conductivity of $0.27\times10^{-3}$ S·cm$^{-1}$ for Nafion®-3:7 (P/Si ratios) at 140 °C / 0 % RH (<$0.05\times10^{-3}$ S·cm$^{-1}$ for pure polymer).* |
| [69] | MxOy nanopowders x = Ti, Zr, Hf, Ta and W | *Conductivity of $2.8\times10^{-2}$ S·cm$^{-1}$ for Nafion® - 5wt. % $(HfO_2)n$ at 135 °C / 100 % RH.* |
| [70] | Mesoporous Zr phosphate | *Power peak density of 0.353 W·cm$^{-2}$ for 5 wt. % filler (0.24 W·cm$^{-2}$ for pure polymer) at 70 °C / 18 % RH in a $H_2$ / $O_2$ fuel cell.* |
| [71] | $SiO_2$, $ZrO_2$, $ZrO_2$–$SiO_2$ | *Higher power peak density (0.683 W·cm$^{-1}$) at 120 °C / 50% RH for Nafion® - 10 wt. % $ZrO_2$ – $SiO_2$ (Zr : Si = 0.5) in a $H_2$ / Air fuel cell.* |
| [72] | esoporous silica with sulfonic groups | *Proton conductivity for Nafion® - 13 wt. % filler 5 times higher than the plain membrane at 95 °C / 90 % RH.* |

### *1.4.1.2 Anhydrous membranes*

In anhydrous proton-conducting polymers the proton conduction does not depend on the water but relies on other proton solvents immobilized in the membrane. In this context, phosphoric acid and aromatic heterocycles have attracted attention. A second approach is the development of polymers that exhibit proton conductivity as an intrinsic property [56]. In all these cases, the proton transport is dominated by the "grotthuss" mechanism.

*Nitrogen-containing aromatic heterocycles as proton carriers*

The use of nitrogen-containing aromatic heterocycle molecules as proton carriers (either as doping agents or immobilized in the polymer backbone) have been studied. Molecules as imidazole, benzimidazole and pyrazole, have been seen as a possible replacers for water at high temperature operation [23; 73-74]. These heterocycles exhibit hydrogen bond interactions and, to a certain extent, undergo self-dissociation [56]. When heterocycles are immobilized in a polymer backbone, extensive aggregates of heterocycle molecules may be formed by hydrogen bonding [23; 74-76].

*Acid-base complexation*

One of the approaches to high temperature proton conducting membranes is acid - base complexation. Polymers bearing basic sites (ether, alcohol, imine, amide, or imide groups) act as a proton acceptor and react with strong or medium strong acids like phosphoric or sulphuric acid, establishing hydrogen bonds [54].

Phosphoric acid ($H_3PO_4$) is very interesting because of its low vapor pressure at elevated temperatures and high proton conductivity in pure state. This feature is due to proton conduction mechanism by self-ionization and self-dehydration. In the presence of basic polymers, phosphoric acid undergoes hydrogen bond interactions and proton transfer reactions.

Several polymers were investigated for preparing acid-base electrolytes. In early investigations, polymers such as polyethyleneimine, polyethyleneoxide or polyacrylamide were studied, as summarized by Schuster *et al.* [56]. At temperatures above 100 °C high conductivities were achieved but the mechanical stability was compromised [49]. A major breakthrough happened when polybenzimidazole was first suggested for acid base complexation by Wainright *et al.* [77] in 1995. Nowadays, the most studied acid-basic polymer complex is phosphoric acid doped polybenzimidazole type polymer [54; 57].

Polybenzimidazole is a linear condensation polymer with benzimidazole moieties in the backbone [57], Figure 1.9, and can be synthesized from tetraamines and diacids in polyphosphoric acid (PPA), named the *PPA process* [78-80]. The commercially named PBI is poly(2,2'-(m-phenylene)-5,5'-bibenzimidazole), from Celazole®. However, the acronym is also used for a large family of aromatic heterocyclic polymers that contain benzimidazole units. Polybenzimidazole is an ionic and electronic insulator, which, after doping with strong or medium strong acid, becomes an ionic conductor.

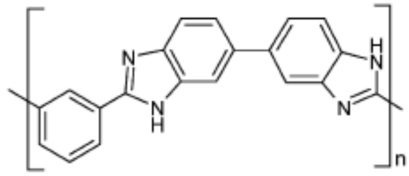

**Figure 1.9** Structure of poly(2,2'-(m-phenylene)-5,5'-bibenzimidazole).

Phosphoric acid doped PBI membranes exhibit a good proton conductivity. Proton transport is related to temperature, acid doping and relative humidity [81-86]. The temperature dependence of the conductivity can be described by the Arrhenius equation [81; 83; 86-87]:

$$\sigma \cdot T = \sigma_0 \exp\left(\frac{-E_a}{\Re T}\right) \tag{1.5}$$

Where $\sigma$, $\sigma_0$, $E_a$, $\Re$ and $T$ are the membrane conductivity ($S \cdot cm^{-1}$), pre-exponential factor ($S \cdot K^{-1} \cdot cm^{-1}$), proton conducting activation energy ($J \cdot mol^{-1}$), gas constant ($J \cdot K^{-1} \cdot mol^{-1}$) and temperature (K), respectively.

For a given temperature and relative humidity, the conductivity increases as the doping level increases. The maximum degree of protonation of PBI is reached when there are two $H_3PO_4$ molecules per polymer repeat unit [81; 83]. In this case all acid molecules are bonded to the polymer backbone and donate a proton to the unprotonated N site. Proton transfer occurs mainly between protonated and nonprotonated imino nitrogen groups. For doping levels below 2, PBI membranes have low conductivity and can't be used as electrolytes in fuel cells. Kawaraha *et al.* [85] reported a conductivity of $10^{-5}$ $S \cdot cm^{-1}$ for a PBI membrane with doping level of 1.9, at 160 °C and anhydrous conditions.

For protonation levels higher than 2, an excess of $H_3PO_4$ exists. For doping levels between 2 and 4, and since the acid molecules are still too far apart, the proton transfer would result mostly from a cooperative motion of two protons along the polymer-anion chain. For doping level higher than 4, however, protons migrate mostly along anions chains $H_3PO_4 \cdots H_2PO_4^-$ and $N\text{-}H^+ \cdots H_2PO_4^-$ by successive proton transfer and anion reorientation step and along the acid and anion chain, $H_2PO_4^-\text{-}H^+ \cdots H_2PO_4^-$. At very high doping levels the proton transfer mechanism approaches those of the liquid acid [82-83].

The amount of water present in phosphoric acid doped PBI affects the proton conductivity as in the case of concentrated phosphoric acid. The increase of relative humidity lowers the viscosity within the membrane, leading to higher mobility. Besides, hydrogen bonds are formed between water molecules and phosphoric acid and the imino group of PBI, allowing faster proton transfer and therefore higher conductivity [77; 83].

Different acid doping levels, relative humidities and temperature origin different dominant mechanisms for proton transfer, along different chains or paths. Ma *et al.* [83] indicated the order of the rate of proton transfer among the involved species:

$$H_3PO_4\left(H_2PO_4^-\right)\cdots H\text{-}OH > H_3PO_4 \cdots H_2PO_4^- > N\text{-}H^+ \cdots H_2PO_4^- > N\text{-}H^+ \cdots H\text{-}OH > N\text{-}H^+ \cdots N\text{-}H$$

The electroosmotic drag coefficient of water for acid doped PBI membranes was found to be almost zero [88] and permeability towards hydrogen and oxygen is low [89]. Good thermal properties were attributed to pristine and doped PBI up to 500 °C [80].

PBI membranes present some drawbacks such poor solubility in common organic solvents [90] and very rigid molecular structure, despite their good mechanical properties [91]. At very high levels of $H_3PO_4$ doping, however, mechanical strength decreases while the conductivity is sacrificed for low levels of $H_3PO_4$ doping [54; 92]. Another negative aspect is the possibility of leaching of free acid in the membrane during fuel cell operation.

Phosphoric acid doped PBI type membranes have been designed and synthesized with tailored properties. The modifications in the polybenzimidazole structure aim to achieve high molecular weight, improved solubility and processibility and tailor the basicity of the polymer. PBI can be modified by 1) synthetically modifying the structure and 2) post polymerization substitution. Some examples are provided.

Poly(2,5-benzimidazole) (ABPBI) is a simple benzimidazole polymer (Figure 1.10 (a)). It does not have a phenylene ring in the backbone, which allows an improved affinity to the phosphoric acid. Besides, it can be prepared easily from a single and inexpensive monomer (3,4-diaminobenzoic acid) by condensation in PPA. Typical conductivity values for ABPBI·$3H_3PO_4$ is $1.5\times10^{-2}$ S·cm$^{-1}$ at temperatures as high as 180 °C in dry conditions [93].

Xiao *et al.* [92] prepared homopolymers from 2,4 -, 2,6 -, 2,5 -, and 3,5 - pyridine dicarboxylic acid (PDA) and 3,3',4,4'-tetra-aminobiphenyl. The incorporation of pyridine group (and additional nitrogen containing aromatic heteroclycle) increased the basicity of the polymer while kept thermo-oxidative stability. The additional nitrogen containing aromatic heteroclycle improved the interaction with phosphoric acid. Moreover, the 2,5-PDA originated a *para* substitution pattern on the pyridine ring (Figure 1.10 (b)). The resulting membranes were mechanically strong at very high doping of phosphoric acid, contributing to proton conductivities up to 0.2 S·cm$^{-1}$ at 200 °C.

Carollo *et al.* [94] showed that improvements on the acid retention and conductivity can be achieved by increasing the molecular weight and including more nitrogen atoms in the PBI backbone and/or changing the spatial arrangement of the N atoms. The studied polymer structures are given in Figure 1.10 (c) - (e).

Kim *et al.* [90] synthesized a PBI containing benzimidazole side groups (BIpPBI) - Figure 1.10 (f). This polymer was found to be more soluble in organic solvents and could absorb more acid than PBI. Thus, it was achieved a maximum proton conductivity of $1.6\times10^{-1}$ S·cm$^{-1}$ for the BIpPBI membrane and $6\times10^{-2}$ S·cm$^{-1}$ for the acid-doped *m*PBI membrane, at 180 °C and anhydrous conditions. The bulky side groups disrupted the rigid structure and increased the free volume.

Organosoluble polymers based on fluorine-containing PBI, Figure 1.10 (g), were also prepared through molecular modification [91]. The resultant membranes had good thermooxidative stability and mechanical properties, and low methanol permeability.

Asencio *et al.* [95] studied the effect of sulfonation of pre-cast ABPBI by sulfuric acid doping and heat treatment followed by phosphoric acid impregnation. They achieved a degree of sulfonation between 35 % and 49 % of the benzimidazole rings. The phosphoric acid absorption increased with the degree of sulfonation, and therefore the conductivity also increased (maximum conductivity measured in dry conditions was $3.5\times10^{-2}$ S·cm$^{-2}$ at 185 °C). The thermal stability was comparable to those of ABPBI and PBI. Recently, polybenzimidazoles containing sulfonic acid groups on the main chain phenyl ring were synthesized [96]. The resultant membranes had high molecular weight, ionic conductivity and excellent mechanical properties. A conductivity of $3.26\times10^{-1}$ S·cm$^{-1}$ was obtained for a doping level of 39 mol phosphoric acid/PBI, at 180 °C.

Other methods for increasing the PBI phosphoric acid level without compromising the mechanical strength includes ionic cross linking [97-99], covalent cross linking [100] and the preparation of composite membranes of PBI with inorganic components. Inorganic fillers can have a positive effect on the membrane water uptake, permeability towards methanol, mechanical stability and proton conductivity. Some examples of recent works are presented in Table 1.2.

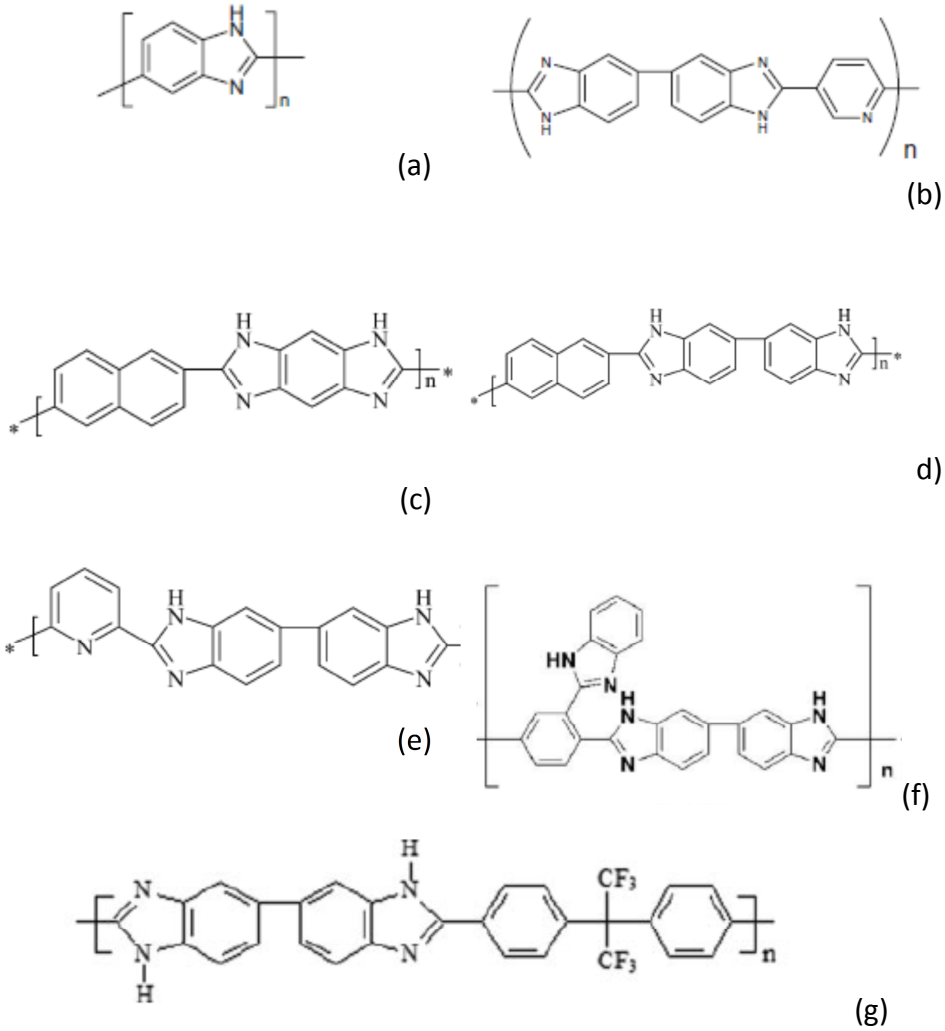


**Figure 1.10** Poly(2,5-benzimidazole) (a); 2,5 PPBI (b); poly(2,6-(2,6-naphtyliden)-1,7-dihydrobenzo[1,2-d;4,5-d']diimidazole) (c); poly(2,2'-(2,6-naphtyliden)-5,5'-bibenzimidazole (d); poly(2,2'-(2,6-pyridin)-5,5'-bibenzimidazole) (e); Poly[2,20-(2-benzimidazole-p-phenylene)-5,5'-bibenzimidazole] (f); fluorine-containing PBI (g).

**Table 1.2** Polybenzimidazole composite membranes.

| Reference | Composite membrane | *Remarks* |
|---|---|---|
| [101] | $H_3PO_4$ doped PBI/ Zirconium tricarboxybutylphosphonate (Zr(PBTC)) | *Conductivity of $5.24\times10^{-3}$ S·cm$^{-1}$ at 200 °C for $P_{H_2O}/P_s = 1$.* |
| [101] | Post-sulfonated PBI/Zr(PBTC) | *Conductivity of $8.14\times10^{-3}$ S·cm$^{-1}$ at 200 °C for $P_{H_2O}/P_s = 1$.* |
| [102] | $H_3PO_4$ doped fluorine-containingPBI/silica | *Increase of thermooxidative stability and mechanical properties with silica addition.* |
| [103] | $H_3PO_4$ doped PBI/ PTFE | *Better fuel cell performance than PBI membranes at 180 °C.* |
| [104] | pyridine-based PBI/ imidazole-silica ($SiO_2$-Im) | *Improvement of thermal stability. Conductivity higher than $10^{-3}$ S·cm$^{-1}$ at 120 °C/ 50 % R.H. by adding 5 wt. % of SiO2-Im.* |
| [105] | $H_3PO_4$ doped PBI/ Sulfonated silica nanoparticles (SA-SNP) | *Highest proton conductivity, ca. $4\times10^{-3}$ S·cm$^{-1}$, obtained with 10 wt. % SA-SNP.* |
| [106] | $H_3PO_4$ doped PBI/PTFE | *Higher conductivity for composite membranes, (>0.3 S·cm$^{-1}$), with a doping of 300 wt. % acid, at 180 °C / 8.4 % RH.* |
| [107] | $H_3PO_4$ doped pyridine-based PBI(pPBI)/ imidazole-silica ($SiO_2$-Im) and MCM-41 silica | *Power density peak twice as much for 20 wt. % of SiO2-Im composite membrane when compared to pPBI and 20 % higher when compared to 5 wt. % of MCM-41.* |

### 1.4.2 PBI / $H_3PO_4$ fuel cell systems

High temperature fuel cells based on phosphoric acid doped PBI [84; 87; 108-109] and phosphoric acid doped PBI type membranes [79; 92; 96; 98; 106] have been tested with hydrogen and oxygen/air in dry or very low humidification conditions.

PBI / $H_3PO_4$ fuel cell systems are the most studied and successful for PEMFC operating at temperatures higher than 120 °C. They appear to be promising for combined heat and power (CHP) generation or as auxiliary power unit in vehicles [54].

### *1.4.2.1 Electrodes preparation*

Attention has been drawn to PBI/$H_3PO_4$-based MEA preparation and its effect on the fuel cell performance.

The phosphoric acid content as well as the resultant distribution in the MEA, affects the fuel cell performance [110-114]. Kwon *et al.* [111] investigated the optimum phosphoric acid content by impregnating the electrodes with acid besides the use of phosphoric acid-doped membrane. These authors also studied the phosphoric acid distribution in the MEA starting from fresh state and up to the steady-state operation at 150 °C [110]. Oono *et al.* [113] experimentally evaluated the acid migration in phosphoric acid-doped PBI membrane during operation at 150 °C. The amount of acid in the membrane was controlled by changing the phosphoric acid solution temperature and the immersion time prior to fuel cell assembling. Mamlouk and Scott [115] studied the effect of anode and cathode electrodes phosphoric acid content on the fuel cell performance at 150 °C by adding different phosphoric acid amounts during the electrodes preparation. These studies showed that catalyst utilization, and therefore the performance of the MEA, are maximized optimizing the phosphoric acid content. The catalyst utilization increases with phosphoric acid content; however, at the cathode, an excess of phosphoric acid has a vicious effect since it blocks the oxygen supply. Wannek *et al.* [114; 116] showed that the phosphoric acid distribution and the fuel cell performance are essentially independent on how the acid was introduced and that redistribution of the electrolyte is a fast process.

The electrocatalyst ink can be prepared with a one-step procedure by directly adding a PBI or PBI type solution to a dispersion of the catalyst or carbon supported catalyst

(and if applicable PTFE) in, for example, dimethylacetamide or N-methylpyrrolidone [114]. The ink is then brushed onto the gas diffusion layers. The effect of proton-conducting polymers content at the catalyst layer has been studied. The weight fraction of PBI doped with a fixed amount of phosphoric acid was introduced in the electrodes and the effect on the high temperature PEMFC performance was assessed [108, 110-113]. An optimum amount has to be introduced in order to achieve maximum performance from the fuel cell. The addition of a small amount of polymer to the catalyst layer allows the reactant gases to reach the platinum surface easily but limits the proton mobility. A larger amount of polymer has a hinder effect on the reactant gases to reach the catalyst surface. For instance, Kim *et al.* [117] found an optimum amount of 20 wt. % of PBI·$6H_3PO_4$ for the cathode prepared with 20 wt. % Pt/C and catalyst load of 0.55 $mg_{Pt}·cm^{-2}$ for a fuel cell operating at 150 °C. Nonetheless, Wanneck *et al.* [114] stated that a small amount as 2 wt. % of ABPBI led to a significant decrease in fuel cell performance at 160 °C and the best performance was obtained for a polymer free electrode.

The effect of platinum concentration on the carbon support of the anode and cathode of PBI / $H_3PO_4$ systems was studied by Seland *et al.* and Lobato *et al.* [118-119]. The optimum amount is a result of a combination of catalytic activity and the mass transfer characteristics of the electrode. Increasing the amount of platinum on the carbon support above the optimum leads to a decrease of catalyst layer thickness that facilitates the mass transport, however, the specific active surface area decreases and therefore the electrochemical activity.

Unlike the low temperature PEMFC system, the water management in PBI / $H_3PO_4$ systems is not a crucial issue. This would suggest that no PTFE is needed at the gas diffusion media. Decreasing the PTFE content leads to a higher porosity and electrical conductivity and avoids the formation of non-active parts of the cell due to large agglomerates of inert. Nevertheless, the mechanical properties of the diffusion layer improve with increasing Teflon content. This way PTFE should be included in minimum amounts to guarantee mechanical stability without compromising reactants and electrical transport [120].

Many parameters influence the performance of the electrodes and designing the optimum electrode is a demanding task. Other studies were performed concerning the importance of the catalyst ink preparation [121-122], the porosity of the gas diffusion layer [123], the use of a dual layer electrode [124] and the use of Pt bimetallic alloys as catalyst [125].

### *1.4.2.2 Durability*

The durability and lifetime is a major concern for PEMFC commercialization. The goal for PBI/$H_3PO_4$-based high temperature PEMFC is to increase lifetime to 5000 h for vehicle applications and 40 000 h for stationary applications [54].

Over the past five years numerous studies were performed to assess durability and the causes of performance decrease over time of high temperature PEMFC based on phosphoric acid doped PBI electrolyte. Steady-state experiments at a fuel cell load of 0.2 $A \cdot cm^{-2}$ were performed at 160 °C during 400 h [126], 780 h [127], 1000 h [128] and 2500 h [129]. Modestov *et al.* [127] and Wannek *et al.* [128] observed a decay of ca. 25 $\mu V \cdot h^{-1}$ over the 700 h and 1000 h test whereas Yu *et al.* [129] observed a decay of 4.9 $\mu V \cdot h^{-1}$. Additionally, PBI system durability was evaluated during 500 h at 150 °C and at current load of ca. 0.7 $A \cdot cm^{-2}$ [130-131] and 0.64 $A \cdot cm^{-2}$ [132]. Hu *et al.* [132] observed degradation rate of about 150 $\mu V \cdot h^{-1}$, at 150 °C.

The performance decay of a fuel cell is related to two reasons:

1) The main cause of performance decay is related to the decrease of electrochemical active area. Modestov reported an increase of platinum (Pt) particle average diameter of the cathode catalyst from 3.8 nm to 7.8 nm (after 780 h of operation), while Hu *et al.* [132] and Zhai *et al.* [131] observed a growth from 3.8 nm to 6.9 nm and from 4.0 nm to 8.3 nm, respectively, after 500 h of operation. Liu *et al.* [130] compared the Pt particle diameter growth at the anode and cathode. At the anode the Pt particle diameter increased 2.0 times its original diameter while at the cathode it increased 2.3 times, after 500 h of operation. The high temperatures can explain the fast particle growth. The Pt particles have high mobility resulting in

sintering of the particles [133]. On the other hand, higher potentials increase the platinum dissolution and reposition rates, explaining the higher particle growth at the cathode [133].

2) A second possible cause for performance decay is the phosphoric acid loss from MEA. It can occur by diffusion, capillary transport, membrane compression, evaporation, and especially, leached assisted by the condensed water [54]. Measuring the pH of the water exiting the cell, it is possible to assess the migration of phosphoric acid from MEA. It was observed by Wannek *et al.* [128], during 1000 h and 160 °C, a constant acid loss at the cathode and an acid loss at the anode only during a short period of time staring from fresh membrane; these losses represented less than 1 % of the initial MEA load. The phosphoric acid loss from the cathode usually dominates the cumulative phosphoric acid from the fuel cell [129]. Other authors [126] experimentally observed that most of the migration of phosphoric acid from MEA happened during the first hours of life test. These studies indicate that acid loss does not seem to be an important reason for the performance degradation during the time range considered, up to 2500 h.

The physical degradation of PBI type membrane is another aspect to consider concerning the durability of the fuel cells. The membrane can be attacked during operation by $HO^{\cdot}$ and $HO_2^{\cdot}$ radicals produced by the incomplete reduction of oxygen on the cathode side [130]. As a result, the hydrogen crossover may increase, decreasing the fuel cell performance.

Oono *et al.* [134] studied the long-term durability at 150 °C, 170 °C and 190 °C at fuel cell load of 0.2 $A \cdot cm^{-2}$. At 150 °C and after 16 000 h, the fuel cell voltage was still within 7 % of its peak value. Besides, no significant changes were observed in the internal resistance of the cell, which is related to the ohmic resistance and the proton conductivity. At 170 °C, these authors reported that the cell voltage increased initially, reaching its peak value after a few hundred hours, and then dropped gradually. After 5 000 h, the cell voltage began to drop with increasing speed reaching a 10 % voltage decline after 6400 h of operation. As the voltage decreased, the internal resistance continued to increase. Finally, at 190 °C, the fuel cell reached a 10 % voltage decline just after 1220 h of operation. The cell voltage decay rate is

strongly dependent of the temperature, with a lower value being obtained for 150 °C (3.6 $\mu V \cdot h^{-1}$). The voltage decay was attributed mainly to catalyst sintering in the early stages of operation and to the hydrogen crossover in the terminal stage of operation, due to the severe depletion of phosphoric acid in the MEA. The phosphoric acid loss originates the proton conductivity decline while enhancing gas diffusion.

The unsteady state operation of the fuel cells also contributes for their early aging. Changing the load, temperature or performing shutdown-startup cycling changes the amount of vapor water formed and originates thermal and mechanical stresses to the fuel cell. By performing load cycles at 160 °C, it was observed that at very high voltages corrosion effects of the carbon support may occur at the cathode and that phosphoric acid loss is favored at high current densities (higher water production at the cathode) [129]. Both factors contribute to a higher degradation rate than the ones prevailing during steady-state tests. Furthermore, it was showed that the voltage decay of Celtec®-P 1000 MEA operated in a start/stop cycling mode is higher than the one operated continuously in steady-state [135]. The higher degradation rate associated to the start/stop cycling mode was attributed to the corrosion of the cathode catalyst support when high potentials are achieved. The carbon corrosion can weaken the interaction between carbon supports and the catalyst particles, accelerating the platinum sintering [133].

## 1.5 Motivation and Outline

This thesis was motivated by two major objectives: it was intended to get insight on high temperature fuel cell systems and to study new materials for HT- PEMFC.

This thesis is divided in four parts being Part I the Introduction. Part II, "Characterization and Modeling", comprehends three chapters as follows:

In Chapter 2, "Activation procedures characterization of MEA based on PBI / $H_3PO_4$ membranes", the activation process of phosphoric acid doped PBI-based MEAs (Celtec® - P1000 MEA an in-house prepared MEA) is studied. Also, it is described the

behavior of a HT-PEMFC based on an in-house prepared MEA, after activation at different temperatures and relative humidities.

Chapter 3, “The influence of CO on the performance of HT-PEMFC”, evaluates the poisoning effect of carbon monoxide on the performance of Celtec® - P1000 MEA. This work was mostly performed at the Institute of Technical Thermodynamics of German Aerospace Center.

In Chapter 4, “A dynamic model for HT-PEMFC”, a dynamic one-dimensional isothermal model was developed for HT-PEMFC. The developed model was used to simulate the steady-state and the impedance spectra of two fuel cells systems operated at 160 °C, based on phosphoric acid polybenzimidazole MEAs (Celtec® - P1000 MEA an in-house prepared MEA).

Part III, “HT-PEMFC Materials”, is divided in three chapters as follows:

Chapter 5, “Single-wall nanohorns as electrocatalyst support for HT-PEMFC”, reports the comparison of the performance of electrodes based on platinum supported in single-wall carbon nanohorns (Pt-SWNHs) and supported in carbon black (Pt-carbon black) for high temperature polymer electrolyte fuel cells. The electrodes were assembled with phosphoric acid doped polybenzimidazole membrane and the resultant MEA was characterized.

In Chapter 6, “Proton conductive membranes based on sulfonated poly(oxadiazole--triazole) copolymer”, the preparation and characterization of sulfonated poly(oxadiazole-triazole) copolymer membranes doped with a amphoteric molecule, 1H-benzimidazole-2-sulfonic acid, is described. This work was performed at the GKSS Research Centre Geesthacht GmbH.

Chapter 7, “Proton conductive membranes based on doped sulfonated polytriazole” describes the preparation and characterization of proton conducting sulfonated polytriazole membranes doped with three different agents: 1H-benzimidazole-2--sulfonic acid, benzimidazole and phosphoric acid. The modified membranes were characterized and the polymer doped with phosphoric acid was tested as polymer electrolyte at HT-PEMFC operation. The preparation and characterization of

sulfonated polytriazole membranes was performed mostly at GKSS Research Centre Geesthacht GmbH while high temperature PEMFC tests were performed at LEPAE.

The Part IV includes the last chapter, Chapter 8, “Conclusions and future work”. This chapter reviews the main conclusions of the present thesis and proposes research topics for the future.

## 1.6 References

[1] Tester, J.W., 2005. Sustainable energy choosing among options. MIT Press, Cambridge.

[2] Boyle, G., 2004. Renewable Energy: Power for a Sustainable Future, Second ed. Oxford University Press, p. 462.

[3] Jefferson, M., 2008. Accelerating the transition to sustainable energy systems. Energ Policy 36, 4116-4125.

[4] Zegers, P., 2006. Fuel cell commercialization: The key to a hydrogen economy. J Power Sources 154, 497-502.

[5] Rand, D.A.J., Dell, R.M., 2005. The hydrogen economy: a threat or an opportunity for lead-acid batteries? J Power Sources 144, 568-578.

[6] Core Writing Team, Pachauri, R.K., Reisinger, A., 2007. Climate Change 2007: Synthesis Report, IPCC Fourth Assessment Report IPCC, Geneva, p. 104.

[7] Bleischwitz, R., Bader, N., 2010. Policies for the transition towards a hydrogen economy: The EU case. Energ Policy 38, 5388-5398.

[8] European Parliament press release: European Parliament seals climate change package, REF.:20081216IPR44857. 17 December 2008.

[9] Winter, C.J., 2005. Electricity, hydrogen - competitors, partners? Int J Hydrogen Energy 30, 1371-1374.

[10] Neef, H.J., 2009. International overview of hydrogen and fuel cell research. Energy 34, 327-333.

[11] Edwards, P.P., Kuznetsov, V.L., David, W.I.F., Brandon, N.P., 2008. Hydrogen and fuel cells: Towards a sustainable energy future. Energ Policy 36, 4356-4362.

[12] Heiman, M.K., Solomon, B.D., 2007. Fueling US transportation: The hydrogen economy and its alternatives. Environment 49, 10-25.

[13] Coelho, B., Oliveira, A.C., Mendes, A., 2010. Concentrated solar power for renewable electricity and hydrogen production from water-a review. Energ Environ Sci 3, 1398-1405.

[14] Cumalioglu, I., Ertas, A., Ma, Y., Maxwell, T., 2008. State of the art: Hydrogen storage. J Fuel Cell Sci Tech 5,

[15] Ross, D.K., 2006. Hydrogen storage: The major technological barrier to the development of hydrogen fuel cell cars. Vacuum 80, 1084-1089.

[16] Haile, S.M., 2003. Fuel cell materials and components. Acta Mater 51, 5981-6000.

[17] Song, C.S., 2002. Fuel processing for low-temperature and high-temperature fuel cells - Challenges, and opportunities for sustainable development in the 21st century. Catal Today 77, 17-49.

[18] O'Hayre, R., Cha, S.-W., Colella, W., Prinz, F.B., 2006. Fuel Cell Fundamentals. John Wiley & Sons, Inc., New York.

[19] August 2004. Sustainable energy: The hydrogen fairy. RTDinfo Magazine on Europeean Research nº 42

[20] Barbir, F., 2005. PEM Fuel Cells: Theory and Practice. Elsevier Academic Press, London.

[21] Sopian, K., Daud, W.R.W., 2006. Challenges and future developments in proton exchange membrane fuel cells. Renew Energ 31, 719-727.

[22] Smitha, B., Sridhar, S., Khan, A.A., 2005. Solid polymer electrolyte membranes for fuel cell applications - a review. J Membrane Sci 259, 10-26.

[23] Kreuer, K.D., 2001. On the development of proton conducting polymer membranes for hydrogen and methanol fuel cells. J Membrane Sci 185, 29-39.

[24] Kreuer, K.D., 1997. Fast proton conductivity: A phenomenon between the solid and the liquid state? Solid State Ionics 94, 55-62.

[25] Anderson, R., Zhang, L.F., Ding, Y.L., Blanco, M., Bi, X.T., Wilkinson, D.P., 2010. A critical review of two-phase flow in gas flow channels of proton exchange membrane fuel cells. J Power Sources 195, 4531-4553.

[26] Bazylak, A., 2009. Liquid water visualization in PEM fuel cells: A review. Int J Hydrogen Energy 34, 3845-3857.

[27] Dai, W., Wang, H.J., Yuan, X.Z., Martin, J.J., Yang, D.J., Qiao, J.L., Ma, J.X., 2009. A review on water balance in the membrane electrode assembly of proton exchange membrane fuel cells. Int J Hydrogen Energy 34, 9461-9478.

[28] Li, H., Tang, Y.H., Wang, Z.W., Shi, Z., Wu, S.H., Song, D.T., Zhang, J.L., Fatih, K., Zhang, J.J., Wang, H.J., Liu, Z.S., Abouatallah, R., Mazza, A., 2008. A review of water flooding issues in the proton exchange membrane fuel cell. J Power Sources 178, 103-117.

[29] Volfkovich, Y.M., Sosenkin, V.E., Bagotsky, V.S., 2010. Structural and wetting properties of fuel cell components. J Power Sources 195, 5429-5441.

[30] Yousfi-Steiner, N., Mocoteguy, P., Candusso, D., Hissel, D., Hernandez, A., Aslanides, A., 2008. A review on PEM voltage degradation associated with water management: Impacts, influent factors and characterization. J Power Sources 183, 260-274.

[31] Hamilton, P.J., Pollet, B.G., 2010. Polymer Electrolyte Membrane Fuel Cell (PEMFC) Flow Field Plate: Design, Materials and Characterisation. Fuel Cells 10, 489-509.

[32] Hermann, A., Chaudhuri, T., Spagnol, P., 2005. Bipolar plates for PEM fuel cells: A review. Int J Hydrogen Energy 30, 1297-1302.

[33] Tawfik, H., Hung, Y., Mahajan, D., 2007. Metal bipolar plates for PEM fuel cell - A review. J Power Sources 163, 755-767.

[34] Cindrella, L., Kannan, A.M., Lin, J.F., Saminathan, K., Ho, Y., Lin, C.W., Wertz, J., 2009. Gas diffusion layer for proton exchange membrane fuel cells-A review. J Power Sources 194, 146-160.

[35] Litster, S., McLean, G., 2004. PEM fuel cell electrodes. J Power Sources 130, 61-76.

[36] Antolini, E., 2009. Carbon supports for low-temperature fuel cell catalysts. Appl Catal B-Environ 88, 1-24.

[37] McNicol, B.D., Rand, D.A.J., Williams, K.R., 2001. Fuel cells for road transportation purposes - yes or no? J Power Sources 100, 47-59.

[38] Deluca, N.W., Elabd, Y.A., 2006. Polymer electrolyte membranes for the direct methanol fuel cell: A review. J Polym Sci Pol Phys 44, 2201-2225.

[39] Frenette, G., Forthoffer, D., 2009. Economic & commercial viability of hydrogen fuel cell vehicles from an automotive manufacturer perspective. Int J Hydrogen Energy 34, 3578-3588.

[40] von Helmolt, R., Eberle, U., 2007. Fuel cell vehicles: Status 2007. J Power Sources 165, 833-843.

[41] Martin, E., Shaheen, S.A., Lipman, T.E., Lidicker, J.R., 2009. Behavioral response to hydrogen fuel cell vehicles and refueling: Results of California drive clinics. Int J Hydrogen Energy 34, 8670-8680.

[42] Ahn, B.K., Lim, T.W., 2006. Fuel cell vehicle development at Hyundai-Kia motors. IFOST 2006: 1st International Forum on Strategic Technology, Proceedings 199-201.

[43] Aso, S., Kizaki, M., 2007. Development of fuel cell hybrid vehicles in TOYOTA. 2007 Power Conversion Conference - Nagoya, Vols 1-3 1562-1567.

[44] Ilic, D., Holl, K., Birke, P., Wohrle, T., Birke-Salam, F., Perner, A., Haug, P., 2006. Fuel cells and batteries: Competition or separate paths? J Power Sources 155, 72-76.

[45] Wu, J.F., Yuan, X.Z., Wang, H.J., Blanco, M., Martin, J.J., Zhang, J.J., 2008. Diagnostic tools in PEM fuel cell research: Part I - Electrochemical techniques. Int J Hydrogen Energy 33, 1735-1746.

[46] Yuan, X.Z., Wang, H.J., Sun, J.C., Zhang, J.J., 2007. AC impedance technique in PEM fuel cell diagnosis - A review. Int J Hydrogen Energy 32, 4365-4380.

[47] Zhang, J.L., Xie, Z., Zhang, J.J., Tanga, Y.H., Song, C.J., Navessin, T., Shi, Z.Q., Song, D.T., Wang, H.J., Wilkinson, D.P., Liu, Z.S., Holdcroft, S., 2006. High temperature PEM fuel cells. J Power Sources 160, 872-891.

[48] Hogarth, W.H.J., da Costa, J.C.D., Lu, G.Q., 2005. Solid acid membranes for high temperature (> 140 degrees C) proton exchange membrane fuel cells. J Power Sources 142, 223-237.

[49] Li, Q.F., He, R.H., Jensen, J.O., Bjerrum, N.J., 2003. Approaches and recent development of polymer electrolyte membranes for fuel cells operating above 100 degrees C. Chem Mater 15, 4896-4915.

[50] Shao, Y.Y., Yin, G.P., Wang, Z.B., Gao, Y.Z., 2007. Proton exchange membrane fuel cell from low temperature to high temperature: Material challenges. J Power Sources 167, 235-242.

[51] Farrell, C.G., Gardner, C.L., Ternan, M., 2007. Experimental and modelling studies of CO poisoning in PEM fuel cells. J Power Sources 171, 282-293.

[52] Li, Q.F., He, R.H., Gao, J.A., Jensen, J.O., Bjerrum, N.J., 2003. The CO poisoning effect in PEMFCs operational at temperatures up to 200 degrees C. J Electrochem Soc 150, A1599-A1605.

[53] Hajbolouri, F., Andreaus, B., Scherer, G.G., Wokaun, A., 2004. CO Tolerance of Commercial Pt and PtRu Gas Diffusion Electrodes in Polymer Electrolyte Fuel Cells. Fuel Cells 4, 160-168.

[54] Li, Q.F., Jensen, J.O., Savinell, R.F., Bjerrum, N.J., 2009. High temperature proton exchange membranes based on polybenzimidazoles for fuel cells. Prog Polym Sci 34, 449-477.

[55] Savadogo, O., 2004. Emerging membranes for electrochemical systems - Part II. High temperature composite membranes for polymer electrolyte fuel cell (PEFC) applications. J Power Sources 127, 135-161.

[56] Schuster, M.E., Meyer, W.H., 2003. Anhydrous proton-conducting polymers. Annu Rev Mater Res 33, 233-261.

[57] Asensio, J.A., Sanchez, E.M., Gomez-Romero, P., 2010. Proton-conducting membranes based on benzimidazole polymers for high-temperature PEM fuel cells. A chemical quest. Chem Soc Rev 39, 3210-3239.

[58] Watanabe, M., Uchida, H., Seki, Y., Emori, M., Stonehart, P., 1996. Self-humidifying polymer electrolyte membranes for fuel cells. J Electrochem Soc 143, 3847-3852.

[59] Marani, D., D'Epifanio, A., Traversa, E., Miyayama, M., Licoccia, S., 2010. Titania Nanosheets (TNS)/Sulfonated Poly Ether Ether Ketone (SPEEK) Nanocomposite Proton Exchange Membranes for Fuel Cells. Chem Mater 22, 1126-1133.

[60] Zhang, Y.F., Wang, S.J., Xiao, M., Bian, S.G., Meng, Y.Z., 2009. The silica-doped sulfonated poly(fluorenyl ether ketone)s membrane using hydroxypropyl methyl cellulose as dispersant for high temperature proton exchange membrane fuel cells. Int J Hydrogen Energy 34, 4379-4386.

[61] Zaidi, S.M.J., Ahmad, M.I., 2006. Novel SPEEK/heteropolyacids loaded MCM-41 composite membranes for fuel cell applications. J Membrane Sci 279, 548-557.

[62] Devrim, Y., Erkan, S., Bac, N., Eroglu, I., 2009. Preparation and characterization of sulfonated polysulfone/titanium dioxide composite membranes for proton exchange membrane fuel cells. Int J Hydrogen Energy 34, 3467-3475.

[63] Li, K., Ye, G.B., Pan, J.J., Zhang, H.N., Pan, M., 2010. Self-assembled Nafion (R)/metal oxide nanoparticles hybrid proton exchange membranes. J Membrane Sci 347, 26-31.

[64] Pan, J.J., Zhang, H.N., Chen, W., Pan, M., 2010. Nafion-zirconia nanocomposite membranes formed via in situ sol-gel process. Int J Hydrogen Energy 35, 2796-2801.

[65] Amjadi, M., Rowshanzamir, S., Peighambardoust, S.J., Hosseini, M.G., Eikani, M.H., 2010. Investigation of physical properties and cell performance of Nafion/TiO2 nanocomposite membranes for high temperature PEM fuel cells. Int J Hydrogen Energy 35, 9252-9260.

[66] Li, Q.O., Xiao, C.A., Li, W., Zhang, H.N., Chen, F.T., Fang, P.F., Pan, M., 2010. Enhanced proton conductivity of polymer electrolyte membrane doped with titanate nanotubes. Colloid Polym Sci 288, 1369-1374.

[67] D'Epifanio, A., Navarra, M.A., Weise, F.C., Mecheri, B., Farrington, J., Licoccia, S., Greenbaum, S., 2010. Composite Nafion/Sulfated Zirconia Membranes: Effect of the Filler Surface Properties on Proton Transport Characteristics. Chem Mater 22, 813-821.

[68] Kannan, A.G., Choudhury, N.R., Dutta, N.K., 2009. In situ modification of Nafion (R) membranes with phospho-silicate for improved water retention and proton conduction. J Membrane Sci 333, 50-58.

[69] Noto, V., Lavina, S., Negro, E., Vittadello, M., Conti, F., Piga, M., Pace, G., 2009. Hybrid inorganic-organic proton conducting membranes based on Nafion and 5 wt% of MxOy (M = Ti, Zr, Hf, Ta and W). Part II: Relaxation phenomena and conductivity mechanism. J Power Sources 187, 57-66.

[70] Sahu, A.K., Pitchumani, S., Sridhar, P., Shukla, A.K., 2009. Co-assembly of a Nafion-Mesoporous Zirconium Phosphate Composite Membrane for PEM Fuel Cells. Fuel Cells 9, 139-147.

[71] Park, K.T., Jung, U.H., Choi, D.W., Chun, K., Lee, H.M., Kim, S.H., 2008. ZrO2-SiO2/Nafion (R) composite membrane for polymer electrolyte membrane fuel cells operation at high temperature and low humidity. J Power Sources 177, 247-253.

[72] Pereira, F., Valle, K., Belleville, P., Morin, A., Lambert, S., Sanchez, C., 2008. Advanced mesostructured hybrid silica-nafion membranes for high-performance PEM fuel cell. Chem Mater 20, 1710-1718.

[73] Kreuer, K.D., Fuchs, A., Ise, M., Spaeth, M., Maier, J., 1998. Imidazole and pyrazole-based proton conducting polymers and liquids. Electrochim Acta 43, 1281-1288.

[74] Schuster, M., Meyer, W.H., Wegner, G., Herz, H.G., Ise, M., Schuster, M., Kreuer, K.D., Maier, J., 2001. Proton mobility in oligomer-bound proton solvents: imidazole immobilization via flexible spacers. Solid State Ionics 145, 85-92.

[75] Munch, W., Kreuer, K.D., Silvestri, W., Maier, J., Seifert, G., 2001. The diffusion mechanism of an excess proton in imidazole molecule chains: first results of an ab initio molecular dynamics study. Solid State Ionics 145, 437-443.

[76] Herz, H.G., Kreuer, K.D., Maier, J., Scharfenberger, G., Schuster, M.F.H., Meyer, W.H., 2003. New fully polymeric proton solvents with high proton mobility. Electrochim Acta 48, 2165-2171.

[77] Wainright, J.S., Wang, J.T., Weng, D., Savinell, R.F., Litt, M., 1995. Acid-Doped Polybenzimidazoles - a New Polymer Electrolyte. J Electrochem Soc 142, L121-L123.

[78] Xiao, L.X., Zhang, H.F., Scanlon, E., Ramanathan, L.S., Choe, E.W., Rogers, D., Apple, T., Benicewicz, B.C., 2005. High-temperature polybenzimidazole fuel cell membranes via a sol-gel process. Chem Mater 17, 5328-5333.

[79] Qian, G.Q., Smith, D.W., Benicewicz, B.C., 2009. Synthesis and characterization of high molecular weight perfluorocyclobutyl-containing polybenzimidazoles (PFCB-PBI) for high temperature polymer electrolyte membrane fuel cells. Polymer 50, 3911-3916.

[80] Lobato, J., Canizares, P., Rodrigo, M.A., Linares, J.J., Manjavacas, G., 2006. Synthesis and characterisation of poly[2,2-(m-phenylene)-5,5-bibenzimidazole] as polymer electrolyte membrane for high temperature PEMFCs. J Membrane Sci 280, 351-362.

[81] Bouchet, R., Siebert, E., 1999. Proton conduction in acid doped polybenzimidazole. Solid State Ionics 118, 287-299.

[82] He, R.H., Li, Q.F., Xiao, G., Bjerrum, N.J., 2003. Proton conductivity of phosphoric acid doped polybenzimidazole and its composites with inorganic proton conductors. J Membrane Sci 226, 169-184.

[83] Ma, Y.L., Wainright, J.S., Litt, M.H., Savinell, R.F., 2004. Conductivity of PBI membranes for high-temperature polymer electrolyte fuel cells. J Electrochem Soc 151, A8-A16.

[84] Li, Q., He, R., Jensen, J.O., Bjerrum, N.J., 2004. PBI-Based Polymer Membranes for High Temperature Fuel Cells - Preparation, Characterization and Fuel Cell Demonstration. Fuel Cells 4 147 - 159.

[85] Kawahara, M., Morita, J., Rikukawa, M., Sanui, K., Ogata, N., 2000. Synthesis and proton conductivity of thermally stable polymer electrolyte: poly(benzimidazole) complexes with strong acid molecules. Electrochim Acta 45, 1395-1398.

[86] Pu, H.T., Meyer, W.H., Wegner, G., 2002. Proton transport in polybenzimidazole blended with H3PO4 or H2SO4. J Polym Sci Pol Phys 40, 663-669.

[87] Zhang, J.L., Tang, Y.H., Song, C.J., Zhang, J.J., 2007. Polybenzimidazole-membrane-based PEM fuel cell in the temperature range of 120-200 degrees C. J Power Sources 172, 163-171.

[88] Li, Q.F., Hjuler, H.A., Bjerrum, N.J., 2001. Phosphoric acid doped polybenzimidazole membranes: Physiochemical characterization and fuel cell applications. J Appl Electrochem 31, 773-779.

[89] He, R.H., Li, Q.F., Bach, A., Jensen, J.O., Bjerrum, N.J., 2006. Physicochemical properties of phosphoric acid doped polybenzimidazole membranes for fuel cells. J Membrane Sci 277, 38-45.

[90] Kim, S.K., Kim, T.H., Jung, J.W., Lee, J.C., 2009. Polybenzimidazole containing benzimidazole side groups for high-temperature fuel cell applications. Polymer 50, 3495-3502.

[91] Chuang, S.W., Hsu, S.L.C., 2006. Synthesis and properties of a new fluorine-containing polybenzimidazole for high-temperature fuel-cell applications. J Polym Sci Pol Chem 44, 4508-4513.

[92] Xiao, L., Zhang, H., Jana, T., Scanlon, E., Chen, R., Choe, E.W., Ramanathan, L.S., Yu, S., Benicewicz, B.C., 2005. Synthesis and characterization of pyridine-based polybenzimidazoles for high temperature polymer electrolyte membrane fuel cell applications. Fuel Cells 5, 287-295.

[93] Asensio, J.A., Borros, S., Gomez-Romero, P., 2004. Proton-conducting membranes based on poly(2,5-benzimidazole) (ABPBI) and phosphoric acid prepared by direct acid casting. J Membrane Sci 241, 89-93.

[94] Carollo, A., Quartarone, E., Tomasi, C., Mustarelli, P., Belotti, F., Magistris, A., Maestroni, F., Parachini, M., Garlaschelli, L., Righetti, P.P., 2006. Developments of new proton conducting membranes based on different polybenzimidazole structures for fuel cells applications. J Power Sources 160, 175-180.

[95] Asensio, J.A., Borros, S., Gomez-Romero, P., 2004. Sulfonated poly(2,5-benzimidazole) (SABPBI) impregnated with phosphoric acid as proton conducting membranes for polymer electrolyte fuel cells. Electrochim Acta 49, 4461-4466.

[96] Mader, J.A., Benicewicz, B.C., 2010. Sulfonated Polybenzimidazoles for High Temperature PEM Fuel Cells. Macromolecules 43, 6706-6715.

[97] Daletou, M.K., Gourdoupi, N., Kallitsis, J.K., 2005. Proton conducting membranes based on blends of PBI with aromatic polyethers containing pyridine units. J Membrane Sci 252, 115-122.

[98] Li, Q., Jensen, J.O., Pan, C., Bandur, V., Nilsson, M.S., Schonberger, F., Chromik, A., Hein, M., Haring, T., Kerres, J., Bjerrum, N.J., 2008. Partially fluorinated aarylene

polyethers and their ternary blends with PBI and H3PO4. Part II. Characterisation and fuel cell tests of the ternary membranes. Fuel Cells 8, 188-199.

[99] Zhai, Y.F., Zhang, H.M., Zhang, Y., Xing, D.M., 2007. A novel H3PO4/Nafion-PBI composite membrane for enhanced durability of high temperature PEM fuel cells. J Power Sources 169, 259-264.

[100] Noy, P., Li, Q.F., Pan, C., Bjerrurn, N.J., 2008. Cross-linked polybenzimidazole membranes for high temperature proton exchange membrane fuel cells with dichloromethyl phosphinic acid as a cross-linker. Polym Advan Technol 19, 1270-1275.

[101] Jang, M.Y., Yamazaki, Y., 2005. Preparation and characterization of composite membranes composed of zirconium tricarboxybutylphosphonate and polybenzimidazole for intermediate temperature operation. J Power Sources 139, 2-8.

[102] Chuang, S.W., Hsu, S.L.C., Liu, Y.H., 2007. Synthesis and properties of fluorine-containing polybenzimidazole/silica nanocomposite membranes for proton exchange membrane fuel cells. J Membrane Sci 305, 353-363.

[103] Lin, H.L., Yu, T.L., Chang, W.K., Cheng, C.P., Hu, C.R., Jung, G.B., 2007. Preparation of a low proton resistance PBI/PTFE composite membrane. J Power Sources 164, 481-487.

[104] Quartarone, E., Magistris, A., Mustarelli, P., Grandi, S., Carollo, A., Zukowska, G.Z., Garbarczyk, J.E., Nowinski, J.L., Gerbaldi, C., Bodoardo, S., 2009. Pyridine-based PBI Composite Membranes for PEMFCs. Fuel Cells 9, 349-355.

[105] Suryani, Liu, Y.L., 2009. Preparation and properties of nanocomposite membranes of polybenzimidazole/sulfonated silica nanoparticles for proton exchange membranes. J Membrane Sci 332, 121-128.

[106] Li, M.Q., Scott, K., 2010. A polymer electrolyte membrane for high temperature fuel cells to fit vehicle applications. Electrochim Acta 55, 2123-2128.

[107] Kurdakova, V., Quartarone, E., Mustarelli, P., Magistris, A., Caponetti, E., Saladino, M.L., 2010. PBI-based composite membranes for polymer fuel cells. J Power Sources 195, 7765-7769.

[108] Lobato, J., Canizares, P., Rodrigo, M.A., Linares, J.J., Aguilar, J.A., 2007. Improved polybenzimidazole films for H3PO4-doped PBI-based high temperature PEMFC. J Membrane Sci 306, 47-55.

[109] Wang, J.T., Savinell, R.F., Wainright, J., Litt, M., Yu, H., 1996. A H-2/O-2 fuel cell using acid doped polybenzimidazole as polymer electrolyte. Electrochim Acta 41, 193-197.

[110] Kwon, K., Park, J.O., Yoo, D.Y., Yi, J.S., 2009. Phosphoric acid distribution in the membrane electrode assembly of high temperature proton exchange membrane fuel cells. Electrochim Acta 54, 6570-6575.

[111] Kwon, Y., Kim, T.Y., Yoo, D.Y., Hong, S.G., Park, J.O., 2009. Maximization of high-temperature proton exchange membrane fuel cell performance with the optimum distribution of phosphoric acid. J Power Sources 188, 463-467.

[112] Modestov, A.D., Tarasevich, M.R., Filimonov, V.Y., Leykin, A.Y., 2009. Influence of Catalyst Layer Binder on Catalyst Utilization and Performance of Fuel Cell with Polybenzimidazole-H3PO4 Membrane. J Electrochem Soc 156, B650-B656.

[113] Oono, Y., Sounai, A., Hori, M., 2009. Influence of the phosphoric acid-doping level in a polybenzimidazole membrane on the cell performance of high-temperature proton exchange membrane fuel cells. J Power Sources 189, 943-949.

[114] Wannek, C., Lehnert, W., Mergel, J., 2009. Membrane electrode assemblies for high-temperature polymer electrolyte fuel cells based on poly(2,5-benzimidazole) membranes with phosphoric acid impregnation via the catalyst layers. J Power Sources 192, 258-266.

[115] Mamlouk, M., Scott, K., 2010. The effect of electrode parameters on performance of a phosphoric acid-doped PBI membrane fuel cell. Int J Hydrogen Energy 35, 784-793.

[116] Wannek, C., Konradi, I., Mergel, J., Lehnert, W., 2009. Redistribution of phosphoric acid in membrane electrode assemblies for high-temperature polymer electrolyte fuel cells. Int J Hydrogen Energy 34, 9479-9485.

[117] Kim, J.H., Kim, H.J., Lim, T.H., Lee, H.I., 2007. Dependence of the performance of a high-temperature polymer electrolyte fuel cell on phosphoric acid-doped polybenzimidazole ionomer content in cathode catalyst layer. J Power Sources 170, 275-280.

[118] Lobato, J., Canizares, P., Rodrigo, M.A., Linares, J.J., Ubeda, D., Pinar, F.J., 2010. Study of the Catalytic Layer in Polybenzimidazole-based High Temperature PEMFC: Effect of Platinum Content on the Carbon Support. Fuel Cells 10, 312-319.

[119] Seland, F., Berning, T., Borresen, B., Tunold, R., 2006. Improving the performance of high-temperature PEM fuel cells based on PBI electrolyte. J Power Sources 160, 27-36.

[120] Lobato, J., Canizares, P., Rodrigo, M.A., Ruiz-Lopez, C., Linares, J.J., 2008. Influence of the Teflon loading in the gas diffusion layer of PBI-based PEM fuel cells. J Appl Electrochem 38, 793-802.

[121] Kim, J.H., Kim, H.J., Lim, T.H., Lee, H.I., 2007. Improvement of high temperature polymer electrolyte fuel cell performance with phosphoric acid-doped polybenzimidazole ionomer binder in catalyst layer. J Ind Eng Chem 13, 850-855.

[122] Lobato, J., Rodrigo, M.A., Linares, J.J., Scott, K., 2006. Effect of the catalytic ink preparation method on the performance of high temperature polymer electrolyte membrane fuel cells. J Power Sources 157, 284-292.

[123] Pan, C., Li, Q.F., Jensen, J.O., He, R.H., Cleemann, L.N., Nilsson, M.S., Bjerrum, N.J., Zeng, Q.X., 2007. Preparation and operation of gas diffusion electrodes for high-temperature proton exchange membrane fuel cells. J Power Sources 172, 278-286.

[124] Kongstein, O.E., Berning, T., Borresen, B., Seland, F., Tunold, R., 2007. Polymer electrolyte fuel cells based on phosphoric acid doped polybenzimidazole (PBI) membranes. Energy 32, 418-422.

[125] Rao, C.V., Parrondo, J., Ghatty, S.L., Rambabu, B., 2010. High temperature polymer electrolyte membrane fuel cell performance of PtxCoy/C cathodes. J Power Sources 195, 3425-3430.

[126] Lin, H.L., Hsieh, Y.S., Chiu, C.W., Yu, T.L., Chen, L.C., 2009. Durability and stability test of proton exchange membrane fuel cells prepared from polybenzimidazole/poly(tetrafluoro ethylene) composite membrane. J Power Sources 193, 170-174.

[127] Modestov, A.D., Tarasevich, M.R., Filimonov, V.Y., Zagudaeva, N.M., 2009. Degradation of high temperature MEA with PBI-H3PO4 membrane in a life test. Electrochim Acta 54, 7121-7127.

[128] Wannek, C., Kohnen, B., Oetien, H.F., Lippert, H., Mergel, J., 2008. Durability of ABPBI-based MEAs for high temperature PEMFCs at different operating conditions. Fuel Cells 8, 87-95.

[129] Yu, S., Xiao, L., Benicewicz, B.C., 2008. Durability studies of PBI-based high temperature PEMFCs. Fuel Cells 8, 165-174.

[130] Liu, G., Zhang, H.M., Hu, J.W., Zhai, Y.F., Xu, D.Y., Shao, Z.G., 2006. Studies of performance degradation of a high temperature PEMFC based on H3PO4-doped PBI. J Power Sources 162, 547-552.

[131] Zhai, Y.F., Zhang, H.M., Xing, D.M., Shao, Z.G., 2007. The stability of Pt/C catalyst in H3PO4/PBI PEMFC during high temperature life test. J Power Sources 164, 126-133.

[132] Hu, J.W., Zhang, H.M., Zhai, Y.F., Liu, G., Yi, B.L., 2006. 500h continuous aging life test on PBI/H3PO4 high-temperature PEMFC. Int J Hydrogen Energy 31, 1855-1862.

[133] Qi, Z.G., Buelte, S., 2006. Effect of open circuit voltage on performance and degradation of high temperature PBI-H3PO4 fuel cells. J Power Sources 161, 1126-1132.

[134] Oono, Y., Fukuda, T., Sounai, A., Hori, M., 2010. Influence of operating temperature on cell performance and endurance of high temperature proton exchange membrane fuel cells. J Power Sources 195, 1007-1014.

[135] Schmidt, T.J., Baurmeister, J., 2008. Properties of high-temperature PEFC Celtec (R)-P 1000 MEAs in start/stop operation mode. J Power Sources 176, 428-434.

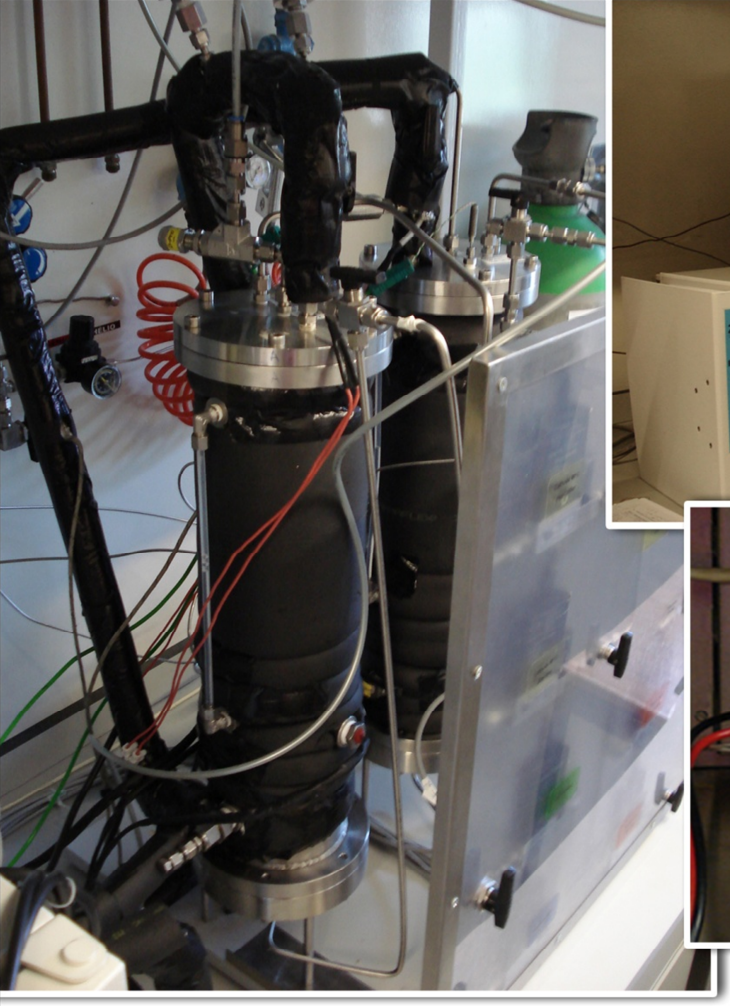

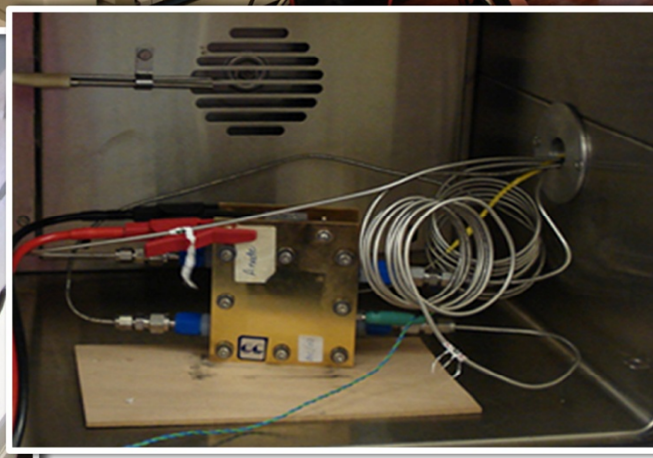

# Part II Characterization and Modeling

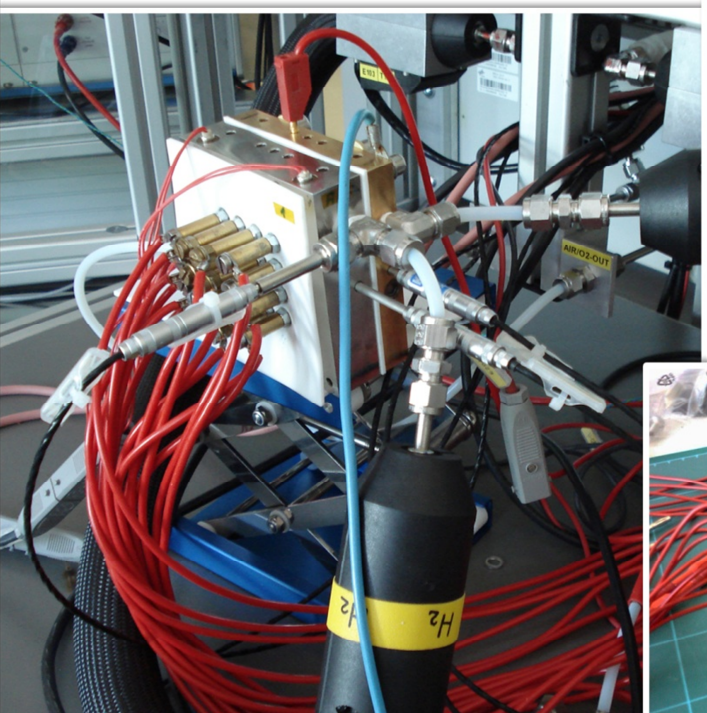


Top: LEPAE fuel cell set-up

Bottom right: DLR fuel cell set-up and S++ segmented cell

Bottom left: DLR segmented cell

# Chapter 2 Activation procedures characterization of MEA based on PBI / $H_3PO_4$ membranes[1]

## 2.1 Abstract

This work aims at better understanding the activation process of phosphoric acid doped PBI-based MEA. The phenomena involved in the activation of Celtec® - P1000 MEA were studied based on current density-voltage curves (I-V curves), electrochemical impedance spectroscopy combined with equivalent circuit modelling and cyclic voltammetry analysis. It was concluded that galvanostatic activation procedure enhanced Celtec® - P1000 MEA performance by increasing the catalyst activity and by decreasing the ohmic resistance. Also, galvanostatic and potential cycling procedures were applied to an in-house prepared MEA; for the same activation time, the galvanostatic allowed a deeper activation of the in-house prepared MEA than the potential cycling activation method.

It is accepted that the humidification of the reactants is not necessary for high temperature PEMFC based on phosphoric acid doped PBI membrane, since water production at the cathode should be enough to ensure high performance of the fuel cell. In this work it is described the behavior of a PEMFC based on an in-house prepared MEA, after activation at different temperatures and relative humidities. It is shown that water has an enhanced effect on ohmic resistance during the PEMFC operation but can also have a detrimental effect on the cathode resistance due to migration of phosphoric acid outside MEA.

[1] The content of this chapter is adapted from: Boaventura, M., Mendes, A., 2010. Activation procedures characterization of MEA based on phosphoric acid doped PBI membranes. Int J Hydrogen Energy 35, 11649-11660.

## 2.2 Introduction

The state of the art of polymer electrolyte membrane fuel cells (PEMFC) is based on perfluorosulfonic acid polymer membranes, such as Nafion®, developed by Dupont in the 1960's. This polymer exhibits good chemical and mechanical stability due to its perfluorinated chain backbone (Teflon like) and exhibits proton conductivities as high as 0.20 $S \cdot cm^{-1}$ [1] in humidified conditions due to perfluoro side chains containing hygroscopic sulfonic acid groups. However, at atmospheric pressure, the maximum operating temperature is 90 °C and typically 80 °C.

There are several motivations and advantages for high temperature PEMFC development [2-5]. These advantages include electrochemical kinetics improvement for anode and cathode, simplified water management by the use of a single phase, simplified cooling system and heat recovery and CO tolerance is dramatically increased.

The most studied system for high temperature PEMFC is PBI membrane doped with phosphoric acid [6-8], first used by Wainwright *et al.* [9]. Several articles emphasize proton transport and its relation with temperature, acid doping and relative humidity [7; 10-12]. Despite this, very few studies were done to observe the effect of humidification in acid doped PBI-based MEA performance under controlled conditions in a fuel cell. Delatou *et al.* [13] studied the effect of humidity in the performance of a high temperature fuel cell. These authors observed that increasing the water partial pressure at the anode, the instantaneous performance of the fuel cell increased too. However, they performed the experiments without allowing the steady-state to be reached so that water produced in the cathode did not equilibrate with the membrane.

When real application and commercialization of high temperature PEMFC is intended, aspects such as activation strategies and durability must be considered. Numerous works were made in order to study the stability of high temperature fuel cells, namely concerning polymer membrane degradation, leaching of doping acid and loss of catalyst activity [14-19], but information about activation protocols is

scarce. A fuel cell should be activated for attaining its maximum performance and enabling reproducible results. Several strategies were proposed for low temperature fuel cells that include exposing the MEA to an elevated temperature and pressure, steaming or boiling an electrode, cycling load, hydrogen evolution and CO oxidative stripping or combination of previous methods [20-25]. Tingelof and Ihonen [26] studied several activation procedures for Celtec® - P1000, from BASF Fuel Cell, through I-V curves, and suggested that a one day galvanostatic operation at 200 °C followed by two days of relaxation at 160 °C, would be suitable for PBI-based MEA, whereas potential cycling activation was not effective for this MEA.

This work aims at to better understanding the activation process of phosphoric acid doped PBI-based MEA. The activation process was systematically followed based on I-V curves, electrochemical impedance spectroscopy combined with equivalent circuit modelling and cyclic voltammetry. This way it was possible to better understand the phenomena involved in galvanostatic activation of Celtec® - P1000 and galvanostatic and potential cycling activation of an in-house prepared MEA. Also, it was studied the behavior of the in-house MEA after activation at different temperatures and relative humidities. Besides the electrolyte, it was assessed for the steady-state the activation effect on both anode and cathode.

## 2.3 Experimental

### 2.3.1 Membrane electrode assembly (MEA) preparation

In this study two different MEAs were used; one from BASF Fuel Cell, Celtec® - P1000 MEA and the other in-house prepared. The commercial MEA was loaded at the cathode with 0.8 $mg \cdot cm^{-2}$ of platinum and at the anode with 1 $mg \cdot cm^{-2}$ of platinum; the total MEA thickness was 880 μm and the active area was 3.24 $cm^2$. The in-house MEA was prepared with a PBI phosphoric acid-doped membrane, 100 μm thick and doped with 10 mol of phosphoric acid per mol of PBI (a commercial membrane provided by a partner), sandwiched between two electrodes with an active area of

4.4 $cm^2$ directly in an Electrochem single cell by applying a torque of 3.5 N·m on the eight screws. The catalyst layer (JM HISPEC 1000, pure platinum, black) was applied to gas diffusion layer (Sigracet 35D) with DLR dry spray technology [27-28]. This method allows an accurate determination of platinum load and has good reproducibility. Both anode and cathode platinum load was 1 $mg \cdot cm^{-2}$ and no electrolyte was added to the catalyst layer. The catalyst powder was pressed to the gas diffusion layer with heated plates at 160 °C and 5.5 bar for 2 minutes.

### 2.3.2 Test station and unit cell performance tests

The Electrochem single cell equipped with either MEA was placed in an in-house fuel cell test station. The schematic diagram of the fuel cell test bench is shown in Figure 2.1. The temperature was controlled using a forced convention oven and relative humidity was obtained by passing the gases through bubbling humidifiers with controlled temperature. The gas inlet tubes were kept at 85 °C, a temperature higher than the humidifiers temperature. The anode and cathode pressure were kept constant with back pressure regulators or relief valves and stoichiometry was assured with mass flow controllers. The system was controlled based on a program written in LabView and electrochemical tests were performed with a Zahner IM6e electrochemical workstation coupled with a potentiostat PP-241.

### 2.3.3 Activation methods

Two MEAs, described above, were used to study the phenomena involved in activation procedure. Celtec® - P1000 MEA was tested in suggested conditions by the supplier, at atmospheric pressure, stoichiometry of 2 for air and 1.2 for hydrogen and using non-humidified inlet gases. It was activated according to producer recommendations, at constant 0.2 $A \cdot cm^{-2}$ load for 50 h and 160 °C.

MEA prepared in our laboratory was tested at atmospheric pressure, hydrogen flow of 1.7 $cm^3 \cdot s^{-1}$ and air flow of 5.0 $cm^3 \cdot s^{-1}$ and 1.0 % relative humidity in inlet gases.

Two activation protocols were used: galvanostatic and potential cycling activation. Galvanostatic activation took place at 0.02 $A \cdot cm^{-2}$ for 48 h and 160 °C whereas potential cycling activation consisted in performing 25 I-V curves for approximately 53 h; EIS spectra were obtained at the end of each cycle at 160 °C. Between cycles the cell was at open circuit voltage (OCV).

Before and after the activation process, I-V curves, EIS experiments and cyclic voltammetry were performed and analyzed.

### 2.3.4 Electrochemical characterization

Each I-V curve was obtained starting at OCV and decreasing the potential until 300 mV, with steps of 0.05 V or 0.1 V. An estimation of the electrochemical surface area (ESA) was obtained from cyclic voltammetry experiments; fuel cell cathode was purged with nitrogen and used as working electrode while anode was used as reference and counter electrode. Scans were performed at a scan rate of 100 $mV \cdot s^{-1}$ between 0 mV and 800 mV. Electrochemical impedance spectroscopy was obtained in the frequency range from 100 kHz to 100 mHz with perturbation amplitude of 5 mV.

### 2.3.5 Influence of temperature and relative humidity on the PEMFC performance

The in-house produced MEA was used to study high temperature PEMFC performance after activation at different temperatures (120 °C, 140 °C and 160 °C) and 2 bar; hydrogen was fed at 1.7 $cm^3 \cdot s^{-1}$ and air at 5.0 $cm^3 \cdot s^{-1}$ with different relative humidities (1.0 %, 2.5 % and 5.0 %). The cell was heated up with dry $H_2$/Air until the operating temperature was reached and then the pressure and relative humidity (RH) were set. MEAs were then activated with the cyclic load procedure until the steady-state was reached (variation below 5 %, relative difference).

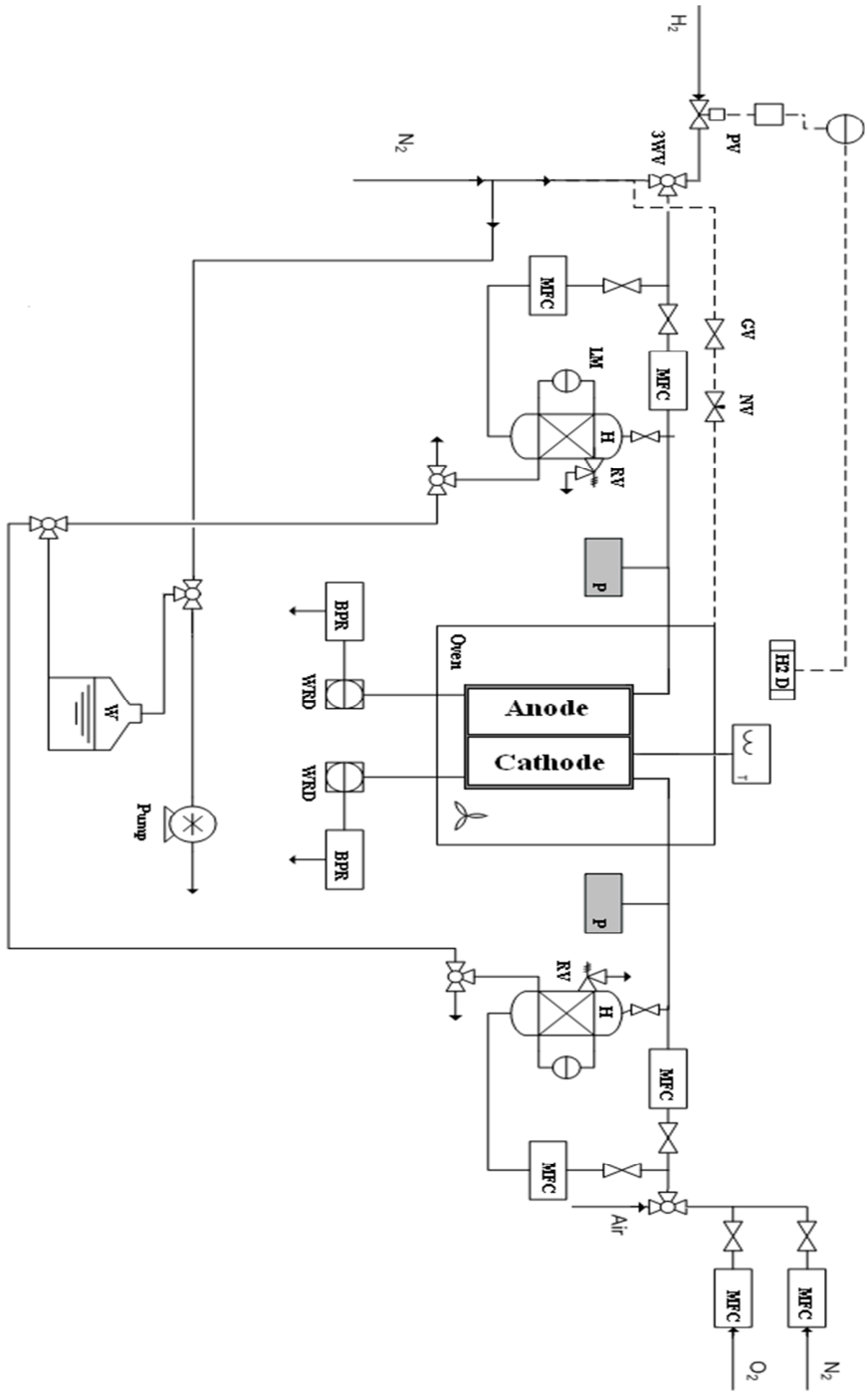


**Figure 2.1** Schematic diagram of fuel cell test bench: MFC, mass flow controller, H, humidifier, BPR, back pressure regulator, P, pressure sensor, LM, level meter, WRD, water removal device, W, water reservoir, 3WV, three way valve, PV, powered valve, GV, gauge valve, NV, needle valve, RV, relief valve and $H_2$ D, hydrogen detector.

## 2.4 Results and Discussion

### 2.4.1 Activation methods

According to BASF Fuel Cell, Celtec® - P1000 MEA should be activated at 0.2 A·cm$^{-2}$ for 50-100 h at 160 °C and stoichiometry of 2 for air and 1.2 for hydrogen. In Figure 2.2 (a) it is plotted the voltage history for the first 50 h. There is a significant increase of about 80 mV while the current density stayed constant. A similar result was already observed before for this commercial MEA [26]. Figure 2.2 (b) shows the I-V curves obtained before and after galvanostatic activation of Celtec® - P1000. The performance increased for the entire current density range, exhibiting improvements in the membrane proton conductivity and catalyst activity.

It was followed the same activation protocol for the in-house prepared MEA, performed at 160 °C, atmospheric pressure and 1.0 % RH in anode and cathode, at a constant load of 0.02 A·cm$^{-2}$. Figure 2.3 (a) shows the voltage history for the first 48 h. A low current density was applied because of low power density at the initial state, as seen in Figure 2.3 (b).

There is a significant increase of voltage values, from 0.450 V to 0.750 V in 48 h, especially in first 24 h. The same trend can also be seen in I-V curves, exhibiting also improvements in the membrane proton conductivity and catalyst activity.

Despite potential cycling activation is not recommended for the commercial MEA, it was performed for the in-house MEA. Successive I-V curves were performed during 53 h at 160 °C, atmospheric pressure and 1.0 % RH in anode and cathode. Figure 2.4 shows I-V curves along the time for potential cycling activation (1 h, 4 h, 25 h and 53 h). It can be seen that performance increases along the time, especially in the initial 25 h, for the entire current density range. A similar behavior is seen for both activation methods performed in in-house MEA, although galvanostatic activation seems to activate in higher extent. To interpret the nature of activation and understand the phenomena involved, cyclic voltammetry and electrochemical impedance spectroscopy were performed.

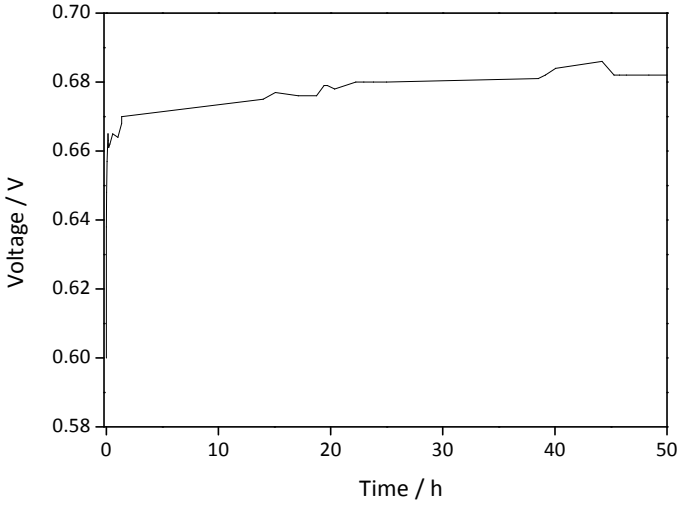


(a)

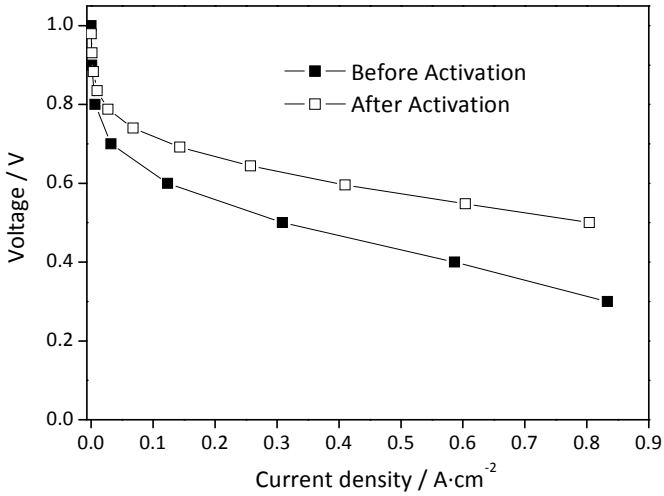


(b)

**Figure 2.2** Fuel cell voltage during galvanostatic activation, at 0.2 A·cm$^{-2}$ current density (a), and I-V curves before (□) and after (■) 50 h galvanostatic activation (b), for Celtec® - P1000 MEA, at 160 °C and 1 bar.

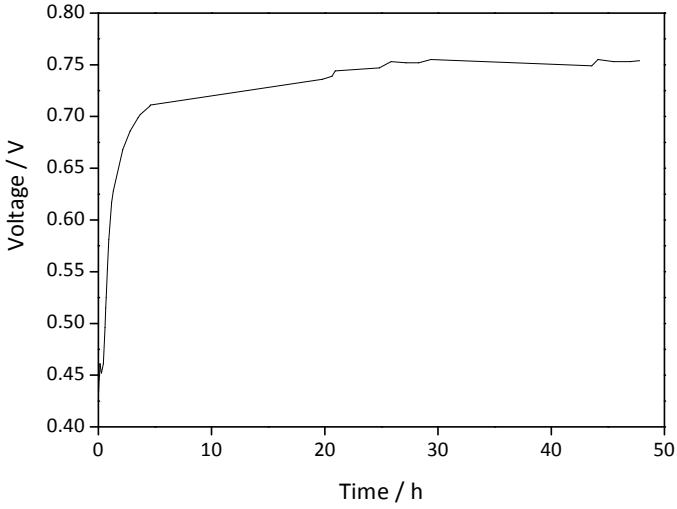


(a)

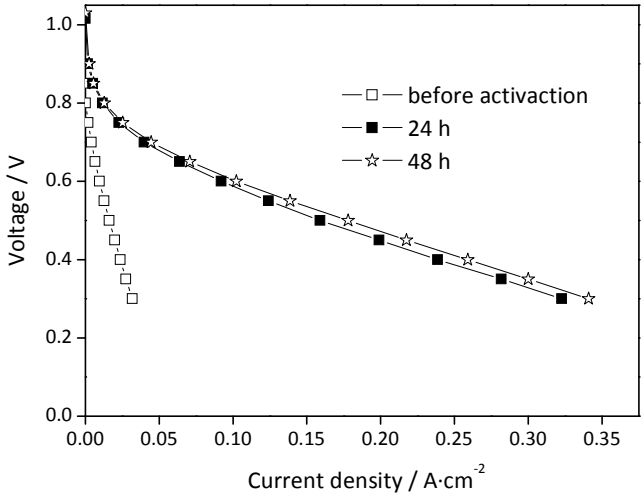


(b)

**Figure 2.3** Fuel cell voltage during galvanostatic activation, at 0.02 A·cm$^{-2}$ current density (a), I-V curves before activation (□), after 24 h (■) and after 48 h (✯) of galvanostatic activation (b), for in-house MEA, at 160 °C and 1 bar.

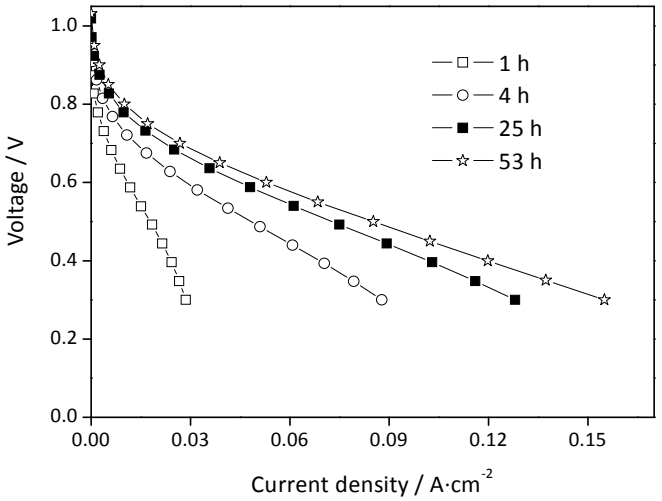


**Figure 2.4** I-V curves for in-house MEA at 160 °C and 1 bar, and at different instants of potential cycling activation, 1 h (□), 4 h (○), 25 h (■) and 53 h (☆).

### *2.4.1.1 Electrochemical impedance spectroscopy (EIS)*

The impedance spectroscopy analysis was used to obtain the ohmic resistance and the charge transfer resistance of anode and cathode.

In Figure 2.5 is plotted the Nyquist plot, before and after activation, obtained at 160 °C and at current densities of 0.03 A·cm$^{-2}$ (a) and 0.3 A·cm$^{-2}$ (b), for Celtec® - P1000 MEA. There is a large semi-circle at lower frequencies that can be attributed to the cathode and a smaller semi-circle at higher frequencies, related to the anode. When the Nyquist plot crosses the real axis, one obtains the pure resistive behaviour that is related to the ohmic resistance of fuel cell. The cathode semi-circle shows a strong dependency on current load, with a smaller loop being obtained for higher current densities. This dependency can often be described by the Tafel equation [29].

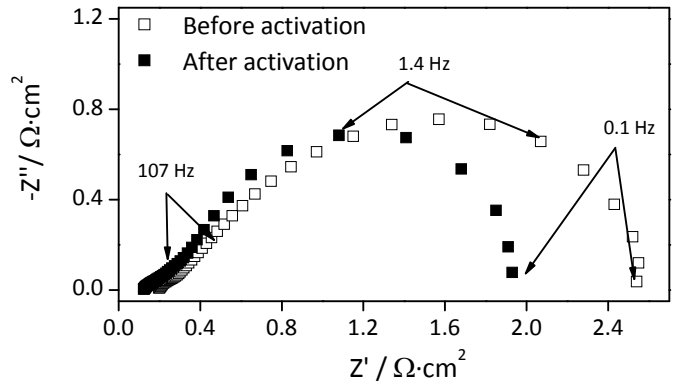


(a)

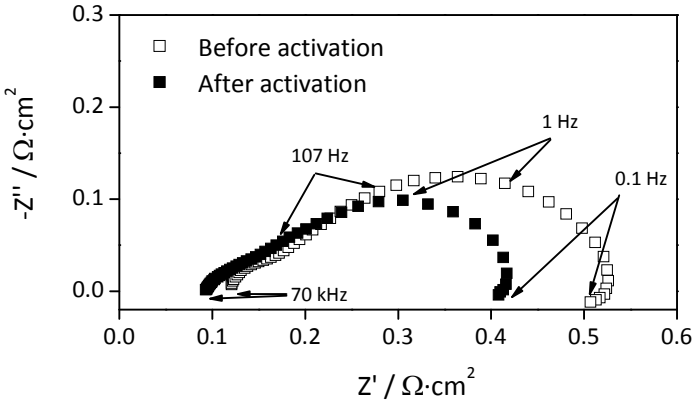


(b)

**Figure 2.5** Nyquist plot for Celtec® - P1000 MEA, at 160 °C and 1 bar, before (□) and after 50 h activation (■), at 0.03 A·cm$^{-2}$ (a) and 0.3 A·cm$^{-2}$ (b) current density.

The ohmic resistance and the charge transfer resistance of anode and cathode were obtained fitting the electrical equivalent circuit represented in Figure 2.6 to the impedance spectra. A typical fuel cell electrical equivalent is separated in cathode and anode parts (with a resistance in parallel with a constant phase element) and ohmic losses (Figure 2.6). The elements 2 and 5 in the electrical equivalent circuit represent the charge transfer resistance of cathode ($R_{ct}^{c}$) and anode ($R_{ct}^{a}$) reactions, whereas elements 3 and 6 represent the charge double layer capacitance ($C_{dl}$). An ohmic resistance is added, element 4, which includes the resistances of the

membrane, end plates, flow fields and contact interfaces. Finally, an inductive element (element 1), representing the inductance of the wires, was also added to the electric equivalent circuit. Since sufficient reactants were supplied, a second semi-circle is not present in the Nyquist plot (Figure 2.5) at lower frequencies (representing the mass transfer resistances at the gas diffusion layer). Jespersen *et al.* [30] suggested that both anode and cathode may be represented by a single charge transfer resistance in parallel with a capacitance; however, we considered the anode separately from the cathode to explain the small loop at high frequencies [31] – Figure 2.5.

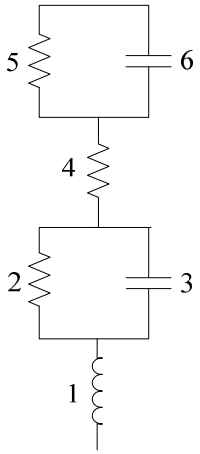


**Figure 2.6** Equivalent electrical circuit of a fuel cell. Element 1 represents the inductance of wires, elements 2 and 5 represent the charge transfer resistance cathode ( $R_{ct}^{c}$ ) and anode ( $R_{ct}^{a}$ ) reactions, elements 3 and 6 represent the represent the double layer capacitance of cathode and anode and element 4 represents the ohmic resistance of the fuel cell.

The SIM module from Thales software (Zahner-Elektrik GmbH) was used to fit the proposed electrical model to the experimental data. The electric equivalent model resistances for the Celtec®-P1000 MEA at 160 °C are given in Table 2.1.

After 50 h of galvanostatic activation of the Celtec® - P1000 MEA, for both current densities, there was a decrease on ohmic resistance (the point where the Nyquist

plot crosses the real axis in Figure 2.5 is shifted slightly to the left) and on the electrodes resistances. The ohmic resistance decreased 31.1 % at 0.03 A·cm$^{-2}$ and 13.7 % at 0.3 A·cm$^{-2}$ (Table 2.1). Since the main contribution to the ohmic resistance is the resistance of the electrolyte membrane [30; 32], the ohmic resistance decrease in impedance spectra at both current densities should be mainly assigned to the membrane humidification. Water effect in phosphoric acid doped PBI membrane will be discussed in more detail in the following section.

There is a decrease on ohmic resistance with current density increase and this effect can be seen before and after galvanostatic activation. This can be explained by the fact that more water is produced at the cathode, at high current densities, from the electrochemical reduction of oxygen from air. As explained by Zhang *et al.* [32], at sufficient high current density, the amount of water sorbed in the membrane levels off and so the membrane ohmic resistance. As expected, the humidification effect is less notorious after activation.

The electrodes charge transfer resistances are related to the electrochemical reactions at the catalyst, having decreased for anode and cathode with galvanostatic activation. The cathode resistance decreased 22.5 % at 0.03 A·cm$^{-2}$ and 27.4 % at 0.3 A·cm$^{-2}$ (Table 2.1), which indicates a higher catalyst activity by removal of impurities from catalyst or redistribution of electrolyte [26].

**Table 2.1** Charge transfer resistance of cathode ( $R_{ct}^{c}$ ) and anode ( $R_{ct}^{a}$ ) reactions and ohmic resistance for Celtec® - P1000 MEA, before and after 50 h galvanostatic activation, at 0.03 A·cm$^{-2}$ and 0.3 A·cm$^{-2}$ current density.

| | Current density/ A·cm$^{-2}$ | | | |
|---|---|---|---|---|
| | 0.03 | | 0.3 | |
| | Before activation | After 50 h activation | Before activation | After 50 h activation |
| $R_{ct}^{a}$ / mΩ·cm$^2$ | 526.5 | 306.4 | 100.8 | 94.9 |
| Ohmic Resistance/ mΩ·cm$^2$ | 169.9 | 117.1 | 104.8 | 90.4 |
| $R_{ct}^{c}$ / mΩ·cm$^2$ | 1983.5 | 1546.5 | 327.6 | 237.7 |

Figure 2.7 (a) shows the EIS spectra for the in-house MEA at 0.02 $A \cdot cm^{-2}$, at the beginning of galvanostatic activation process (instant 0.5 h), during activation (instants 1 h and 24 h) and at the end of the activation process (instant 48 h). There was a dramatic decrease in ohmic resistance over time, particularly, during the first 24 h. Figure 2.7 (b) shows the EIS spectra, at the same value of current density, for potential cycling activation, at the beginning of the activation process (instant 1 h), during activation (instants 4 h and 25 h) and at the end of the activation process (instant 53 h). Also, during the first 24 h, a great decrease in ohmic resistance was observed. By fitting the proposed electrical model of Figure 2.6 to the impedance spectra of the in-house prepared MEA, at the beginning and after the activation process, the ohmic and charge transfer resistances of anode and cathode were obtained (Table 2.2).

The ohmic resistance decreased 89.9 % in 48 h of galvanostatic activation, whereas in potential cycling activation, the ohmic resistance decreased 78.6 % in 53 h. This considerable difference should be related to the membrane humidification over time, due to gas feed humidification, and water production at the cathode. The presence of water increased proton conductivity by ionizing phosphoric acid [33]. In Table 2.2, it can be seen that ohmic and charge transfer resistances of the electrodes had different values in the beginning of the galvanostatic and potential cycling activation. This can be explained with different humidification levels at the time of EIS measurements.

The cathode charge transfer resistance decreased 30.0 % in potential cycling activation mode, after 53 h, and 45.6 % in galvanostatic activation mode, after 48 h. No ionomer was added during electrode preparation, however, it is expected that both liquid acid from $H_3PO_4$ doped membranes and reactant gases reach the catalyst establishing a three-phase zone, especially when water is present. There was a significant enlargement of the electrochemical reaction zone.

Galvanostatic activation seems to be more effective than potential cycling activation since at the end of the activation process, electrodes and ohmic resistances are smaller (Table 2.2). Potential cycling activation was performed intermittently with the cell being kept at OCV between cycles (25 cycles were performed in 53 h). It has

been shown that operating at OCV has a vicious effect on the PEMFC performance [34]. Cathode resistance and cathode platinum crystallite size increase due to platinum dissolution and re-deposition and to corrosion of the carbon catalyst support. The in-house prepared MEA, as described, uses non-supported catalyst and over the 53 h potential cycling activation, no decrease in performance nor in open circuit voltage value was observed.

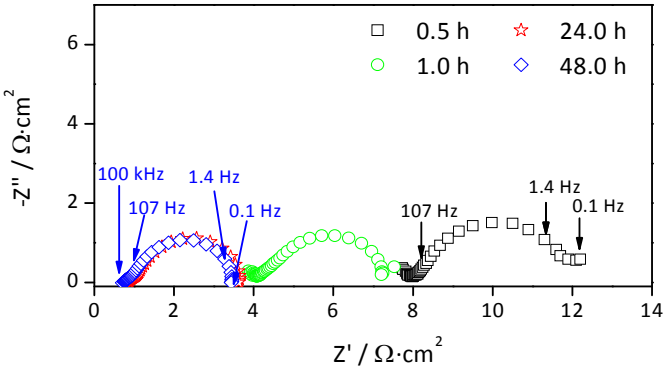


(a)

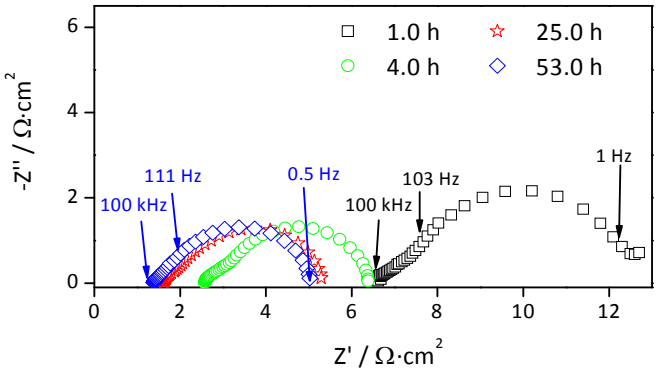


(b)

**Figure 2.7** Nyquist plot at different instants of galvanostatic activation process, 0.5 h (□), 1 h (○), 24 h (☆) and 48 h (◊) (a), and Nyquist plot at different instants of potential cycling activation, 1 h (□), 4 h (○), 25 h (☆) and 53 h (◊) (b), for in-house MEA, at 0.02 A·cm$^{-2}$ current density, 160 °C and 1 bar.

**Table 2.2** Charge transfer resistances of cathode ( $R_{ct}^{c}$ ) and anode ( $R_{ct}^{a}$ ) reactions and ohmic resistance, in beginning and after activation, for in-house prepared MEA at 0.02 A·cm$^{-2}$.

| | Galvanostatic activation | | Potential cycling activation | |
|---|---|---|---|---|
| | 0.5 h activation | 48 h activation | 1 h activation | 53 h activation |
| $R_{ct}^{a}$ / mΩ·cm$^2$ | 915.2 | 505.6 | 2598.2 | 699.2 |
| Ohmic Resistance/ mΩ·cm$^2$ | 7194.0 | 725.6 | 6221.6 | 1329.2 |
| $R_{ct}^{c}$ / mΩ·cm$^2$ | 4133.8 | 2250.2 | 4417.6 | 3090.7 |

### *2.4.1.2 Cyclic Voltammetry*

With cyclic voltammetry it is possible to obtain an estimation of the electrochemical surface area (ESA) of the working electrode. For performing a cyclic voltammetry scan the cathode was purged with nitrogen and used as working electrode while anode was used as reference and counter electrode.

ESA values was determined by using equation 2.1 [35], where *q* represents the atomic hydrogen charge density (in C·m$^{-2}$), $\Gamma$ is the necessary charge to reduce a monolayer of protons on platinum ($\Gamma = 210\times10^{-4}$ C·$m_{Pt}^{-2}$) and *L* is the platinum load in the electrode (in $g_{Pt}$·m$^{-2}$):

$$\mathrm{ESA}(m_{Pt}^{2}\cdot g_{Pt}^{-1}) = \frac{q}{\Gamma \cdot L} \qquad (2.1)$$

From cyclic voltammetry scan it is possible to determine the atomic hydrogen charge density due to proton reduction and following adsorption on platinum (reaction equation 2.2) by integration of the corresponding peak with double charge current as base line.

$$Pt + H^{+} + e^{-} \leftrightarrow Pt\text{-}H_{ads} \qquad (2.2)$$

Considering that proton reduction occurs in the potential region between 0.4 V and 0.05 V [35], the charge density of cathode was obtained using the Thales software.

Figure 2.8 plots the cyclic voltammetry diagrams before and after 50 h galvanostatic activation, for Celtec® - P1000 MEA. There was an increase of ESA from 42 $m_{Pt}^2 \cdot g_{Pt}^{-1}$ to 53 $m_{Pt}^2 \cdot g_{Pt}^{-1}$ in the cathode of Celtec® - P1000 MEA, which is in agreement with the resistance decrease at the cathode observed by EIS (Table 2.1). Typical values of ESA for low temperature PEMFC working with Nafion® membrane is 40-60 $m_{Pt}^2 \cdot g_{Pt}^{-1}$ [19].

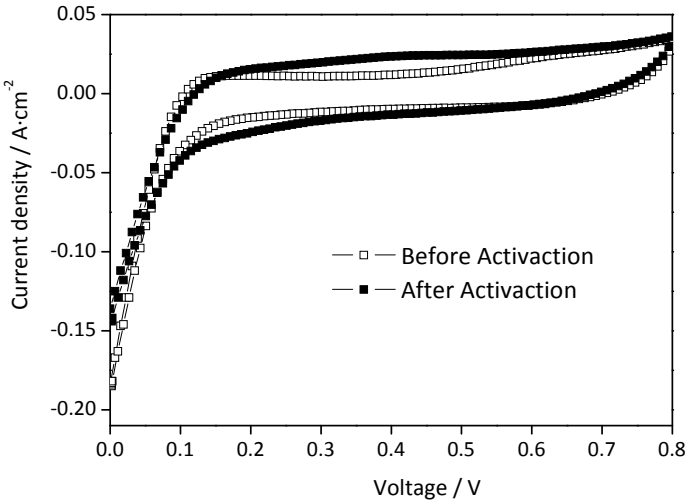


**Figure 2.8** Cyclic voltammetry diagrams for Celtec® - P1000 MEA, before (□) and after 50 h galvanostatic activation (■), at 160 °C and 1 bar.

Similarly, for the in-house prepared MEA, Figure 2.9 (a) and Figure 2.9 (b) shows cyclic voltammetry diagrams before and after 48 h galvanostatic activation and 53 h potential cycling activation, respectively. ESA increased from 6 $m_{Pt}^2 \cdot g_{Pt}^{-1}$ to 17 $m_{Pt}^2 \cdot g_{Pt}^{-1}$ in galvanostatic activation mode, and from 5 $m_{Pt}^2 \cdot g_{Pt}^{-1}$ to 10 $m_{Pt}^2 \cdot g_{Pt}^{-1}$ in potential cycling activation method. ESA values for in-house MEA are lower when compared to the values of the commercial electrodes. However and for the in-house MEA, ESA increase shows that the three phase zone in the electrode was extended

during activation. This should be related to the phosphoric acid bleeding from the membrane to the catalyst layer, serving there as electrolyte to conduct protons [14].

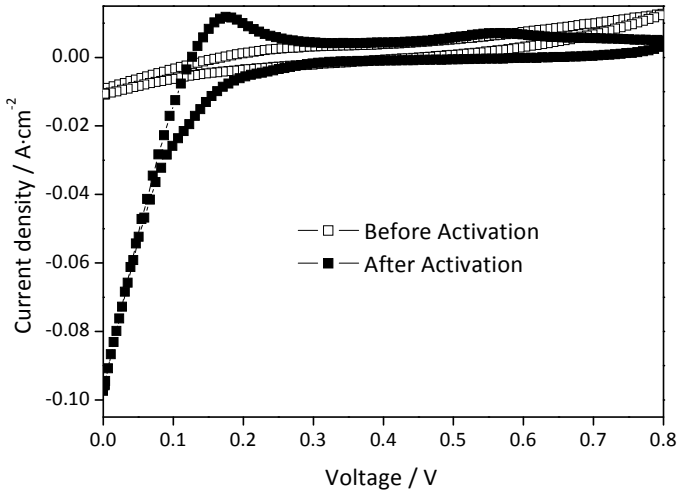


(a)

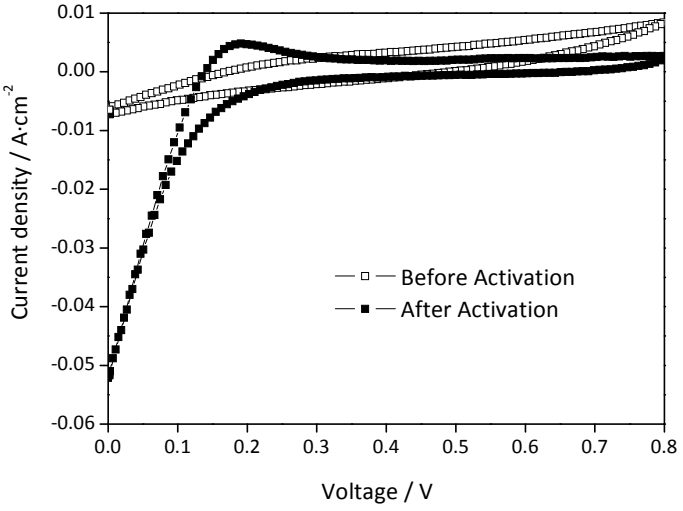


(b)

**Figure 2.9** Cyclic voltammetry diagrams, before (□) and after 48 h galvanostatic activation (■) (a), and before (□) and after 53 h potential cycling activation process (■) (b), for the in-house prepared MEA, at 160 °C and 1 bar.

The results obtained show the importance of the electrolyte to improve the protonic access from the catalyst to the membrane, when the catalyst is not in direct contact with it. In order to achieve a maximum active area the catalyst must be in contact with an electron conductor (carbon support) and with an ionic conductor (electrolyte) and have a good access to the reactants. As explained by Seland *et al.* [36] at very low current density, only a small fraction of catalyst is needed and the electrochemical reaction takes place preferentially close to the membrane. With increasing current density the current generation shifts away from the membrane and protons have to migrate longer distances. The amount of electrolyte must be determined in order to optimize the fuel cell performance since an excessive amount of electrolyte (either in the membrane or in the catalyst layer) can block the access of reactants to active sites, leading to low utilization of platinum [36-37].

Results from in-house prepared MEA show a tremendous decrease in ohmic resistance and an increase in catalyst activity. However, a higher activation time should be needed to increase ESA and decrease the ohmic resistance furthermore. In our study, a PBI membrane doped with 12.5 $mg \cdot cm^{-2}$ of phosphoric acid was used with a gas diffusion layer coated with 23-μm thick catalyst layer. Oono *et al.* [38] studied the acid migration from phosphoric acid doped PBI to the catalyst layer during high temperature PEMFC operation. As in present work, electrodes did not contain any electrolyte. These authors suggested an optimum concentration of phosphoric acid in the membrane of 10 $mg \cdot cm^{-2}$, for a 20-μm thick catalyst layer. They needed 200 h period for the fuel cell voltage to reach a stationary value in anhydrous conditions.

Concerning the Celtec® - P1000 MEA, changes were observed in electrochemical tests after 50 h galvanostatic activation, but in a smaller extent compared to the in-house MEA. Tingelof and Ihonen [26] activated four different Celtec® - P1000 MEA and showed that they were not activated to the same extent, for the same activation time and procedure.

### 2.4.2 Influence of temperature and relative humidity

The behavior of HT-PEMFC, equipped with the in-house prepared MEA, was studied after potential cycling activation at different temperatures and relative humidities. This activation process needed different activation times, since at higher temperatures and humidities the activation was faster. A fresh MEA was used for each operating condition.

It has been shown that, in anhydrous conditions, the proton conductivity of phosphoric acid doped PBI membrane can decrease whenever the fuel cell is operated above 140 °C [31] due to the formation of pyrophosphoric acid, which is less conductive than phosphoric acid. The pyrophosphoric acid is formed from the dehydration of the phosphoric acid. So, there are two opposed effects when temperature increases: from one side the reaction and transport kinetics increase but, from the other side, the membrane conductivity may experience some degradation. This makes the study of the relative humidity interesting, especially for temperatures above 140 °C. Figure 2.10 shows I-V curves obtained at 160 °C and three different relative humidities, 1.0 %, 2.5 % and 5.0 %.

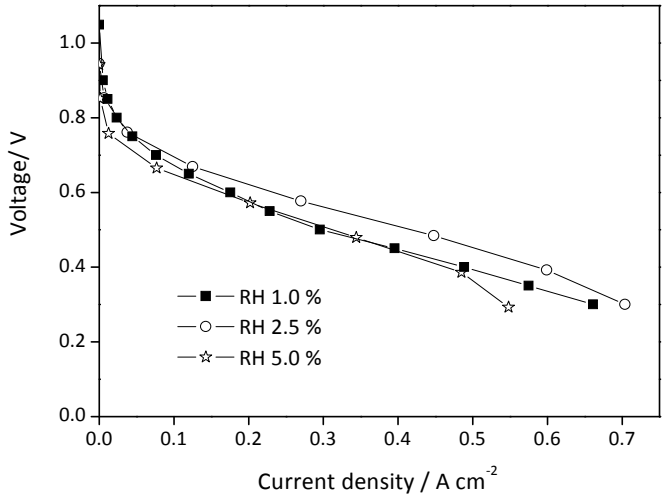


**Figure 2.10** I-V curves for the in-house MEA at 160 °C and 2 bar, at 1.0 % RH (■), 2.5 % RH (○) and 5.0 % RH (✯).

A performance increase was observed when relative humidity of gas feed increased from 1.0 % to 2.5 % in anode and cathode. However, the performance of the cell for 5.0 % RH degraded when compared to 2.5 % RH, for the entire current density range, and when compared to 1.0 % RH, for low and high current density ranges.

It is well established that proton conductivity of phosphoric acid doped PBI membranes increases with the relative humidity [6; 12; 33; 39]. PBI polymer acts as a frame that immobilizes phosphoric acid and phosphoric acid is bonded to PBI through hydrogen bonds. Proton conductivity is recognized to be due to phosphoric acid domains [7; 12], where protons transfer follows “grotthuss” mechanism [10; 12]. Proton conductivity increases with the relative humidity because water provides more hydrogen bonds for protons to jump, between water-phosphoric acid and between water-imino groups of PBI, this whenever the humidity is high enough. This allows faster proton transfer since hydrogen bond between water and phosphoric acid has the longest distance (and thus weaker hydrogen bond) and a high degree of mobility, in comparison to hydrogen bonds of other species [13]. Besides, relative humidity affects the content of free water in the electrolyte, which lowers the viscosity of the polymer rendering it more conductive [9] and facilitating oxygen transport within the cathode [33]. Water presence also facilitates the migration of aqueous phosphoric acid to the electrodes and to the space between the electrodes and membrane, thus serving as electrolyte for proton conduction. All these enhancing factors explain the increase of performance when relative humidity increased from 1.0 % to 2.5 %. However, the fuel cell performance decreased when relative humidity was increased from 2.5 % to 5.0 %. Figure 2.11 shows the Nyquist plot at 0.18 $A \cdot cm^{-2}$ for 1.0 % and 5.0 % RH. At this current density the steady-state voltage values for both relative humidities were close (Figure 2.10), however, the Nyquist plot for these humidities was very different (Figure 2.11). This happens because the ohmic resistance at 5.0 % RH was lower than at 2.5 % RH but the cathode charge transfer resistance was much higher. Likely, there was phosphoric acid leaching from the cathode catalyst layer, decreasing the three-phase zone, making proton transfer more difficult and increasing the cathode resistance. Water production at the cathode side makes it more liable to suffer phosphoric acid leaching than the anode side.

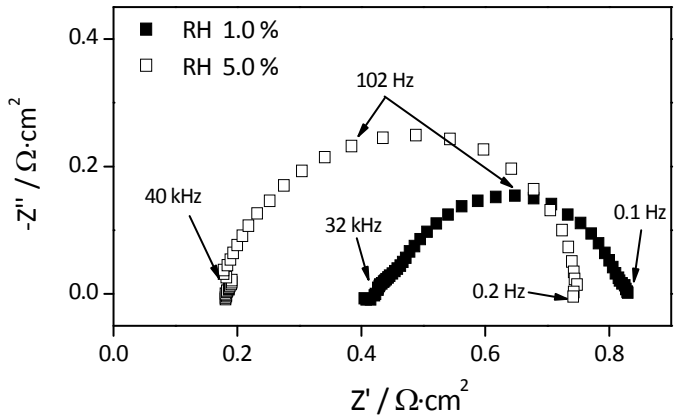


**Figure 2.11** Nyquist plots for the in-house MEA at 0.18 A·cm$^{-2}$ current density, 160 °C and 2 bar, at 1.0 % RH (□) and 5.0 % RH (■).

Figure 2.12 plots the I-V curves at 120 °C, 140 °C and 160 °C for 2.5 % and 5.0 % RH. When the operating temperature increased, for the same relative humidity, the fuel cell performance also increased. The temperature affected not only the steady-state cell voltage, as seen in Figure 2.12, but also the Nyquist plots. Nyquist plots at 120 °C, 140 °C and 160 °C and 5.0 % RH and for 0.18 A·cm$^{-2}$ can be seen in Figure 2.13. The values of ohmic resistance and electrodes charge transfer resistances were obtained by fitting the electrical equivalent model of Figure 2.6 to the Nyquist spectra, Table 2.3. The ohmic resistance decreased 48.3 % with the increasing temperature from 120 °C to 160 °C. A decrease in cathode resistance can also be observed, suggesting that the increase of temperature speeds up the electrochemical reaction.

In Figure 2.14, it is plotted the membrane conductivity as a function of the current density at 120 °C, 140 °C and 160 °C, and 2.5 % and 5.0 % RH. The values were obtained by fitting the electrical equivalent model (Figure 2.6) to the Nyquist plot at different temperatures, relative humidities and current densities; the membrane conductivities obtained were in the range of 0.015-0.055 S·cm$^{-1}$. Higher values of proton conductivity were obtained for higher temperatures and relative humidities. Ma *et al.* [12] reported conductivity values between 0.005 S·cm$^{-1}$ and 0.02 S·cm$^{-1}$ at 140 °C and 5.0 % RH, varying the phosphoric acid doping level between 300 wt. % and 630 wt. % and Scott *et al.* [39] reported values between 0.02 and 0.03 S·cm$^{-1}$ for

120 °C and for relative humidities between 1.5 % and 7.1 %, for a fixed doping level of 5.6 mol of phosphoric acid per PBI unit.

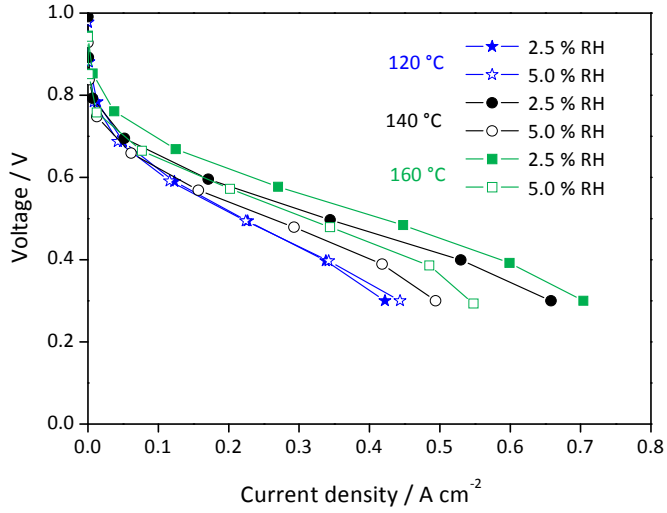


**Figure 2.12** I-V curves for the in-house MEA as a function of temperature, 120 °C (☆), 140 °C (○) and 160 °C (□), at 2.5 % RH (full symbols) and 5.0 % RH (open symbols).

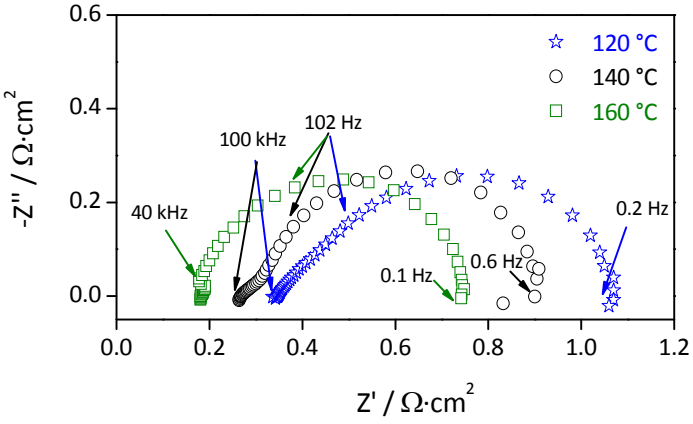


**Figure 2.13** Nyquist plots for the in-house MEA, at 0.18 A·cm$^{-2}$ current density, 2 bar, and 5.0 % RH, at 120 °C (☆), 140 °C (○) and 160 °C (□).

**Table 2.3** Charge transfer resistances of anode ($R_{ct}^{a}$) and cathode ($R_{ct}^{c}$) reactions and ohmic resistance, for the in-house MEA, at 0.18 A·cm$^{-2}$ current density and 120 °C, 140 °C and 160 °C.

| | Fuel Cell temperature/ °C | | |
|---|---|---|---|
| | 120 | 140 | 160 |
| $R_{ct}^{a}$ / mΩ·cm$^2$ | 113.1 | 71.4 | 77.6 |
| Ohmic Resistance/ mΩ·cm$^2$ | 346.5 | 267.2 | 179.1 |
| $R_{ct}^{c}$ / mΩ·cm$^2$ | 617.3 | 573.3 | 491.9 |

The temperature dependence of the conductivity can be described by the Arrhenius equation (equation 1.5) [10; 12; 32]. It is possible to obtain the proton conducting activation energy ($E_a$) and the pre-exponential factor (ln($\sigma_0$)) from the Arrhenius plot. Table 2.4 shows $E_a$ and ln($\sigma_0$) for various current densities, obtained for the temperature range of 120 °C - 160 °C and 5 % RH. The average value of $E_a$ for current densities between 0.02 A·cm$^{-2}$ and 0.18 A·cm$^{-2}$ is 28.7 kJ·mol$^{-1}$ and the average value of ln($\sigma_0$) is 11.1 S·K$^{-1}$·cm$^{-1}$. Ma *et al.* [12] reported $E_a$ of 28 $\pm$2 kJ·mol$^{-1}$ and ln($\sigma_0$) of 10.43 S·K$^{-1}$·cm$^{-1}$, for 630 wt. % phosphoric acid doped PBI membrane at 5.0 % RH in the temperature range of 80 °C - 200 °C.

**Table 2.4** Proton conducting activation energy and pre-exponential factor, for the in-house MEA, for different current densities, at 5.0 % RH and 2 bar, in temperature range of 120 °C - 160 °C.

| Current density / A·cm$^{-2}$ | Proton conducting activation energy ($E_a$) / kJ·mol$^{-1}$ | Pre-exponential factor (ln($\sigma_0$)) / (S·K$^{-1}$·cm$^{-1}$) |
|---|---|---|
| 0.02 | 33.4 | 12.4 |
| 0.07 | 29.3 | 11.3 |
| 0.14 | 26.7 | 10.6 |
| 0.18 | 25.7 | 10.3 |

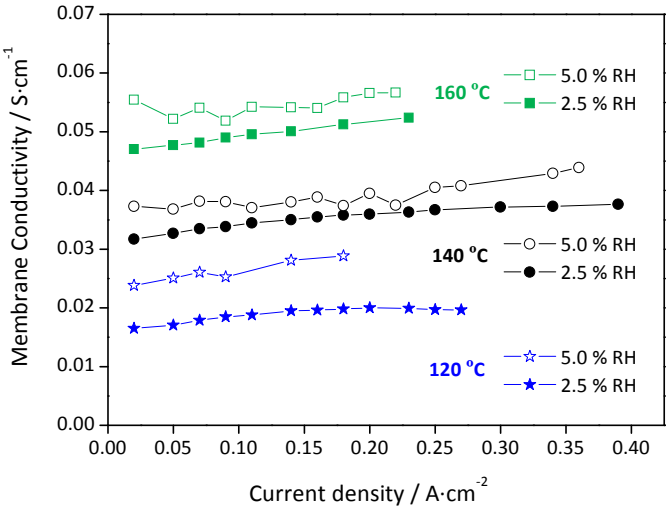


**Figure 2.14** Membrane conductivity for the in-house MEA as a function of temperature, 120 °C (☆), 140 °C (○) and 160 °C (□), at 2.5 % (full symbols) and 5.0 % (open symbols).

It was already seen before that the power density decreased for 160 °C when relative humidity increased from 2.5 % to 5.0 %. The same effect can be seen for the other two temperatures, especially for 140 °C. Figure 2.15 (a) shows the Nyquist plot for 140 °C, at current density of 0.18 A·cm$^{-2}$ and at 2.5 % and 5.0 % RH whereas Figure 2.15 (b) shows the charge transfer resistance of cathode and anode reactions for both relative humidities, as a function of current density (from 0.02 A·cm$^{-2}$ to 0.4 A·cm$^{-2}$). For low current densities the anode resistance is significantly smaller than the cathode resistance. However, above a certain current density (> 0.07 A·cm$^{-2}$) the charge transfer resistances of both anode and cathode have to be considered. A similar trend for cathode resistance was obtained by Zhang *et al.* [32]. When the relative humidity increased from 2.5 % to 5.0 % RH, the anode resistance decreased for very low current densities but no effect was observed for current densities higher than 0.1 A·cm$^{-2}$. On the other hand, the cathode resistance increased for all current densities. A similar trend was also observed for 120 °C (not shown). The water produced at the cathode together with the humidified air may have originated phosphoric acid bleeding, and the loss of electrolyte decreased the proton conduction in electrode.

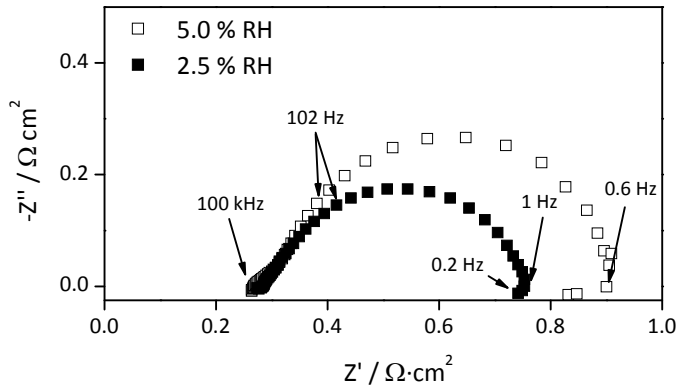


(a)

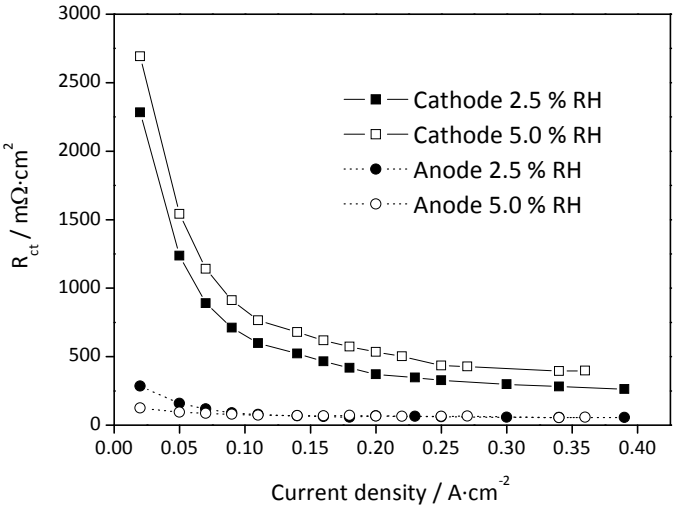


(b)

**Figure 2.15** Nyquist plots at 0.18 A·cm$^{-2}$ current density (a) and charge transfer resistance ($R_{ct}$) of cathode (□) and anode (○) as a function of current density (b), for the in-house MEA, at 140 °C, 2 bar and 2.5 % RH (full symbols) and 5.0 % RH (open symbols).

## 2.5 Conclusions

The activation process of phosphoric acid doped PBI-based MEA was studied based on I-V curves, EIS technique and cyclic voltammetry analysis. Celtec® - P1000 MEA

was activated using galvanostatic procedure while an in house MEA was activated using galvanostatic and potential cycling. For approximately the same activation time the galvanostatic procedure originated a MEA with a higher performance. For both MEAs, ohmic resistance decreased during the activation procedure and the catalyst activity increased. The ohmic resistance decreased due to PBI membrane humidification. The catalyst activity increased because the migration of phosphoric acid from the membrane to the catalyst layer increased the three-phase zone, in the case of in-house prepared MEA and by the removal of impurities from catalyst or redistribution of electrolyte in the case of commercial MEA.

The in-house prepared MEA was activated at different temperatures and humidities. It was verified that the membrane humidification is important for reducing the ohmic resistance and to improve the triple phase contact but an excess of water increases the cathode resistance, most likely because the excessive bleeding of phosphoric acid. Within the temperature range studied, 120 °C - 160 °C, and for the three levels of relative humidity considered, 1.0 %, 2.5 % and 5.0 %, the best performance of the in-house prepared MEA was obtained for 2.5 % relative humidity at 160 °C. It was obtained a maximum power density of 0.24 $W \cdot cm^{-2}$.

## 2.6 Acknowledgments

The work of M. Boaventura was supported by FCT (Grant SFRH/BD/28187/2006). The present work was also partially supported by FCT project PTDC/EQU-EQU/70574/2006. The authors would like to thank DLR (Institute of Technical Thermodynamics - German Aerospace Center) for receiving M. Boaventura and for the support on electrodes production and Dr. Alfredo Tanaka for the help on acid doping determination. Dr. Lúcia Brandão is acknowledged for the helpful discussions.

## 2.7 References

[1] Savadogo, O., 2004. Emerging membranes for electrochemical systems - Part II. High temperature composite membranes for polymer electrolyte fuel cell (PEFC) applications. J Power Sources 127, 135-161.

[2] Hogarth, W.H.J., da Costa, J.C.D., Lu, G.Q., 2005. Solid acid membranes for high temperature (> 140 degrees C) proton exchange membrane fuel cells. J Power Sources 142, 223-237.

[3] Jensen, J.O., Li, Q.F., Pan, C., Vestbo, A.P., Mortensen, K., Petersen, H.N., Sorensen, C.L., Clausen, T.N., Schramm, J., Bjerrum, N.J., 2007. High temperature PEMFC and the possible utilization of the excess heat for fuel processing. Int J Hydrogen Energy 32, 1567-1571.

[4] Mallant, R.K.A.M., 2003. PEMFC systems: the need for high temperature polymers as a consequence of PEMFC water and heat management. J Power Sources 118, 424-429.

[5] Zhang, J.L., Xie, Z., Zhang, J.J., Tanga, Y.H., Song, C.J., Navessin, T., Shi, Z.Q., Song, D.T., Wang, H.J., Wilkinson, D.P., Liu, Z.S., Holdcroft, S., 2006. High temperature PEM fuel cells. J Power Sources 160, 872-891.

[6] Asensio, J.A., Gomez-Romero, P., 2005. Recent developments on proton conducting poly(2,5-benzimidazole) (ABPBI) membranes for high temperature polymer electrolyte membrane fuel cells. Fuel Cells 5, 336-343.

[7] Li, Q., He, R., Jensen, J.O., Bjerrum, N.J., 2004. PBI-Based Polymer Membranes for High Temperature Fuel Cells - Preparation, Characterization and Fuel Cell Demonstration. Fuel Cells 4 147 - 159.

[8] Li, Q.F., Jensen, J.O., Savinell, R.F., Bjerrum, N.J., 2009. High temperature proton exchange membranes based on polybenzimidazoles for fuel cells. Prog Polym Sci 34, 449-477.

[9] Wainright, J.S., Wang, J.T., Weng, D., Savinell, R.F., Litt, M., 1995. Acid-Doped Polybenzimidazoles - a New Polymer Electrolyte. J Electrochem Soc 142, L121-L123.

[10] Bouchet, R., Siebert, E., 1999. Proton conduction in acid doped polybenzimidazole. Solid State Ionics 118, 287-299.

[11] He, R.H., Li, Q.F., Xiao, G., Bjerrum, N.J., 2003. Proton conductivity of phosphoric acid doped polybenzimidazole and its composites with inorganic proton conductors. J Membrane Sci 226, 169-184.

[12] Ma, Y.L., Wainright, J.S., Litt, M.H., Savinell, R.F., 2004. Conductivity of PBI membranes for high-temperature polymer electrolyte fuel cells. J Electrochem Soc 151, A8-A16.

[13] Daletou, M.K., Kallitsis, J.K., Voyiatzis, G., Neophytides, S.G., 2009. The interaction of water vapors with H3PO4 imbibed electrolyte based on PBI/polysulfone copolymer blends. J Membrane Sci 326, 76-83.

[14] Hu, J.W., Zhang, H.M., Zhai, Y.F., Liu, G., Hu, J., Yi, B.L., 2006. Performance degradation studies on PBI/H3PO4 high temperature PEMFC and one-dimensional numerical analysis. Electrochim Acta 52, 394-401.

[15] Hu, J.W., Zhang, H.M., Zhai, Y.F., Liu, G., Yi, B.L., 2006. 500h continuous aging life test on PBI/H3PO4 high-temperature PEMFC. Int J Hydrogen Energy 31, 1855-1862.

[16] Lin, H.L., Hsieh, Y.S., Chiu, C.W., Yu, T.L., Chen, L.C., 2009. Durability and stability test of proton exchange membrane fuel cells prepared from polybenzimidazole/poly(tetrafluoro ethylene) composite membrane. J Power Sources 193, 170-174.

[17] Liu, G., Zhang, H.M., Hu, J.W., Zhai, Y.F., Xu, D.Y., Shao, Z.G., 2006. Studies of performance degradation of a high temperature PEMFC based on H3PO4-doped PBI. J Power Sources 162, 547-552.

[18] Yu, S., Xiao, L., Benicewicz, B.C., 2008. Durability studies of PBI-based high temperature PEMFCs. Fuel Cells 8, 165-174.

[19] Zhai, Y.F., Zhang, H.M., Xing, D.M., Shao, Z.G., 2007. The stability of Pt/C catalyst in H3PO4/PBI PEMFC during high temperature life test. J Power Sources 164, 126-133.

[20] Qi, Z.G., Kaufman, A., 2002. Activation of low temperature PEM fuel cells. J Power Sources 111, 181-184.

[21] Qi, Z.G., Kaufman, A., 2003. Quick and effective activation of proton-exchange membrane fuel cells. J Power Sources 114, 21-31.

[22] Xu, Z.Q., Qi, Z.G., He, C.Z., Kaufman, A., 2006. Combined activation methods for proton-exchange membrane fuel cells. J Power Sources 156, 315-320.

[23] Xu, Z.Q., Qi, Z.G., Kaufman, A., 2006. Activation of proton-exchange membrane fuel cells via CO oxidative stripping. J Power Sources 156, 281-283.

[24] He, C.Z., Qi, Z.Q., Hollett, M., Kaufman, A., 2002. An electrochemical method to improve the performance of air cathodes and methanol anodes. Electrochem Solid St 5, A181-A183.

[25] Qi, Z., Kaufman, A., 2002. Enhancement of PEM fuel cell performance by steaming or boiling the electrode. J Power Sources 109, 227-229.

[26] Tingelof, T., Ihonen, J.K., 2009. A rapid break-in procedure for PBI fuel cells. Int J Hydrogen Energy 34, 6452-6456.

[27] Gulzow, E., Kaz, T., 2002. New results of PEFC electrodes produced by the DLR dry preparation technique. J Power Sources 106, 122-125.

[28] Gulzow, E., Schulze, M., Wagner, N., Kaz, T., Reissner, R., Steinhilber, G., Schneider, A., 2000. Dry layer preparation and characterisation of polymer electrolyte fuel cell components. J Power Sources 86, 352-362.

[29] Andreasen, S.J., Jespersen, J.L., Schaltz, E., Kaer, S.K., 2009. Characterisation and Modelling of a High Temperature PEM Fuel Cell Stack using Electrochemical Impedance Spectroscopy. Fuel Cells 9, 463-473.

[30] Jespersen, J.L., Schaltz, E., Kaer, S.K., 2009. Electrochemical characterization of a polybenzimidazole-based high temperature proton exchange membrane unit cell. J Power Sources 191, 289-296.

[31] Lobato, J., Canizares, P., Rodrigo, M.A., Linares, J.J., 2007. PBI-based polymer electrolyte membranes fuel cells - Temperature effects on cell performance and catalyst stability. Electrochim Acta 52, 3910-3920.

[32] Zhang, J.L., Tang, Y.H., Song, C.J., Zhang, J.J., 2007. Polybenzimidazole-membrane-based PEM fuel cell in the temperature range of 120-200 degrees C. J Power Sources 172, 163-171.

[33] Liu, Z.Y., Wainright, J.S., Litt, M.H., Savinell, R.F., 2006. Study of the oxygen reduction reaction (ORR) at Pt interfaced with phosphoric acid doped polybenzimidazole at elevated temperature and low relative humidity. Electrochim Acta 51, 3914-3923.

[34] Qi, Z.G., Buelte, S., 2006. Effect of open circuit voltage on performance and degradation of high temperature PBI-H3PO4 fuel cells. J Power Sources 161, 1126-1132.

[35] Cooper, K.R., Ramani, V., Fenton, J.M., Kunz, H.R., 2005. Experimental Methods and Data Analysis for Polymer Electrolyte Fuel Cells. Scribner Associates, Southern Pines.

[36] Seland, F., Berning, T., Borresen, B., Tunold, R., 2006. Improving the performance of high-temperature PEM fuel cells based on PBI electrolyte. J Power Sources 160, 27-36.

[37] Kim, J.H., Kim, H.J., Lim, T.H., Lee, H.I., 2007. Dependence of the performance of a high-temperature polymer electrolyte fuel cell on phosphoric acid-doped polybenzimidazole ionomer content in cathode catalyst layer. J Power Sources 170, 275-280.

[38] Oono, Y., Sounai, A., Hori, M., 2009. Influence of the phosphoric acid-doping level in a polybenzimidazole membrane on the cell performance of high-temperature proton exchange membrane fuel cells. J Power Sources 189, 943-949.

[39] Scott, K., Pilditch, S., Mamlouk, M., 2007. Modelling and experimental validation of a high temperature polymer electrolyte fuel cell. J Appl Electrochem 37, 1245-1259.

# Chapter 3 The influence of CO on the performance of HT-PEMFC[2]

## 3.1 Abstract

In this work the poisoning effect of carbon monoxide (CO) on the performance of high temperature polymer electrolyte membrane fuel cell (HT-PEMFC) is reported. The poisoning was assessed at 160 °C and 180 °C based on the transient behavior of the fuel cell voltage and current density distribution. The current density distribution at similar voltage and global current density were also critically compared for CO-free hydrogen feed and for CO-contaminated hydrogen feed. Furthermore, the current density-voltage and power density curves and impedance spectra were obtained.

Two different cell anodes were used to obtain the current density distribution, 1) a metal segmented flow field and 2) a non-segmented graphite flow field where it was applied a printed circuit board as segmented current collector.

The presence of CO caused a performance loss which is aggravated for higher CO concentrations and higher current densities and for lower temperatures. The transient behavior of the fuel cell voltage and current density distribution showed that the poisoning effect of carbon monoxide at the anode is very fast.

The current density distributions obtained with the metal segmented flow field showed that the use of hydrogen streams containing CO, at the anode, yields an anisotropic distribution of carbon monoxide, which is accentuated for higher carbon monoxide concentrations and current densities. On the other hand, no significant change on the current density distribution was observed with the graphite flow field.

[2] Part of this chapter is adapted from: Boaventura, M., Sander, H., Friedrich, K.A., Mendes, A., 2011. The influence of CO on the current density distribution of high temperature polymer electrolyte membrane fuel cells. Submitted to Electrochim Acta.

## 3.2 Introduction

Polymer electrolyte membrane fuel cell (PEMFC) is a clean technology that has been considered for stationary applications and as an alternative to internal combustion engines.

The most used and effective catalyst for the oxidation of pure hydrogen is platinum. When pure hydrogen is feed to the anode and air/oxygen to the cathode, high power densities of the fuel cell are achieved without any emissions beside water vapor. Since hydrogen production from renewable sources is still under development, it is expected in the near future that low cost hydrogen is generated by steam reforming of natural gas, by partial oxidation of hydrocarbons or by gasification of coal. Hydrogen produced by these processes contains usually 1-2 % of CO [1-3]. An on-board production of hydrogen is often considered due to hydrogen storage constrains and lack of refueling infrastructures.

At typical fuel cell operating temperature (below 90 °C), a decrease in the catalyst activity is observed when small amounts of carbon monoxide (CO), such as 10 ppm, is introduced into the hydrogen feed. The poisoning effect of CO can be mitigated by i) advanced purification of the reformate gas, ii) introduction of an oxidant bleed at the anode feed or iii) use of a more CO tolerant catalyst [1; 4-5]. The first approach increases the system complexity and cost whereas the second compromises safety [3; 6-8]. The development of new electrocatalysts has been focused on bimetallic catalysts (like PtRu/C and PtSn/C), but the effectiveness and durability is still an issue [8].

The carbon monoxide strongly adsorbs on platinum surface, reducing the activity of the catalyst. The adsorption of CO is associated with a negative entropy change and therefore disfavored at higher temperatures [6; 8-10]. The behavior of high temperature PEMFC (100 - 200 °C) was assessed by some authors that performed experiments with hydrogen containing different concentrations of CO [9; 11-15]. Higher temperatures lead to lower performance degradation in the presence of CO when compared to the lower operation temperatures. Good tolerance of a Pt/C

catalyst was observed with 3 % of CO at 200 °C up to 1.0 $A \cdot cm^{-2}$ or cell voltage above 0.50 V [9], and with 3 % and 5 % of CO at 180 °C, at moderate values of voltage [11]. It is also shown that the performance of the fuel cell operating at 210 °C was not affected by 1.0 % of CO in the anode feed [12]. These studies demonstrate that the increase of the fuel cell temperature is an alternative to diminish the contamination of the anode catalyst, showing the viability of direct use of reformate gas on the fuel cell anode and the possibility of successful incorporation of reformers in high temperature PEMFC systems. Pan *et al.* integrated a high temperature PEMFC with a methanol reformer [16]. The CO amount at the reformate gas was below 0.2 % and at temperatures between 135 °C and 170 °C only a slightly decrease in performance was observed in a single fuel cell.

The operating conditions, the design and the membrane electrode assembly materials impose a spatial dependence on the electrochemical behavior of the fuel cell [17-18]. The knowledge of the local performance allows the testing and optimization of new fuel cell materials [18] and to identify local degradation processes [19]. On the other hand, it was shown that imposing non-uniformities and gradients at the fuel cell, whether by manipulating operating conditions or using non-uniform MEA structures, can be beneficial to the fuel cell performance [20]. Segmented fuel cells (SFC) have been used as tool to study the local responses and to identify factors responsible for the unequal performance at the fuel cell active area. The most important SFC designs and the SFC application to the study of low temperature PEMFC have been recently reviewed [21].

The use of a CO contaminated fuel can originate a spatially heterogeneous poisoning of the anode catalyst, thereby changing the local properties. The determination of the degree of poisoning and the respective location is of particular interest since customized anodes can be developed taking into account the poisoning distribution. Bender and Zawodzinski [17] observed a special dependency along the anode channel when the CO partial pressure is stepped from 0 to 100 ppm on a Pt/C catalyst at 80 °C. Tingelof *et al.* [22] used a segmented cathode and two different CO concentration levels, 10 and 80 ppm, in the reformate mix fed to the anode (50 % $H_2$, 40 % $CO_2$ and 10 % $N_2$) in order to evaluate poisoning effect on Pt/C and PtRu/C

catalysts at 60 °C. CO adsorbed more strongly onto Pt/C than onto PtRu/C catalyst and the poisoning effect was uneven throughout the fuel cell. Furthermore, Brett *et al.* [18; 23] showed that the extent and distribution of CO in a fuel cell anode could be obtained by localized CO-stripping voltammetry.

In this work the effect of stepping the CO amount at the anode gas feed from 0.0 % to 1.5 % or 3.0 % on the performance of a high temperature PEMFC, at 160 °C and 180 °C, is reported. A segmented anode was used to obtain the current density profile and the I-V and power density curves and electrochemical impedance spectra of this cell were obtained.

## 3.3 Experimental

### 3.3.1 Materials

The MEAs used in this study cell were Celtec® - P1000 MEA from BASF Fuel Cell. The MEA cathode side was loaded with 0.8 $mg \cdot cm^{-2}$ of platinum and at the anode with 1 $mg \cdot cm^{-2}$ of platinum; the total MEA thickness was 905 μm and the active area was 20.25 $cm^2$. The membrane thickness was approximately 120 μm.

In the experiments, besides pure hydrogen, certified gas mixtures were used to evaluate the poisoning effect of carbon monoxide, i) 97.000 % $H_2$ / 3.000 % $N_2$, ii) 97.000 % $H_2$ /1.5000 % $N_2$ / 1.5000 % CO (hereafter referred as 1.5 % CO mixture) and iii) 97.000 % $H_2$ / 3.000 % CO (hereafter referred as 3.0 % CO mixture).

### 3.3.2 Segmented cell

A DLR segmented cell was used to obtain the current density distribution [24-25]. The anode flow field (and therefore the current collector) is segmented, consisting of a chocolate wafer structure with perpendicular channels of 1 mm depth and 1 mm width (Figure 3.1 (a)). The 25 $cm^2$ flow field was divided into 16 individual segments,

isolated among each other and the frame. In order to fit the surface of all segments into the same plane, a Teflon plate was used on the backside of the segments (Figure 3.1 (b)). The cathode was not segmented and had a single serpentine structure. Both anode and cathode flow fields were gold coated.

A second segmented cell (S++, Germany) was used to evaluate the poisoning effect of carbon monoxide on the current density distribution. The S++ cell has 25 $cm^2$ non-segmented graphite flow fields with serpentine configuration. At the anode side a printed circuit board was used as segmented current collector (16 segments) – Figure 3.1 (c).

The current generated in the 16 segments flowed through a series of small measurement resistances. The voltage drop along the resistances was scanned and the resulting current density distribution was recorded. The entire fuel cell current was collected using a copper current collector behind the resistances (Figure 3.1 (b)).

### 3.3.3 Poisoning experiments and electrochemical characterization

The Celtec® - P1000 MEAs were used accordingly to supplier's specifications. The MEAs were operated at atmospheric pressure with stoichiometry of 2 for air and 1.2 for hydrogen or hydrogen/CO mixture and using non-humidified inlet gases. The MEAs were activated at constant load of 0.20 $A \cdot cm^{-2}$ and 160 °C for at least 100 h. The poisoning of the anode, at 160 °C and 180 °C, was initiated by switching the gas source from clean hydrogen to a hydrogen/carbon monoxide mixture bottle (either 1.5 % or 3.0 % of CO), with unchanged anode flow rate. The poisoning was performed in galvanostatic mode, at 0.20 $A \cdot cm^{-2}$. The poisoning of the fuel cell was assessed based on the transient behavior of the fuel cell voltage and current density distribution. Moreover, global I-V and power density curves were obtained and electrochemical impedance spectroscopy was performed to evaluate the CO poisoning effect. Each polarization curve was obtained starting at OCV and decreasing the potential until 0.350 V, with steps of 0.05 V. Electrochemical impedance spectroscopy was obtained in the frequency range from 100 kHz to

100 mHz with a perturbation amplitude of 5 mV using a Zahner IM6e electrochemical workstation coupled with a potentiostat PP-241.

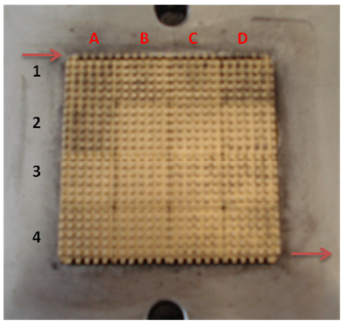


(a)

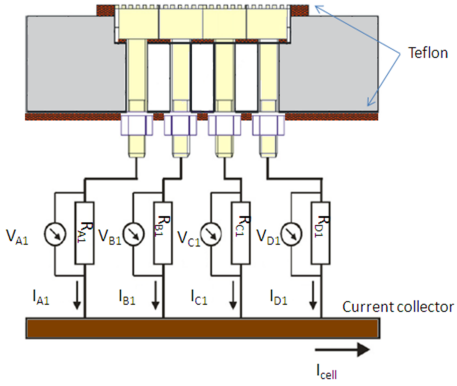


(b)

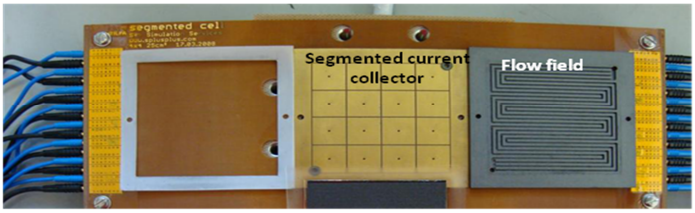


(c)

**Figure 3.1** DLR anode flow field and the respective orientation: the flow field gas inlet at segment *A1* and exhaust at segment *D4* (a); scheme of the first row of the flow field and the measuring system (b); S++ cell anode (c).

## 3.4 Results and Discussion

### 3.4.1 Electrochemical reaction mechanism of hydrogen and CO

Reaction equations (3.1) and (3.2) show the dissociative chemisorption and electrochemical oxidation of hydrogen [1] at the platinum sites. The first requires two free adjacent platinum sites and the later originates two free platinum sites besides two hydrogen ions and two electrons. In case of use of pure hydrogen at the anode electrode, these reactions are very fast.

When a contaminated feed is used, CO adsorbs strongly on bare platinum sites (equation (3.3)) and platinum hydride (equation (3.4)) at low electrode potentials, blocking the Pt active sites used for the hydrogen electrochemical oxidation.

$$H_2 + 2Pt \rightarrow 2Pt - H_{ads} \quad (3.1)$$

$$2Pt - H_{ads} \rightarrow 2Pt + H^+ + 2e^- \quad (3.2)$$

$$CO + Pt \rightarrow Pt - CO_{ads} \quad (3.3)$$

$$2CO + 2Pt - H_{ads} \rightarrow 2Pt - CO_{ads} + H_2 \quad (3.4)$$

The adsorbed CO is inert at potential regions where the fuel cell anode usually operates. The desorption of CO takes place after oxidation to $CO_2$ at high electrode potentials, where oxygen containing species are formed at the platinum surface [9] and can be described by equations (3.5) and (3.6):

$$Pt + H_2O \rightarrow Pt - OH_{ads} + e^- + H^+ \quad (3.5)$$

$$Pt - OH_{ads} + Pt - CO_{ads} \rightarrow 2Pt + CO_2 + e^- + H^+ \quad (3.6)$$

The water needed for the first reaction (equation (3.5)) comes either from the humidification of the feeding gases or from the water produced at the cathode side.

### 3.4.2 DLR cell

The CO effect was studied switching the anode feed from pure hydrogen to the gas mixture of hydrogen/CO (1.5 % and 3.0 % of CO). Figure 3.2 shows the transient behavior of the fuel cell when pure hydrogen was replaced by 3.0 % CO balanced hydrogen, at 0.20 A·cm$^{-2}$ and 160 °C and 180 °C. The voltage decrease for 160 °C was twice as much as for 180 °C. The voltage decrease occurred mainly during the first 5 min after switching the anode fuel.

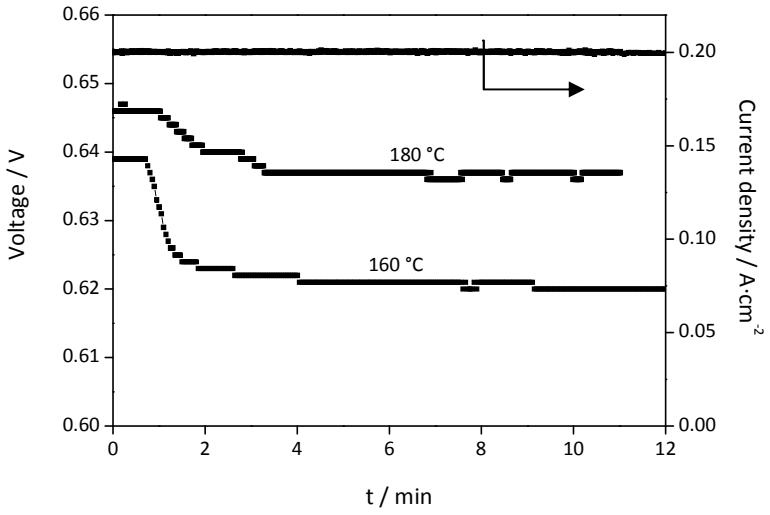


**Figure 3.2** Voltage and current density histories after switching from pure hydrogen to 3.0 % CO balanced hydrogen, at 0.20 A·cm$^{-2}$ and 160 °C and 180 °C.

The I-V and power density curves were obtained to examine the impact of the anode poisoning on the fuel cell (Figure 3.3). The power density peak decreased 30 % and 39 % at 160 °C and 18 % and 25 % at 180 °C, respectively, when feeding hydrogen containing 1.5 % and 3.0 % of CO, and the global current density at 0.520 V decreased 21 % and 29 % at 160 °C and decreased 15 % and 22 % at 180 °C.

Das *et al.* [11] observed a current density decrease of ca. 20 %, at 0.5 V and 160 °C, after adding 2 % of CO to the feeding hydrogen, and Li *et al.* [9] observed a decrease of 24 % when they added 3 % of CO to the feeding hydrogen, at 0.50 V and 150 °C.

The current density decrease reported by these authors is slightly lower than the obtained in this work.

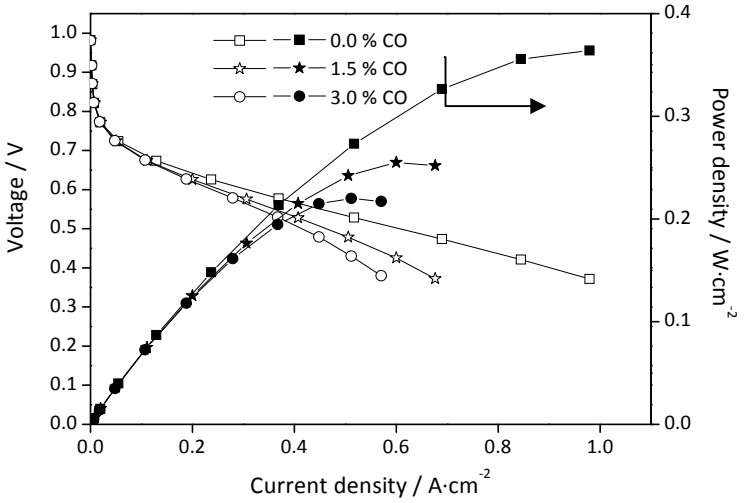


(a)

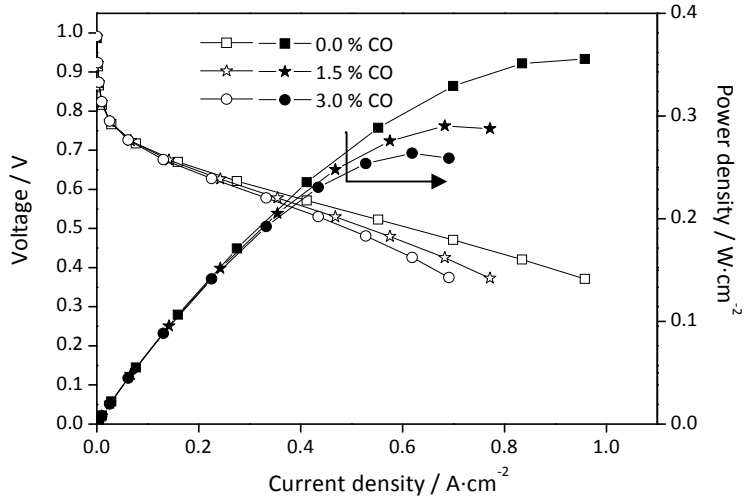


(b)

**Figure 3.3** I-V and power density curves at 160 °C (a) and 180 °C (b), for non-contaminated fuel (□) and for hydrogen feed containing 1.5 % of CO (✯) and 3.0 % of CO (○).

The metal bipolar plates used in the segmented cell are susceptive to corrosion when exposed to acidic environment and high temperatures [26-27]. To avoid corrosion, the metal flow field plates of the segmented fuel cell were coated with gold. However, after 2 weeks of continuous operation at 160 °C, XRD analysis showed the presence of gold, iron, chromium, and nickel in the MEA gas diffusion layer (results not shown); some metals leached into the MEA due to the corrosion of the metallic bipolar plates despite the use of a gold coating to protect. The results were obtained within one week of operation; however, the effect of ion contaminants in the MEA performance is not known. The effect of ion contamination on low temperature PEM performance has been recently reviewed [26; 28]

The CO anode poisoning can be further characterized by electrochemical impedance spectroscopy [10; 29-30]. The impedance spectroscopy analysis was performed galvanostatically, between 0.10 $A \cdot cm^{-2}$ and 0.60 $A \cdot cm^{-2}$, at 160 °C and 180 °C. The impedance spectra at 0.20 $A \cdot cm^{-2}$ and 0.50 $A \cdot cm^{-2}$ are depicted in Figure 3.4 and Figure 3.5.

The impedance spectra of the cell operated with pure hydrogen are dominated by the cathode charge transfer resistance, especially at lower current densities. After poisoning, a change is observed, which can be mostly attributed to the anode side. A typical spectrum for poisoned fuel cell may include an inductive behavior at low frequencies [30-31], not observed in Figure 3.4 and Figure 3.5. Hajbolouri *et al.* [10] concluded that the inductive loop appears due to the CO oxidation when the catalyst surface has reached a certain level of CO coverage and the anode overpotential is high enough.

A typical fuel cell electrical equivalent circuit is divided in cathode and anode analogs and ohmic losses, connected in series. Each electrode is represented by a resistance in parallel with a capacitance (RC) linked with a pore resistance [32-33]. Since the electrodes have a porous structure, the ideal capacitance is replaced by a constant phase element (CPE) in the simulation. An extra RC was included to represent the gas transport in the gas diffusion layers (associated with the low frequency part of the spectrum) originating the electric equivalent circuit of Figure 3.6.

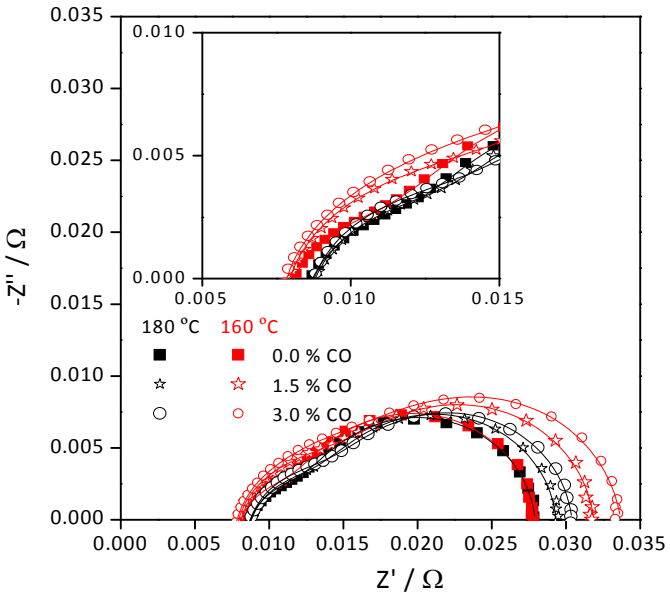


(a)

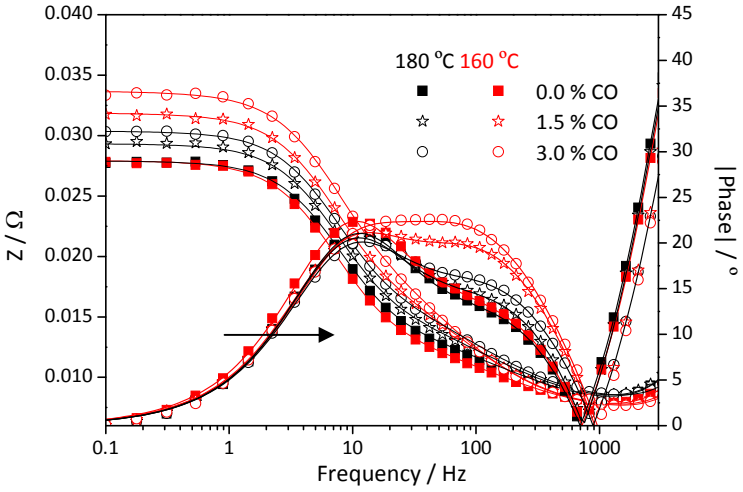


(b)

**Figure 3.4** Nyquist (a) and Bode (b) plots at 0.20 A·cm$^{-2}$, 160 °C (red points) and 180 °C (black points), with non-contaminated fuel (■) and hydrogen feed containing 1.5 % of CO (✯) and 3.0 % of CO (○). Lines represent the fitting electrical equivalent model.

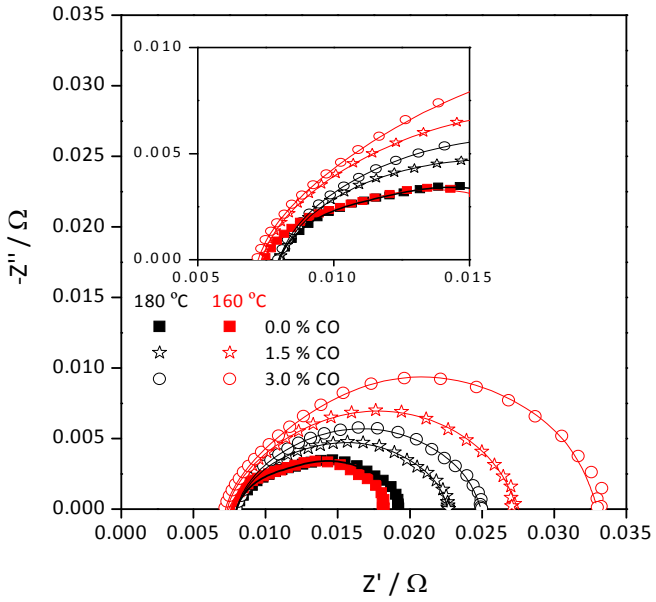


(a)

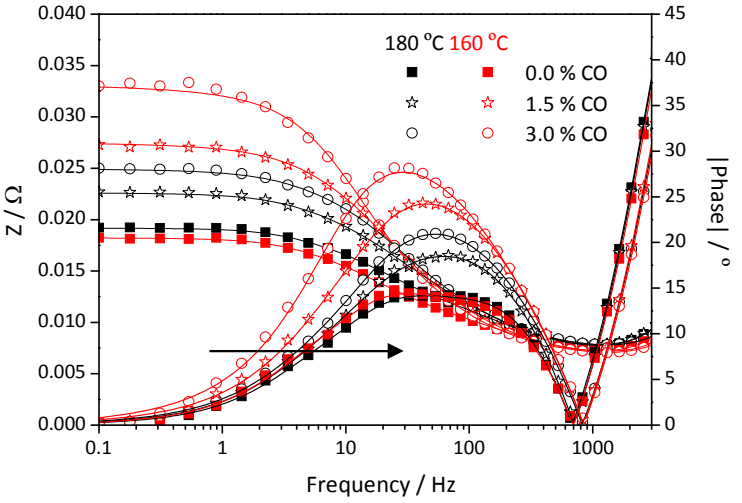


(b)

**Figure 3.5** Nyquist (a) and Bode (b) plots at 0.50 A·cm$^{-2}$, 160 °C (red points) and 180 °C (black points), with non-contaminated fuel (■) and hydrogen feed containing 1.5 % of CO (☆) and 3.0 % of CO (○). Lines represent the fitting electrical equivalent model.

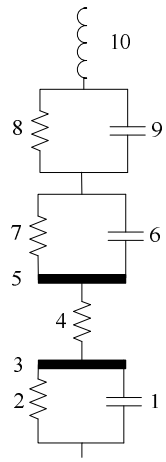


**Figure 3.6** Fuel cell electrical equivalent circuit. Elements 2 and 7 represent anode ($R_{ct}^{a}$) and cathode ($R_{ct}^{c}$) charge transfer resistance; elements 1 and 6 represent anode ($C_{dl}^{a}$) and cathode ($C_{dl}^{c}$) double layer capacitance; elements 3 and 5 represent the charge resistance of electrodes pores filled with electrolyte; elements 8 and 9 represent the resistance ($R_N$) and capacitance ($C_N$) associated with gas phase mass transfer; element 4 is the ohmic resistance and element 10 is the parasitic inductance.

Resistances 2 and 7 represent the charge transfer resistance of anode ($R_{ct}^{a}$) and cathode ($R_{ct}^{c}$) whereas capacitances 1 and 6 represent the double layer capacitance of anode ($C_{dl}^{a}$) and cathode ($C_{dl}^{c}$). Elements 3 and 5 represent the charge resistance of electrodes pores filled with electrolyte. Elements 8 and 9 represent the resistance ($R_N$) and capacitance ($C_N$) associated with gas phase mass transfer. The ohmic resistance represented by element 4 includes membrane resistances, end plates, flow fields and contact interfaces and element 10 accounts for the parasitic inductance. The SIM module from Thales software was used (Zahner-Elektrik GmbH) to fit this electrical equivalent model to the experimental data (full lines in Figure 3.4 and Figure 3.5). The fitting parameters can be seen in Figure 3.7-Figure 3.9.

For a given temperature and increasing the current density, the anode charge transfer resistance decreases when pure hydrogen is used. When CO is added to the hydrogen feed, the charge transfer resistance of the anode increases with CO

concentration. Moreover, for both CO concentrations the charge transfer resistance increases as a function of the current density especially for current densities above 0.20 A·cm$^{-2}$ – see Figure 3.7 (a) and (b). The rate of the charge transfer is controlled by the amount of hydrogen chemisorbed on the platinum sites. As a result, the charge transfer resistance increases with the fraction of occupied sites by carbon monoxide, and therefore with the CO concentration. The fraction of free catalytic sites depends on carbon monoxide concentration and temperature [9]. At low current densities there are enough active sites to support the hydrogen electro oxidation but as the current density increases the hydrogen oxidation is controlled by the platinum active sites and consequently the anode overpotential increases. The double layer capacitance of anode, however, is hardly dependent of the carbon monoxide concentration or global current density of the fuel cell.

At 180 °C the values for the charge transfer resistance of the contaminated anode are lower when compared to the correspondent ones at 160 °C. The ratio between the anode charge transfer resistance obtained with pure hydrogen and hydrogen containing CO, at 0.2 A·cm$^{-2}$ and 0.5 A·cm$^{-2}$ is shown in Table 3.1 for both 160 °C and 180 °C.

**Table 3.1** Ratio between the anode charge transfer resistance obtained with pure hydrogen and hydrogen containing CO, at 0.2 A·cm$^{-2}$ and 0.5 A·cm$^{-2}$, for 160°C and 180°C.

| | Global current density / A·cm$^{-2}$ | 0.2 | | 0.5 | |
|---|---|---|---|---|---|
| | CO / % vol. | 1.5 | 3.0 | 1.5 | 3.0 |
| Temperature / °C | 160 | 1.7 | 2.1 | 2.8 | 3.3 |
| | 180 | 1.2 | 1.4 | 1.7 | 2.1 |

At 180 °C, there are no significant changes on the values of the elements representing the cathode electrode after contamination of the anode - Figure 3.8 (b). The charge transfer resistance decreases significantly as a function of the current density and is independent of the fuel. At 160 °C, however, a significant increase of cathode charge transfer resistance and double layer capacitance is observed for the 3.0 % CO balanced hydrogen feed stream for current densities higher than

0.30 A·cm$^{-2}$ - Figure 3.8 (a). If one considers that the introduction of carbon monoxide originates a non-homogeneous contamination of the anode, which is more significant for higher CO concentrations and lower temperatures, this can also affect the cathode since this originates significant inhomogeneous local current densities.

The major contribution to the mass transfer is usually attributed to the cathode side since hydrogen diffuses easily than oxygen through the gas diffusion layer. For both temperatures, the parameters characterizing the RC element representing the mass transfer resistance suffered no significant changes - Figure 3.9 (a) and (b). The mass transfer resistance can be identified by the higher value of the formal capacitance in the RC element which, however, does not represent a capacitance in a traditional way as for anode and cathode.

Both I-V curves and AC impedance spectra showed that the presence of CO causes a performance loss, which is aggravated for higher CO concentrations and current densities and decreases for higher temperatures. The CO adsorption equilibrium on the platinum sites is strongly dependent on the temperature. For both temperatures and current densities below 0.3 A·cm$^{-2}$, the impact of 1.5 % or 3 % of CO is very low. Increasing the current density, the CO effect is more pronounced. However, switching the anode feed to pure hydrogen results in the restoration of the original performance which indicates the reversible behavior of CO poisoning.

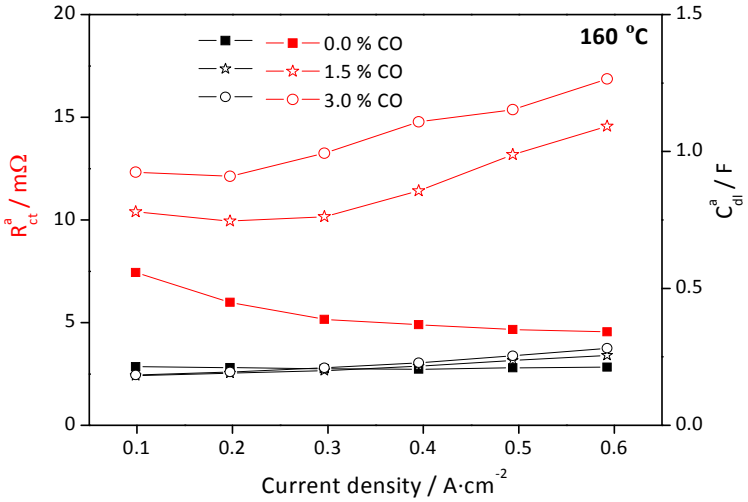


(a)

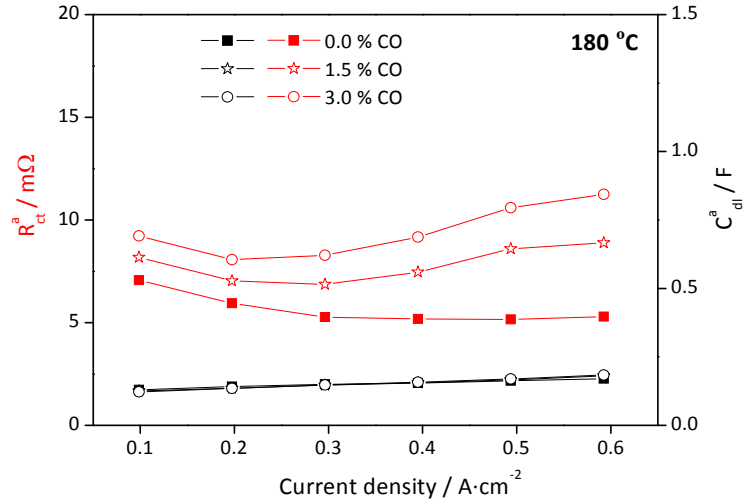


(b)

**Figure 3.7** Anode charge transfer resistance ($R^a_{ct}$, red) and double layer capacitance ($C^a_{dl}$, black), at 160 °C (a) and 180 °C (b), as a function of current density and CO concentration: non-contaminated fuel (■), 1.5 % of CO (☆) and 3.0 % of CO (○).

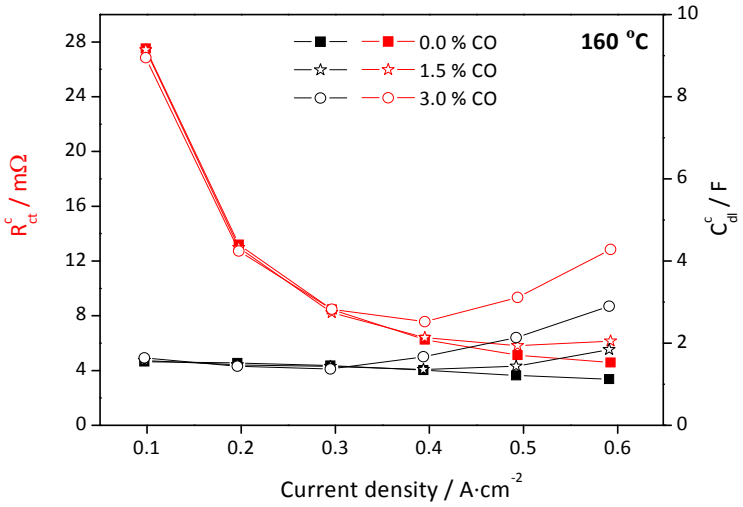


(a)

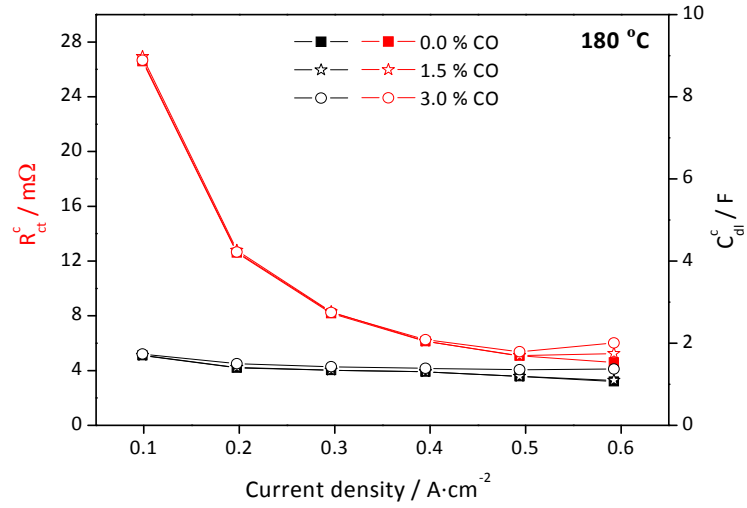


(b)

**Figure 3.8** Cathode charge transfer resistances ($R_{ct}^{c}$, red) and double layer capacitance ($C_{dl}^{c}$, black), at 160 °C (a) and 180 °C (b), as a function of current density and CO concentration: non-contaminated fuel (■), 1.5 % of CO (✯) and 3.0 % of CO (○).

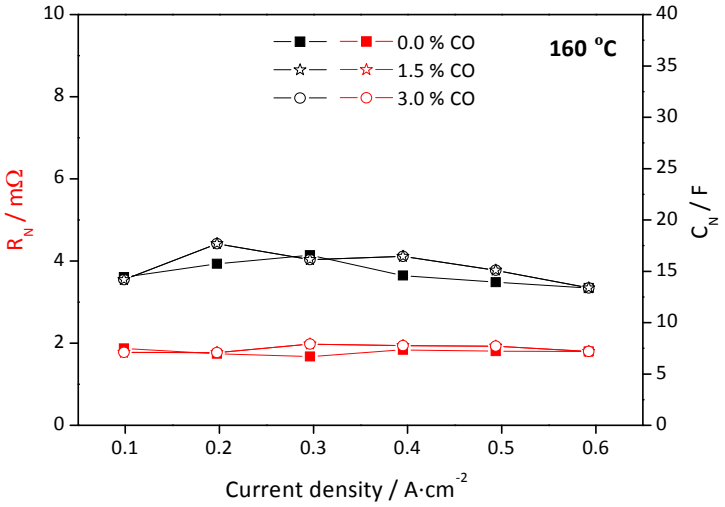


**(a)**

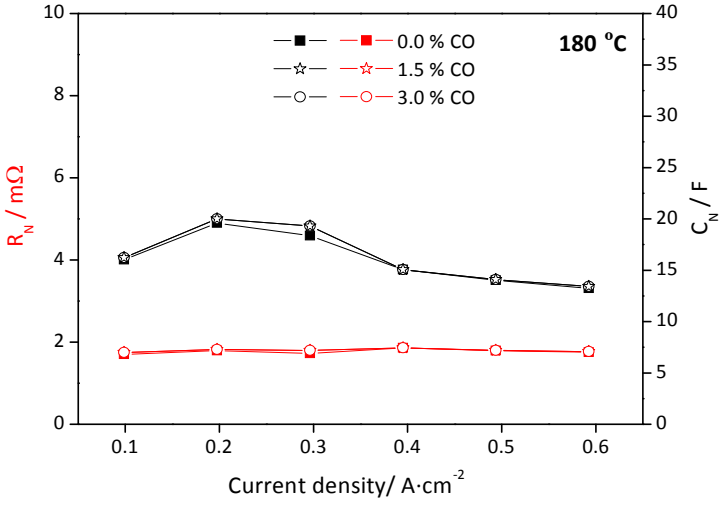


(b)

**Figure 3.9** Resistance ( $R_N$ ) and capacitance ( $C_N$ ) associated with gas phase mass transfer at 160 °C (a) and 180 °C (b), as a function of current density and CO concentration: non-contaminated fuel (■), 1.5 % of CO (☆) and 3.0 % of CO (○).

### 3.4.3 DLR cell current density distribution

The transient behavior of the fuel cell segments at 0.20 A·cm$^{-2}$, when the feed was switched to 3.0 % CO balanced hydrogen, is shown in Figure 3.10 and Figure 3.11, for 160 °C and 180 °C. The current distribution at $t$ = 0 (without poisoning) and $t$ = 12 min and $t$ = 11 min (for 160 °C and 180 °C, respectively) is depicted in Figure 3.12 (a) and (b).

For a global current density of 0.20 A·cm$^{-2}$ and pure hydrogen feed, the current density varied between 0.181 A·cm$^{-2}$ (at segment *C3*) and 0.225 A·cm$^{-2}$ (*D4*) at 160 °C and between 0.177 A·cm$^{-2}$ (*C3*) and 0.220 A·cm$^{-2}$ (*D4*) at 180 °C. Upon introduction of carbon monoxide there is a decrease of the current density of the segments close to the inlet *(A1, A2, B1* and *C1*). On the other hand, there is an increase of current density at segments close to the exit of the flow field (*C3, C4*, *D2, D3* and *D4*), for both temperatures. The behavior was similar when hydrogen containing 1.5 % of CO was introduced at the anode (not shown).

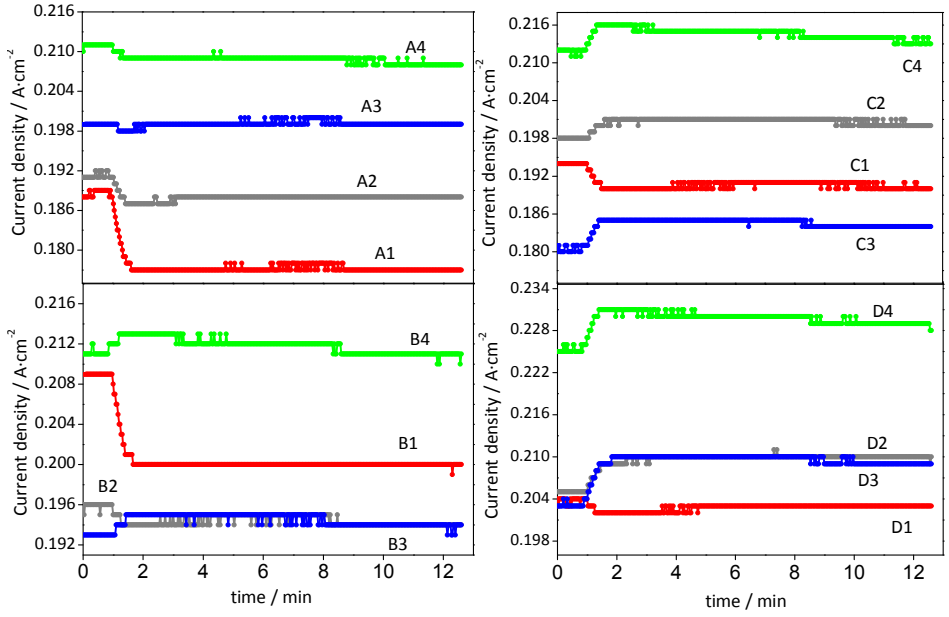


**Figure 3.10** Transient behavior of the fuel cell segments when pure hydrogen was switched to 3.0 % CO balanced hydrogen, for 0.20 A·cm$^{-2}$ and 160 °C**.**

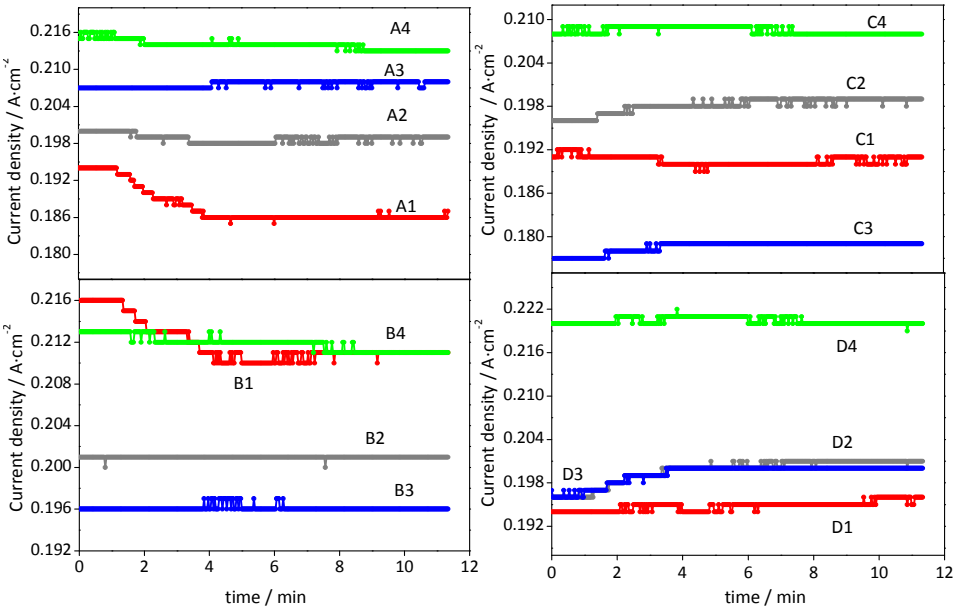


**Figure 3.11** Transient behavior of the fuel cell segments when pure hydrogen was switched to 3.0 % CO balanced hydrogen, for 0.20 A·cm$^{-2}$ and 180 °C.

The change in the current density of the segments is fast and remains stable after this initial effect. During galvanostatic poisoning the fuel cell voltage fluctuates, decreasing as CO is adsorbed at the catalyst surface (Figure 3.2), and therefore increasing the charge transfer resistance of the anode (Figure 3.7 (a) and (b)) and the anodic overpotential ( $\eta_{act}^{a}$ ) according to equation 3.7:

$$\eta_{act}^{a} = E_{therm} - V_{cell} - \eta_{ohm} - \eta_{act}^{c} \qquad (3.7)$$

$E_{therm}$ is the thermodynamically predicted voltage, $V_{cell}$ is the fuel cell voltage, $\eta_{ohm}$ is the ohmic loss of the fuel cell and $\eta_{act}^{c}$ is the cathode overpotential. As the carbon monoxide coverage increases at the inlet, the increase of the anodic overpotential can cause a small rate of CO oxidation (reaction equations (3.5) and (3.6)) [22], oxidizing the CO that is being continuously sent to the anode active layer, consequently maintaining the steady-state.

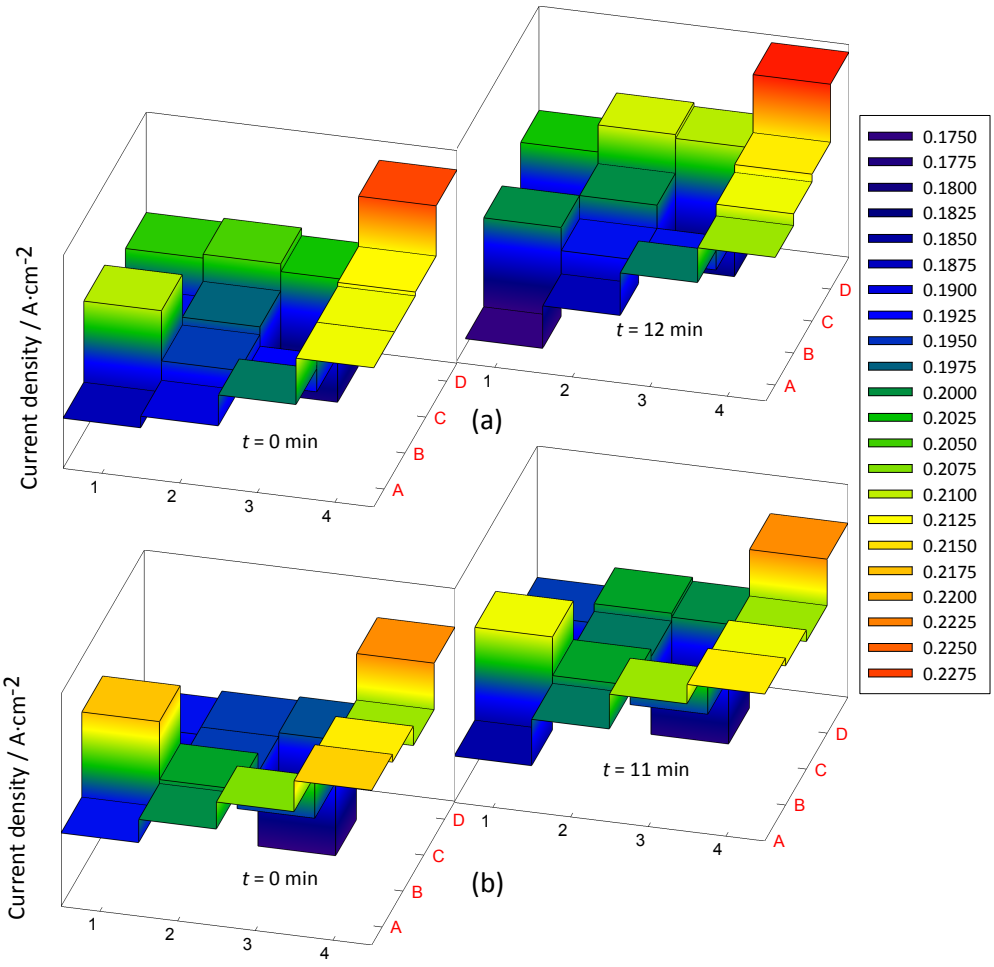


**Figure 3.12** Current density distribution at *t* = 0 min (without poisoning) and for *t* = 12 min (3.0 % CO balanced hydrogen), at 160 °C (a) and current density distribution at *t* = 0 min (without poisoning) and for *t* = 11 min (3.0 % CO balanced hydrogen), at 180 °C (b).

As discussed in the previous section, at global current density of 0.20 A·cm$^{-2}$ the CO poisoning effect is small. The current density distribution is therefore evaluated at higher global current densities - 0.51 A·cm$^{-2}$ at 160 °C and 0.69 A·cm$^{-2}$ at 180 °C (Figure 3.13).

For pure hydrogen, at 160 °C the current density varied between 0.472 A·cm$^{-2}$ (*A1* and *C3*) and 0.562 A·cm$^{-2}$ (*D4*) whereas at 180 °C the current density varied between 0.598 A·cm$^{-2}$ (*A1*) and 0.772 A·cm$^{-2}$ (*A4* and *B4*) - Figure 3.13 (a) and (b). The current

density is higher in row *4* of the flow field and the overall current distribution is fairly even in both cases.

At 160 °C operation temperature, the fuel cell voltage decreased from 0.529 V to 0.479 V for 1.5 % of CO and from 0.529 V to 0.430 V for 3.0 % of CO. Moreover, the relative difference between the current density of the best and worst performing segments increased significantly - 1.4 times for 1.5 % of CO and 3 times for 3.0 % of CO - Figure 3.13 (a).

For 180 °C, the voltage decreased from 0.470 V to 0.427 V for 1.5 % of CO and 0.375 V for 3.0 % of CO. An increase of 1.3 times and 2.1 times was observed between the relative difference of the current density of the best and worst performing segments, for 1.5 % and 3.0 % of CO respectively, Figure 3.13 (b).

The most poisoned segment was *A1*, where the current density for 3 % CO and 180 °C decreased 11 % (global current density 0.69 $A \cdot cm^{-2}$), while for 160 °C it decreased twice as much for a smaller global current density (0.51 $A \cdot cm^{-2}$).

There is a general poisoning trend when the fuel cell is operated in galvanostatic mode (Figure 3.14): at the region closest to the inlet there is a decrease of the current density of the segments and in the region close to the exit of the flow field there is an increase of the segment´s current density. The inhomogeneous behavior is more notorious for higher CO concentrations and current densities. A similar behavior was observed when 10 ppm and 80 ppm of CO were fed to a low temperature PEMFC (operating at 60 °C) using Pt/C catalyst and for a global current density of 0.5 $A \cdot cm^{-2}$ [22].

For a given fuel cell voltage, different global fuel cell current densities were obtained for the hydrogen feed streams containing different concentrations of CO. For instance, at 160 °C and 0.570 V, a global current density of 0.37 $A \cdot cm^{-2}$ for pure hydrogen was recorded, while was observed a current density of 0.31 $A \cdot cm^{-2}$ and 0.28 $A \cdot cm^{-2}$ for hydrogen feed containing 1.5 % and 3.0 %of CO, respectively. At same voltage and 180 °C, a global current density of 0.41 $A \cdot cm^{-2}$ was determined for pure hydrogen, while a current density of 0.35 $A \cdot cm^{-2}$ and 0.33 $A \cdot cm^{-2}$ was recorded for hydrogen feed containing 1.5 % and 3.0 %of CO, respectively. For both temperatures, the current density distribution is fairly even for the three anode fuels, see Figure

3.15 (a) and (b). The difference between the maximum/minimum values of current density distribution decreases slightly with increasing CO concentration.

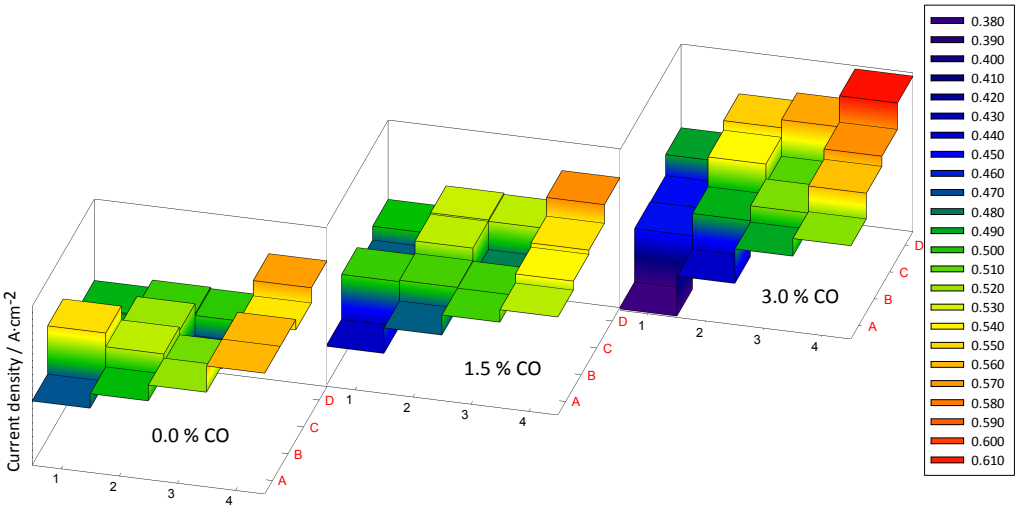


(a)

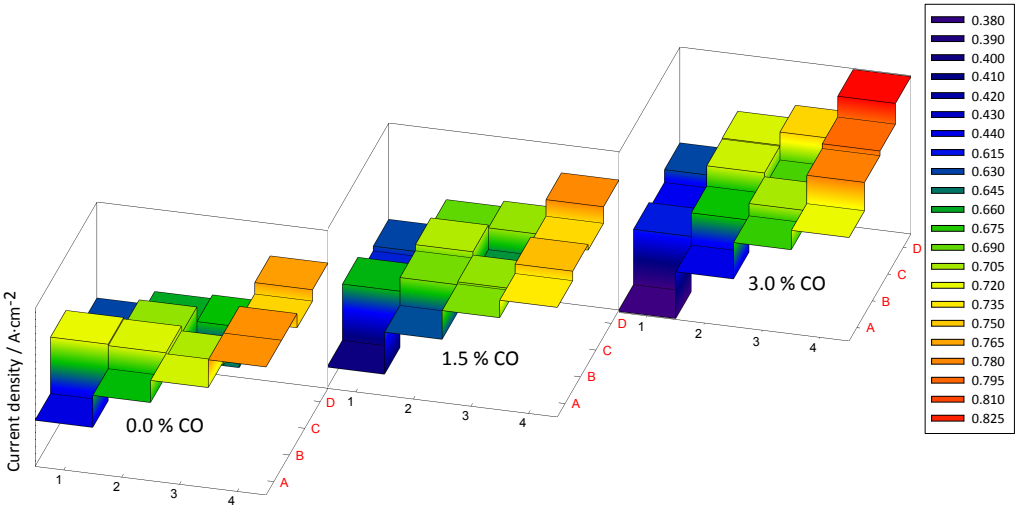


(b)

**Figure 3.13** Current density distribution at fuel cell load of 0.51 A·cm$^{-2}$ and 160 °C (a) and for 0.69 A·cm$^{-2}$ and 180 °C (b), for pure hydrogen fuel and hydrogen feed containing 1.5 % of CO and 3.0 % of CO.

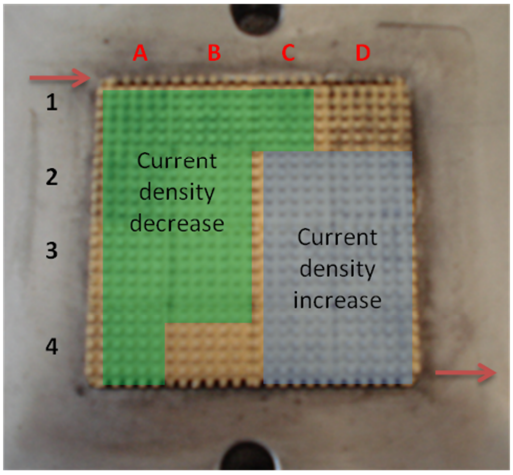


**Figure 3.14** Anode segments where current density changed after the introduction of carbon monoxide.

For a higher fuel cell potential, 0.720 V, similar global current densities were obtained (between 0.05 $A \cdot cm^{-2}$ and 0.06 $A \cdot cm^{-2}$ at 160 °C and between 0.06 $A \cdot cm^{-2}$ and 0.08 $A \cdot cm^{-2}$ at 180 °C) and the current density distribution, using the different fuels, are even - Figure 3.16 (a) and (b).

When the poisoning effect is evaluated in potentiostatic mode, it should be emphasized that there are no significant changes in the anodic polarization of the fuel cell, and the adsorbed carbon monoxide is not oxidized, originating an even distribution of CO poisoning. Bender *et al.* [17] observed a spatial dependence of the CO poisoning at 0.6 V and 80 °C: the current density of the segments close to the inlet of the fuel cell started decreasing, followed by the next segments, until all segments reaching a similar current density.

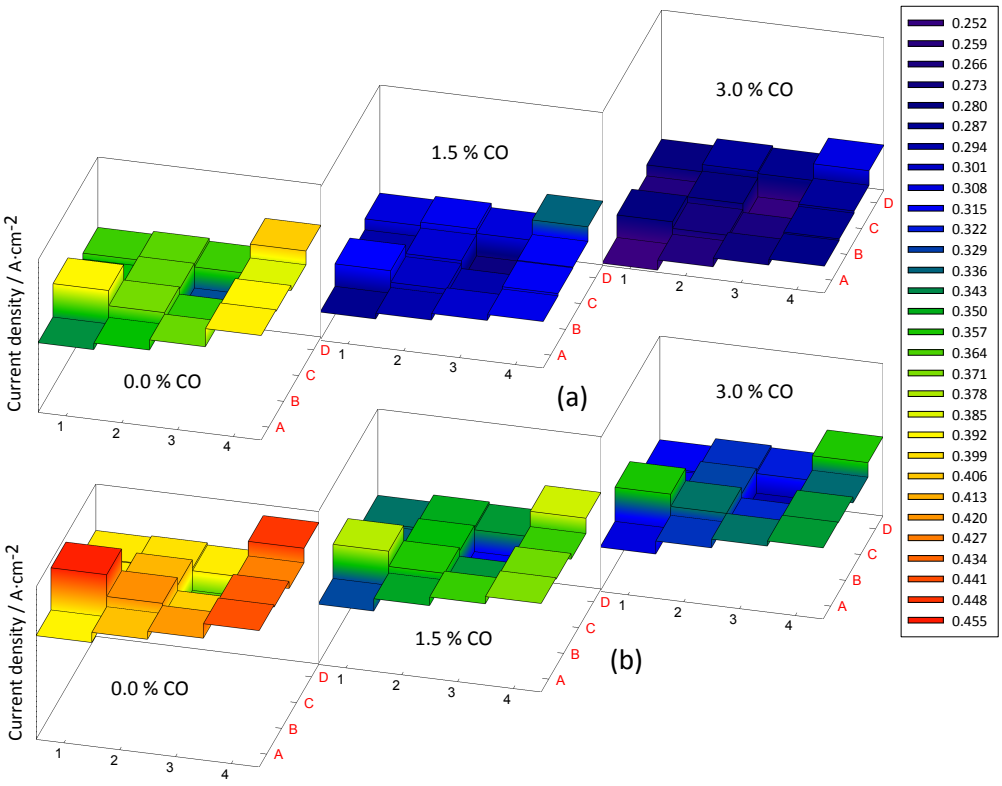


**Figure 3.15** Current density distribution at 0.570 V for 160 °C (a) and 180 °C (b) for pure hydrogen fuel and hydrogen feed containing 1.5 % of CO and 3.0 % of CO.

### 3.4.4 S++ cell performance

A second segmented cell was used to evaluate the poisoning effect of carbon monoxide on the current density distribution. In this cell, a printed circuit board was used as segmented current collector.

The transient behavior of the fuel cell when pure hydrogen was switched to 3.0 % CO balanced hydrogen feed, at global current density of 0.20 A·cm$^{-2}$, can be seen in Figure 3.17; the voltage decreased 33 mV during ca. 10 min.

A comparison of the I-V curves for the three different fuels is depicted on Figure 3.18. When pure hydrogen was used, higher potentials were obtained with this cell compared to the DLR cell up to a current density of 0.70 A·cm$^{-2}$; the trend is inverted at higher values of current density.

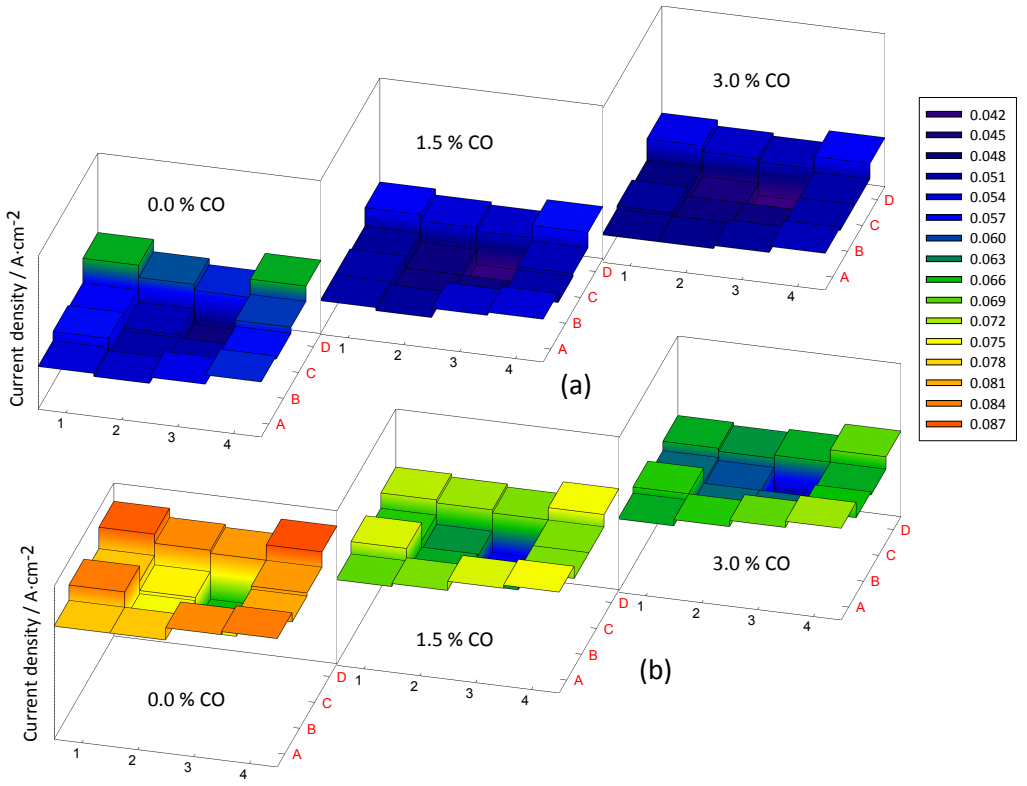


**Figure 3.16** Current density distribution at 0.720 V for 160 °C (a) and 180 °C (b) for pure hydrogen fuel and hydrogen feed containing 1.5 % of CO and 3.0 % of CO.

When the anode feed was hydrogen containing 1.5 % and 3.0 % of CO, the power density peak decreased 30 % and 39 %, respectively (Figure 3.18); similar behavior was observed for the DLR cell. On the other hand, at 0.520 V the current density decreased 29 % and 38 %, respectively. These values are higher than the ones obtained with the DLR cell.

To better understand the carbon monoxide poisoning process and the differences between both cells, galvanostatic impedance experiments were performed, between 0.10 A·cm$^{-2}$ and 0.60 A·cm$^{-2}$. The impedance measurements at 0.20 A·cm$^{-2}$ and 0.50 A·cm$^{-2}$ current densities are plotted in Figure 3.19.

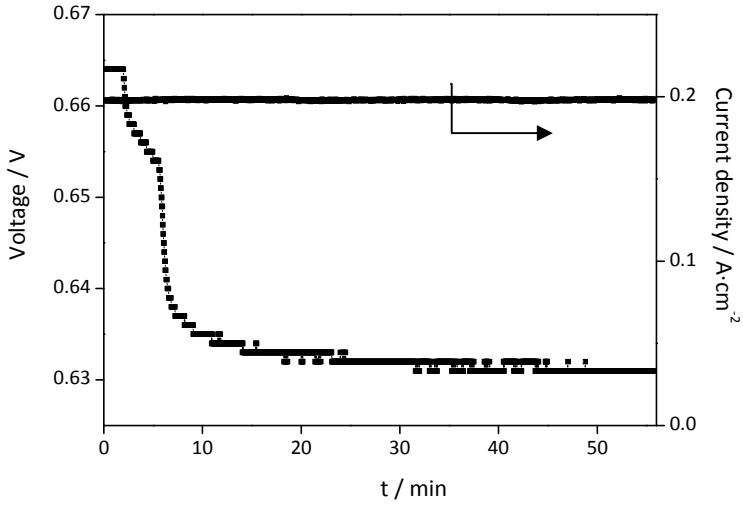


**Figure 3.17** Voltage and current density histories after switching from pure hydrogen to 3.0 % CO balanced hydrogen, at 0.20 A·cm$^{-2}$ and 160 °C, using the S++ cell.

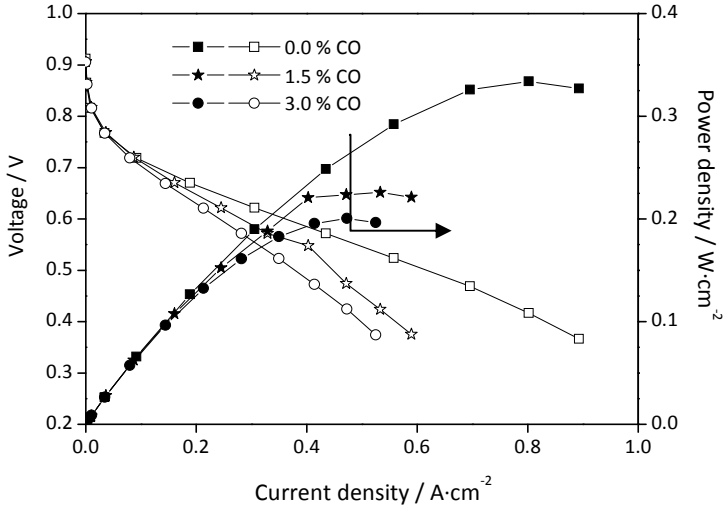


**Figure 3.18 I**-V and power density curves at 160 °C, for non-contaminated fuel (□) and for hydrogen feed containing 1.5 % of CO (✯) and 3.0 % of CO (○), using the S++ cell.

The SIM module from Thales software was used to fit the electrical equivalent model illustrated on Figure 3.6 to the experimental data (lines in Figure 3.19). The fitting

parameters for current densities between 0.10 A·cm$^{-2}$ and 0.60 A·cm$^{-2}$ can be seen in Figure 3.20.

When pure hydrogen was used, the anode charge transfer resistance is lower for the S++ cell, when compared to the segmented metal flow field cell. A notorious increase of anode charge transfer resistance is observed when clean hydrogen was replaced by hydrogen feed containing CO, increasing as CO concentration increases – Figure 3.20 (a). Moreover, for the feed streams containing CO (1.5 % and 3.0 %) the charge transfer resistance increases as current density increases. At 0.20 A·cm$^{-2}$, the anode charge transfer resistance increased 3.7 and 6.1 times, for 1.5 % and 3.0 % of CO hydrogen balanced feed streams, respectively, whereas at 0.50 A·cm$^{-2}$ it is observed an increase of 8.4 and 13.7 times. These ratios are higher than the ones obtained with the DLR cell (Table 3.1). The same anode flow rate was used in the experiments with both cells; it should, however, be stressed that the anode flow fields configuration is different for the cells (Figure 3.1).

As observed previously with DLR segmented cell for 3.0 % CO balanced hydrogen feed stream, the use of CO at the anode fuel increased the cathode charge transfer resistance and double layer capacitance at current densities higher than 0.3 A·cm$^{-2}$ (Figure 3.20 (b)).

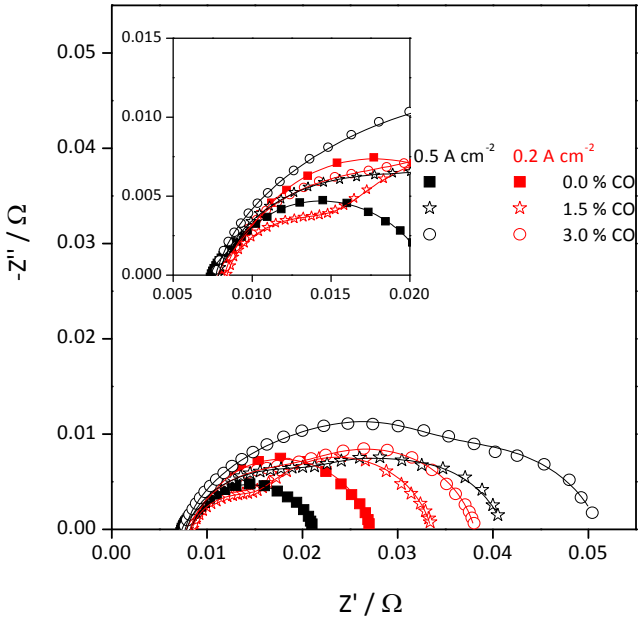


(a)

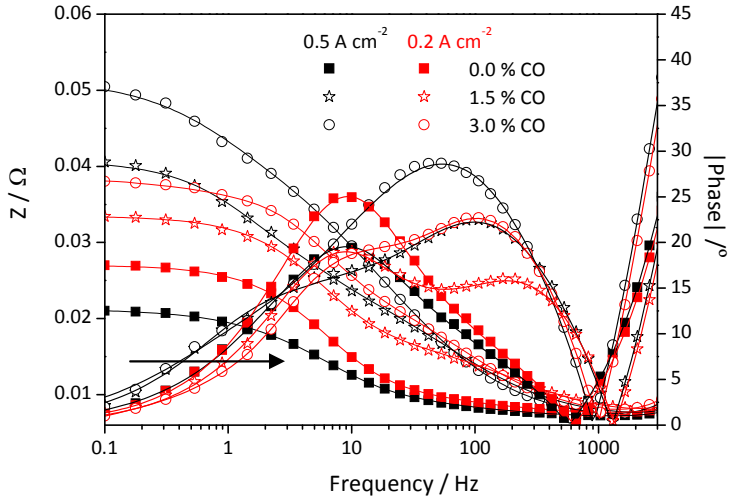


(b)

**Figure 3.19** Nyquist (a) and Bode (b) plots for 0.20 A·cm$^{-2}$ (red points) and 0.50 A·cm$^{-2}$ (black points), at 160 °C, with non-contaminated fuel (■) and hydrogen feed containing 1.5 % of CO (✯) and 3.0 % of CO (○), using the S++ cell. Lines represent the fitting electrical equivalent model.

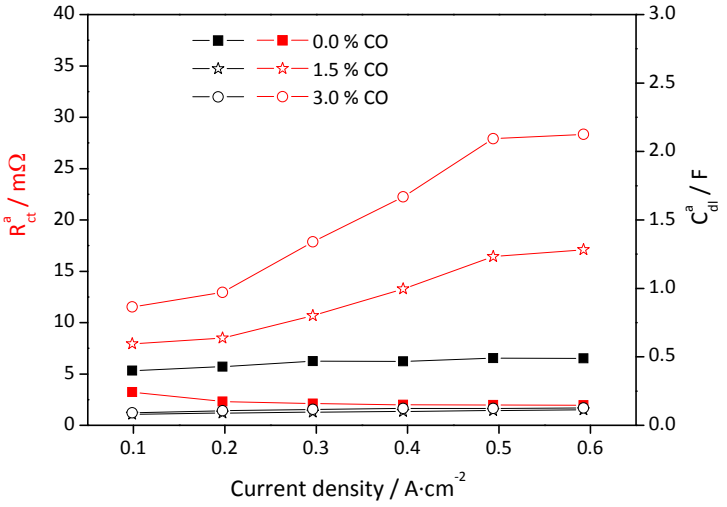


(a)

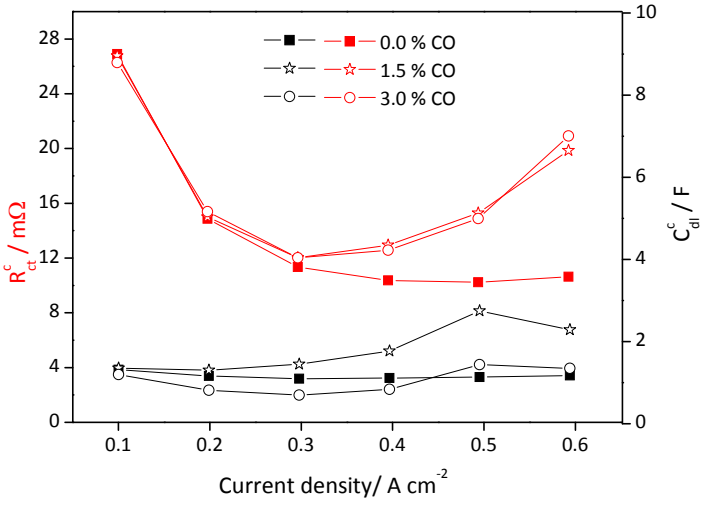


(b)

**Figure 3.20** Anode charge transfer resistance ($R^a_{ct}$, red) and double layer capacitance ($C^a_{dl}$, black) (a); cathode charge transfer resistances ($R^c_{ct}$, red) and double layer capacitance ($C^c_{dl}$, black) (b), at 160 °C, as a function of current density and CO concentration: pure hydrogen (■), 1.5 % of CO (☆) and 3.0 % of CO (○), using the S++ cell.

### 3.4.5 S++ cell current density distribution

The transient behavior of the fuel cell segments when pure hydrogen feed was switched to 3.0 % CO balanced hydrogen, at 160 °C and 0.20 A·cm$^{-2}$, is shown in Figure 3.21. The current density of the segments remains unchanged despite the decrease on the fuel cell voltage. The lowest current density value was observed at segment *D3* (0.159 A·cm$^{-2}$) and the highest current density value was observed at segment *A1* (0.267 A·cm$^{-2}$), Figure 3.22.

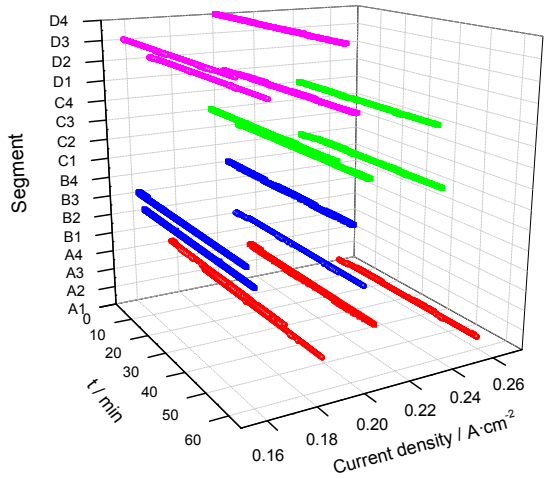


**Figure 3.21** Transient behavior of the fuel cell segments when pure hydrogen was switched to 3.0 % CO balanced hydrogen feed for 0.20 A·cm$^{-2}$ and 160 °C, using the S++ cell.

The current density distribution was also evaluated at overall current density of 0.52 A·cm$^{-2}$. When hydrogen is balanced with carbon monoxide, the fuel cell voltage decreased from 0.522 V to 0.424 V for 1.5 % of CO and to 0.373 V for 3.0 % of CO hydrogen balanced feed streams. Despite this decrease in the fuel cell voltage no significant change on the current density distribution was observed – Figure 3.23. A non-homogeneous behavior is suggested from EIS analysis, which was not translated into current density distributions; this should be related to the design of the segmented fuel cell that averages the electrical signals from adjacent segments.

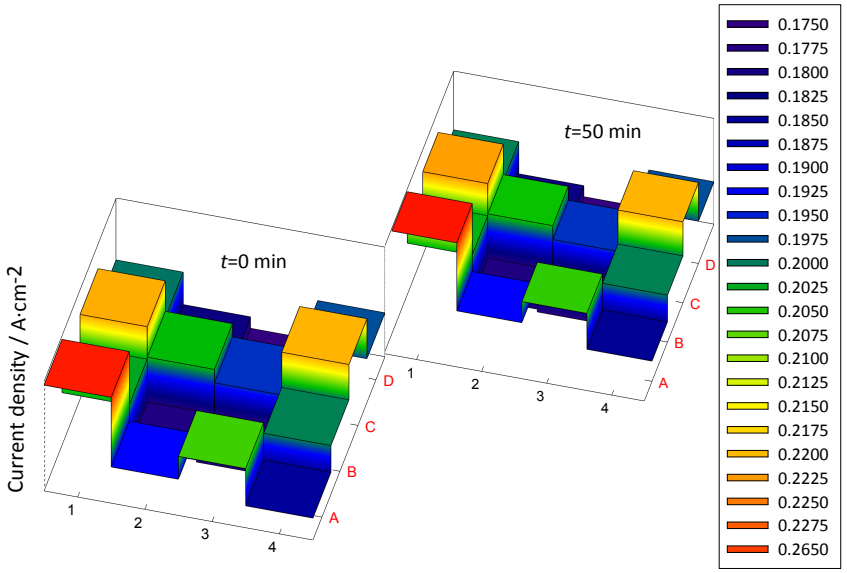


**Figure 3.22** Current density distribution at $t$ = 0 min (without poisoning) and for $t$ = 50 min (3.0 % CO balanced hydrogen), for 0.20 A·cm$^{-2}$ current density and 160 °C, using the S++ cell.

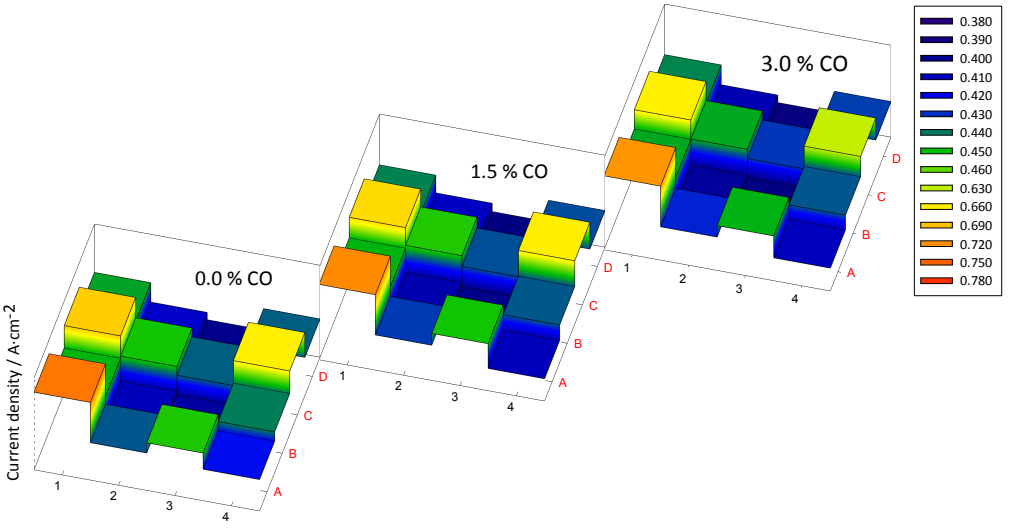


**Figure 3.23** Current density distribution at 160 °C, and global current density of 0.52 A·cm$^{-2}$, with pure hydrogen and hydrogen feed containing 1.5 % of CO and 3.0 % of CO, using the S++ cell.

Figure 3.24 (a) and (b) show the current density distribution for the three different fuels at 0.570 V and 0.720 V. At 0.570 V it was recorded a global current density of

0.44 A·cm$^{-2}$ for pure hydrogen, while it was recorded a current density of 0.33 A·cm$^{-2}$ and 0.28 A·cm$^{-2}$ for hydrogen feed containing 1.5 % and 3.0 % of CO.

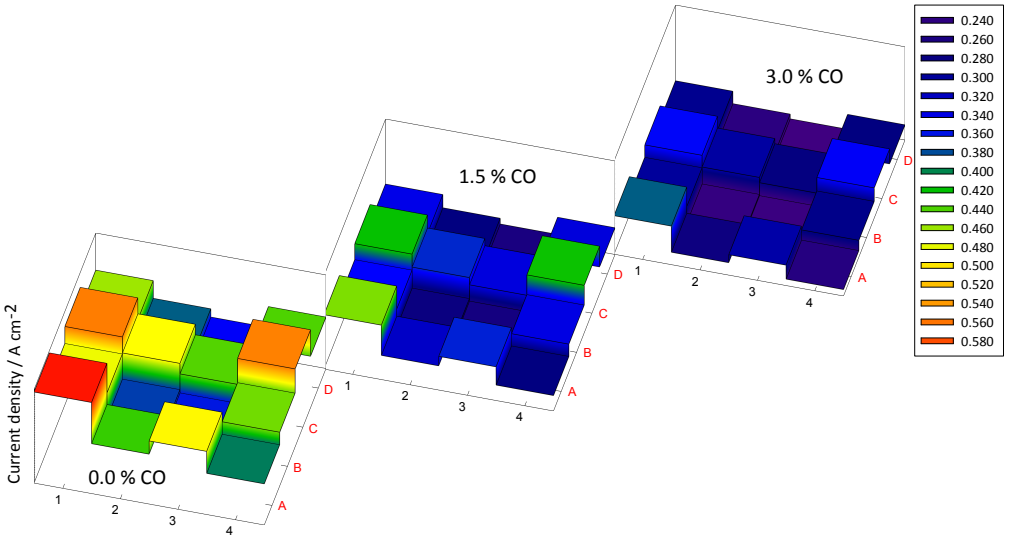


(a)

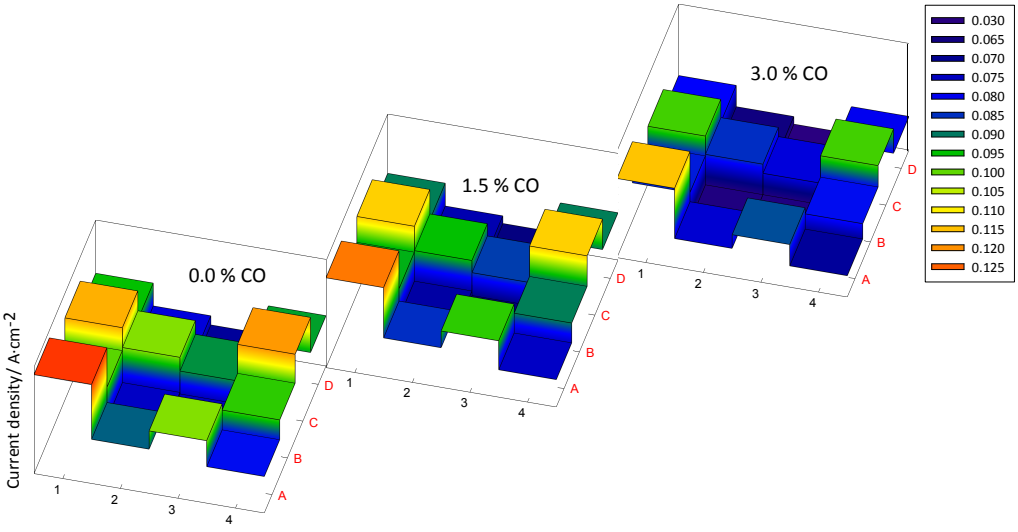


(b)

**Figure 3.24** Current density distribution at 160 °C, 0.570 V (a) and 0.720 V (b), with pure hydrogen fuel and hydrogen feed containing 1.5 % of CO and 3.0 % of CO, using the S++ cell.

An even distribution was obtained for the three fuels and the difference between the highest and lowest performing segments decreases as the CO concentration

increases – Figure 3.24 (a). At more than of ca. 0.720 V, the current densities differences for the three fuels and the difference between the highest and lowest performing segments does not significantly change as a function of the CO feed concentration – Figure 3.24 (b).

## 3.5 Conclusions

In this work the effect of carbon monoxide on the current density distribution of high temperature PEMFC is reported. The transient behavior of the fuel cell voltage and current density distribution was assessed when pure hydrogen was switched to hydrogen feed containing 1.5 % and 3.0 % of CO. Moreover the current density distribution was compared for the three different fuel compositions at similar voltage and global current density. The corresponding I-V and power density curves as well as impedance spectra were obtained for all fuel compositions.

The current distribution was obtained with two different cell anodes, 1) a metal segmented flow field and 2) a non-segmented graphite flow field where it was applied a printed circuit board as segmented current collector.

In both cells, the presence of CO caused a performance loss, which was worsened for higher CO concentrations and current densities and for lower temperatures. The original performance could, however, be easily restored by switching the anode fuel back to pure hydrogen. The voltage and current density histories after switching from pure hydrogen to 3.0 % CO balanced hydrogen, at 0.20 $A \cdot cm^{-2}$ and 160 °C or 180 °C, showed that the poisoning of the catalyst occurs very quickly, within few minutes.

The current density distributions obtained with metal segmented flow field showed that the introduction of CO resulted in a heterogeneous behavior across the MEA, which was aggravated by the increase of CO concentration and global current density.

When the current density distribution for the three anode fuel compositions is compared at a given voltage, in both cells, even current density distributions are obtained, but at different global current densities.

## 3.6 Acknowledgments

The work of M. Boaventura was supported by FCT (Grant SFRH/BD/28187/2006). The present work was also partially supported by FCT projects PTDC/EQU-EQU/70574/2006 and PTDC/EQU-EQU/104217/2008.

M. Boaventura acknowledges DLR (Institute of Technical Thermodynamics - German Aerospace Center) for the support and hospitality. Dr. José Sousa is acknowledged for the helpful suggestions. The authors thank Dr. Ruckdäschel for the EDX analysis of the GDL.

## 3.7 References

[1] Cheng, X., Shi, Z., Glass, N., Zhang, L., Zhang, J.J., Song, D.T., Liu, Z.S., Wang, H.J., Shen, J., 2007. A review of PEM hydrogen fuel cell contamination: Impacts, mechanisms, and mitigation. J Power Sources 165, 739-756.

[2] Divisek, J., Oetjen, H.F., Peinecke, V., Schmidt, V.M., Stimming, U., 1998. Components for PEM fuel cell systems using hydrogen and CO containing fuels. Electrochim Acta 43, 3811-3815.

[3] Jiang, R.C., Kunz, H.R., Fenton, J.M., 2006. Influence of temperature and relative humidity on performance and CO tolerance of PEM fuel cells with Nafion (R)-Teflon (R)-Zr(HPO4)(2). Electrochim Acta 51, 5596-5605.

[4] Baschuk, J.J., Li, X.G., 2001. Carbon monoxide poisoning of proton exchange membrane fuel cells. Int J Energ Res 25, 695-713.

[5] Wee, J.H., Lee, K.Y., 2006. Overview of the development of CO-tolerant anode electrocatalysts for proton-exchange membrane fuel cells. J Power Sources 157, 128-135.

[6] Farrell, C.G., Gardner, C.L., Ternan, M., 2007. Experimental and modelling studies of CO poisoning in PEM fuel cells. J Power Sources 171, 282-293.

[7] Yu, H.M., Hou, Z.J., Yi, B.L., Lin, Z.Y., 2002. Composite anode for CO tolerance proton exchange membrane fuel cells. J Power Sources 105, 52-57.

[8] Zhang, J.L., Xie, Z., Zhang, J.J., Tanga, Y.H., Song, C.J., Navessin, T., Shi, Z.Q., Song, D.T., Wang, H.J., Wilkinson, D.P., Liu, Z.S., Holdcroft, S., 2006. High temperature PEM fuel cells. J Power Sources 160, 872-891.

[9] Li, Q.F., He, R.H., Gao, J.A., Jensen, J.O., Bjerrum, N.J., 2003. The CO poisoning effect in PEMFCs operational at temperatures up to 200 degrees C. J Electrochem Soc 150, A1599-A1605.

[10] Hajbolouri, F., Andreaus, B., Scherer, G.G., Wokaun, A., 2004. CO Tolerance of Commercial Pt and PtRu Gas Diffusion Electrodes in Polymer Electrolyte Fuel Cells. Fuel Cells 4, 160-168.

[11] Das, S.K., Reis, A., Berry, K.J., 2009. Experimental evaluation of CO poisoning on the performance of a high temperature proton exchange membrane fuel cell. J Power Sources 193, 691-698.

[12] Krishnan, P., Park, J.S., Kim, C.S., 2006. Performance of a poly(2,5-benzimidazole) membrane based high temperature PEM fuel cell in the presence of carbon monoxide. J Power Sources 159, 817-823.

[13] Kwon, K., Yoo, D.Y., Park, J.O., 2008. Experimental factors that influence carbon monoxide tolerance of high-temperature proton-exchange membrane fuel cells. J Power Sources 185, 202-206.

[14] Modestov, A.D., Tarasevich, M.R., Filimonov, V.Y., Davydova, E.S., 2010. CO tolerance and CO oxidation at Pt and Pt-Ru anode catalysts in fuel cell with polybenzimidazole-H3PO4 membrane. Electrochim Acta 55, 6073-6080.

[15] Wang, C.P., Chu, H.S., Yan, Y.Y., Hsueh, K.L., 2007. Transient evolution of carbon monoxide poisoning effect of PBI membrane fuel cells. J Power Sources 170, 235-241.

[16] Pan, C., He, R.H., Li, Q.F., Jensen, J.O., Bjerrum, N.J., Hjulmand, H.A., Jensen, A.B., 2005. Integration of high temperature PEM fuel cells with a methanol reformer. J Power Sources 145, 392-398.

[17] Bender, G., Zawodzinski, T.A., 2005. Spatial distribution of the CO transient response of a PEFC. Proton Conducting Membrane Fuel Cells Iii, Proceedings 2002, 212-219.

[18] Brett, D.J.L., Atkins, S., Brandon, N.P., Vesovic, V., Vasileiadis, N., Kucernak, A.R., 2004. Investigation of reactant transport within a polymer electrolyte fuel cell using localised CO stripping voltammetry and adsorption transients. J Power Sources 133, 205-213.

[19] Schulze, M., Gulzow, E., Schonbauer, S., Knori, T., Reissner, R., 2007. Segmented cells as tool for development of fuel cells and error prevention/prediagnostic in fuel cell stacks. J Power Sources 173, 19-27.

[20] Wilkinson, D.P., St-Pierre, J., 2003. In-plane gradients in fuel cell structure and conditions for higher performance. J Power Sources 113, 101-108.

[21] Pérez, L.C., Brandão, L., Sousa, J.M., Mendes, A., 2010. Segmented polymer electrolyte membrane fuel cells—A review. Renewable and Sustainable Energy Reviews, in press: doi 10.1016/j.rser.2010.1008.1024.

[22] Tingelof, T., Hedstrom, L., Holmstrom, N., Alvfors, P., Lindbergh, G., 2008. The influence of CO2, CO and air bleed on the current distribution of a polymer electrolyte fuel cell. Int J Hydrogen Energy 33, 2064-2072.

[23] Brett, D.J.L., Aguiar, P., Brandon, N.P., Kucernak, A.R., 2007. Measurement and modelling of carbon monoxide poisoning distribution within a polymer electrolyte fuel cell. Int J Hydrogen Energy 32, 863-871.

[24] Gulzow, E., Kaz, T., Reissner, R., Sander, H., Schilling, L., von Bradke, M., 2002. Study of membrane electrode assemblies for direct methanol fuel cells. J Power Sources 105, 261-266.

[25] Knori, T., Schulze, M., 2009. Spatially resolved current density measurements and real-time modelling as a tool for the determination of local operating conditions in polymer electrolyte fuel cells. J Power Sources 193, 308-314.

[26] Antunes, R.A., Oliveira, M.C.L., Ett, G., Ett, V., 2010. Corrosion of metal bipolar plates for PEM fuel cells: A review. Int J Hydrogen Energy 35, 3632-3647.

[27] Hermann, A., Chaudhuri, T., Spagnol, P., 2005. Bipolar plates for PEM fuel cells: A review. Int J Hydrogen Energy 30, 1297-1302.

[28] Tawfik, H., Hung, Y., Mahajan, D., 2007. Metal bipolar plates for PEM fuel cell - A review. J Power Sources 163, 755-767.

[29] Kim, J.D., Park, Y.I., Kobayashi, K., Nagai, M., Kunimatsu, M., 2001. Characterization of CO tolerance of PEMFC by ac impedance spectroscopy. Solid State Ionics 140, 313-325.

[30] Wagner, N., Gulzow, E., 2004. Change of electrochemical impedance spectra (EIS) with time during CO-poisoning of the Pt-anode in a membrane fuel cell. J Power Sources 127, 341-347.

[31] Wagner, N., Schulze, M., 2003. Change of electrochemical impedance spectra during CO poisoning of the Pt and Pt-Ru anodes in a membrane fuel cell (PEFC). Electrochim Acta 48, 3899-3907.

[32] Gohr, H., 1997. Impedance Modelling of Porous Electrodes. Electrochem. Appl. 1, 2-3 (http://www.zahner.de).

[33] Wagner, N., Kaz, T., Friedrich, K.A., 2008. Investigation of electrode composition of polymer fuel cells by electrochemical impedance spectroscopy. Electrochim Acta 53, 7475-7482.

# Chapter 4 A dynamic model for HT-PEMFC[3]

## 4.1 Abstract

A dynamic one-dimensional isothermal phenomenological model was developed in order to describe the steady-state and transient behaviors of high temperature polymer electrolyte membrane fuel cells (PEMFC). The model accounts for transient species mass transport at the bipolar plates and gas diffusion layers and the electric double layers charge/discharge. To record the impedance spectra, a small sinusoidal voltage perturbation was imposed to the simulator over a wide range of frequencies, and the resultant current density amplitude and phase were recorded.

The steady-state behavior of the fuel cell, as well as the impedance spectra were obtained and compared to experimental data of two different fuel cells equipped with different MEAs based on phosphoric acid polybenzimidazole membrane. The model fitted quite well the I-V curves for both systems, but fairly well the Nyquist plots. The differences observed in the Nyquist plots were attributed to proton resistance in the catalyst layer and the gas diffusion limitations to cross the phosphoric acid layer that coats the catalyst, phenomena not included in the proposed phenomenological model.

3 The content of this chapter is adapted from: Boaventura, M., Sousa, J.M., Mendes, A., 2011. A dynamic model for high temperature polymer electrolyte membrane fuel cells. Int J Hydrogen Energy, in press: doi 10.1016/j.ijhydene.2011.1004.1218.

## 4.2 Introduction

The interest in hydrogen fuel cells has increased because of their ability to produce electricity with minimal environmental pollution. Typical polymer electrolyte membrane fuel cells (PEMFC) operate at temperatures below the water boiling point; recently, attention has been drawn to high temperature systems (>120 °C) due to the advantages they present, such as increased tolerance to carbon monoxide and simplified water management.

Mathematical models are widely used to simulate the behavior of fuel cells and play an important role in the development of fuel cells devices. They allow a better comprehension of the phenomena occurring inside the fuel cell and the parameters that control the performance. Models can be classified into theoretical or system models [1-2]. Theoretical models are based on phenomenological equations, representing the electrochemical kinetics, the charge transport and the thermodynamic relations. A system model (analytic, semi-empirical, or empirical) is based in experimental results, specific for the system object of the study. The later does not provide as detailed information as theoretical models do, but can be considered a first approximation to fuel cell modeling. Fuel cell models have been revised by several authors [1-7].

Most of experimental fuel cells results are obtained in steady-state conditions and therefore mathematical models, considering different spatial dimensions, have been developed for these conditions. One dimensional (1D) models for low temperature PEMFC have been developed since the early 90's by Springer *et al.* [8] and Bernardi and Verbrugge [9]. Springer *et al.* developed an isothermal model that provided insight into the water transport mechanisms of the fuel cell and their effect on the respective performance. Bernardi and Verbrugge developed an isothermal model for the cathode electrode focusing on the cell polarization characteristics, water transport and catalyst utilization. Both models account only for diffusive mass transport and electrochemical kinetics. Recently, more detailed 1D models were developed. Ramousse *et al.* [10] included in the fuel cell modeling the gas diffusion in

the porous electrodes, water balance in the membrane and heat transfer in the membrane electrodes assembly (MEA) and bipolar plates. Although a single domain models provide important information concerning fluxes, species concentration, temperatures, and electrical potentials, two-dimensional (2D) models were developed in order to take into account spatially affected phenomena, usually along a single channel [11-15]. Three dimensional (3D) models, with improved transport models and based on computational fluid dynamics were also developed [16-24]. Recently, Ko *et al.* [25] obtained the local temperature, water content in the MEA and gas velocity in the channel of the PEMFC, at different operation temperature and under the cathode starvation conditions using a commercial flow solver.

In the last 5 years, several steady-state models have been developed for high temperature fuel cells based in phosphoric acid doped polybenzimidazole; nonetheless, models for Nafion®-based PEMFC outnumber models for high temperature PEMFC. Korsgaard *et al.* [26] and Scott *et al.* [27] developed a zero-dimensional semi-empirical model to express the relationship between voltage and current density; Scott *et al.* considered the effect of mass transport through the electrolyte film covering the catalyst layers. Cheddie and Munroe presented two 1D non-isothermal models focused on polarization performance of a fuel cell [28] and geometric factors such as porous media characteristics, membrane and catalyst properties [29]. Scott *et al.* [30] followed with an isothermal 1D model which included the potential and current distributions in the catalyst layers. Similarly to low temperature PEMFC, multidimensional models were developed. Hu *et al.* [31-32] constructed 2D models based on electrochemical methods (cathode exchange current density and cell internal resistance were supplied by linear sweep voltammetry and electrochemical impedance spectroscopy techniques) while Shamardina *et al.* [33] developed an analytical pseudo 2D isothermal model accounting for the crossover of reactant gases through the membrane. Furthermore, Cheddie and Munroe [34] developed a 2D model considering two phase media. These authors considered that oxygen and hydrogen dissolve in the electrolyte before undergoing electrochemical reaction, assuming, this way, aqueous phase kinetics. Moreover, steady-state 3D models were developed for phosphoric acid doped polybenzimidazole fuel cells [35-37].

When integrated in a complex system that includes humidifiers, compressors and reformers, among others, a fuel cell has a response time associated to changes in the load or in the gas feed concentrations. The dynamic response of a PEMFC is a central issue for mobile applications such as in automobiles. Therefore, transient models have been developed to study the fuel cell response to changes in current density/voltage [38-43] and operation conditions [44-47], as well as its own start-up [45; 48-49]. Andreasen and Kaer [50] developed a control oriented model for predicting the dynamic temperature of a high temperature PEMFC stack. Moreover, Wang *et al.* [51] developed a transient model to predict the CO tolerance of high temperature PEMFC and observed the transient degradations of fuel cell performance.

The dynamic models referred above take into account three of the four main transient processes in a PEM fuel cell, namely species mass transport, membrane hydration/dehydration and heat transfer. The electric double layer charge/discharge is often neglected, since its time constant is considered very short [52-53]. The double layer is, nevertheless, essential for understanding the cell dynamics [54-56]. The double layer occurs in a thin layer adjacent to the reaction interface: electrons accumulate on the surface of the electrode and protons on the surface of the electrolyte and therefore the interface stores electrical charge and acts as an electric capacitor [42; 53-54; 57]. Upon a load change, it will take some time for this charge to build up or dissipate [53-54; 57-58]. High temperature PEMFC dynamic models incorporating double layer effect were developed by Zenith *et al.* [59] and Peng *et al.* [58]. Zenith *et al.* developed a control-oriented model considering only the transient behavior of the activation overvoltage when changing the resistance of the external load whereas Peng *et al.* developed a transient three-dimensional model accounting for transient convective and diffusive transport. These authors considered a macro-homogeneous model to describe the catalyst layer.

Fuel cells are usually characterized by the steady-state response, but more detailed information can be obtained from transient response measurements such electrochemical impedance spectroscopy (EIS) experiments. This technique measures the fuel cell impedance along the frequency domain and allows the separation of

contribution of processes occurring at the same time at steady-state [60]. The EIS spectra can be modeled using an electrical equivalent circuit (analogs composed of resistors, capacitors and inductors) and the system parameters can be obtained [61-62]. However, this analysis can involve a simplification of the representation of the fuel cell system and it is difficult to convert the values of resistances/capacitances into meaningful parameters [63]. The EIS spectra's parameters can also be obtained using a dynamic phenomenological model derived from conservation laws. Several impedance models were developed for porous cathode electrodes. Springer *et al.* [64] developed a model based on macro homogeneous porous electrode theory and considered the ternary diffusion on the GDL. Later, Jaouen *et al.* [60] considered a spherical agglomerate model for the porous electrode. They considered that gases are firstly transported by diffusion and/or convection before dissolving in the electrolyte phase and reaching the catalyst particles. This work was further extended by Guo *et al.* [65]. The analysis of EIS based on continuum mechanics approach was reviewed by Gomadam and Weidner [63].

In this work, a dynamic one-dimensional isothermal model was developed for high temperature PEMFC taking into account two transient processes: the mass transport on the bipolar plates and gas diffusion layers and the double layers charge/discharge. The EIS experiments were mimicked by imposing a small sinusoidal voltage perturbation to the simulator, over a wide range of frequencies. The developed model was used to simulate the steady-state and transient behavior of two fuel cells systems operated at 160 °C, based on phosphoric acid polybenzimidazole MEAs.

## 4.3 Fuel Cell Model

A simple dynamic phenomenological model, accounting for the transient mass transport (on the bipolar plates and GDLs) and the double layers charge/discharge, was developed in order to describe the steady-state behavior and the impedance spectra of high temperature PEMFC. To obtain the impedance spectra, a small voltage perturbation was imposed to the simulator and the current density

amplitude and phase were recorded. It was intended to obtain a valuable tool for analyzing experimental data, without being computationally and time consuming.

The schematic diagram of the fuel cell cross section considered in this study is presented in Figure 4.1.

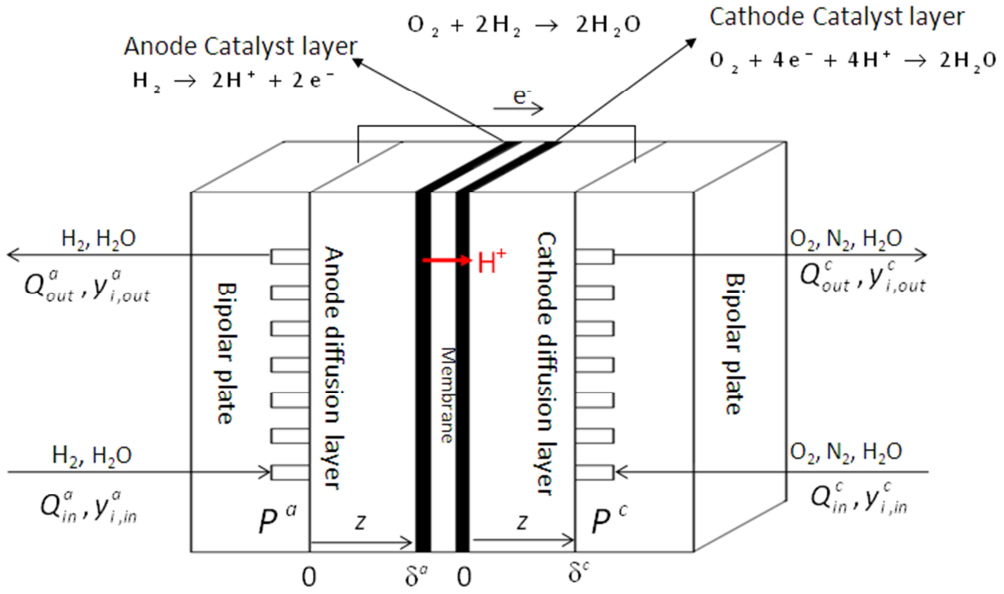


**Figure 4.1** Schematic diagram of the fuel cell cross section.

The anode feed stream was composed by hydrogen (and water vapor, if applicable) whereas a feed stream of oxygen and nitrogen (and water vapor, if applicable) was considered for the cathode side. In case of water presence in the inlet stream, the gases pass through a humidifier. The humidifier temperature determines the partial pressure of water.

For the sake of simplicity, constant temperature operation and perfectly mixed flow pattern in the flow field channels were assumed. This assumption is reasonable, considering that pure hydrogen or hydrogen with very low relative humidity is fed at the anode side, whereas high volumetric flow rate was used at the cathode side.

Other model main assumptions are:

- only gas phase present on the anode and cathode: the water produced was assumed to be in gas phase, noticing the operating temperature above 120 °C;
- ideal gas behavior;
- water drag coefficient through membrane was neglected;
- membrane was assumed impermeable to gases;
- anode and cathode double layer capacitances were assumed to be homogeneous;
- catalyst layers were assumed very thin and having homogeneous properties (planar catalyst layer model).

### 4.3.1 Mass balances

The unsteady state partial and total mass balance equations for the flow fields (anode or cathode) are described in the following by equations (4.1) and (4.2):

$$\frac{V^{FF}}{\Re T}\frac{dp_i^{FF}}{dt} = Q_{in}^{FF}\frac{p_{i,in}^{FF}}{\Re T} - Q_{out}^{FF}\frac{p_i^{FF}}{\Re T} - AN_i \tag{4.1}$$

$$Q_{in}^{FF}\frac{P^{FF}}{\Re T} - Q_{out}^{FF}\frac{P^{FF}}{\Re T} - A\sum_{i=1}^{nc} N_i = 0 \tag{4.2}$$

where the subscript *i* refers to the species present in the respective electrode (with *nc* components) and the superscript *FF* means flow field (anode or cathode). *p* means partial pressure and *P* the total pressure, *N* represents the flux across the respective GDL, *t* is the time, $\Re$ is the gas constant, *T* the fuel cell temperature, *Q* represents volumetric flow rate, *V* is the flow field volume and *A* is the active area.

The mass transport (flux) in the gas diffusion layers was considered by diffusion (Fick's law) and convection (Darcy's law) [30-32]. The concerning unsteady state mass balance equation is described by:

$$\frac{\partial p_i}{\partial t} = \frac{\partial}{\partial z}\left( D_i P^{gdl} \frac{\partial}{\partial z}\left( \frac{p_i^{gdl}}{P^{gdl}} \right) + \frac{p_i^{gdl} \beta}{\mu_{mix}} \frac{\partial P^{gdl}}{\partial z} \right) \tag{4.3}$$

where $\beta$ is the permeability of the gas diffusion layer, $\mu_{mix}$ is the fluid viscosity, $z$ is the spatial coordinate, and $D$ is the effective diffusivity, obtained taking into account the effect of the GDL porosity, according to the Bruggeman expression [33; 37]:

$$D_i = D_i^r \varepsilon^{1.5} \tag{4.4}$$

where $\varepsilon$ is the gas diffusion layer porosity and $D^r$ is the "true" diffusion, calculated by the Chapman-Enskog correlation [66].

To solve the mass balance equations (4.1) and (4.2), only an initial condition is necessary. In principle, any initial condition may be used, because the objective of the model is to study the pseudo steady-state, that is, the response of the system when subjected to a sinusoidal perturbation of the voltage. To simplify the problem, we consider that the initial composition is the same as the feed operation composition:

$$t = 0, \quad p_i^{FF} = p_{i,in}^{FF} \tag{4.5}$$

To solve the mass balance equation (4.3), an initial and two boundary conditions are needed.

$$t = 0, \quad p_i^{gdl}\left(\forall z\right) = p_{i,in}^{FF} \qquad \text{(for both anode and cathode)} \tag{4.6}$$

$$z = 0, \quad p_i^{gdl,a}\left(\forall t\right) = p_i^{FF,a} \quad \textit{and} \quad z = \delta^a, \quad N_i^{gdl,a}\left(\forall t\right) = S_i^{cl,a} \tag{4.7}$$

$$z = 0, \quad N_i^{gdl,c}\left(\forall t\right) = S_i^{cl,c} \quad \textit{and} \quad z = \delta^c, \quad p_i^{gdl,c}\left(\forall t\right) = p_i^{FF,c} \tag{4.8}$$

where the superscripts *a* and *c* refers to anode and cathode electrodes, respectively, and *cl* means catalytic layer. $\delta$ is the gas diffusion layer thickness and $S_i$ is a source term, defined as:

$$S_{H_2} = \frac{j_r^a}{2F}; \quad S_{O_2} = \frac{j_r^c}{4F}; \quad S_{H_2O} = -\frac{j_r^c}{2F} \tag{4.9}$$

For the species that doesn't take part in the reaction, $S_i$=0. *F* is the Faraday constant and $j_r$ is the reaction current density, calculated by the Butler-Volmer equation [67]:

$$j_r = j_0 \left( \frac{p_i^{cl}}{p_{i,in}} \right)^{\gamma} \left( e^{\frac{\alpha n F \eta_{act}}{\Re T}} - e^{-\frac{(1-\alpha) n F \eta_{act}}{\Re T}} \right) \tag{4.10}$$

where $j_0$ is the exchange current density, $\alpha$ is the transfer coefficient and $\gamma$ is the reaction order. For simplicity, it was assumed that $\alpha_{ox}$=1-$\alpha_{red}$ for both electrodes [67]. The subscripts *ox* and *red* stand for oxidation and reduction reactions, respectively. $\eta_{act}$ represents the activation losses (also called activation overpotential), that is, the voltage loss necessary to overcome the energy barrier of the electrochemical reactions [68].

### 4.3.2 Fuel cell voltage

The fuel cell operating voltage ($V_{cell}$) results from the balance between the thermodynamic voltage and a set of voltage losses, related with activation overpotentials and ohmic losses ($\eta_{ohm}$) [69], as described in the following:

$$V_{cell} = E_{therm} - \eta_{ohm} - \eta_{act}^a - \eta_{act}^c \tag{4.11}$$

Mass transfer resistance to the catalyst surface imposes an additional voltage loss due to transport limitations through the gas diffusion layer and catalyst layer, especially significant at high current densities. However, this voltage drop is included

in the activation losses (equation 4.10) and in the thermodynamic voltage, $E_{therm}$, obtained using the Nernst equation:

$$E_{therm} = E^0 + \frac{\Delta\hat{S}}{nF}\left(T - T_{ref}\right) + \frac{\Re T}{nF}\ln\left(\frac{p_{H_2}^{cl,a}\left(p_{O_2}^{cl,c}\right)^{1/2}}{p_{H_2O}^{cl,c}}\right) \tag{4.12}$$

where $E^0$ is the standard state reversible fuel cell voltage, $\Delta\hat{S}$ is the entropy change, $n$ represents the number of electrons transferred ($n$=2) and $T_{ref}$ is the reference temperature (25 °C).

For temperatures in the range 400–500 K, the entropy change is given by [30-32]:

$$\frac{\Delta\hat{S}}{n} = -18.449 - 0.01283T \tag{4.13}$$

At 25 °C, 1 bar and considering that the reaction product water is in gas phase, $E^0$=1.18 V [30]. Combining equations (4.12) and (4.13), the following equation is obtained:

$$E_{thermo} = 1.18 + \frac{-18.449 - 0.01283T}{F}\left(T - T_{ref}\right) + \frac{\Re T}{nF}\ln\left(\frac{p_{H_2}^{CL,a}\left(p_{O_2}^{CL,c}\right)^{1/2}}{p_{H_2O}^{CL,c}}\right) \tag{4.14}$$

The fuel cell ohmic resistance, $\eta_{ohm}$, results from the contribution of proton conductivity of the membrane and electron conductivity of the electrodes. Hence, the ohmic loss ($\eta_{ohm}$) is given by:

$$\eta_{ohmic} = j_{cell}\left[\left(\frac{\delta^m}{k}\right) + \left(\frac{\delta^a}{\sigma^a}\right) + \left(\frac{\delta^c}{\sigma^c}\right)\right] \tag{4.15}$$

where $j_{cell}$ is the fuel cell current density due to an external load, $k$ is the proton conductivity of the membrane and $\sigma$ is the electron conductivity of the GDL. The superscript $m$ refers to the membrane.

In transient conditions, electrons and protons accumulate at the electrode and electrolyte, in a thin layer neighboring the reacting interface. For instance, in case of voltage increase, the charge will take some time to vanish and in case of voltage decrease, the charge will take some time to increase. Therefore, in transient conditions, the reaction current density ($j_r$) is different from the current density due to the external load ($j_{cell}$). A capacitive current must also be considered, influencing the activation overvoltage [59; 70]:

$$j_{cell} = j_r + C_{dl}\frac{d\eta_{act}}{dt} \tag{4.16}$$

where $C_{dl}$ is the differential capacitance of either anode or cathode.

In an EIS experiment, a sinusoidal voltage of known amplitude ($V_0$) is imposed to the fuel cell voltage ($V_{cell}$), over a wide range of frequencies ($f$), (equation 4.17). The system response is a sinusoidal current density with the same frequency, with amplitude $J_0$ and phase delayed by $\varphi$ (equation 4.18).

$$V(t) = V_{cell} + V_0 \sin(\omega t) \tag{4.17}$$

$$J(t) = j_{cell} + J_0 \sin(\omega t + \varphi) \tag{4.18}$$

where $V(t)$ *and* $J(t)$ are the voltage and current density for instant time $t$ and $\omega$ is the radial frequency, which is related to the frequency by $\omega = 2\pi f$ .

The impedance of the system ($Z$) can be defined as [67]:

$$Z = Z_0(\cos\varphi + j\sin\varphi) \tag{4.19}$$

where $Z_0$ is the impedance magnitude. The real component of the impedance is $Z' = Z_0(\cos\varphi)$ and the imaginary component of the impedance is $Z'' = Z_0(\sin\varphi)$.

### 4.3.3 Dimensionless equations

The model variables were made dimensionless with respect to the anode feed conditions ($P^a, Q_{in}^a$), to the hydrogen ($D_{H_2}$) and anode GDL thickness ($\delta^a$). Changing for dimensionless variables and introducing suitable dimensionless parameters, equations (4.1) – (4.3), (4.5) – (4.8) and (4.16) – (4.17) become as:

$$\frac{dp_i^{FF,a^*}}{d\theta} = \Big[ Q_{in}^{FF,a^*} p_{i,in}^{FF,a^*} - Q_{out}^{FF,a^*} p_i^{FF,a^*} + \\ + \Gamma \left( D_i^{gdl,a^*} P^{gdl,a^*} \frac{d}{dx}\left( \frac{p_i^{gdl,a^*}}{P^{gdl,a^*}} \right)\Big|_{x=0} + \beta^* \left( p_i^{gdl,a^*} \frac{dP^{gdl,a^*}}{dx} \right)\Big|_{x=0} \right) \Big] \frac{\tau_{ref}}{\tau^{FF,a}} \tag{4.20-a}$$

$$\frac{dp_i^{FF,c^*}}{d\theta} = \Big[ Q_{in}^{FF,c^*} p_{i,in}^{FF,c^*} - Q_{out}^{FF,c^*} p_{i,out}^{FF,c^*} + \\ + \Gamma \frac{\delta_{ref}}{\delta^c} \left( D_i^{gdl,c^*} P^{gdl,c^*} \frac{d}{dx}\left( \frac{p_i^{gdl,c^*}}{P^{gdl,c^*}} \right)\Big|_{x=\delta^c/\delta_{ref}} + \beta^* \left( p_i^{gdl,c^*} \frac{dP^{gdl,c^*}}{dx} \right)\Big|_{x=\delta^c/\delta_{ref}} \right) \Big] \frac{\tau_{ref}}{\tau^{FF,c}} \tag{4.20-b}$$

$$Q_{in}^{FF,a^*} P^{FF,a^*} - Q_{out}^{FF,a^*} P^{FF,a^*} + \Gamma \sum_{i=1}^{nc} \left( D_i^{gdl,a^*} P^{gdl,a^*} \frac{d}{dx}\left( \frac{p_i^{gdl,a^*}}{P^{gdl,a^*}} \right)\Big|_{x=0} + \beta^* \left( p_i^{gdl,a^*} \frac{dP^{gdl,a^*}}{dx} \right)\Big|_{x=0} \right) = 0 \tag{4.21-a}$$

$$Q_{in}^{FF,c^*} P^{FF,c^*} - Q_{out}^{FF,c^*} P^{FF,c^*} + \\ + \Gamma \frac{\delta_{ref}}{\delta^c} \sum_{i=1}^{nc} \left( D_i^{gdl,c^*} P^{gdl,c^*} \frac{d}{dx}\left( \frac{p_i^{gdl,c^*}}{P^{gdl,c^*}} \right)\Big|_{x=\delta^c/\delta_{ref}} + \beta^* \left( p_i^{gdl,c^*} \frac{dP^{gdl,c^*}}{dx} \right)\Big|_{x=\delta^c/\delta_{ref}} \right) = 0 \tag{4.21-b}$$

$$\frac{\partial p_i^{gdl,a^*}}{\partial \theta}=\left[\frac{\partial}{\partial x}\left(D_i^{gdl,a^*}P^{gdl,a^*}\frac{\partial}{\partial x}\left(\frac{p_i^{gdl,a^*}}{P^{gdl,a^*}}\right)+\beta^* p_i^{gdl,a^*}\frac{\partial P^{gdl,a^*}}{\partial x}\right)\right]\frac{\tau_{ref}}{\tau^{gdl,a}} \tag{4.22-a}$$

$$\frac{\partial p_i^{gdl,c^*}}{\partial \theta}=\left[\frac{\partial}{\partial x}\left(D_i^{gdl,c^*}P^{gdl,c^*}\frac{\partial}{\partial x}\left(\frac{p_i^{gdl,c^*}}{P^{gdl,c^*}}\right)+\beta^* p_i^{gdl,c^*}\frac{\partial P^{gdl,c^*}}{\partial x}\right)\right]\frac{\tau_{ref}}{\tau^{gdl,c}} \tag{4.22-b}$$

$$-D_{H_2}^{gdl,a^*}P^{gdl,a^*}\frac{d}{dx}\left(\frac{p_{H_2}^{gdl,a^*}}{P^{gdl,a^*}}\right)\Bigg|_{x=1}-\beta^*\left(p_{H_2}^{gdl,a^*}\frac{dP^{gdl,a^*}}{dx}\right)\Bigg|_{x=1}=\frac{\delta_{ref}\Re T}{D_{ref}P_{ref}}\frac{j_r^a}{2F} \tag{4.23-a}$$

$$-D_{H_2O}^{gdl,a^*}P^{gdl,a^*}\frac{d}{dx}\left(\frac{p_{H_2O}^{gdl,a^*}}{P^{gdl,a^*}}\right)\Bigg|_{x=1}-\beta^*\left(p_{H_2O}^{gdl,a^*}\frac{dP^{gdl,a^*}}{dx}\right)\Bigg|_{x=1}=0 \tag{4.23-b}$$

$$D_{O_2}^{gdl,c^*}P^{gdl,c^*}\frac{d}{dx}\left(\frac{p_{O_2}^{gdl,c^*}}{P^{gdl,c^*}}\right)\Bigg|_{x=0}+\beta^*\left(p_{O_2}^{gdl,c^*}\frac{dP^{gdl,c^*}}{dx}\right)\Bigg|_{x=0}=\frac{\delta^c\Re T}{D_{ref}P_{ref}}\frac{j_r^c}{4F} \tag{4.24-a}$$

$$D_{H_2O}^{gdl,c^*}P^{gdl,c^*}\frac{d}{dx}\left(\frac{p_{H_2O}^{gdl,c^*}}{P^{gdl,c^*}}\right)\Bigg|_{x=0}+\beta^*\left(p_{H_2O}^{gdl,c^*}\frac{dP^{gdl,c^*}}{dx}\right)\Bigg|_{x=0}=-\frac{\delta^c\Re T}{D_{ref}P_{ref}}\frac{j_r^c}{2F} \tag{4.24-b}$$

$$D_{N_2}^{gdl,c^*}P^{gdl,c^*}\frac{d}{dx}\left(\frac{p_{N_2}^{gdl,c^*}}{P^{gdl,c^*}}\right)\Bigg|_{x=0}+\beta^*\left(p_{N_2}^{gdl,c^*}\frac{dP^{gdl,c^*}}{dx}\right)\Bigg|_{x=0}=0 \tag{4.24-c}$$

$$\frac{d\eta_{act}^a}{d\theta}=\left(\frac{j_{cell}-j_r^a}{C_{dl}^a}\right)\tau_{ref} \tag{4.25-a}$$

$$\frac{d\eta_{act}^{c}}{d\theta}=\left(\frac{j_{cell}-j_{r}^{c}}{C_{dl}^{c}}\right)\tau_{ref} \tag{4.25-b}$$

$$V(\theta)=V_{cell}+V_{0}sin\left(\omega\theta\tau_{ref}\right) \tag{4.26}$$

where $x=\frac{z}{\delta_{ref}}$, $D_{i}^{*}=\frac{D_{i}^{eff}}{D_{ref}}$, $P^{*}=\frac{P}{P_{ref}}$, $p_{i}^{*}=\frac{p_{i}}{P_{ref}}$, $\beta^{*}=\frac{P_{ref}}{D_{ref}}\frac{\beta}{\mu_{mix}}$, $\theta=\frac{t}{\tau_{ref}}$, $\tau_{ref}=\frac{\left(\delta_{ref}\right)^{2}}{D_{ref}}$, $\tau^{FF,a}=\frac{V^{a}}{Q_{ref}}$, $\tau^{FF,c}=\frac{V^{c}}{Q_{ref}}$, $\tau^{gdl,a}=\frac{\left(\delta^{a}\right)^{2}}{D_{ref}}$, $\tau^{gdl,c}=\frac{\left(\delta^{c}\right)^{2}}{D_{ref}}$, $Q^{*}=\frac{Q}{Q_{ref}}$ and $\Gamma=\frac{AD_{ref}}{Q_{ref}\delta_{ref}}$. The dimensionless variables are denoted by the superscript *. The subscript *ref* refers to the reference conditions or component.

### 4.3.4 Solution of the model equations

The partial differential equations (4.22-a) and (4.22-b) were spatially discretized using finite differences (11 points). The resulting time dependent system of equations, connected with equations (4.20)-(4.21) and (4.23)-(4.26), were integrated using the routine LSODA [71]. The solution was considered to reach the steady-state when the time derivative of each dependent variable and for each of the spatial coordinate was smaller than a pre-defined value. To record the impedance spectra, a small voltage perturbation of 5 mV was imposed after the steady-state has been reached. For each frequency, the simulator guarantees that pseudo steady-state was reached before starting with a new frequency (at least five periods were recorded for each frequency).

## 4.4 Experimental

Two different MEAs, based on phosphoric acid doped polybenzimidazole (PBI) membrane were characterized: an in-house assembled MEA and a Celtec® - P1000 MEA. The preparation and electrochemical characterization of the in-house assembled MEA is described in detail in Chapter 2 (sections 2.3.1 and 2.3.4). The fuel cell equipped with the in-house MEA was operated at 160 °C, 2 bar and 1.0 % relative humidity (RH) in both streams. The cell was fed with 1.7 $cm^3 \cdot s^{-1}$ of hydrogen and with 5.0 $cm^3 \cdot s^{-1}$ of air. The electrochemical characterization of Celtec® - P1000 MEA is described in detail in Chapter 3 (section 3.3.3); the I-V curves and the impedance spectra were obtained at 160 °C and at atmospheric pressure with an air/$H_2$ stoichiometry of 2/1.2, and using non-humidified feed streams.

## 4.5 Results and discussion

The most common way to analyze EIS spectra is using an electrical equivalent circuit. Fitting this electrical equivalent model to the EIS spectra it is possible to obtain the parameters that characterize the electrochemical system. The use of electric equivalent circuits can be a very easy and straightforward method for EIS spectra analysis, but the transposition of the capacitance and resistance values into physical significant parameters is not always evident or easy.

An alternative way to relate directly the EIS spectra's parameters with the electrochemical system is to use dynamic phenomenological models. The model presented in this study considers two transient processes, namely the mass transport at the bipolar plate and gas diffusion layer and the double layer charge/discharge, either for the anode or for the cathode. When a sinusoidal perturbation is applied to the model, three semi-circles can appear in the Nyquist plot showing the impedance related with the mass transport (at low frequencies) and the combination of charge transfer resistance with catalyst double layer capacitance of anode and cathode (at

medium to high frequencies). The semi-circles are associated to a time constant ($\tau_{EIS}$), which depends on the values of capacitance ($C$) and resistance ($R$) ($\tau_{EIS} = R \cdot C$).

### 4.5.1 Simulator validation

The phenomenological model was first used to predict the response of two very simple fuel cell systems, represented by the electrical analogs in Figure 4.2.

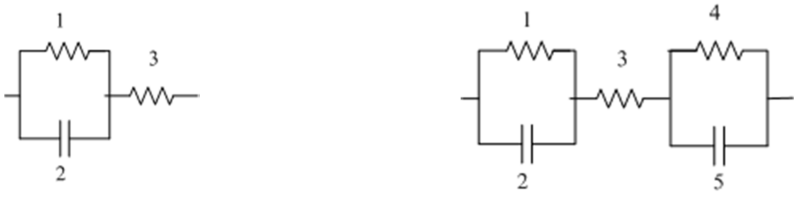


(a) (b)

**Figure 4.2** Simple electrical analogs of fuel cell systems.

The electric equivalent circuit of a fuel cell is composed by cathode and anode analogs and ohmic losses, connected in series. The electric analog of the anode and cathode can be well represented by a resistance (representing the charge transfer resistance) in parallel with a capacitance (representing the double layer capacitance), called RC analog. In both electric analogs, element 1 represents the cathode charge transfer resistance (it was attributed a value of $R_{ct}^{c}$ = 227 $\Omega \cdot cm^2$), element 2 represents cathode double layer capacitance ($C_{dl}^{c}$ =50 $mF \cdot cm^{-2}$) and element 3 is the ohmic resistance ($R_{ohm}$ =200.5 $\Omega \cdot cm^2$). Additionally, element 4 in the electric analog in Figure 4.2 (b) represents the anode charge transfer resistance ($R_{ct}^{a}$ =118 $\Omega \cdot cm^2$) and element 5 represents anode double layer capacitance ($C_{dl}^{a}$ =5 $mF \cdot cm^{-2}$).

The Nyquist and Bode plots of these electric circuits were also obtained by using the following equations:

$$Z = Z' + jZ'' \tag{4.27}$$

With $Z = \sqrt{(Z')^2 + (Z'')^2}$ and $\tan\varphi = \frac{Z''}{Z'}$. The real and imaginary parts of the impedance can be obtained as [72]:

$$Z' = R_{ohm} + \frac{R_{ct}^a}{1+\omega^2 \left(C_{dl}^a\right)^2 \left(R_{ct}^a\right)^2} + \frac{R_{ct}^c}{1+\omega^2 \left(C_{dl}^c\right)^2 \left(R_{ct}^c\right)^2} \tag{4.28}$$

$$Z'' = \omega \left[ \frac{C_{dl}^a \left(R_{ct}^a\right)^2}{1+\omega^2 \left(C_{dl}^a\right)^2 \left(R_{ct}^a\right)^2} + \frac{C_{dl}^c \left(R_{ct}^c\right)^2}{1+\omega^2 \left(C_{dl}^c\right)^2 \left(R_{ct}^c\right)^2} \right] \tag{4.29}$$

For the analog of Figure 4.2 (a), $R_{ct}^a = 0$. The phase shift was obtained by

$$\varphi = \arctan\left(\frac{Z''}{Z'}\right) \tag{4.30}$$

A set of operating conditions and properties, listed in Table 4.1, were chosen for run the developed phenomenological model. To predict the Nyquist plots of the electrical analogs in Figure 4.2 (a) and Figure 4.2 (b) it was assumed an exchange current density for the anode ( $j_0^a$ ) of 10 A·cm$^{-2}$ and 0.1 A·cm$^{-2}$, respectively, and no mass transfer resistance at the GDLs. A high anode exchange current density will make the anode charge transfer resistance negligible.

Figure 4.3 shows the Nyquist and Bode plots obtained by equations (4.27) - (4.30), representing the electric analog of Figure 4.2 (a) (analytical sol. (a)), and predicted by the model using data from Table 4.1 and $j_0^a$ =10 A·cm$^{-2}$. Figure 4.4 shows the Nyquist and Bode plots predicted by equations (4.27) - (4.30), representing the electric analog of Figure 4.2 (b) (analytical sol. (b)), and obtained by the model using data from Table 4.1 and $j_0^a$ =0.1 A·cm$^{-2}$. Nyquist and Bode plots obtained from the phenomenological model and by the analytical equations show that the model

describes correctly electrochemical systems that can be well described by elemental electric analogs.

**Table 4.1** Parameters used in phenomenological model for simulator validation.

| | Symbol | Value | Units |
|---|---|---|---|
| Fuel cell current density | $j_{cell}$ | 0.23 | $A \cdot cm^{-2}$ |
| Anode pressure | $P^a$ | 1 | bar |
| Cathode pressure | $P^c$ | 1 | bar |
| Membrane proton conductivity | $k$ | 0.06 | $S \cdot cm^{-1}$ |
| Membrane thickness | $\delta^m$ | 100 | μm |
| GDL electrical conductivity | $\sigma$ | 2.22 | $S \cdot cm^{-1}$ |
| GDL thickness anode | $\delta^a$ | 375 | μm |
| GDL thickness cathode | $\delta^c$ | 375 | μm |
| Cathode exchange current density | $j_0^c$ | $8 \times 10^{-6}$ | $A \cdot cm^{-2}$ |
| Anode transfer coefficient | $\alpha^a$ | 0.5 | - |
| Cathode transfer coefficient | $\alpha^c$ | 0.2 | - |
| Anode capacitance | $C_{dl}^a$ | 5 | $mF \cdot cm^{-2}$ |
| Cathode capacitance | $C_{dl}^c$ | 50 | $mF \cdot cm^{-2}$ |

### 4.5.2 Fuel cell modeling

The purpose of a phenomenological model is to provide a good fitting of the experimental values and to assist understanding the physical problem and to optimize the operating and design conditions. In the present case, two fuel cells operating at 160 °C and equipped with two different MEAs, based on phosphoric acid doped PBI membranes, were considered: an in-house MEA tested with 1.0 % relative humidity in an in-house test station and a Celtec® - P1000 MEA tested in a DLR (Institut für Technische Thermodynamik, Deutsches Zentrum für Luft- und Raumfahrt e.V.) test station in anhydrous conditions. The experimental (exp.) conditions and parameters used in the simulation of both fuel cells are shown in Table 4.2. The values of transfer coefficient ($\alpha^c$) and exchange current density ($j_0^c$) for the cathode

were estimated by fitting the Tafel equation to experimental I-V curves for Celtec® - P1000 MEA and for very low current densities and are $\alpha^c = 0.2$ (or $n\alpha^c = 0.8$) and $j_0^c = 5\times10^{-6}$ A·cm$^{-2}$, respectively. These values are in agreement with the literature for similar operating conditions [29; 33].

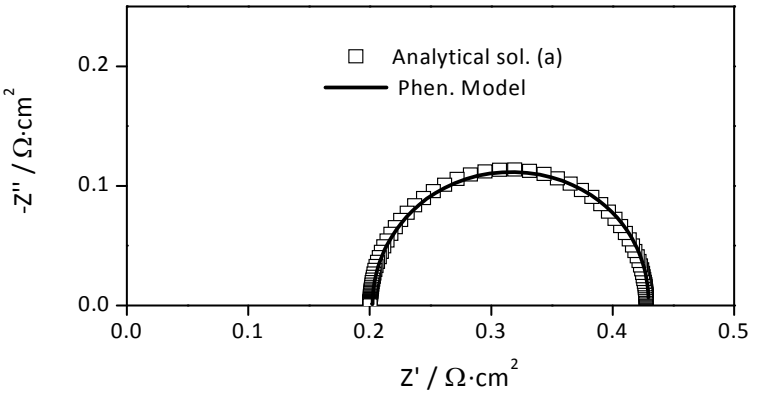


(a)

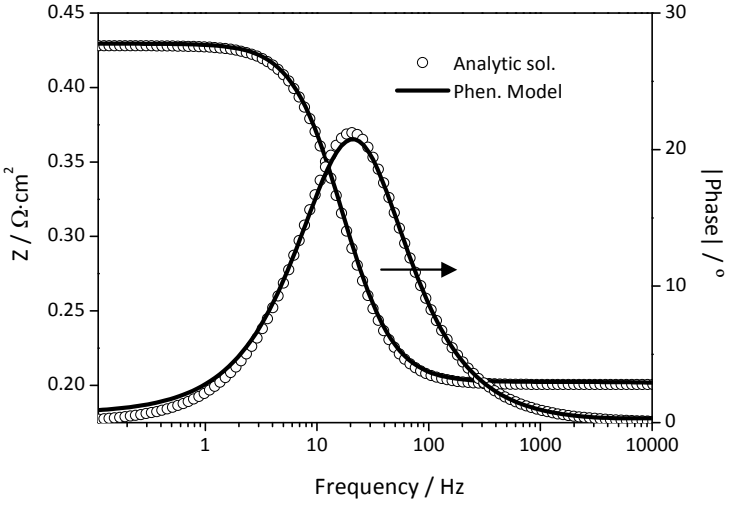


(b)

**Figure 4.3** Nyquist (a) and Bode (b) plots obtained using the equations (4.27) - (4.30), representing the electric circuit of Figure 4.2 (a), and the model, using data from Table 4.1 and $j_0^a$ =10 A·cm$^{-2}$.

The same cathode exchange current density was also used for the in-house MEA, since the experimental values of the I-V curves in the relevant region are very few. Moreover, Lui *et al.* [73] showed that the exchange current density of oxygen reduction does not markedly change with relative humidity (up to 10 %) or the phosphoric acid loading in a platinum interface with phosphoric acid doped PBI.

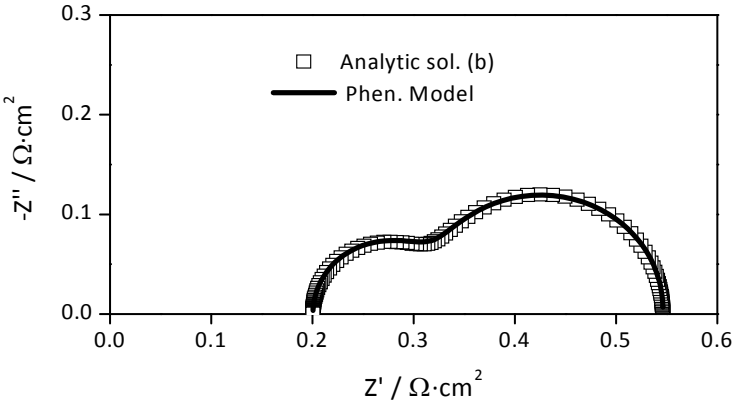


(a)

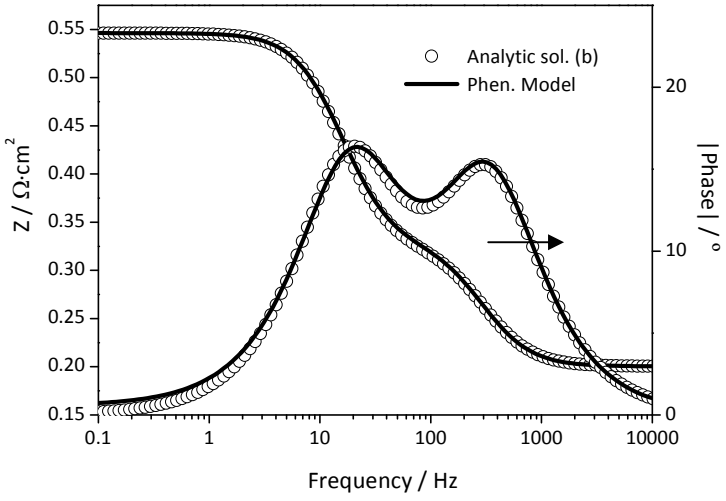


(b)

**Figure 4.4** Nyquist (a) and Bode (b) plots obtained using the equations (4.27) - (4.30), representing the electric circuit of Figure 4.2 (b), and the model, using data from Table 4.1 and $j_0^a$ =0.1 A·cm$^{-2}$.

**Table 4.2** Parameters used to simulate the fuel cells behavior.

| | Symbol | In-house MEA | Celtec® MEA | Units | Reference |
|---|---|---|---|---|---|
| Fuel cell temperature | $T$ | 160 | 160 | °C | [exp. condition] |
| Anode pressure | $P^a$ | 2 | 1 | bar | [exp. condition] |
| Cathode pressure | $P^c$ | 2 | 1 | bar | [exp. condition] |
| Anode gas supply rate | $Q^a$ | 1.7 | 3.5 | $cm^3 \cdot s^{-1}$ | [exp. condition] |
| Cathode gas supply rate | $Q^c$ | 5.0 | 13.8 | $cm^3 \cdot s^{-1}$ | [exp. condition] |
| MEA active area | $A$ | 4.4 | 20.25 | $cm^2$ | [exp. condition] |
| Membrane proton conductivity | $k$ | 0.025 | 0.090 | $S \cdot cm^{-1}$ | [determined] |
| Membrane thickness | $\delta^m$ | 100 | 120 | μm | BASF |
| GDL electrical conductivity | $\sigma$ | 2.22 | 2.22 | $S \cdot cm^{-1}$ | [37] |
| GDL porosity anode | $\varepsilon^a$ | 0.76 | 0.6 | - | [determined] |
| GDL porosity cathode | $\varepsilon^c$ | 0.76 | 0.6 | - | [determined] |
| GDL Gas permeability | $\beta$ | $5.8\times10^{-8}$ | $5.8\times10^{-8}$ | $cm^2$ | [58] |
| GDL thickness anode | $\delta^a$ | 375 | 375 | μm | [determined] |
| GDL thickness cathode | $\delta^c$ | 375 | 375 | μm | [determined] |
| $H_2$ effective diffusivity | $D_{H_2}^{gdl}$ | 0.519 | 0.727 | $cm^2 \cdot s^{-1}$ | [66] |
| $O_2$ effective diffusivity | $D_{O_2}^{gdl}$ | 0.130 | 0.176 | $cm^2 \cdot s^{-1}$ | [66] |
| $H_2O$ effective diffusivity Anode | $D_{H_2O}^{gdl,a}$ | 0.519 | - | $cm^2 \cdot s^{-1}$ | [66] |
| $H_2O$ effective diffusivity cathode | $D_{H_2O}^{gdl,c}$ | 0.147 | 0.206 | $cm^2 \cdot s^{-1}$ | [66] |
| Anode exchange current density | $j_0^a$ | 0.5 | 0.4 | $A \cdot cm^{-2}$ | [determined] |
| Cathode exchange current density | $j_0^c$ | $5\times10^{-6}$ | $5\times10^{-6}$ | $A \cdot cm^{-2}$ | [determined] |
| Anode transfer coefficient | $\alpha^a$ | 0.5 | 0.5 | - | [determined] |
| Cathode transfer coefficient | $\alpha^c$ | 0.2 | 0.2 | - | [determined] |
| Reaction order anode | $\gamma^a$ | 0.5 | 0.5 | - | [29] |
| Reaction order cathode | $\gamma^c$ | 1 | 1 | - | [29] |

The membrane conductivity, the transfer coefficient ($\alpha^a$) and the exchange current density of the anode ($j_0^a$), the GDL porosity ($\varepsilon$) and the anode and cathode capacitances were obtained by fitting the model to the I-V curve for each MEA and to

the impedance spectra at fuel cell current density of 0.18 A·cm$^{-2}$ for the in-house MEA and at 0.20 A·cm$^{-2}$ for the Celtec® - P1000 MEA.

*I-V modeling*

The experimental and the modeled I-V curves are shown in Figure 4.5 (a) and Figure 4.6 (a) for the Celtec® - P1000 MEA and for the in-house MEA, respectively. The predicted I-V curves are quite close to the experimental values. Figure 4.5 (b) and Figure 4.6 (b) also show the simulated anode and cathode activation losses and ohmic losses as a function of the current density for the Celtec® - P1000 MEA and the in-house MEA, respectively. As expected, the major contribution for the voltage loss was due to the cathode activation.

*EIS modeling - Celtec® - P1000 MEA*

The experimental and predicted (Phen. model) Nyquist and Bode plots of the Celtec® - P1000 MEA at fuel cell current density of 0.20 A·cm$^{-2}$ are shown in Figure 4.7. The best fit to the impedance spectra was obtained for $C_{dl}^{a}$ =20 mF·cm$^{-2}$ and $C_{dl}^{c}$ =74 mF·cm$^{-2}$.

Since the relative importance of the several phenomena occurring in the fuel cell varies with the current density, the phenomenological model results were compared with the experimental ones for the Celtec® - P1000 MEA at higher current densities (0.3 A·cm$^{-2}$, 0.4 A·cm$^{-2}$ and 0.5 A·cm$^{-2}$), using the same parameters used for current density 0.2 A·cm$^{-2}$ –Table 4.2. The only parameters fitted for each current density were the anode and the cathode capacitances. According to the experimental data, the membrane conductivity at current densities 0.4 A·cm$^{-2}$ and 0.5 A·cm$^{-2}$ increased from 0.09 S·cm$^{-1}$ to 0.1 S·cm$^{-1}$. Figure 4.8 shows the experimental and best fitting Nyquist plots. A capacitance value of 40 mF·cm$^{-2}$ was used for the anode, for all current densities, and capacitances of 100 mF·cm$^{-2}$, 120 mF·cm$^{-2}$ and 140 mF·cm$^{-2}$ were used for the cathode side, for current densities of 0.30 A·cm$^{-2}$, 0.40 A·cm$^{-2}$ and 0.50 A·cm$^{-2}$, respectively.

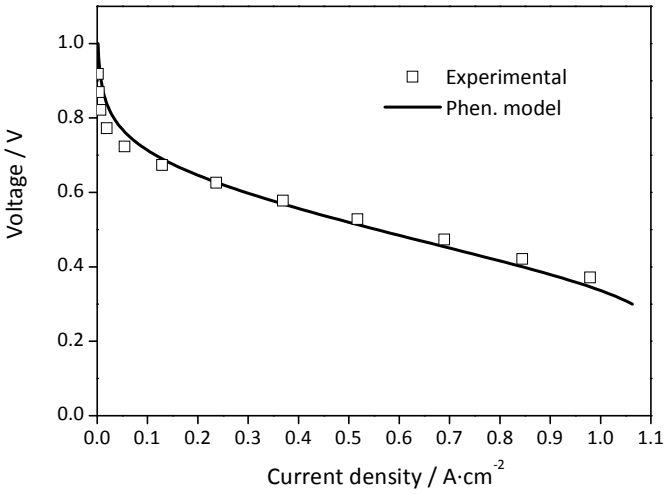


(a)

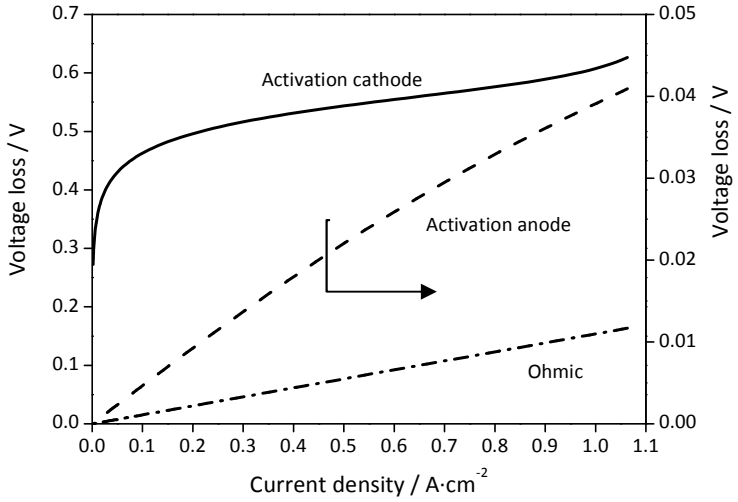


(b)

**Figure 4.5** Experimental and simulated I-V curves for the Celtec® - P1000 MEA operated at 160 °C, 1 bar and with unhumidified air and hydrogen gas flow (a), and sources of voltage loss obtained from simulation: anode (right Y-axis) and cathode activation losses and ohmic losses (b).

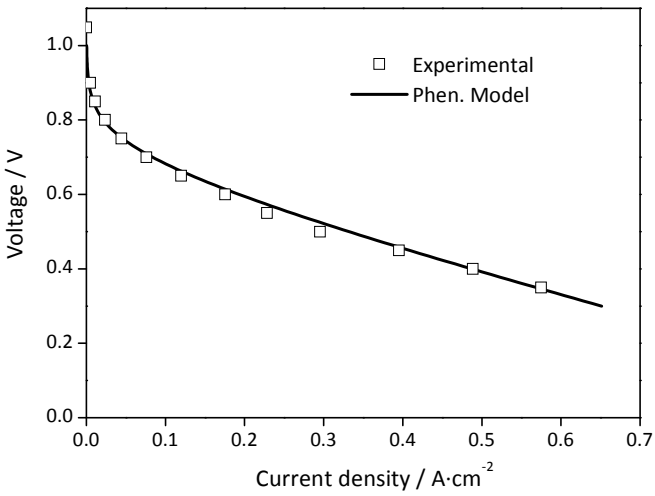


(a)

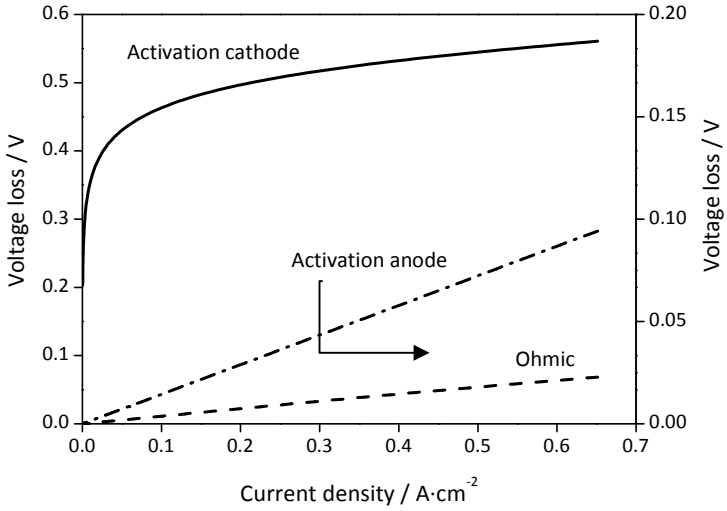


(b)

**Figure 4.6** Experimental and simulated I-V curves for the in-house MEA operated at 160 °C, 2 bar and 1.0 % RH (a) and sources of voltage loss obtained from simulation: anode (right Y-axis) and cathode activation losses and ohmic losses (b).

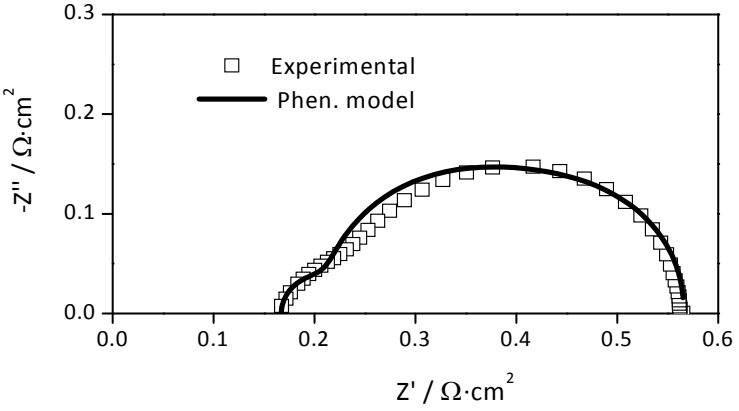


(a)

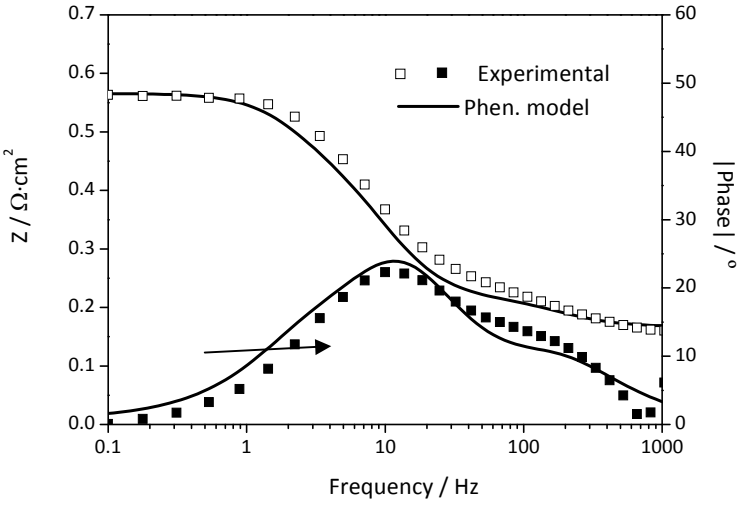


(b)

**Figure 4.7** Experimental and simulated Nyquist plot (a) and Bode plot (b) for the Celtec® - P1000 MEA operated at 160 °C, 1 bar and with unhumidified air and hydrogen gas flow, at 0.20 A·cm$^{-2}$ current density.

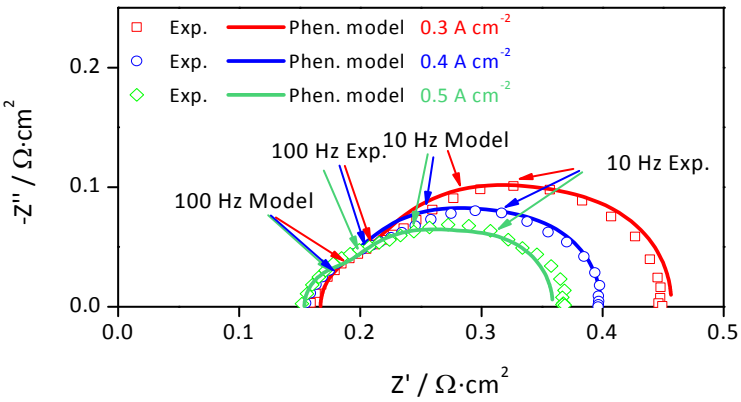


**Figure 4.8** Experimental and simulated Nyquist plots for the Celtec® - P1000 MEA operated at 160 °C, 1 bar, and with unhumidified air and hydrogen gas flow, at 0.30 A·cm$^{-2}$, 0.40 A·cm$^{-2}$ and 0.50 A·cm$^{-2}$ current density.

The phenomenological model captures the qualitative response of the fuel cell impedance at 0.2 A·cm$^{-2}$ (Figure 4.7). Nonetheless, at this point it is interesting to compare the model results with the parameters obtained by fitting the electric equivalent circuit presented in Figure 4.9 to the experimental spectrum (Figure 4.7).

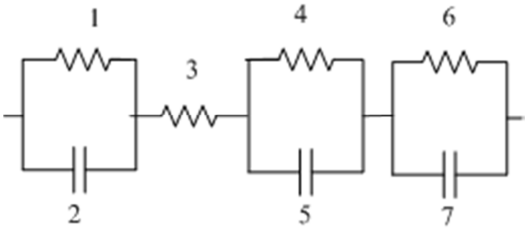


**Figure 4.9** Fuel cell electrical equivalent circuit. Elements 1 and 4 represent anode and cathode charge transfer resistance, elements 2 and 5 represent anode and cathode double layer capacitance, elements 6 and 7 represent the resistance and capacitance associated with gas phase mass transfer; element 3 is the ohmic resistance.

Resistances 1 and 4 represent the charge transfer resistance of anode and cathode whereas capacitances 2 and 4 represent the double layer capacitance of anode ($C_{dl}^{a}$)

and cathode ( $C_{dl}^{c}$ ). An extra RC was included to describe the mass transfer resistance of the reactant species to the active sites [62; 74]. Elements 6 and 7 represent the resistance and capacitance associated with mass transfer. The ohmic resistance represented by element 3 includes membrane proton resistance and the electronic resistance of the electrodes.

Usually, when electrical equivalent circuits are employed to study fuel cell EIS spectra's, the capacitance of anode and cathode is replaced by a constant phase element, mainly because of the electrodes porous structure (the capacitance caused by the double layer charging is distributed along the pore depths [63; 75]). To compare the electrical equivalent circuit with the phenomenological model, pure capacitive elements were considered, because the model assumes flat electrodes. The Thales software (Zahner-Elektrik GmbH) was used to fit this electrical model to the experimental data, Figure 4.10. From the electrical circuit fitting to the experimental data, it was obtained a capacitance of 10 $mF \cdot cm^{-2}$ and 74 $mF \cdot cm^{-2}$ for the anode and cathode, respectively. These values are close to the ones obtained by the proposed model.

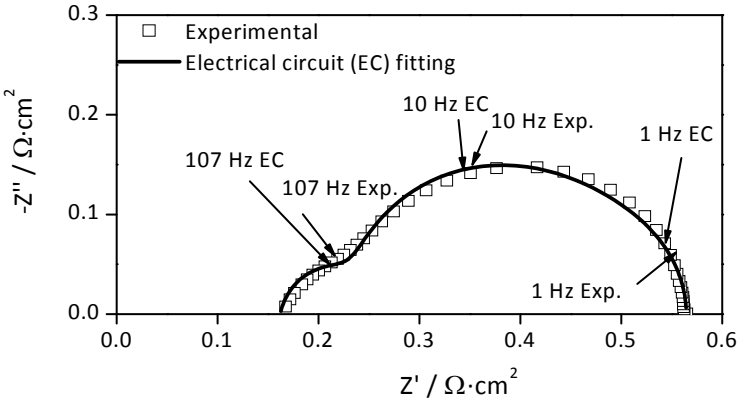


**Figure 4.10** Experimental Nyquist plot and predicted by the Thales software using the electric circuit of Figure 4.9, for the Celtec® - P1000 MEA operated at 160 °C, 1 bar, and with unhumidified air and hydrogen gas flow, at 0.20 $A \cdot cm^{-2}$ current density.

For higher current densities, the model also predicts qualitatively the Nyquist spectra. However, the predicted cathode semi-circles are associated to lower frequencies than the experimental ones (Figure 4.8).

The phenomenological model results were compared with the parameters obtained from fitting the electrical circuit of Figure 4.9 to the experimental spectra (Figure 4.11).

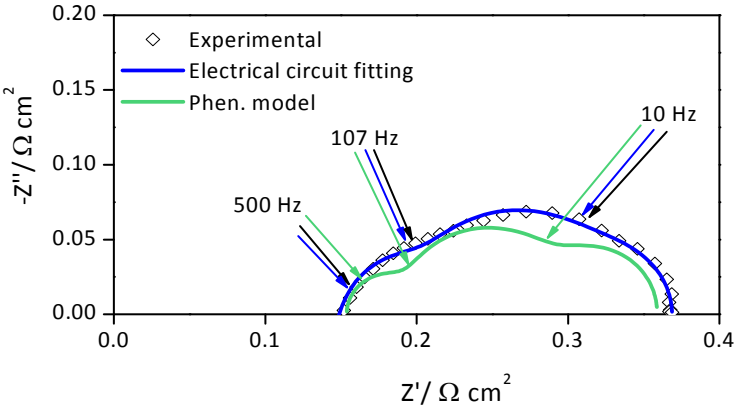


**Figure 4.11** Experimental Nyquist plot and predicted Nyquist plots by Thales software using the electric circuit analog of Figure 4.9 (blue line) and by the phenomenological model (green line), for the Celtec® - P1000 MEA operated at 160 °C, 1 bar, and with unhumidified air and hydrogen gas flow, at 0.50 A·cm$^{-2}$ current density.

The capacitances predicted by the model are also higher than the capacitances obtained by fitting the electrical circuit to experimental points. For instance, at current density 0.50 A·cm$^{-2}$, the electric circuit best fitting was for $C_{dl}^{a}$ =10 mF·cm$^{-2}$ and $C_{dl}^{c}$ =62 mF·cm$^{-2}$. These two parameters were then introduced in the model and the resultant Nyquist plot is shown in Figure 4.11 together with the original electric circuit fitting. As it can be seen, the results from the electric equivalent circuit fits quite well the experimental results, contrarily to the model ones.

The proposed dynamic model is very simple and considers a planar model for the catalyst layer at the anode and cathode. According to this approach, the

characteristic semi-circles associated to the anode and cathode depend only on the interfacial kinetics of the electrochemical reactions, with the diameter of the EIS loops determined by the charge transfer resistances. Two other processes, however, can affect the kinetic loop, namely the diffusion coefficient of gases towards the catalyst layer and the resistance associated with the proton leaving the catalyst layer [64]. When proton transport resistance within catalyst layer becomes noticeable, a 45° branch should appear at high frequencies in the Nyquist plot [60; 63-64]. Furthermore, Springer *et al.* [64] showed that, with air cathodes (at low temperature operation) the charge transfer resistance of the cathode decreases for higher current densities until reaching a minimum value; afterwards, the charge transfer resistance increases due to a depletion of oxygen within the catalyst layer. The gas diffusion on the phosphoric acid before undergoing electrochemical reaction as well as proton conductivity within the catalyst layer were not considered in the present phenomenological model, and, therefore, qualitative differences in the kinetic loop would be expected, especially at high current densities. For increasingly high current densities, the charge transfer resistance at the cathode decreases as a result of the increasing driving force for the oxygen reduction reaction (Figure 4.8); at the same time, the oxygen concentration within the catalyst layer decreases. So, considering similar capacitances, the Nyquist plot predicted by the model has lower charge transfer resistances than the experimental plot. The mass transfer resistance associated with the transport in the gas diffusion layer (represented by the semi-circle at low frequencies) is the only mass transport resistance inserted in the model.

*EIS modeling - in-house MEA*

The experimental and simulated Nyquist and Bode plots of the in-house MEA at 0.18 A·cm$^{-2}$ are shown in Figure 4.12. The best fit to the impedance spectra was obtained for $C_{dl}^{a}$ =40 mF·cm$^{-2}$ and $C_{dl}^{c}$ =80 mF·cm$^{-2}$. The model Nyquist plot is in agreement with the experimental values, Figure 4.12. However, the semi-circles are associated to much lower frequencies.

The model predictions were again compared with the parameters obtained from fitting the electrical circuit of Figure 4.9 to the experimental spectra (Figure 4.13). The electric circuit best fitting was for $C_{dl}^{a}$ =1.3 mF·cm$^{-2}$ and $C_{dl}^{c}$ =5.5 mF·cm$^{-2}$. These two parameters were then introduced in the model and the resultant Nyquist plot is shown in Figure 4.13, together with the original electric circuit fitting.

The use of lower values of capacitance in the simulator originated a different Nyquist plot compared to the experimental values. The model predicts a semi-circle at lower frequencies that is related to the gas diffusion layer resistances.

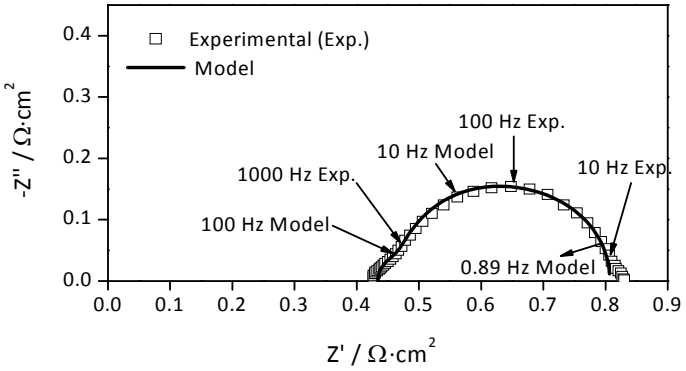


**Figure 4.12** Experimental and simulated Nyquist plot for the in-house MEA operated at 160 °C, 2 bar, and 1.0 % RH, at 0.18 A·cm$^{-2}$ current density.

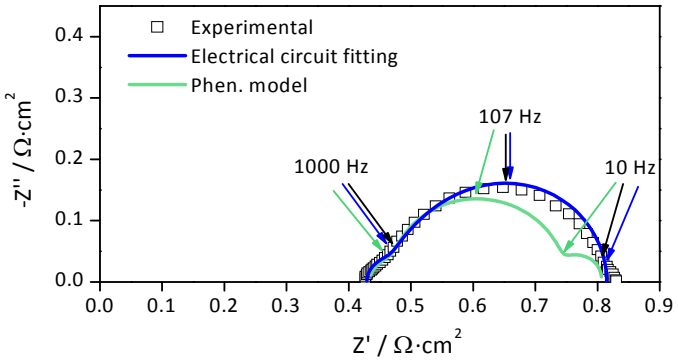


**Figure 4.13** Experimental Nyquist plot, predicted Nyquist plot by Thales software using the electric circuit analog of Figure 4.9 (blue line) and by the phenomenological model (green

line), for the in-house MEA operated at 160 °C, 2 bar, and 1.0 % RH, at 0.18 $A \cdot cm^{-2}$ current density.

At low current densities, it is expected that the charge transfer resistance be dominated by the electrochemical reactions. Nonetheless, the proton resistance and the gas diffusion limitations in the catalyst layer can also contribute to the effective charge transfer resistance making it noticeable in the Nyquist plot. Indeed, this MEA has no ionomer in the catalyst layer and proton-bridge between catalyst and electrolyte is assured by migrating phosphoric acid from the electrolyte membrane. As a consequence, for a similar value of capacitance, a lower value of charge transfer resistance is obtained using the model when compared to the experimental values.

## 4.6 Conclusions

A dynamic one-dimensional isothermal phenomenological model was developed for simulating high temperature polymer electrolyte membrane fuel cells. The phenomenological model was used to simulate the steady-state and the impedance spectra of two fuel cells operated at 160 °C, one equipped with an in-house assembled MEA and the other with Celtec® - P1000 MEA. To obtain the impedance spectra a small voltage perturbation over a wide range of frequencies was imposed to the simulator.

The steady-state behavior was captured and the phenomenological model proved to predict qualitatively well the Nyquist plots of both fuel cell systems. The observed differences were assigned to proton resistance and the gas diffusion limitations within the catalyst layer, which were not considered in the model.

A new phenomenological model is under development that takes into account the porous structure of the catalyst layer.

## 4.7 Acknowledgments

The work of M. Boaventura was supported by FCT (Grant SFRH/BD/28187/2006). The present work was also partially supported by FCT projects PTDC/EQU-EQU/70574/2006 and PTDC/EQU-EQU/104217/2008.

## 4.8 Nomenclature

| Symbol | Parameter | Units |
|---|---|---|
| $A$ | Active area | $cm^2$ |
| $C_{dl}$ | differential capacitance | $F \cdot m^{-2}$ |
| $D^r$ | diffusivity | $cm^2 \cdot s^{-1}$ |
| $D$ | effective diffusivity | $cm^2 \cdot s^{-1}$ |
| $E_{therm}$ | thermodynamic voltage | V |
| $E^0$ | Standard state reversible fuel cell | V |
| $F$ | Faraday constant | $C \cdot mol^{-1}$ |
| $f$ | frequency | Hz |
| $J_0$ | Amplitude of current response | $A \cdot cm^{-2}$ |
| $j_0$ | exchange current density | $A \cdot cm^{-2}$ |
| $j_{cell}$ | fuel cell current density | $A \cdot cm^{-2}$ |
| $j_r$ | reaction current density | $A \cdot cm^{-2}$ |
| $k$ | membrane proton conductivity | $S \cdot cm^{-1}$ |
| $N$ | flux | $mol \cdot cm^{-2} \cdot s^{-1}$ |
| $n$ | electrons transferred | mol |
| $P$ | total pressure | bar |
| $p$ | partial pressure | bar |
| $Q$ | volumetric flow rate | $cm^3 \cdot s^{-1}$ |
| $R$ | resistance | $\Omega \cdot cm^2$ |
| $\mathfrak{R}$ | Gas constant | $bar \cdot cm^3 \cdot mol^{-1} \cdot K^{-1}$ |
| $\Delta\hat{S}$ | Entropy change | $J \cdot K^{-1}$ |
| $S$ | Source term | $mol \cdot cm^{-2} \cdot s^{-1}$ |
| $T$ | temperature | K |
| $t$ | time | s |
| $V$ | volume | $cm^3$ |
| $V_{cell}$ | operating voltage | V |
| $V_0$ | amplitude of the perturbation | V |
| $z$ | spatial coordinate | cm |
| $Z$ | impedance | $\Omega \cdot cm^2$ |
| $Z_0$ | impedance magnitude | $\Omega \cdot cm^2$ |
| $Z'$ | real component of impedance | $\Omega \cdot cm^2$ |
| $Z''$ | imaginary component of impedance | $\Omega \cdot cm^2$ |

Greek

| Symbol | Parameter | Units |
|---|---|---|
| $\delta$ | thickness | cm |
| $\beta$ | Permeability of gas diffusion layer | $cm^2$ |
| $\varepsilon$ | porosity | - |
| $\sigma$ | electrode electric conductivity | $S \cdot cm^{-1}$ |
| $\alpha$ | transfer coefficient | - |
| $\eta$ | voltage loss | V |
| $\gamma$ | Reaction order | - |
| $\mu$ | Fluid viscosity in electrode | bar·s |
| $\varphi$ | Phase shift | - |
| $\omega$ | Radial frequency | $rad \cdot s^{-1}$ |

Superscripts

| | |
|---|---|
| * | dimensionless variables |
| m | membrane |
| a | anode |
| c | cathode |
| cl | catalyst layer |
| gdl | gas diffusion layer |
| FF | flow field channels |

Subscripts

| | |
|---|---|
| ox | oxidation reaction |
| red | reduction reaction |
| i | relative to component i |
| ref | relative to the reference conditions or component |
| act | activation |
| ohm | ohmic |

## 4.9 References

[1] Haraldsson, K., Wipke, K., 2004. Evaluating PEM fuel cell system models. J Power Sources 126, 88-97.

[2] Siegel, C., 2008. Review of computational heat and mass transfer modeling in polymer-electrolyte-membrane (PEM) fuel cells. Energy 33, 1331-1352.

[3] Biyikoglu, A., 2005. Review of proton exchange membrane fuel cell models. Int J Hydrogen Energy 30, 1181-1212.

[4] Cheddie, D., Munroe, N., 2005. Review and comparison of approaches to proton exchange membrane fuel cell modeling. J Power Sources 147, 72-84.

[5] Sousa, R., Gonzalez, E.R., 2005. Mathematical modeling of polymer electrolyte fuel cells. J Power Sources 147, 32-45.

[6] Wang, C.Y., 2004. Fundamental models for fuel cell engineering. Chem Rev 104, 4727-4765.

[7] Weber, A.Z., Newman, J., 2004. Modeling transport in polymer-electrolyte fuel cells. Chem Rev 104, 4679-4726.

[8] Springer, T.E., Zawodzinski, T.A., Gottesfeld, S., 1991. Polymer Electrolyte Fuel-Cell Model. J Electrochem Soc 138, 2334-2342.

[9] Bernardi, D.M., Verbrugge, M.W., 1991. Mathematical-Model of a Gas-Diffusion Electrode Bonded to a Polymer Electrolyte. Aiche J 37, 1151-1163.

[10] Ramousse, J., Deseure, J., Lottin, O., Didierjean, S., Maillet, D., 2005. Modelling of heat, mass and charge transfer in a PEMFC single cell. J Power Sources 145, 416-427.

[11] Dannenberg, K., Ekdunge, P., Lindbergh, G., 2000. Mathematical model of the PEMFC. J Appl Electrochem 30, 1377-1387.

[12] Ge, S.H., Yi, B.L., 2003. A mathematical model for PEMFC in different flow modes. J Power Sources 124, 1-11.

[13] Huang, W.B., Zhou, B., Sobiesiak, A., 2005. Along-channel mathematical modelling for proton exchange membrane fuel cells. Int J Energ Res 29, 1051-1071.

[14] Tsai, C.R., Chen, F.L., Ruo, A.C., Chang, M.H., Chu, H.S., Soong, C.Y., Yan, W.M., Cheng, C.H., 2006. An analytical solution for transport of oxygen in cathode gas diffusion layer of PEMFC. J Power Sources 160, 50-56.

[15] Zamel, N., Li, X.G., 2008. A parametric study of multi-phase and multi-species transport in the cathode of PEM fuel cells. Int J Energ Res 32, 698-721.

[16] Berning, T., 2008. A Three-Dimensional, Two-Fluid Model of PEM Fuel Cell Cathodes. Proton Exchange Membrane Fuel Cells 8, Pts 1 and 2 16, 23-34

2188.

[17] Berning, T., Lu, D.M., Djilali, N., 2002. Three-dimensional computational analysis of transport phenomena in a PEM fuel cell. J Power Sources 106, 284-294.

[18] Carcadea, E., Ene, H., Ingham, D.B., Lazar, R., Ma, L., Pourkashanian, M., Stefanescu, I., 2005. Numerical simulation of mass and charge transfer for a PEM fuel cell. Int Commun Heat Mass 32, 1273-1280.

[19] Meng, H., Wang, C.Y., 2005. Model of two-phase flow and flooding dynamics in polymer electrolyte fuel cells. J Electrochem Soc 152, A1733-A1741.

[20] Nguyen, P.T., Berning, T., Djilali, N., 2004. Computational model of a PEM fuel cell with serpentine gas flow channels. J Power Sources 130, 149-157.

[21] Shimpalee, S., Greenway, S., Spuckler, D., Van Zee, J.W., 2004. Predicting water and current distributions in a commercial-size PEMFC. J Power Sources 135, 79-87.

[22] Sivertsen, B.R., Djilali, N., 2005. CFD-based modelling of proton exchange membrane fuel cells. J Power Sources 141, 65-78.

[23] Wang, Y., Wang, C.Y., 2006. A nonisothermal, two-phase model for polymer electrolyte fuel cells. J Electrochem Soc 153, A1193-A1200.

[24] Weng, F.B., Su, A., Jung, G.B., Chiu, Y.C., Chan, S.H., 2005. Numerical prediction of concentration and current distributions in PEMFC. J Power Sources 145, 546-554.

[25] Ko, D., Kang, Y., Yang, J., Jeong, J., Choi, G., Kim, D., 2010. Polarization characteristics and property distributions of a proton exchange membrane fuel cell under cathode starvation conditions. Int J Energ Res 34, 865-877.

[26] Korsgaard, A.R., Refshauge, R., Nielsen, M.P., Bang, M., Kaer, S.K., 2006. Experimental characterization and modeling of commercial polybenzimidazole-based MEA performance. J Power Sources 162, 239-245.

[27] Scott, K., Mamlouk, M., 2009. A cell voltage equation for an intermediate temperature proton exchange membrane fuel cell. Int J Hydrogen Energy 34, 9195-9202.

[28] Cheddie, D., Munroe, N., 2006. Mathematical model of a PEMFC using a PBI membrane. Energ Convers Manage 47, 1490-1504.

[29] Cheddie, D., Munroe, N., 2006. Parametric model of an intermediate temperature PEMFC. J Power Sources 156, 414-423.

[30] Scott, K., Pilditch, S., Mamlouk, M., 2007. Modelling and experimental validation of a high temperature polymer electrolyte fuel cell. J Appl Electrochem 37, 1245-1259.

[31] Hu, J.W., Zhang, H.M., Gang, L., 2008. Diffusion-convection/electrochemical model studies on polybenzimidazole (PBI) fuel cell based on AC impedance technique. Energ Convers Manage 49, 1019-1027.

[32] Hu, J.W., Zhang, H.M., Hu, J., Zhai, Y.F., Yi, B.L., 2006. Two dimensional modeling study of PBI/H3PO4 high temperature PEMFCs based on electrochemical methods. J Power Sources 160, 1026-1034.

[33] Shamardina, O., Chertovich, A., Kulikovsky, A.A., Khokhlov, A.R., 2010. A simple model of a high temperature PEM fuel cell. Int J Hydrogen Energy 35, 9954-9962.

[34] Cheddie, D.F., Munroe, N.D.H., 2007. A two-phase model of an intermediate temperature PEM fuel cell. Int J Hydrogen Energy 32, 832-841.

[35] Cheddie, D.F., Munroe, N.D.H., 2006. Three dimensional modeling of high temperature PEM fuel cells. J Power Sources 160, 215-223.

[36] Peng, J., Lee, S.J., 2006. Numerical simulation of proton exchange membrane fuel cells at high operating temperature. J Power Sources 162, 1182-1191.

[37] Ubong, E.U., Shi, Z., Wang, X., 2009. Three-Dimensional Modeling and Experimental Study of a High Temperature PBI-Based PEM Fuel Cell. J Electrochem Soc 156, B1276-B1282.

[38] Hou, Y.P., Zhuang, M.X., Wan, G., 2007. A transient semi-empirical voltage model of a fuel cell stack. Int J Hydrogen Energy 32, 857-862.

[39] Kim, H.I., Cho, C.Y., Nam, J.H., Shin, D., Chung, T.Y., 2010. A simple dynamic model for polymer electrolyte membrane fuel cell (PEMFC) power modules: Parameter estimation and model prediction. Int J Hydrogen Energy 35, 3656-3663.

[40] Meng, H., 2007. Numerical investigation of transient responses of a PEM fuel cell using a two-phase non-isothermal mixed-domain model. J Power Sources 171, 738-746.

[41] Shimpalee, S., Lee, W.K., Van Zee, J.W., Naseri-Neshat, H., 2006. Predicting the transient response of a serpentine flow-field PEMFC I. Excess to normal fuel and air. J Power Sources 156, 355-368.

[42] Wang, Y., Wang, C.Y., 2006. Dynamics of polymer electrolyte fuel cells undergoing load changes. Electrochim Acta 51, 3924-3933.

[43] Yerramalla, S., Davari, A., Feliachi, A., Biswas, T., 2003. Modeling and simulation of the dynamic behavior of a polymer electrolyte membrane fuel cell. J Power Sources 124, 104-113.

[44] Bhatia, K.K., Wang, C.Y., 2004. Transient carbon monoxide poisoning of a polymer electrolyte fuel cell operating on diluted hydrogen feed. Electrochim Acta 49, 2333-2341.

[45] Hu, G.L., Fan, J.R., 2007. Transient computation fluid dynamics modeling of a single proton exchange membrane fuel cell with serpentine channel. J Power Sources 165, 171-184.

[46] Mora, J.A., Husar, A.P., Serra, M., Riera, J., 2009. Numerical model for polymer electrolyte membrane fuel cells with experimental application and validation. ASIA-PACIFIC JOURNAL OF CHEMICAL ENGINEERING 4, 55-67.

[47] Um, S., Wang, C.Y., Chen, K.S., 2000. Computational fluid dynamics modeling of proton exchange membrane fuel cells. J Electrochem Soc 147, 4485-4493.

[48] Khajeh-Hosseini-Dalasm, N., Fushinobu, K., Okazaki, K., 2010. Three-dimensional transient two-phase study of the cathode side of a PEM fuel cell. Int J Hydrogen Energy 35, 4234-4246.

[49] Zhang, Z., Jia, L., Wang, X., Ba, L., 2010. Effects of inlet humidification on PEM fuel cell dynamic behaviors

Int J Energ Res DOI: 10.1002/er.1692.

[50] Andreasen, S.J., Kaer, S.K., 2009. Dynamic Model of the High Temperature Proton Exchange Membrane Fuel Cell Stack Temperature. J Fuel Cell Sci Tech 6, -.

[51] Wang, C.P., Chu, H.S., Yan, Y.Y., Hsueh, K.L., 2007. Transient evolution of carbon monoxide poisoning effect of PBI membrane fuel cells. J Power Sources 170, 235-241.

[52] Wang, Y., Wang, C.Y., 2005. Transient analysis of polymer electrolyte fuel cells. Electrochim Acta 50, 1307-1315.

[53] Wu, H., Li, X.G., Berg, P., 2007. Numerical analysis of dynamic processes in fully humidified PEM fuel cells. Int J Hydrogen Energy 32, 2022-2031.

[54] Asl, S.M.S., Rowshanzamir, S., Eikani, M.H., 2010. Modelling and simulation of the steady-state and dynamic behaviour of a PEM fuel cell. Energy 35, 1633-1646.

[55] Ciancetta, F., Fiorucci, E., Ometto, A., Rotondale, N., 2009. The Modeling of a PEM Fuel Cell - Supercapacitor - Battery System in Dynamic Conditions. 2009 Ieee Bucharest Powertech, Vols 1-5 3127-3131.

[56] Correa, J.M., Farret, F.A., Canha, L.N., Simoes, M.G., 2004. An electrochemical-based fuel-cell model suitable for electrical engineering automation approach. Ieee T Ind Electron 51, 1103-1112.

[57] Pathapati, P.R., Xue, X., Tang, J., 2004. A new dynamic model for predicting transient phenomena in a PEM fuel cell system. Renew Energ 30, 1-22.

[58] Peng, J., Shin, J.Y., Song, T.W., 2008. Transient response of high temperature PEM fuel cell. J Power Sources 179, 220-231.

[59] Zenith, F., Seland, F., Kongstein, O.E., Borresen, B., Tunold, R., Skogestad, S., 2006. Control-oriented modelling and experimental study of the transient response of a high-temperature polymer fuel cell. J Power Sources 162, 215-227.

[60] Jaouen, F., Lindbergh, G., 2003. Transient techniques for investigating mass-transport limitations in gas diffusion electrodes - I. Modeling the PEFC cathode. J Electrochem Soc 150, A1699-A1710.

[61] Jespersen, J.L., Schaltz, E., Kaer, S.K., 2009. Electrochemical characterization of a polybenzimidazole-based high temperature proton exchange membrane unit cell. J Power Sources 191, 289-296.

[62] Wagner, N., Kaz, T., Friedrich, K.A., 2008. Investigation of electrode composition of polymer fuel cells by electrochemical impedance spectroscopy. Electrochim Acta 53, 7475-7482.

[63] Gomadam, P.M., Weidner, J.W., 2005. Analysis of electrochemical impedance spectroscopy in proton exchange membrane fuel cells. Int J Energ Res 29, 1133-1151.

[64] Springer, T.E., Zawodzinski, T.A., Wilson, M.S., Gottesfeld, S., 1996. Characterization of polymer electrolyte fuel cells using AC impedance spectroscopy. J Electrochem Soc 143, 587-599.

[65] Guo, Q.Z., White, R.E., 2004. A steady-state impedance model for a PEMFC cathode. J Electrochem Soc 151, E133-E149.

[66] Poling, B.E., Prausnitz, J.M., O'Connell, J.P., 2001. The Properties of Gases and Liquids. Fifth Edition. McGraw-Hill, New York

[67] O'Hayre, R., Cha, S.-W., Colella, W., Prinz, F.B., 2006. Fuel Cell Fundamentals. John Wiley & Sons, Inc., New York.

[68] Cooper, K.R., Ramani, V., Fenton, J.M., Kunz, H.R., 2005. Experimental Methods and Data Analysis for Polymer Electrolyte Fuel Cells. Scribner Associates, Southern Pines.

[69] Wu, J.F., Yuan, X.Z., Wang, H.J., Blanco, M., Martin, J.J., Zhang, J.J., 2008. Diagnostic tools in PEM fuel cell research: Part I - Electrochemical techniques. Int J Hydrogen Energy 33, 1735-1746.

[70] Mocoteguy, P., Druart, F., Bultel, Y., Besse, S., Rakotondrainibe, A., 2007. Monodimensional modeling and experimental study of the dynamic behavior of proton exchange membrane fuel cell stack operating in dead-end mode. J Power Sources 167, 349-357.

[71] Petzold, L.R., Hindmarsh, A.C., 1997. LSODA. Computing and Mathematics Research Division, Lawrence Livermore National Laboratory

[72] Lasia, A., 1999. Electrochemical Impedance Spectroscopy and its Applications, in: Conway, B.E., Bockris, J.O.M., White, R.E. (Eds.), Modern Aspects of Electrochemistry: no. 32. KluwerAcademic / Plenum Publishers, New York.

[73] Liu, Z.Y., Wainright, J.S., Litt, M.H., Savinell, R.F., 2006. Study of the oxygen reduction reaction (ORR) at Pt interfaced with phosphoric acid doped

polybenzimidazole at elevated temperature and low relative humidity. Electrochim Acta 51, 3914-3923.

[74] Wagner, N., Friedrich, K.A., 2009. Dynamic Operational Conditions, in: Garche, J., Dyer, C., Moseley, P., Ogumi, Z., Rand, D., Scrosati, B. (Eds.), Encyclopedia of Electrochemical Power Sources. Elsevier, Amsterdam, pp. 912-930.

[75] Yuan, X.Z., Wang, H.J., Sun, J.C., Zhang, J.J., 2007. AC impedance technique in PEM fuel cell diagnosis - A review. Int J Hydrogen Energy 32, 4365-4380.

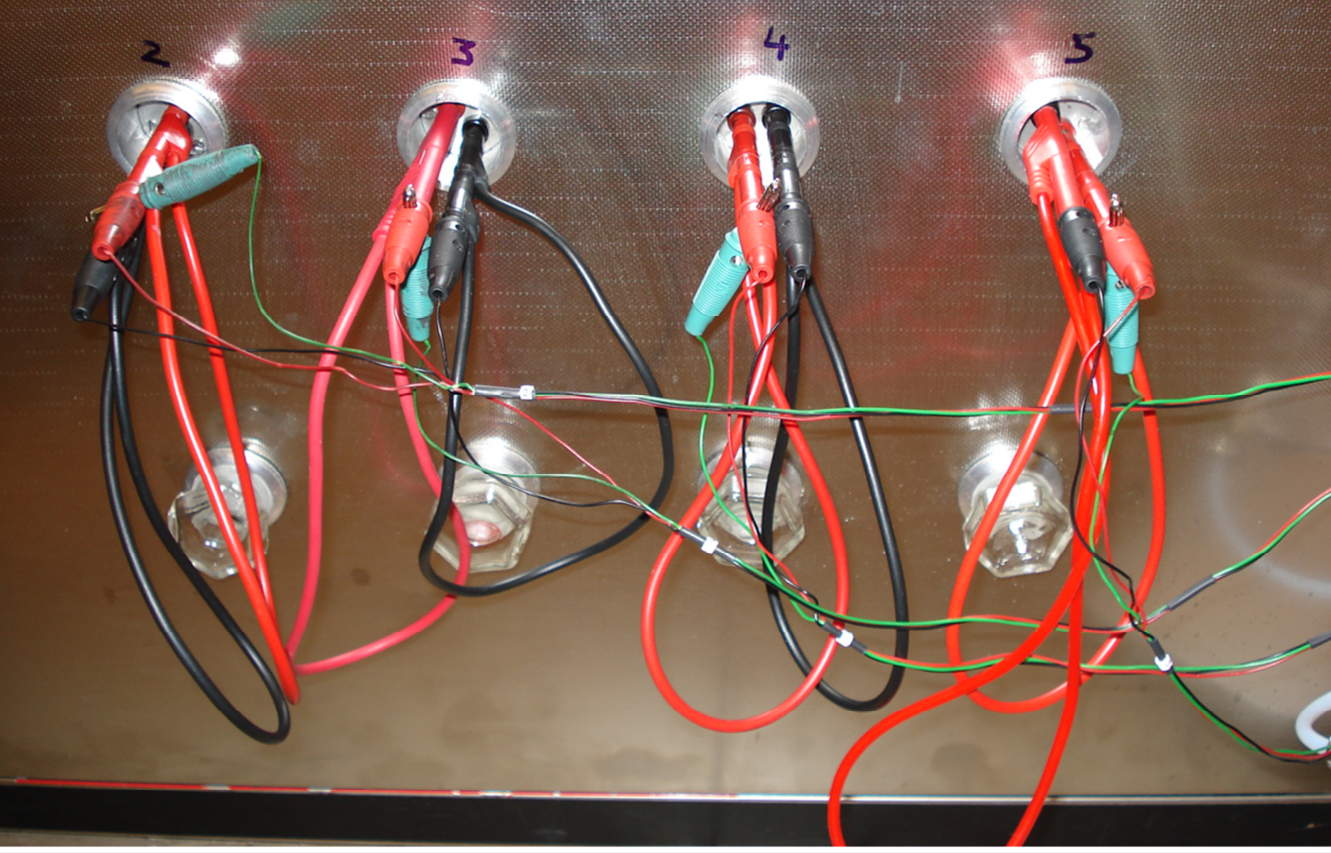


# Part III HT-PEMFC Materials

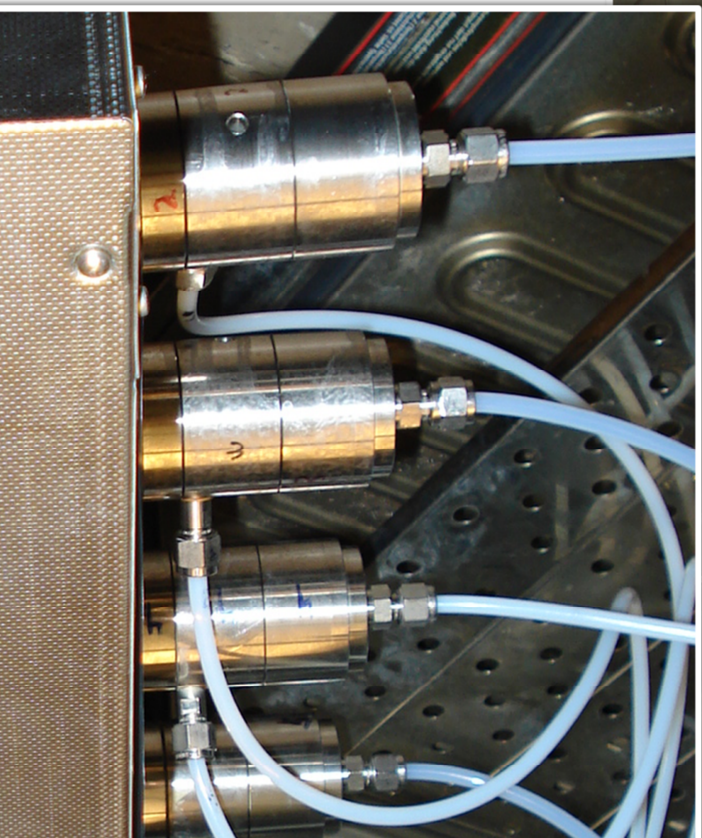

Top and bottom left: GKSS conductivity measurement set-up

Bottom right: PEM casting

# Chapter 5 Single-wall nanohorns as electrocatalyst support for HT-PEMFC[4]

## 5.1 Abstract

This work compares the performance of electrodes prepared with electrocatalysts based on platinum supported in single-wall carbon nanohorns (Pt-SWNHs) and supported in carbon black (Pt-carbon black) for high temperature polymer electrolyte fuel cells (HT-PEMFC). Membrane electrode assemblies (MEAs) assembled with phosphoric acid doped polybenzimidazole (PBI/$H_3PO_4$) membrane were characterized by I-V curves, electrochemical impedance spectroscopy (EIS) and cyclic voltammetry (CV), at 160 °C.

A similar power density peak was obtained for both MEAs, at 160 °C and 1.0 % relative humidity. The electrochemical characterization showed a higher ohmic resistance for the Pt-SWNH compared to carbon black-based MEA, due to the higher hydrophobic character of the SWNH carbon support. Furthermore, the Pt- SWNH anode presented lower charge transfer resistance than the correspondent carbon black but similar cathode charge transfer resistance.

[4] The content of this chapter is adapted from: Boaventura, M., Brandão, L., Mendes, A., 2011. Single-Wall Nanohorns as Electrocatalyst Support for High Temperature PEM Fuel Cells. J Electrochem Soc, in press: doi 10.1149/1141.3551495.

## 5.2 Introduction

Fuel cells hold a promise of a very efficient and clean technology [1]; recent advances have succeeded to reduce the catalyst loading for the same power density, leading fuel cells closer to commercialization [2]. The state of the art of polymer electrolyte fuel cells (PEMFC) is based on perfluorosulfonic acid polymer membranes, such as Nafion®. This polymer exhibits good chemical and mechanical stability; however, proton conductivity is dependent on the hydration level making the maximum operating temperature to be 90 °C. A higher operating temperature is desired for fuel cell operation due to the improvement of electrochemical kinetics, simplified water management, cooling system and heat recovery and an increased CO tolerance.

In order to increase the active electrochemical surface and minimize the use of platinum, fuel cell catalysts are usually supported in nano structured carbon materials with a high surface area. Such supports should have suitable porosity to allow mass transport of reactants to the catalyst and high electrical conductivity to permit the transfer of electrons to the collecting surface of the electrode [3-4]. The most widely used carbon support for fuel cells electrocatalysts is carbon black, such as Vulcan XC-72 from Cabot. Carbon black presents a high electrical conductivity and surface area and is available at a low cost. This material, on the other hand, has a high amount of micropores, which can obstruct the access of the reactants, and low stability at temperatures higher than 100 °C [3].

Non-conventional nanocarbon materials, such as graphene [4-6], carbon nanofibers [7-8], carbon nanotubes [9-12], carbon nanospheres [13] and carbon nanohorns [14-19], are under study due to their tailored morphology and excellent electrical and mechanical properties. The carbon supports used in low temperature fuel cells have been recently revised by Antolini [3].

Single-wall carbon nanohorns (SWNHs) have a horn shaped sheath of single-wall graphitic sheets [19] and usually have an individual diameter of 2-4 nm and a length of 40-50 nm [15]. SWNHs auto assemble and form different spherical aggregates called dahlia, bud and seed types, depending on the experimental conditions, with an

approximate diameter of 100 nm [14-15; 18]. SWNHs are usually produced by $CO_2$ laser ablation of carbon [15; 18-19] and arc discharge between two graphite electrodes [16-17].

SWNHs have been studied as electrocatalyst support of platinum showing a higher surface chemical activity toward platinum deposition when compared to carbon black and multi-walled carbon nanotubes [16]. Moreover, the power density peak of low temperature fuel cells based on platinum supported on SWNH is higher for PEMFC and direct methanol fuel cells (DMFC) when compared to the traditional carbon black support. For instance, Yoshitake *et al.* [19] obtained higher current densities for a PEMFC operating with SWNH electrocatalyst support compared to carbon black support, at room temperature and 1 bar. Our group reported an increase of 60 % in the power density peak at 50 °C for both PEMFC and DMFC when carbon black was replaced by SWNH as electrocatalyst support [20-22]. The increase of PEMFC performance resulted from the decrease on the cathode charge transfer resistance [22]. Oxygen treated SWNH carbon support was also studied for low temperature PEMFCs by Brandão *et al.* [20]. These authors reported an increase of 60 % in the power density peak when the electrocatalyst support was changed from carbon black to SWNH that they related to a decrease in charge transfer resistance in the anode and cathode.

The most studied polymer electrolyte for high temperature PEMFC is a polybenzimidazole membrane doped with phosphoric acid (PBI / $H_3PO_4$). The preparation of electrodes for this system and its effect on the performance of high temperature PEMFC has been studied regarding catalyst ink preparation [23], platinum load and content in the carbon support [24-25], electrode porosity [26], phosphoric acid and PBI loads [25; 27-29] and phosphoric acid impregnation in the electrocatalyst [30-31]. The importance of the electrocatalyst carbon support in fuel cell systems based on phosphoric acid doped PBI has also been demonstrated. Mamlouk and Scott [28] compared two commercial carbon supports with similar electrochemical surface area and average particles size but featuring different morphologies and hydrophobic properties. The I-V curves obtained suggests that differences in the electrochemical surface area lead to different oxygen reduction

kinetics and differences in hydrophobicity of electrocatalyts supports influence their interaction with the phosphoric acid and the ohmic losses. Additionally, Nakashima and co-workers [32-33] designed electrocatalysts where platinum nanoparticles were deposited on PBI-wrapped multiwalled carbon nanotubes (MWNTs) or pyridine-containing PBI (PyPBI)-wrapped MWCNTs. PBI works as platinum adsorbent due to the coordination of the platinum ions with the PBI molecules. The Pt-PBI-wrapped MWNTs show a higher utilization efficiency compared to plain Pt-MWNT and Pt-carbon black and the (PyPBI)-wrapped MWCNTs show a high electrochemical surface area due to a nanostructured triple-phase boundary.

In this work, the performance of high temperature PEMFC assembled with Pt-SWNH and Pt-carbon black-based electrodes is compared for the first time, using a PBI / $H_3PO_4$ membrane. Characterization techniques included I-V and power density curves, electrochemical impedance spectroscopy and cyclic voltammetry (CV). The chemical composition of PBI membrane was also analyzed and catalyst layer after the electrochemical tests by energy dispersive X-ray spectroscopy (EDS).

## 5.3 Experimental

### 5.3.1 Supported electrocatalysts

Synthesis of SWNH was performed by using AC arc discharge in air, according to previous works [17; 21]. Ethylene glycol (EG) was used as a reducing agent in order to anchor Pt nanoparticles on the carbon black (Vulcan XC-72R, Cabot) and SWNH supports [21].

The detailed electrocatalyst deposition and characterization of the different materials are presented elsewhere [22]. The main SWNH aggregate type is the bud like structure with a very few graphitic giant balls. The SWNH analysis indicated that it was composed of 84.5 wt. % SWNH aggregates, 3 wt. % amorphous carbon, and 12.5 wt. % graphitic carbon. The platinum particle diameter was approximately 3 nm for both carbon supports and uniformly distributed.

The final platinum content on carbon black and SWNH was 18 wt. % and 12 wt. %, respectively.

### 5.3.2 Electrodes preparation

A homogeneous suspension of the catalyst powder was prepared with isopropyl alcohol. Catalytic active layers based on different carbon supports were spray dried on a commercial Sigracet gas diffusion layer (GDL) microporous surface (SGL Carbon, ref.: GDL 24 BC) followed by drying at room temperature overnight.

The catalyst load was obtained based on the difference between the weights of microporous GDL before and after the spray drying. Both the electrodes had an approximately equal amount of carbon support and thickness. The platinum load was 0.25 $mg_{Pt} \cdot cm^{-2}$ and 0.43 $mg_{Pt} \cdot cm^{-2}$, respectively, for the SWNH and for the carbon black electrodes.

### 5.3.3 Membrane electrode assembly (MEA) preparation

The high temperature PEMFC MEA was assembled using a PBI phosphoric acid doped membrane, 100 μm thick and doped with 10 mol of phosphoric acid per mol of PBI, sandwiched between two electrodes of either SWNHs or carbon black. The assembled MEA, with an active area of 4.4 $cm^2$, was placed in an ElectroChem single cell by applying a torque of 3.5 N·m on each of the eight screws.

The Electrochem single cell was placed in an in-house made fuel cell test station described in Chapter 2. The system was controlled using an application developed in LabView (National Instruments) and electrochemical tests were performed using a Zahner IM6e electrochemical workstation coupled with a potentiostat PP-241.

### 5.3.4 HT-PEMFC performance tests and MEA characterization

Both MEAs were activated at constant 0.12 $A \cdot mg_{Pt}^{-1} \cdot cm^2$, at 160 °C and 1 bar; hydrogen was fed at 1.7 $cm^3 \cdot s^{-1}$ and air at 5.0 $cm^3 \cdot s^{-1}$, at 1.0 % relative humidity (RH) during approximately 50 h. I-V curves were performed at 1.0 % RH for the Pt-carbon black-based MEA and 1.0 %, 2.5 %, 4.0 % and 5.0 % RH for the Pt-SWNH-based MEAs. Each polarization curve was obtained starting at OCV and decreasing the potential until 200 or 300 mV, with with a step of 50 mV. An estimation of the electrochemical surface area (ESA) was obtained at 160 °C and 1 bar from cyclic voltammetry experiments; the fuel cell cathode was purged with nitrogen and used as working electrode while anode was used as reference and counter electrode. Scans were performed at a scan rate of 100 $mV \cdot s^{-1}$ between 0 mV and 800 mV. Electrochemical impedance spectroscopy was obtained in the frequency range from 100 kHz to 100 mHz with a perturbation amplitude of 5 mV.

After electrochemical tests, the membrane and catalyst layer were characterized by field emission scanning electron microscopy (FE-SEM) equipped with an energy dispersive X-ray spectroscopy (EDS) detector.

## 5.4 Results and Discussion

### 5.4.1 HT-PEMFC performance

The electrodes prepared with electrocatalysts based on platinum supported in single-wall carbon nanohorns (Pt-SWNHs) and supported in carbon black (Pt-carbon black) were assembled on a high temperature MEA using a phosphoric acid doped PBI membrane. Figure 5.1 shows the I-V curves obtained for Pt-carbon black and Pt-SWNH-based MEAs at 160 °C. Current densities were based on the catalyst load for both types of electrodes. Pt-carbon black MEA exhibits higher voltages at lower current densities while Pt-SWNH MEA presented a better performance at higher current densities. Furthermore, the peak power density for these two MEAs is

similar, ca. 0.45 $W \cdot mg_{Pt}^{-1} \cdot cm^2$. This contrasts with the previous results for low temperature PEMFC studies from our group, performed at 50 °C, where an increase of 60 % in the peak power density was observed when carbon black was replaced by SWNH as electrocatalyst support [20-22]. In order to understand this different behavior from our previous studies, electrochemical impedance spectroscopy was used (see below).

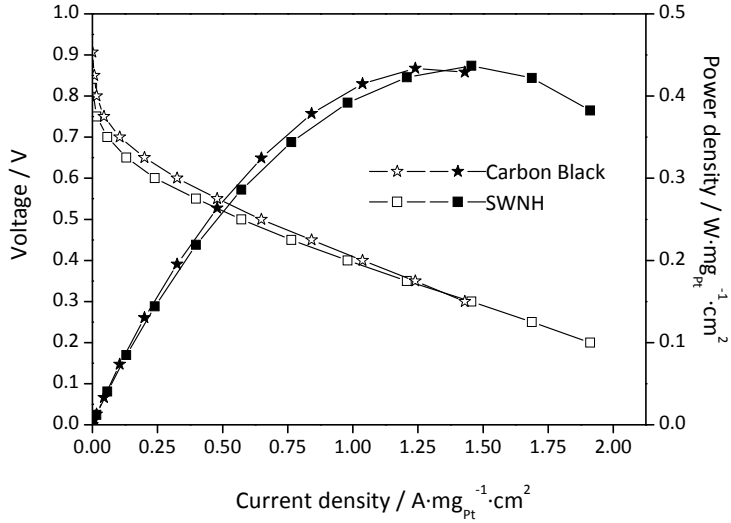


**Figure 5.1** I-V and power density curves for Pt-carbon black (☆) and Pt-SWNH (□) based electrodes with phosphoric acid doped PBI membrane, at 160 °C, 1 bar and 1.0 % RH.

### 5.4.2 Electrochemical impedance spectroscopy (EIS)

To understand the influence of the electrocatalyst carbon support on the high temperature PEMFC performance, EIS measurements were performed for MEAs with both types of carbon supports. Figure 5.2 presents the impedance spectra for the Pt-carbon black and Pt-SWNH MEAs, at two different current densities (normalized by the active area), 11 $mA \cdot cm^{-2}$ and 68 $mA \cdot cm^{-2}$. Because the catalyst load was different for the Pt-carbon black and the Pt-SWNH electrodes (see Experimental section), the

impedance spectra were compared at two current densities normalized by the catalyst load: 0.1 $A \cdot mg_{Pt}^{-1} \cdot cm^2$ and 0.7 $A \cdot mg_{Pt}^{-1} \cdot cm^2$ - Figure 5.3.

Figure 5.2 (a) and Figure 5.3 (a) show the Nyquist spectra for both MEAs for the same current density normalized by the area and catalyst load, respectively; it presents a large semi-circle at low frequencies that can be attributed to the cathode and a smaller semi-circle, at high frequencies, related to the anode. The pure resistive behaviour that is associated to the ohmic resistance of the fuel cell is obtained when the Nyquist plot crosses the real axis.

Figure 5.2 (b) and Figure 5.3 (b) show the Bode spectra for the same current density normalized by the area and catalyst load, respectively. The frequency range between 0.1 Hz and 100 Hz is dominated by the charge transfer resistance of the cathode and the frequency range between 100 Hz and 10 kHz is dominated by the charge transfer resistance of the anode. At the highest frequency range, the impedance value reaches a minimum value (the angle phase approaches to zero) and is associated to the ohmic resistance of the fuel cell.

The cathode semi-circle of Nyquist spectra (Figure 5.2 (a) and Figure 5.3 (a)) show a strong dependency on the current density load for both carbon supports; for higher current densities a smaller loop is obtained. This dependency can often be described by the Tafel equation [34]. Besides, Nyquist and Bode spectra (Figure 5.2 and Figure 5.3) indicate that ohmic resistance of the fuel cell is different for the SWNH and for the carbon black-based MEAs, despite the same operation time and humidification (1 % RH). This suggests that the membrane and electrodes of the Pt-SWNH-based MEA were probably less hydrated than the Pt-carbon black-based MEA. Regardless the higher ohmic resistance of the SWNH-based MEA, a similar power peak was obtained for the two studied MEAs (Figure 5.1). This indicates different hydrophobicity and electrochemical activity characteristics of the electrodes.

In order to evaluate the performance of the electrodes for both MEAs, all the spectra were simulated using the equivalent electrical circuit shown in Figure 5.4.

A typical fuel cell electrical equivalent is divided into cathode and anode parts and ohmic losses, connected in series. Each electrode is represented by a resistance in parallel with a capacitance (RC element) linked with a pore resistance [35-36].

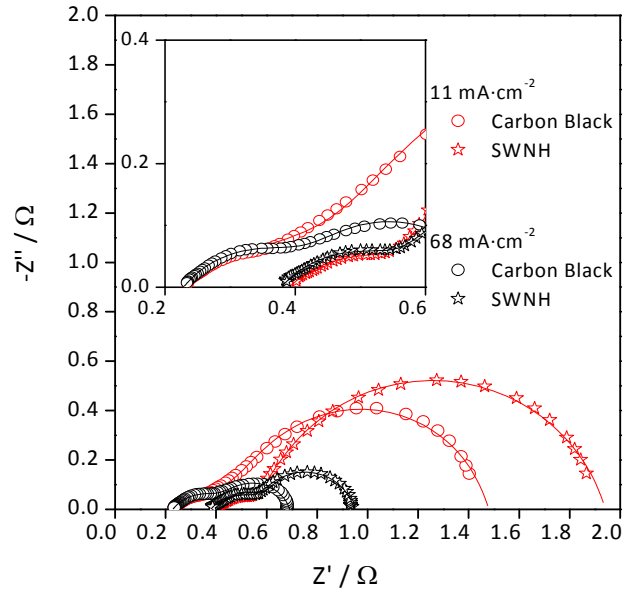


(a)

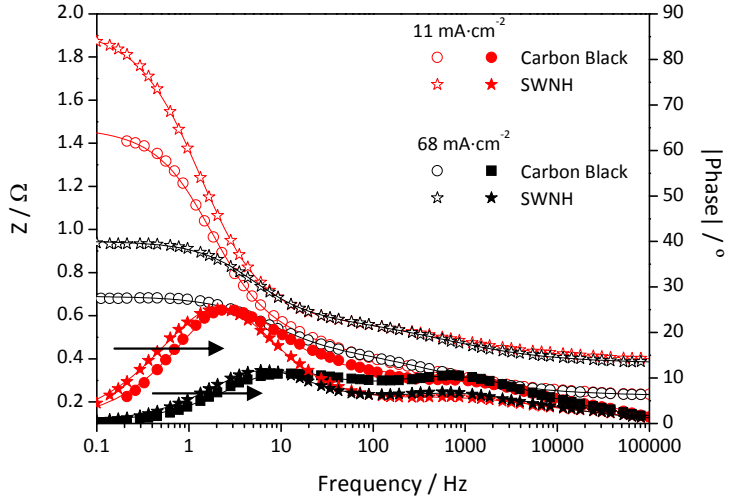


(b)

**Figure 5.2** Nyquist (a) and Bode (b) plots for Pt-carbon black (○) and Pt-SWNH (✯) MEAs, at 11 mA·cm$^{-2}$ (red points) and 68 mA·cm$^{-2}$ (black points), 160 °C, 1 bar and 1.0 % RH. Lines represent the fitting electrical equivalent model.

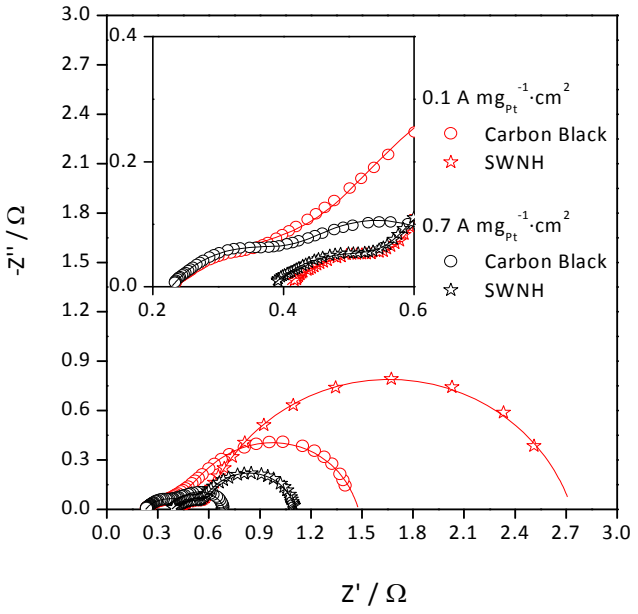


(a)

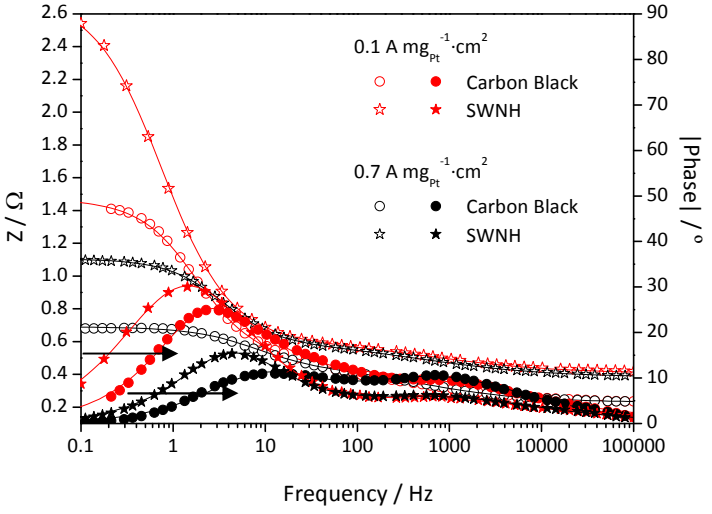


(b)

**Figure 5.3** Nyquist (a) and Bode (b) plots for Pt-carbon black (○) and Pt-SWNH (✯) MEAs, at 0.1 A·mg$_{Pt}^{-1}$·cm$^2$ (red points) and at 0.7 A·mg$_{Pt}^{-1}$·cm$^2$ (black points), 160 °C, 1 bar and 1.0 % RH. Lines represent the fitting electrical equivalent model.

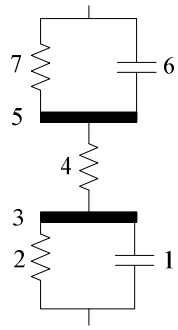


**Figure 5.4** Equivalent electrical circuit of a fuel cell. Elements 2 and 7 represent the charge transfer resistance ($R_{ct}$) of cathode and anode reactions; elements 1 and 6 represent the double layer capacitance ($C_{dl}$) of cathode and anode; elements 3 and 5 represent the resistance of pores filled with electrolyte ($R_p$) at the anode and cathode and element 4 represents the ohmic resistance of the fuel cell.

Because the electrodes have a porous structure, the ideal capacitance is replaced by a constant phase element (CPE) in the simulation [37]. The resistances at the RC elements (2 and 7 in Figure 5.4) represent the charge transfer resistance ($R_{ct}$) of anode and cathode whereas the capacitances 1 and 6 represent the double layer capacitance ($C_{dl}$) of anode and cathode. The elements 3 and 5 represent the charge resistance of pores filled with electrolyte ($R_p$) at the electrodes. The ohmic resistance represented by element 4 includes the resistances of the membrane, end plates, flow fields and contact interfaces. The mass transfer resistances, which arise from the diffusion of reactants to catalyst surface, were considered to be included in charge transfer resistances [38-39]. The SIM module from Thales software was used (Zahner-Elektrik GmbH) to fit this model to the experimental data. The fit (full lines) and experimental data are shown in Figure 5.2 and Figure 5.3. The fitting parameters can be seen in Table 5.1: ohmic resistance, anode ($R_{ct}^{a}$) and cathode ($R_{ct}^{c}$) charge transfer resistances, anode ($R_{p}^{a}$) and cathode ($R_{p}^{c}$) pore resistances and the constant phase elements, double layer capacitance of anode ($C_{dl}^{a}$) and cathode ($C_{dl}^{c}$) and exponent parameter of anode ($\alpha^{a}$) and cathode ($\alpha^{c}$).

**Table 5.1** EIS parameters obtained from the equivalent electrical circuit (Figure 5.4) for Pt-carbon black and Pt-SWNH based MEAs.

| | Pt-SWNH MEA | | | | Pt-carbon black MEA | |
|---|---|---|---|---|---|---|
| | Current density/ $mA \cdot cm^{-2}$ | | Current density/ $A \cdot mg_{Pt}^{-1} \cdot cm^{2}$ | | 11 $mA \cdot cm^{-2}$ | 68 $mA \cdot cm^{-2}$ |
| | 11 | 68 | 0.1 | 0.7 | 0.1 $A \cdot mg_{Pt}^{-1} \cdot cm^{2}$ | 0.7 $A \cdot mg_{Pt}^{-1} \cdot cm^{2}$ |
| $R_{ct}^{a}$ / mΩ | 197.0 | 207.4 | 190.8 | 205.4 | 352.7 | 210.2 |
| $R_{ct}^{a}$ / $m\Omega \cdot mg_{Pt} \cdot cm^{-2}$ | 49.30 | 51.90 | 47.70 | 51.40 | 151.7 | 90.40 |
| $C_{dl}^{a}$ / mF | 1.000 | 1.000 | 1.000 | 1.100 | 1.400 | 1.200 |
| $\alpha^{a}$ | 0.5300 | 0.5800 | 0.5300 | 0.5300 | 0.4300 | 0.6100 |
| $R_{p}^{a}$ / mΩ | 10.20 | 10.50 | 10.50 | 10.50 | 6.200 | 6.600 |
| Ohmic Resistance / mΩ | 388.2 | 375.8 | 400.3 | 378.3 | 220.2 | 226.6 |
| $R_{ct}^{c}$ / mΩ | 1351 | 359.5 | 2140 | 520.4 | 903.0 | 251.1 |
| $R_{ct}^{c}$ /$m\Omega \cdot mg_{Pt} \cdot cm^{-2}$ | 337.8 | 89.90 | 535.0 | 130.1 | 388.3 | 108.0 |
| $C_{dl}^{c}$ / mF | 36.60 | 44.10 | 31.50 | 48.00 | 59.00 | 36.50 |
| $\alpha^{c}$ | 0.8300 | 0.8500 | 0.8100 | 0.8700 | 0.8800 | 0.8200 |
| $R_{p}^{c}$ / mΩ | 3.800 | 3.900 | 3.200 | 3.900 | 15.10 | 4.200 |

The ohmic resistance, at 68 $mA \cdot cm^{-2}$, is 375.8 mΩ and 226.6 mΩ for the Pt-SWNH and the Pt-carbon black based MEAs, respectively (Table 5.1). The increase of 1.6 times is related to a more hydrophobic character of the SWNH support compared to the carbon black that affects the humidification of the PBI membrane (and therefore the proton conductivity) of the Pt-SWNH-based MEA. Both carbon supports were compared regarding water adsorption (not shown). After stabilization on a controlled environment concerning temperature and relative humidity (50 °C and 50 % RH) carbon black support showed to adsorb ca. twice as much of water.

The charge transfer resistance of the Pt-SWNH-based anode is smaller than the correspondent Pt-carbon black-based electrode (Table 5.1). This difference is even more noticeable if the values of the charge transfer resistance of the anode are normalized by the catalyst load: at 68 $mA \cdot cm^{-2}$ the charge transfer resistance for Pt-SWNH anode is 1.7 times lower than the Pt-carbon black anode while at 11 $mA \cdot cm^{-2}$ is 3.1 times lower. Table 5.1 also shows the fitting parameters for the spectra presented in Figure 5.3, at the same current normalized by the catalyst load. The charge transfer resistance at the anode is 1.8 times lower for the electrode with SWNH compared to the Pt-carbon black electrode at 0.7 $A \cdot mg_{Pt}^{-1} \cdot cm^2$ and 3.2 times lower for 0.1 $A \cdot mg_{Pt}^{-1} \cdot cm^2$.

The differences in the carbon support hydrophobicity can affect the interaction with the acid electrolyte [28] and the water from the inlet humidified gases. In this work, no ionomer was added during electrode preparation, however, it is expected that the phosphoric acid from the doped membrane reaches the catalyst surface and establishes the three-phase zone. When water is present in the reactants feed, the migration of the phosphoric acid from the membrane to the electrodes is enhanced; on the other hand, the use of inlet humidified gases can also potentiate phosphoric acid leaching from the electrodes, particularly if no PBI polymer is present to act as a matrix for holding the phosphoric acid to the electrode. It was showed that PBI / $H_3PO_4$ MEAs may suffer phosphoric acid leaching even at unhumidified conditions [40-41].

The results from the EIS experiments suggest that a higher amount of phosphoric acid is retained at the interface between the membrane and the catalyst layer of Pt-SWNH anode when compared to the Pt-carbon black anode. On one hand, the hydrophobicity of the carbon support may avoid the washout of the phosphoric acid by the humidified gases supplied. On the other hand, the more open structure of the SWNH may facilitate the phosphoric acid diffusion from the membrane [22]. Both phenomena probably lead to a higher electrochemical surface area and to a higher charge conductivity at the anode.

Mamlouk and Scott [28] studied the effect of the anode phosphoric acid doping on the fuel cell performance at 150 °C with PBI loading of 0.7 $mg \cdot cm^{-2}$ and at 120 °C

without any polymer electrolyte. In both cases, an increase of the phosphoric doping level greatly enhanced the anode performance, even at very high doping levels. The performance increase was attributed to an increase in the catalyst layer conductivity and more accessible electrochemical surface area.

Concerning the cathode electrodes, higher charge transfer resistances were obtained for Pt-SWNH at 11 $mA \cdot cm^{-2}$ and 68 $mA \cdot cm^{-2}$ - Table 5.1. If one takes into account the catalyst load, the cathode charge transfer resistance is slightly higher for Pt-carbon black electrode. For instance, 89.90 $m\Omega \cdot mg_{Pt} \cdot cm^{-2}$ and 108.0 $m\Omega \cdot mg_{Pt} \cdot cm^{-2}$ were obtained for the Pt-SWNH and Pt-carbon black electrodes, respectively, at 68 $mA \cdot cm^{-2}$ (Table 5.1). The opposite trend is observed at 0.7 $A \cdot mg_{Pt}^{-1} \cdot cm^{2}$ and 0.1 $A \cdot mg_{Pt}^{-1} \cdot cm^{2}$ (it is emphasized that for obtaining these values it was imposed a lower current density to the Pt-SWNH MEA) with cathode charge transfer being 1.4 and 1.2 times higher for Pt-SWNH MEA, respectively.

### 5.4.3 Cyclic voltammetry

The electrochemical surface area (ESA) was estimated for the cathodes with different carbon supports by cyclic voltammetry, before and with 50 h of operation.

After 50 h of operation, the switch of air feed to nitrogen feed in the cathode side lead to a decrease of OCV. Kwon *et al.* [42] showed that as long as OCV decreases, after gas feed switch, the hydrogen desorption plot area decreases. If the cyclic voltammetry is performed just after the gas feed switch, on the other hand, oxygen would still remain at the catalyst layer.

In the present work, nitrogen flowed at the cathode side for at least 6 h in order to guarantee that the cathode side was oxygen-free. Several voltammetric cycles were performed in order to obtain the steady-state (equal response in two of more consecutive voltammetric cycles). As a result, OCV decreased to ca. 0.280 V, at 160 °C, for both MEAs. The objective was to compare the ESA values at similar OCV for both carbon supports, despite the chosen conditions not being the most suitable for obtaining well-defined hydrogen peaks. During cycling voltammetry experiments,

the nitrogen gas was as humidified as air gas during the fuel cell operation, to best reflect the operating conditions.

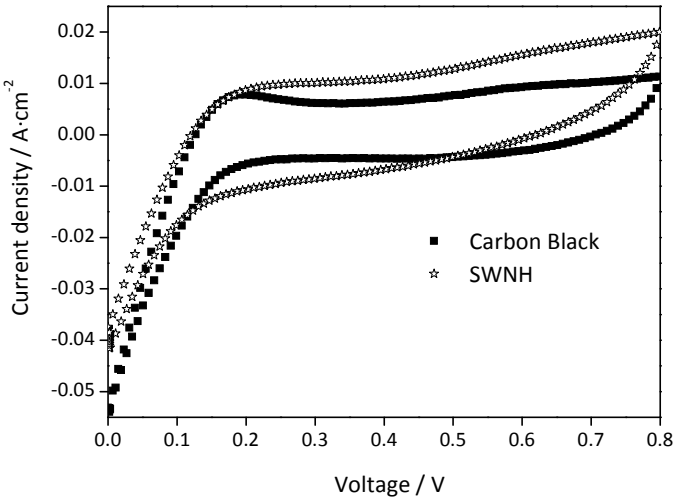


**Figure 5.5** Cyclic voltammetry diagrams for Pt-carbon black (■) and Pt-SWNH (✯) based MEA with phosphoric acid doped membrane, at 160 °C, 1 bar and 1.0 % relative humidity.

Figure 5.5 shows the current density response plotted as a function of the applied potential after 50 h of operation. During these tests, a very poor definition of the hydrogen peaks was observed due to the low catalyst loading. Moreover, unlike low temperature fuel cells, only one pair of adsorption and desorption peaks was observed instead of two pairs. Because of these limitations, a great error exists in obtaining the ESA absolute values for both Pt-carbon black and Pt-SWNH electrodes. Nonetheless, ESA values can still be used for a relative comparison between the two types of electrodes because ESA values were determined under the same conditions.

ESA values was determined by using equation 2.1 [43]. The Thales software was used to obtain the atomic hydrogen charge density. The hydrogen desorption area was obtained between 0.4 V and 0.05 V with double charge current as base line. Relative ESA values for each electrode were obtained by comparing initial ESA values, before activation, with the ones obtained after 50 h of operation for both types of electrodes. Both electrodes exhibited similar ESA values before activation (data not

shown); after 50 h of operation and at 0.12 $A \cdot mg_{Pt}^{-1} \cdot cm^2$ and 160 °C, the ESA values obtained for the cathode electrodes increased 88 % and 236 % respectively for Pt-carbon black and Pt-SWNH. These results indicate that phosphoric acid should leach at the cathode side of the Pt-carbon black MEA during fuel cell performance, reducing the electrolyte pathway from the catalyst to the membrane and consequently the relative ESA. One can then assume that less phosphoric acid was leached with the Pt-SWNH catalyst layer. The presence of phosphoric acid in the electrodes improves the ionic charge transport and increases the ESA but when in excess it can hinder the reactants to reach the platinum active sites due to the reduced oxygen solubility in the phosphoric acid. This may justify why the charge transport resistance of Pt-SWNH cathode electrode was only slightly lower than the Pt- carbon black one -Table 5.1.

It has been reported that an excessive amount of phosphoric acid may originate kinetic limitations of the oxygen reduction due to co-adsorption of phosphate [27-28; 41]. Adding PBI to the electrode structure could mitigate these effects by increasing the solubility of oxygen and the kinetics of oxygen reduction and decreasing the adsorption of phosphate at catalyst sites [27; 41].

Mamlouk and Scott [28] studied the effect of cathode phosphoric acid amount on the fuel cell performance, at 150 °C and PBI loading of 0.55 $mg \cdot cm^{-2}$. Using oxygen as oxidant, the increase of acid doping from 0.0 to 2.5 mol of phosphoric acid per repeat unit of PBI shifted the current density to higher voltage values without changing slope of the I-V curve, suggesting no changes at of the charge transfer coefficient. A further increase to 11 mol of phosphoric acid per repeat unit of PBI, led to lower performance due a decreasing of the charge transfer coefficient.

### 5.4.4 Influence of relative humidity

Because of the higher ohmic resistance in the Pt-SWNH MEA, it was studied the impact of increasing the humidification level of the gases supplied to the fuel cell on the ohmic resistance, electrodes resistances and the electrochemical surface area.

Figure 5.6 shows the I-V and power density curves obtained for Pt-SWNH-based electrode with phosphoric acid doped membrane, at 160 °C, with an increasing RH at both anode and cathode from 1.0 % to 5.0 %. There was a significant improvement of the voltage values when the RH was increased, especially after 0.2 $A \cdot mg_{Pt}^{-1} \cdot cm^2$, indicating that the membrane was more efficiently hydrated.

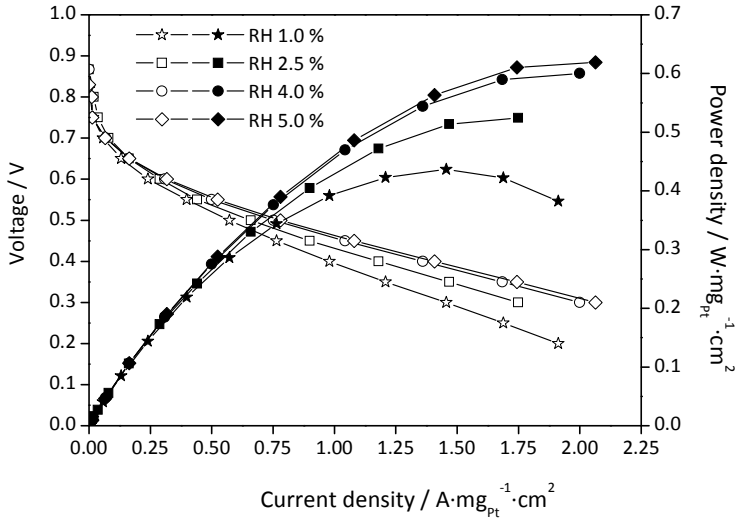


**Figure 5.6** I-V and power curves obtained for Pt-SWNH-based electrode with phosphoric acid doped PBI membrane, at 160 °C, 1 bar and RH between 1.0 % and 5.0 %.

Figure 5.7 presents the impedance spectra for Pt-SWNH-based MEA for the different RH tested (open and full symbols), at 68 $mA \cdot cm^{-2}$, and Table 5.2 shows the impedance spectroscopy parameters obtained by fitting the electric analog of Figure 5.4 to the experimental data. The fitting model is represented by the solid lines on Figure 5.7.

The ohmic resistance decreases with RH increase; this is in accordance with other studies, where the effect of increasing water content in phosphoric acid doped PBI membrane increases the conductivity [44-47]. Only at 4.0 % RH the ohmic resistance reaches a value - 214.9 mΩ, Table 5.2– lower than the one obtained for Pt-carbon black MEA at 1.0 % relative humidity -226.6 mΩ, Table 5.1.

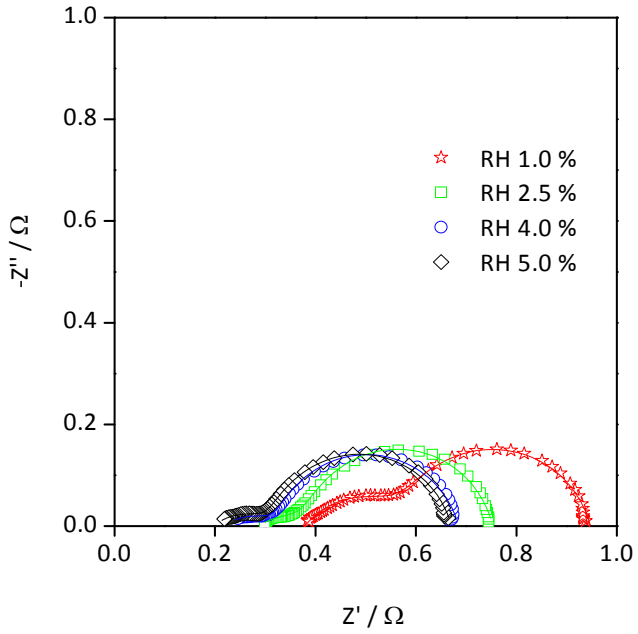


(a)

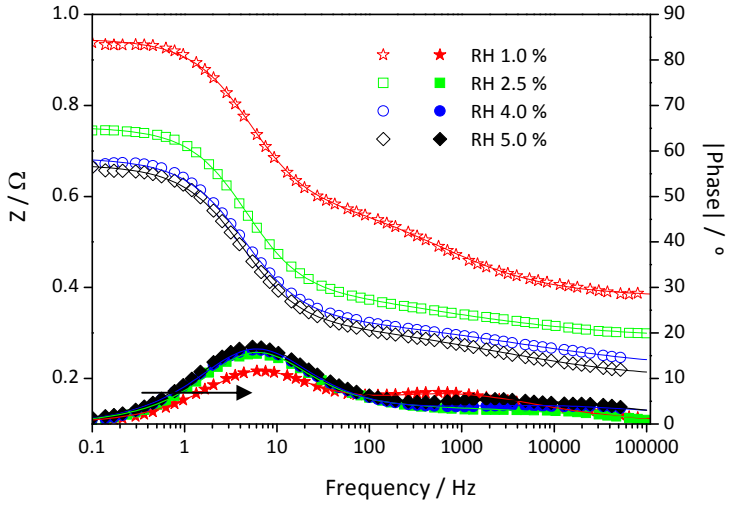


(b)

**Figure 5.7** Nyquist (a) and Bode (b) plots for Pt-SWNH MEAs, at 68 mA·cm$^{-2}$, 160 °C, 1 bar and relative humidity (RH) between 1.0 % and 5.0 %. Lines represent the fitting electrical equivalent model**.**

The effect of RH was also observed in the anode charge transfer resistance (Table 5.2). Water molecules facilitated the migration of phosphoric acid to the catalyst layer and to the space between the electrode and membrane, serving as electrolyte for proton conduction. This way, the anode charge transfer resistance decreased.

**Table 5.2** EIS parameters obtained from the electrical equivalent circuit (Figure 5.4) for Pt-SWNH-based electrode with phosphoric acid doped PBI membrane, at 68 mA·cm$^{-2}$ (1.2 A·mg$_{Pt}^{-1}$·cm$^2$).

| Relative humidity/ % | 1.0 | 2.5 | 4.0 | 5.0 |
|---|---|---|---|---|
| $R_{ct}^{a}$ / mΩ | 207.4 | 110.9 | 116.7 | 121.2 |
| $R_{ct}^{a}$ / mΩ·mgPt·cm$^{-2}$ | 51.90 | 27.70 | 29.20 | 30.30 |
| $C_{dl}^{a}$ / mF | 1.000 | 1.700 | 0.800 | 0.900 |
| $\alpha^{a}$ | 0.5800 | 0.4000 | 0.3900 | 0.4400 |
| $R_{p}^{a}$ / mΩ | 10.50 | 7.800 | 6.100 | 5.500 |
| Ohmic Resistance /mΩ | 375.8 | 285.8 | 214.9 | 195.3 |
| $R_{ct}^{c}$ / mΩ | 359.5 | 354.6 | 351.5 | 351.7 |
| $R_{ct}^{c}$ / mΩ·mgPt·cm$^{-2}$ | 89.90 | 88.70 | 87.90 | 87.90 |
| $C_{dl}^{c}$ / mF | 44.10 | 55.10 | 50.20 | 53.20 |
| $\alpha^{c}$ | 0.8500 | 0.8700 | 0.8400 | 0.8400 |
| $R_{p}^{c}$ / mΩ | 3.900 | 2.700 | 3.400 | 3.500 |

The cyclic voltammetry diagrams, obtained at the different RH, are presented in Figure 5.8. It is observed an increase of the ESA at the cathode with the RH; when relative humidity increases from 1.0 % to 2.5 % and to 5.0 %, the ESA values increase 22 % and 39 %, respectively. The increase of ESA with RH should result from the migration of phosphoric acid from the membrane to the electrode, assuming negligible acid phosphoric washing out. The cathode charge transfer resistance does not follow the increase of the ESA with the RH (Table 5.2). The presence of water increases the proton activity by ionizing phosphoric acid at cathode catalyst layer and

increase the oxygen diffusion by decreasing the viscosity of the phosphoric acid [45]. However, the relative ESA values indicate that, as a result of RH increase, the amount of phosphoric acid increased at the catalyst layer. As mentioned previously, an excess of phosphoric acid can originate kinetic limitations of the oxygen reduction and reduce the solubility of oxygen (see section 3.3).

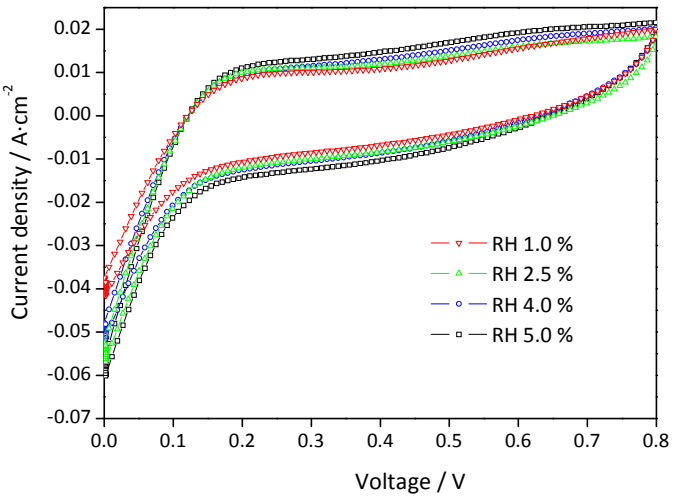


**Figure 5.8** Cyclic voltammetry diagrams obtained for Pt-SWNH-based electrode with phosphoric acid doped PBI membrane, at 160 °C, 1 bar and relative humidity between 1.0 % and 5.0 %.

### 5.4.5 Characterization after performance tests

The membrane and catalyst layer were characterized by field emission scanning electron microscopy (FE-SEM) equipped with an EDS detector, after performance tests at 160 °C. The Pt-carbon black MEA was characterized after running at 1.0 % RH and the SWNH MEA was characterized after running at different RH.

Figure 5.9 and Figure 5.10 show the SEM micrographs of the interfaces PBI membrane / electrode for the SWNH and the carbon black MEAs, respectively. EDS

analysis allowed the chemical characterization of the PBI membrane and the catalyst layer of both MEAs (Figure 5.9 and Figure 5.10).

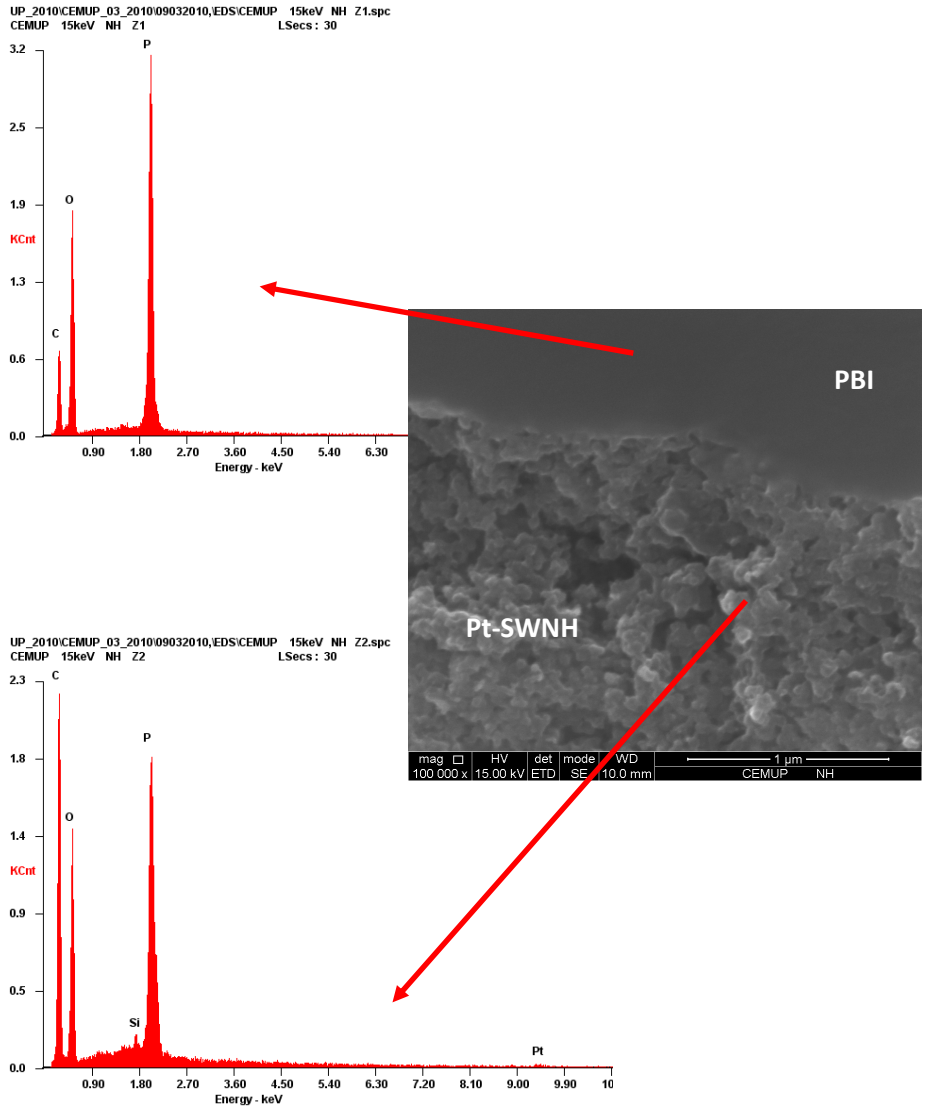


**Figure 5.9** SEM micrograph of interface of PBI membrane and SWNHbased catalytic layer after performance tests and EDS at PBI membrane and catalyst layer.

The ratios between phosphorus and carbon peaks for the PBI membrane and for the catalyst layer of Pt-SWNH MEA are higher than these for the Pt-carbon black MEA. This may indicate that a higher amount of phosphoric acid is retained in the

membrane and in the catalyst layer when SWNH are used as catalyst support due to the hydrophobic behavior of SWNH support and could explain the higher relative ESA obtained for the Pt-SWNH electrode.

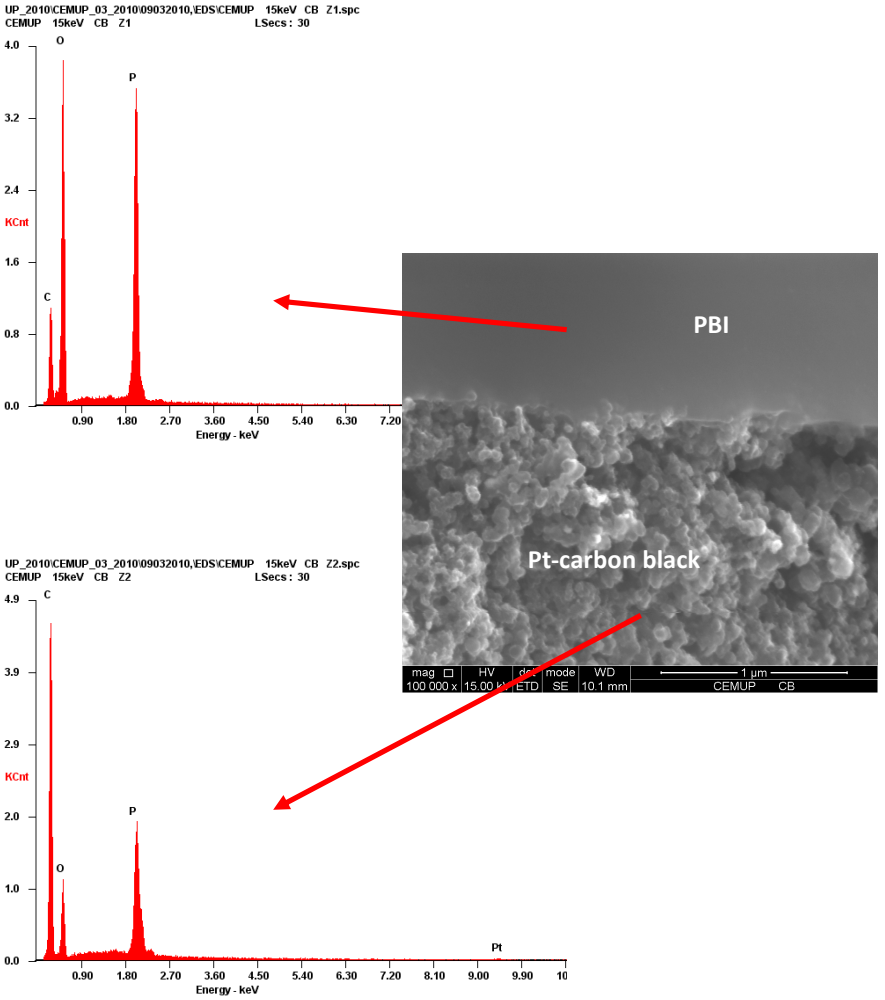


**Figure 5.10** SEM micrograph of interface of PBI membrane and carbon black-based catalytic layer after performance tests and EDS at PBI membrane and catalyst layer.

The thickness of the PBI membrane decreased after 50 h running period. Starting with 100 μm, the final thickness of the membranes was ca. 56 μm for the Pt- carbon

black MEA and ca. 60 μm for the Pt- SWNH MEA, showing the migration of phosphoric acid to the electrodes (data not shown).

Future work is in progress in order to characterize the carbon supports regarding its hydrophobicity and the effect of this property in the high temperature PEMFC performance.

## 5.5 Conclusions

This work aimed to compare the performance of electrocatalysts based on platinum supported in single-wall carbon nanohorns (Pt-SWNH) and supported in carbon black (Pt-carbon black) during high temperature PEM fuel operation.

A higher ohmic resistance was obtained for the Pt-SWNH-based MEA when compared with the Pt-carbon black-based MEA due to likely the higher hydrophobic character of the SWNH carbon support. Moreover, the Pt-SWNH anode presented lower charge transfer resistance compared to Pt-carbon black anode but similar cathode charge transfer resistance. These features contributed to a similar peak power density for the MEAs assembled with phosphoric acid doped polybenzimidazole (PBI/$H_3PO_4$) membrane. The morphologies and hydrophobicities of the carbon electrocatalyst supports originated different performances of the three-phase boundary in the catalyst layer during fuel cell operation.

## 5.6 Acknowledgments

The work of M. Boaventura was supported by FCT (Grant SFRH/BD/28187/2006). L. Brandão is also thankful to FCT for her post-doc grant (SFRH/BPD/41233/2007).The present work was also partially supported by FCT project PTDC/EQU-EQU/70574/2006.

## 5.7 References

[1] Hogarth, W.H.J., da Costa, J.C.D., Lu, G.Q., 2005. Solid acid membranes for high temperature (> 140 degrees C) proton exchange membrane fuel cells. J Power Sources 142, 223-237.

[2] Zhang, J.L., Xie, Z., Zhang, J.J., Tanga, Y.H., Song, C.J., Navessin, T., Shi, Z.Q., Song, D.T., Wang, H.J., Wilkinson, D.P., Liu, Z.S., Holdcroft, S., 2006. High temperature PEM fuel cells. J Power Sources 160, 872-891.

[3] Antolini, E., 2009. Carbon supports for low-temperature fuel cell catalysts. Appl Catal B-Environ 88, 1-24.

[4] Seger, B., Kamat, P.V., 2009. Electrocatalytically Active Graphene-Platinum Nanocomposites. Role of 2-D Carbon Support in PEM Fuel Cells. J Phys Chem C 113, 7990-7995.

[5] Xu, C., Wang, X., Zhu, J.W., 2008. Graphene-Metal Particle Nanocomposites. J Phys Chem C 112, 19841-19845.

[6] Yoo, E., Okata, T., Akita, T., Kohyama, M., Nakamura, J., Honma, I., 2009. Enhanced Electrocatalytic Activity of Pt Subnanoclusters on Graphene Nanosheet Surface. Nano Lett 9, 2255-2259.

[7] Li, W.Z., Waje, M., Chen, Z.W., Larsen, P., Yan, Y.S., 2010. Platinum nanopaticles supported on stacked-cup carbon nanofibers as electrocatalysts for proton exchange membrane fuel cell. Carbon 48, 995-1003.

[8] Calvillo, L., Gangeri, M., Perathoner, S., Centi, G., Moliner, R., Lazaro, M.J., 2009. Effect of the support properties on the preparation and performance of platinum catalysts supported on carbon nanofibers. J Power Sources 192, 144-150.

[9] Zhang, S., Shao, Y.Y., Li, X.H., Nie, Z.M., Wang, Y., Liu, J., Yin, G.P., Lin, Y.H., 2010. Low-cost and durable catalyst support for fuel cells: Graphite submicronparticles. J Power Sources 195, 457-460.

[10] Jha, N., Reddy, A.L.M., Shaijumon, M.M., Rajalakshmi, N., Ramaprabhu, S., 2008. Pt-Ru/multi-walled carbon nanotubes as electrocatalysts for direct methanol fuel cell. Int J Hydrogen Energy 33, 427-433.

[11] Wu, G., Xu, B.Q., 2007. Carbon nanotube supported Pt electrodes for methanol oxidation: A comparison between multi- and single-walled carbon nanotubes. J Power Sources 174, 148-158.

[12] Ocampo, A.L., Miranda-Hernandez, M., Morgado, J., Montoya, J.A., Sebastian, P.J., 2006. Characterization and evaluation of Pt-Ru catalyst supported on multi-walled carbon nanotubes by electrochemical impedance. J Power Sources 160, 915-924.

[13] Su, F.B., Tian, Z.Q., Poh, C.K., Wang, Z., Lim, S.H., Liu, Z.L., Lin, J.Y., 2010. Pt Nanoparticles Supported on Nitrogen-Doped Porous Carbon Nanospheres as an Electrocatalyst for Fuel Cells. Chem Mater 22, 832-839.

[14] Azami, T., Kasuya, D., Yoshitake, T., Kubo, Y., Yudasaka, M., Ichihashi, T., Iijima, S., 2007. Production of small single-wall carbon nanohorns by CO2 laser ablation of graphite in Ne-gas atmosphere. Carbon 45, 1364-1367.

[15] Azami, T., Kasuya, D., Yuge, R., Yudasaka, M., Iijima, S., Yoshitake, T., Kubo, Y., 2008. Large-scale production of single-wall carbon nanohorns with high purity. J Phys Chem C 112, 1330-1334.

[16] Gattia, D.M., Antisari, M.V., Giorgi, L., Marazzi, R., Piscopiello, E., Montone, A., Bellitto, S., Licoccia, S., Traversa, E., 2009. Study of different nanostructured carbon supports for fuel cell catalysts. J Power Sources 194, 243-251.

[17] Gattia, D.M., Antisari, M.V., Marazzi, R., 2007. AC arc discharge synthesis of single-walled nanohorns and highly convoluted graphene sheets. Nanotechnology 18, -.

[18] Iijima, S., Yudasaka, M., Yamada, R., Bandow, S., Suenaga, K., Kokai, F., Takahashi, K., 1999. Nano-aggregates of single-walled graphitic carbon nano-horns. Chem Phys Lett 309, 165-170.

[19] Yoshitake, T., Shimakawa, Y., Kuroshima, S., Kimura, H., Ichihashi, T., Kubo, Y., Kasuya, D., Takahashi, K., Kokai, F., Yudasaka, M., Iijima, S., 2002. Preparation of fine platinum catalyst supported on single-wall carbon nanohorns for fuel cell application. Physica B 323, 124-126.

[20] Brandão, L., Boaventura, M., Passeira, C., Gattia, D.M., Marazzi, R., Antisari, M.V., Mendes, A., 2010. An Electrochemical Impedance Spectroscopy Study of PEMFC Electrocatalyst SWNH-supported. J Nanosci Nanotechno, in press: doi 10.1166/jnn.2011.3466.

[21] Brandão, L., Gattia, D.M., Marazzi, R., Antisari, M.V., Licoccia, S., D'Epifanio, A., Traversa, E., Mendes, A., 2010. Improvement of DMFC Electrode Kinetics by Using Nanohorns Catalyst Support. Materials Science Forum 638 - 642, 1106-1111.

[22] Brandão, L., Passeira, C., Gattia, D.M., Mendes, A., 2010. Use of single wall carbon nanohorns in polymeric electrolyte fuel cells. Journal of Material Science, in press: doi 10.1007/s10853-10010-14638-10856.

[23] Lobato, J., Rodrigo, M.A., Linares, J.J., Scott, K., 2006. Effect of the catalytic ink preparation method on the performance of high temperature polymer electrolyte membrane fuel cells. J Power Sources 157, 284-292.

[24] Kongstein, O.E., Berning, T., Borresen, B., Seland, F., Tunold, R., 2007. Polymer electrolyte fuel cells based on phosphoric acid doped polybenzimidazole (PBI) membranes. Energy 32, 418-422.

[25] Seland, F., Berning, T., Borresen, B., Tunold, R., 2006. Improving the performance of high-temperature PEM fuel cells based on PBI electrolyte. J Power Sources 160, 27-36.

[26] Pan, C., Li, Q.F., Jensen, J.O., He, R.H., Cleemann, L.N., Nilsson, M.S., Bjerrum, N.J., Zeng, Q.X., 2007. Preparation and operation of gas diffusion electrodes for high-temperature proton exchange membrane fuel cells. J Power Sources 172, 278-286.

[27] Lobato, J., Canizares, P., Rodrigo, M.A., Linares, J.J., Pinar, F.J., 2010. Study of the influence of the amount of PBI-H3PO4 in the catalytic layer of a high temperature PEMFC. Int J Hydrogen Energy 35, 1347-1355.

[28] Mamlouk, M., Scott, K., 2010. The effect of electrode parameters on performance of a phosphoric acid-doped PBI membrane fuel cell. Int J Hydrogen Energy 35, 784-793.

[29] Oono, Y., Sounai, A., Hori, M., 2009. Influence of the phosphoric acid-doping level in a polybenzimidazole membrane on the cell performance of high-temperature proton exchange membrane fuel cells. J Power Sources 189, 943-949.

[30] Kim, J.H., Kim, H.J., Lim, T.H., Lee, H.I., 2007. Improvement of high temperature polymer electrolyte fuel cell performance with phosphoric acid-doped polybenzimidazole ionomer binder in catalyst layer. J Ind Eng Chem 13, 850-855.

[31] Wannek, C., Lehnert, W., Mergel, J., 2009. Membrane electrode assemblies for high-temperature polymer electrolyte fuel cells based on poly(2,5-benzimidazole) membranes with phosphoric acid impregnation via the catalyst layers. J Power Sources 192, 258-266.

[32] Fujigaya, T., Okamoto, M., Nakashima, N., 2009. Design of an assembly of pyridine-containing polybenzimidazole, carbon nanotubes and Pt nanoparticles for a fuel cell electrocatalyst with a high electrochemically active surface area. Carbon 47, 3227-3232.

[33] Okamoto, M., Fujigaya, T., Nakashima, N., 2009. Design of an assembly of poly(benzimidazole), carbon nanotubes, and Pt nanoparticles for a fuel-cell electrocatalyst with an ideal interfacial nanostructure. Small 5, 735-740.

[34] Andreasen, S.J., Jespersen, J.L., Schaltz, E., Kaer, S.K., 2009. Characterisation and Modelling of a High Temperature PEM Fuel Cell Stack using Electrochemical Impedance Spectroscopy. Fuel Cells 9, 463-473.

[35] Wagner, N., Kaz, T., Friedrich, K.A., 2008. Investigation of electrode composition of polymer fuel cells by electrochemical impedance spectroscopy. Electrochim Acta 53, 7475-7482.

[36] Gohr, H., 1997. Impedance Modelling of Porous Electrodes. Electrochem. Appl. 1, 2-3 (http://www.zahner.de).

[37] Wagner, N., Friedrich, K.A., 2009. Dynamic Operational Conditions, in: Garche, J., Dyer, C., Moseley, P., Ogumi, Z., Rand, D., Scrosati, B. (Eds.), Encyclopedia of Electrochemical Power Sources. Elsevier, Amsterdam, pp. 912-930.

[38] Jespersen, J.L., Schaltz, E., Kaer, S.K., 2009. Electrochemical characterization of a polybenzimidazole-based high temperature proton exchange membrane unit cell. J Power Sources 191, 289-296.

[39] Zhang, J.L., Tang, Y.H., Song, C.J., Zhang, J.J., 2007. Polybenzimidazole-membrane-based PEM fuel cell in the temperature range of 120-200 degrees C. J Power Sources 172, 163-171.

[40] Lin, H.L., Hsieh, Y.S., Chiu, C.W., Yu, T.L., Chen, L.C., 2009. Durability and stability test of proton exchange membrane fuel cells prepared from polybenzimidazole/poly(tetrafluoro ethylene) composite membrane. J Power Sources 193, 170-174.

[41] Liu, G., Zhang, H.M., Hu, J.W., Zhai, Y.F., Xu, D.Y., Shao, Z.G., 2006. Studies of performance degradation of a high temperature PEMFC based on H3PO4-doped PBI. J Power Sources 162, 547-552.

[42] Kwon, K., Park, J.O., Yoo, D.Y., Yi, J.S., 2009. Phosphoric acid distribution in the membrane electrode assembly of high temperature proton exchange membrane fuel cells. Electrochim Acta 54, 6570-6575.

[43] Cooper, K.R., Ramani, V., Fenton, J.M., Kunz, H.R., 2005. Experimental Methods and Data Analysis for Polymer Electrolyte Fuel Cells. Scribner Associates, Southern Pines.

[44] Asensio, J.A., Gomez-Romero, P., 2005. Recent developments on proton conducting poly(2,5-benzimidazole) (ABPBI) membranes for high temperature polymer electrolyte membrane fuel cells. Fuel Cells 5, 336-343.

[45] Liu, Z.Y., Wainright, J.S., Litt, M.H., Savinell, R.F., 2006. Study of the oxygen reduction reaction (ORR) at Pt interfaced with phosphoric acid doped polybenzimidazole at elevated temperature and low relative humidity. Electrochim Acta 51, 3914-3923.

[46] Ma, Y.L., Wainright, J.S., Litt, M.H., Savinell, R.F., 2004. Conductivity of PBI membranes for high-temperature polymer electrolyte fuel cells. J Electrochem Soc 151, A8-A16.

[47] Scott, K., Pilditch, S., Mamlouk, M., 2007. Modelling and experimental validation of a high temperature polymer electrolyte fuel cell. J Appl Electrochem 37, 1245-1259.

# Chapter 6 Proton conductive membranes based on sulfonated poly(oxadiazole-triazole) copolymer[5]

## 6.1 Abstract

This work reports for the preparation of sulfonated poly(oxadiazole-triazole) copolymer membranes doped with a amphoteric molecule, 1H-benzimidazole-2-sulfonic acid, and their characterization as proton conductors at 120 °C and low relative humidity. The membranes had not only high proton conductivities, up to 4x10-3 S·cm-1 at 120 °C and low relative humidity (5.0 % and 10.0 %), but also had good mechanical properties with storage modulus of about 3 GPa at 300 °C and high thermal stability with Tg up to around 420 °C. Because of their superior ion conducting and mechanical properties they have potential as proton conducting membrane for fuel cell applications, in particular at high temperature and extremely low-humidity conditions.

[5] The content of this chapter is adapted from: Ponce, M.L., Boaventura, M., Gomes, D., Mendes, A., Madeira, L.M., Nunes, S.P., 2008. Proton conducting membranes based on benzimidazole sulfonic acid doped sulfonated poly(oxadiazole-triazole) copolymer for low humidity operation. Fuel Cells 8, 209-216.

## 6.2 Introduction

High temperature is mainly advantageous for polymer electrolyte fuel cell to enhance the performance and catalyst tolerance to CO, as well as to profit from a more efficient cooling system. However, practical restrictions are imposed by the currently used PEM which are perfluorinated polymers containing sulfonic groups (Nafion®, Flemion®, Aciplex-S®, Dow®, Hyflon® Ion and 3M membranes), in which high proton conductivity is usually achieved at high hydration levels.

Interesting approaches to develop proton exchange membrane for high operation temperature and very low humidity conditions are mainly based on 1) basic polymers doped with strong acids, 2) polymers containing high boiling point protonic molecules such as liquid imidazole ($T_b$ ~ 257 °C) in place of water and 3) composites of acid polymers with basic heterocycles such as imidazole, pyrazole, 1-methylimidazole, or benzimidazole [1-6].

In the first case, the most used basic polymer is polybenzimidazole (PBI), doped usually with phosphoric acid. The imidazole group acts as proton acceptor in an acid-base "reaction" with the doping acid [7-8] but large amounts of free acid are necessary to assure high conductivity. A problem is the leaching out of this acid of the membrane during the operation conditions. Another disadvantage of these PBI-doped membranes is their low proton conductivity at room temperature. Complexity, connectivity and cooperativity are said to have important contributions to the proton conductivity in membranes [9-10]. Attempts to better describe the proton transport and the water influence have been conducted with help of different molecular models which include, for instance, approaches of non-equilibrium statistics considering the friction experienced by the proton due to interaction with water, sulfonated groups and other sites in the polymer. The connectivity is related to hydrogen bonding to water and sites in the polymer. It is believed that uniformity in the distribution of sulfonated ions (or other hydrogen bonding sites in the polymer) is very important, particularly under minimal hydration conditions. The chemical groups near the polymer site, which directly interact with the protons are relevant as well as the dielectric constant of the proton environment.

A strategy to develop proton conductive membranes for operation at nearly anhydrous conditions has been the use of basic heterocycle molecules (imidazole, pyrazole, triazole) as solvent for acidic protons in polymers [4; 11-12]. In this kind of materials, the proton conducting mechanism might be based on “grotthuss mechanism”, in which only protons are mobile from site to site without additional assistance of diffusible vehicle molecules, such as water molecules [13]. The protonated and non-protonated nitrogen atoms in the heterocycles may act as donors and acceptors in proton-transfer reactions [5-6; 14]. There is an intermolecular proton transfer controlled by hydrogen bond breaking and forming. Pyrazole seems to lead to lower conductivity than imidazole due to lower tendency to form hydrogen bonded structures. Triazole, similar to imidazole, has been investigated to promote proton conduction and additionally to the molecular motion itself and intermolecular proton exchange, intramolecular proton transfer related (tautomerization) is possible [12]. An important aspect for the proton transfer in imidazole like molecules is the dielectric constant of the medium. High dielectric constant is needed to favour the formation of the protonic charge carriers [3] and assure effective proton conduction.

The GKSS fuel cell group has reported the doping of sulfonated polyoxadiazole membranes by doping with different concentrations of sulfuric acid and different immersion times in the acid bath. After treating the sulfonated polyoxadiazole membranes with a 1.6 M $H_2SO_4$ solution, the measured proton conductivity was around $1x10^{-2}$ $S{\cdot}cm^{-1}$ at 50 °C and 100 % relative humidity [15]. The relatively high proton conductivity values for sulfonated polyoxadiazoles and polytriazoles are believed to be due to the availability of well distribute acidic and amphoteric sites for hydrogen bonding. Especially at low humidity levels the “bonding-debonding” dynamic of protons is also important. A very strong proton attachment to the polymer amphoteric sites might lead to an excessively high friction and therefore to a lower conductivity. Therefore the basicity of this site should not be too strong. Groups like oxadiazole and triazole besides imidazole offer a well balanced amphoteric character.

In this work, sulfonated poly (oxadiazole-triazole) copolymer membranes were investigated, which have both acidic (-$SO_3H$ group) and basic sites (basic nitrogen) in the repeating unit. According to some previous reports [16-18], sulfonated polyoxadiazoles and polytriazole copolymers offer a very convenient possibility for formation of a hydrogen bonding network to promote proton conduction. In the present work particularly emphasis is given to the improvement of the polymer proton conductivity by doping molecules. Benzimidazole sulfonic acid (Figure 6.1), an amphoteric molecule containing both sulfonic and imidazole groups, has been chosen as doping agent.

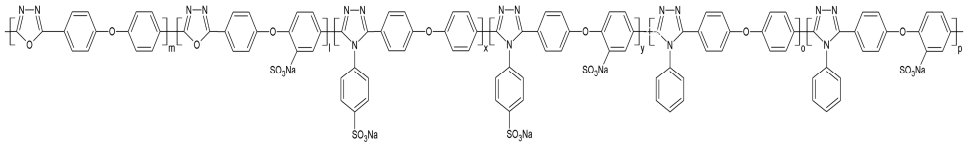

(a)

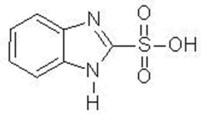

(b)

**Figure 6.1** Molecular structures of (a) SPOD-SPT and (b) BiSA.

## 6.3 Experimental

### 6.3.1 Materials

All chemicals were used as received: 4-aminobenzenesulfonic acid (S-ANI, 99 %, Aldrich), 4,4'-diphenylether dicarboxylic diacid (DPE, 99 %, Aldrich), hydrazine sulphate (HS, >99 %, Aldrich), poly(phosphoric acid) (PPA, Aldrich), sodium hydroxide (NaOH, 99 %, Vetec), dimethyl sulfoxide (DMSO, Merck), 1H-benzimidazole-2-sulfonic acid (BiSA, 98 %, Aldrich).

### 6.3.2 Synthesis of sulfonated poly(oxadiazole- triazole) copolymer

The synthesis conditions have been selected considering previously reported synthesis method for sulfonated poly(oxadiazole-triazole) copolymers (SPOD-SPT) with high molecular weight (330000 g $mol^{-1}$) and high sulfonation level (IEC around 1.48 mequiv·$g^{-1}$) [17-19]. The molar dilution rate (PPA/HS), the molar monomer rate (HS/DPE) and the molar aromatic amine-pre polymer rate (S-ANI/PH) were kept constants and equal to 10, 1.2, and 1.0 respectively. After finishing the batch and to precipitate the polymer, the reaction medium was poured into a 5 % w/v of cold (0 °C) sodium hydroxide solution. The pH of this precipitation bath was controlled by addition of additional amounts of 5 % (w/v) NaOH aqueous solutions. The final polymer yield was always close to 100 % regarding the limiting reactant (DPE). Calc.: N/C 0.1728 S/C 0.099; Found: N/C 0.1726 S/C 0.077.

### 6.3.3 Membrane preparation

A solution containing 5 wt. % of SPOD-SPT copolymer dissolved in DMSO was stirred for 4 hours at 65 °C. Meanwhile, a certain amount of BiSA was added into the polymer solution with stirring. Finally, the homogeneous solution was poured on a glass plate and left during 24 hours at 65 °C for solvent evaporation. The final film thickness was controlled by pouring the polymer solution into a stainless steel ring of 10 cm diameter. To facilitate the membrane removal, surface of the glass plate has been previously hydrophobized with octadecyl trichlorosilane. After casting, the membrane was dried in a vacuum oven for 24 hours at 115 °C in order to remove residual solvent. The final thickness of the membranes was around 100 µm.

### 6.3.4 Characterization

Ionic conductivity was measured by the electrochemical impedance spectroscopy in the frequency range 10-$10^6$ Hz at signal amplitude $\leq$ 10 mV and derived from the high frequency intercept of the complex impedance with the real axis, using a two electrodes arrangement. Measurements were performed with a flow cell purged with wet nitrogen; relative humidity was controlled by bubbling nitrogen gas in water heated at a suitable temperature to obtain desired humidity. The impedance measurements were carried out on stacks containing up to five membranes (similar cumulative thickness, around 500 μm). The spectrometer used was a Zahner IM6 electrochemical workstation.

Dynamic mechanical thermal analysis (DMTA) was used for determination of glass transition temperature ($T_g$), storage modulus (E'), loss modulus (E'') and loss tangent (Tan $\delta$). DMTA was performed using a TA instrument RSA 2 with a film tension mode at a frequency of 1Hz and initial static force of 0.1 N. The temperature was varied from 25 to 500 °C at a heating rate of 2 °C·$min^{-1}$ and at a constant strain of 0.05 %, under dry air atmosphere.

Infrared spectra were recorded on a Bruker Equinox IFS 55 spectrophotometer in the range 4000 - 400 $cm^{-1}$, using polymer films and BiSA powder.

The membrane morphology was observed by scanning electron microscopy (SEM) type LEO 1550VP. The samples were previously coated with gold in a sputtering device.

Thermogravimetric analysis (TGA) was carried out in a Netzsch 209 TG, equipped with a TASC 414/3 thermal analysis controller. The polymers, under argon atmosphere, were heated from 0 to 700 °C at 10 °C·$min^{-1}$.

## 6.4 Results and Discussion

The main scope of this work is the exploitation of sulfonated oxadiazole-triazole copolymers (SPOD-SPT) as proton conductive membranes for fuel cell operation at intermediate temperature and low humidity conditions. An important advantage of this polymer class, besides good thermal stability, is the amphoteric character and the possibility of doping with molecules, which through the formation of hydrogen bonds or by proton acceptor-donor interaction would significantly contribute for the proton conductivity [18]. The copolymer backbone alone has a combination of acidic (-$SO_3H$ group) and basic sites (basic nitrogen) for effective interaction with protons, water and additional doping molecules. Doping of sulfonated polyoxadiazole with sulfuric acid, analogously to what is usually performed with polybenzimidazole, has been recently reported to increase the proton conductivity [15]. In this chapter the idea is to dope the sulfonated oxadiazole-triazole copolymers with small amphoteric molecules containing acid and basic groups similar to those forming the polymer background, increasing the possibility of hydrogen bond formation: benzimidazole sulfonic acid (BiSA). Different doping levels were tested (expressed as the molar ratio (mol %) of additive per nitrogen sites in the polymer): 3, 9 and 22 mol %.

### 6.4.1 Scanning electron microscopy (SEM)

All the membranes were transparent, flexible, and homogeneous (Figure 6.2). The high transparency of the hybrid materials is a first indication of homogeneity at nanoscale. This is confirmed by SEM for the materials with low level of doping (Figure 6.3). However the nanoscale homogeneity is lost for the membrane containing 22 mol % of doping agent. At this concentration the doping molecules crystallize in the polymer matrix. Therefore membranes with higher level of doping were not prepared. High proton conductivity in composite material is due not only to the concentration of doping agent but also to the molecular structure and the miscibility limits of dopping agent-polymer blends [16-22].

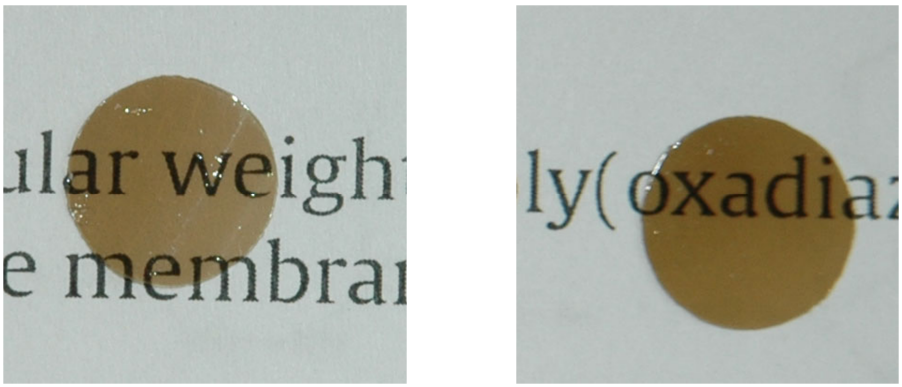

(a) (b)

**Figure 6.2** Photograph of pure SPOD-SPT (a) and SPOD-SPT doped with 22 mol % of BiSA (b).

### 6.4.2 Infrared spectra

The molecular structures of SPOD-SPT/BiSA composite materials were characterized by using IR analysis. Figure 6.4 (a) and (b) shows two different frequency ranges of the IR spectra of pure BiSA and SPOD-SPT/BiSA membranes.

*Region 4000 - 2000 $cm^{-1}$*

In the IR spectrum of BiSA (Figure 6.4 (a)), there are characteristic peaks due to hydrogen bonded NH vibrations between 2100 and 3300 $cm^{-1}$; for the doped materials these NH vibrations are shifted to lower wavenumber and the intensity of them is more pronounced for higher contents of doping agent, which substantiate hydrogen bonding interactions between the BiSA molecules.

For pure SPOD-SPT, the spectra show peaks at 3400 - 3200 $cm^{-1}$ which are related to the absorbed water and can be assigned to the OH stretch of the hydrogen-bonded groups (intra- and intermolecular). The week peak at 2590 $cm^{-1}$, whose intensity increases with the content of BiSA, may be related to the proton transfer between the BiSA molecules and probably also from BiSA to the nitrogen atoms in the heterocyclic rings of SPOD-SPT.

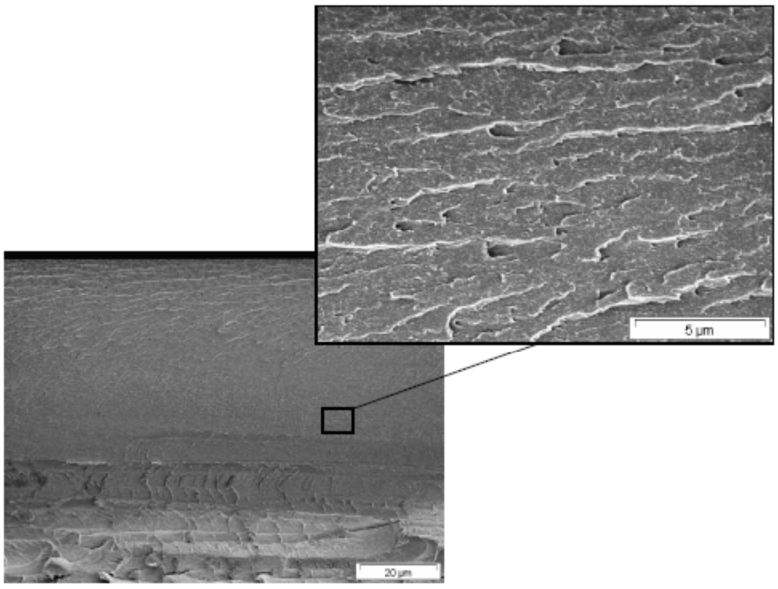


(a)

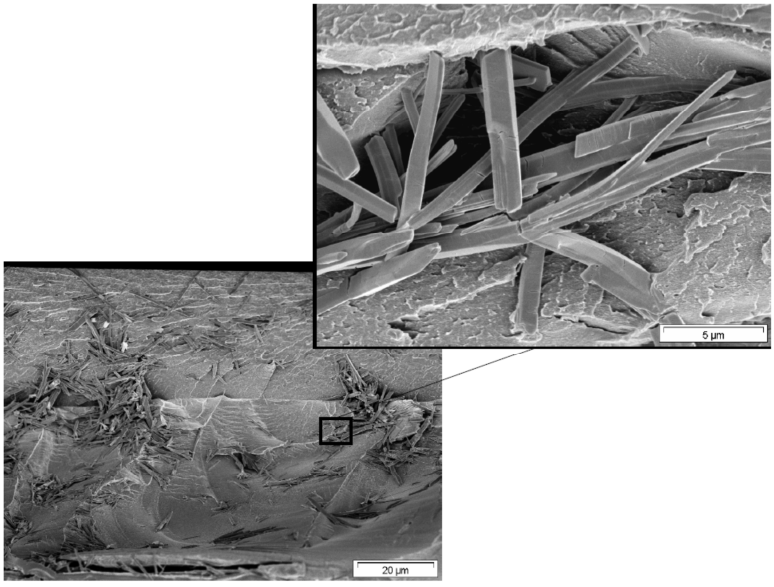


(b)

**Figure 6.3** SEM photomicrographs of cross sections of SPOD-SPT/BiSA membranes with different doping levels, 9 mol % (a) and 22 mol % (b).

*Region 1800 - 900 $cm^{-1}$*

In the IR spectra of doped membranes, (Figure 6.4 (b)), the shoulders at 1620 $cm^{-1}$ and 1290 $cm^{-1}$, which grow when increasing the concentration of doping agent, may be assigned to C=N stretching in the heteroatomic ring (imidazole) of the doping agent, whereas the shoulder at 1290 $cm^{-1}$, growing with the concentration of doping agent, can be assigned to CN stretching vibrations.

The CN stretching vibrations produce intense bands at 1200 – 1310 $cm^{-1}$; for pure BiSA the CN stretching should be the intense peak at 1278 $cm^{-1}$ [21]. The frequency range 1400 - 1000 $cm^{-1}$ comprises also absorptions due to the sulfonic groups [15; 17]. The peak at 1395 $cm^{-1}$ has been attributed to the $SO_2$ asymmetric stretching of the sulfonic group covalently bonded to the SPOD-SPT polymer, showing an increasing intensity with increasing amount of doping, whereas the peak at 1197 $cm^{-1}$ in the composite materials is attributed to the $SO_2$ symmetric stretching of the sulfonic group covalently bonded to SPOD-SPT. With increasing amounts of BiSA, the absorption intensity of the shoulder at 1147 $cm^{-1}$ also increases and it is relative to the $SO_3$ asymmetric stretching of the sulfonic group in BiSA. The peaks at 1061 – 1067 $cm^{-1}$, with intensity increasing when increasing the doping level, has been assigned to $SO_3$ symmetric stretching of the sulfonic group in BiSA.

### 6.4.3 Dynamical mechanical thermal analysis (DMTA)

Dynamical mechanical relaxations of the pure and doped materials have been investigated. The main goal of the mechanical characterization was to identify the relaxations of the pure SPOD-SPT and how they are affected by the dispersed doping agent. Figure 6.5 and Figure 6.6 show plots of tan $\delta$ (mechanical damping) and E' (storage modulus), respectively, versus temperature for each of the membranes.

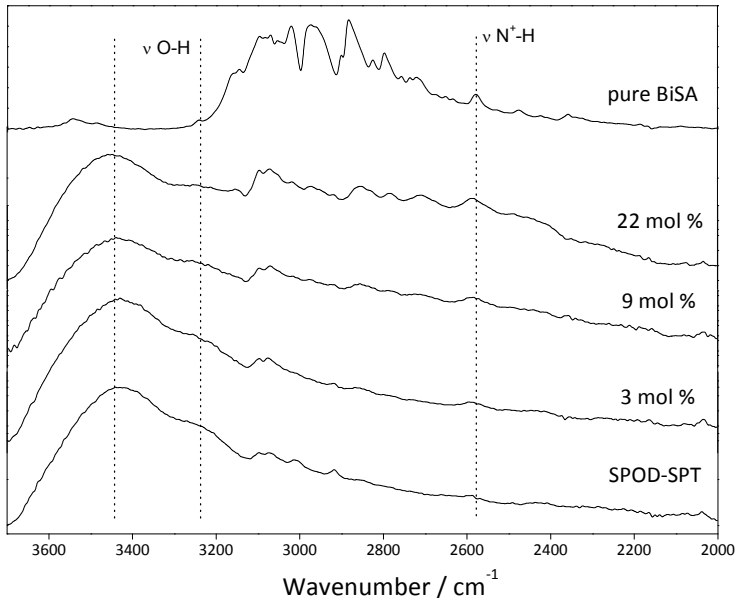


(a)

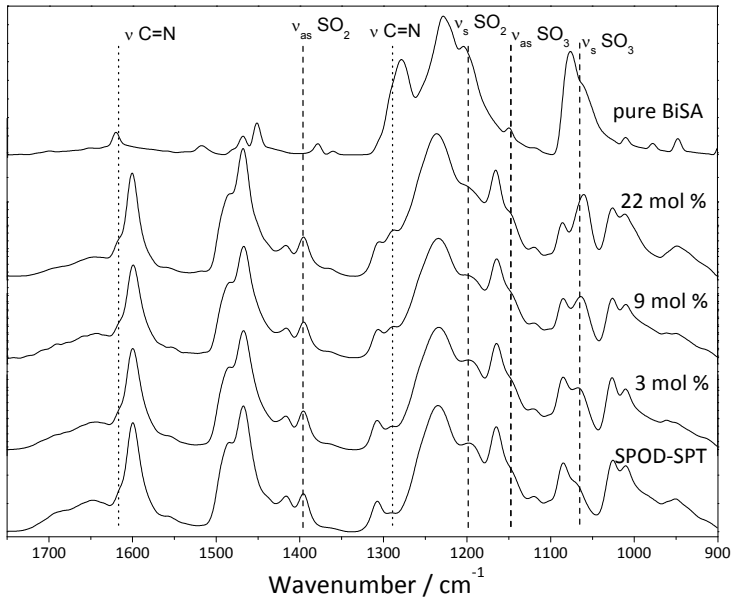


(b)

**Figure 6.4** FTIR spectra of pure BiSA, pure SPOD-SPT and SPOD-SPT/BiSA membranes with different doping levels, in the region 4000 - 2000 $cm^{-1}$ (a) and 1800 - 900 $cm^{-1}$ (b).

For the membrane from pure SPOD-SPT, the glass transition temperature ($T_g$) at 420 °C is related to $\alpha$-transition of the polymer backbone. The bulky triazole side groups make the rotation difficult and contribute to the high temperature transition. Interactions between ionic groups and basic nitrogen of neighbouring chains can additionally contribute to the high value. For the same membrane a $T_\beta$ relaxation peak appears at 291 °C. This probably corresponds to the motion of the ether containing segment.

For the doped materials, the general trend is that both $T_g$ and $T_\beta$ decrease with increasing the concentration of doping agent, which is rationalized in terms of a plasticization of the chain backbone including the ether segments, since the interchain distance increases with the intercalation of the more mobile low molecular weight additive molecule. Also, lower values of E' are observed for doped membranes (Figure 6.6) reinforcing this affirmation.

The intrinsic transitions of the doping agent are other general characteristic of dynamical mechanical relaxations in the doped materials. It has been reported that imidazole molecule, with two protonation sites, assembles into a molecular clusters through intermolecular hydrogen-bonding [20]. Therefore, we can assume that BiSA, with two protonation sites and a proton donor, may also form molecular assemblies, which would lead to fast proton transfer. The assembly is responsible for the broad transitions at 200 °C and 300 °C, as can be seen in the plots of tan $\delta$ and E' versus temperature (Figure 6.5 and Figure 6.6). The transition around 200 °C could be probably due to changes in state of the benzimidazole-rich phase, like disassembling, what leads to a higher system mobility, with dramatic decrease of E' module. The decrease starts just above 120 °C, which is reported as the melting temperature for pure BiSA. The transition at 300 °C could be additionally related to significant weakening of the interaction (ionic and H-bond) between the additive and the polymer chain backbone. For low concentrations, the BiSA molecules do not form assemblies and no measurable changes could be seen at 200 °C.

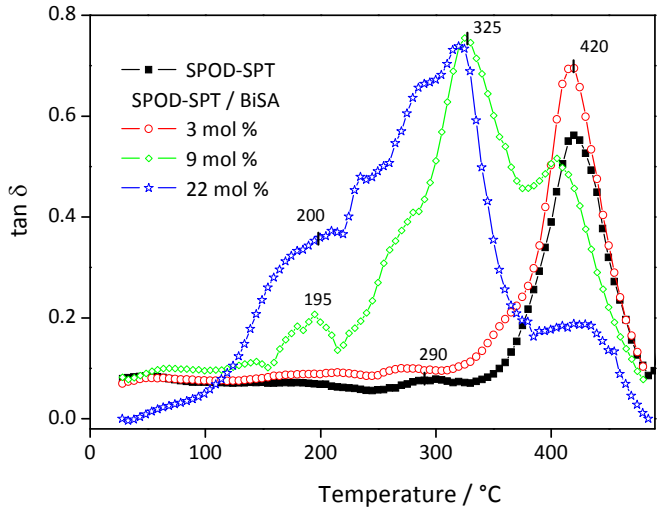


**Figure 6.5** Tan δ versus T for pure SPOD-SPT (■) and SPOD-SPT/BiSA membranes with different doping levels: 3 mol % (○), 9 mol % (◊) and 22 mol % (☆).

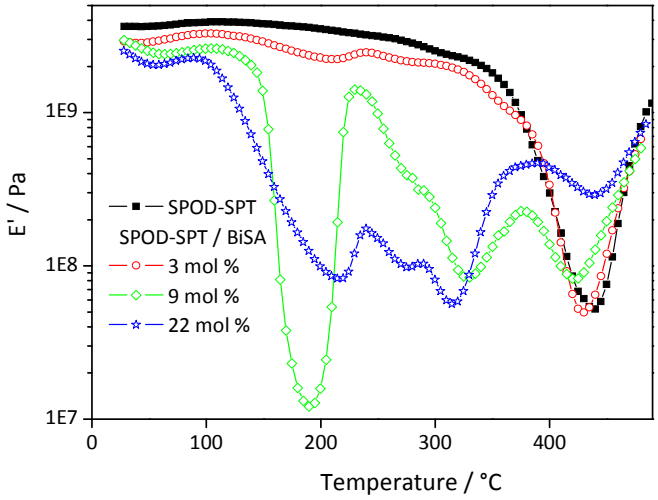


**Figure 6.6** E' versus T for pure SPOD-SPT (■) and SPOD-SPT/BiSA membranes with different doping levels: 3 mol % (○), 9 mol % (◊) and 22 mol % (☆).

### 6.4.4 Thermogravimetric analysis (TGA)

The thermal gravimetric analysis of BiSA, plain SPOD-SPT (in membrane and powder form) and SPOD-SPT doped with 22 mol % of BiSA can be seen in Figure 6.7. A weight loss of about 5 % and 2.5 % were observed for plain and doped SPOD-SPT, respectively, at 120 °C, which can be assigned to water. Above 250 °C another weight loss can be observed, which might be related to the loss of sulfonic groups attached to the polymer chain. Above 450 °C the polymer backbone starts to degrade.

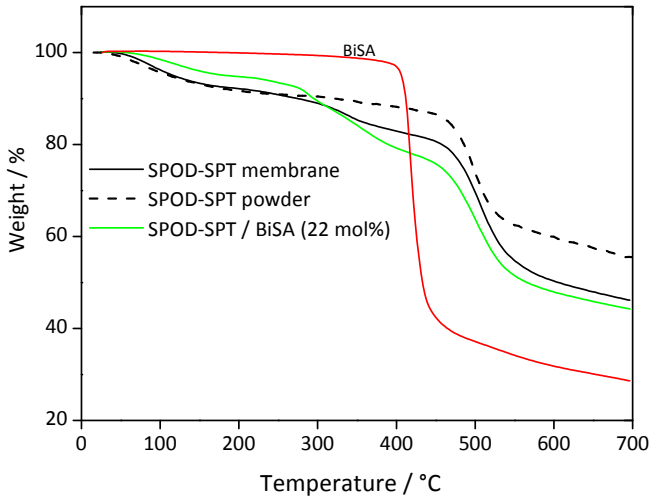


**Figure 6.7** TGA curve for BiSA (red line), SPOD-SPT in powder form (dotted line) and membrane form (black line) and SPOD-SPT doped with 22 mol % of BiSA (green line).

### 6.4.5 Conductivity measurements

The proton conductivities of the polymer at 120 °C and very low relative humidity (5.0 % and 10.0 %) are plotted as a function of the BiSA doping level and shown in Figure 6.8. Before the measurements the membranes were kept at the measuring temperature under the desired humidity level for at least one hour.

The proton conductivity increases with increasing content of the doping agent until 9 mol %. These results suggest that the proton transport is mainly facilitated by the hydrogen bonds, being transferred between different acceptor and donor sites in the polymer and in the BiSA molecules without an assistance of diffusible vehicle molecules. The proton conductivity measurements were performed at 120 °C and therefore below all the transitions of dynamical mechanical relaxations in the doped materials. In these conditions the mobility is quite low to significantly contribute to a vehicle mechanism.

It has been proposed that under anhydrous conditions, the proton transport can primarily depend on the distance between the hopping sites. Therefore, a continuous medium with minimum jumping distances from site to site should improve the proton transfer processes.

Figure 6.9 shows a proposed proton-conducting scheme in BiSA molecular crystals, in which proton hopping occurs from sulfonic acid groups in BiSA to imidazole rings in neighboring molecules; a similar mechanism has been proposed for sulfonated pyridine in the literature [14].

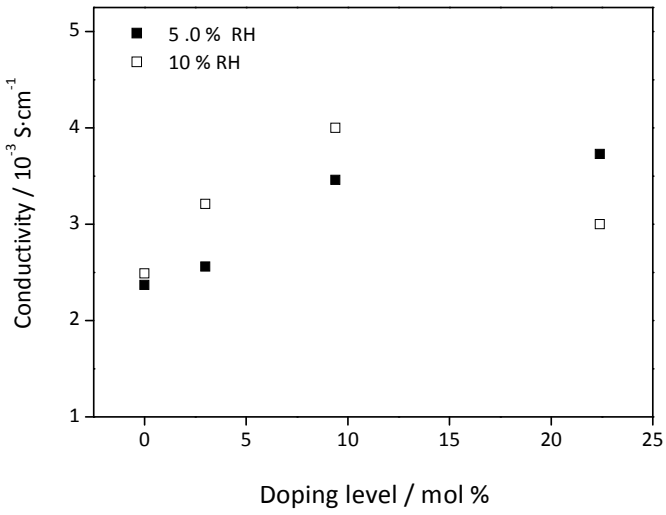


**Figure 6.8** Proton conductivity of SPOD-SPT/BiSA membranes as a function of the doping level at 120 °C and at 5.0 % (■) and 10.0 % RH (□).

The protonated and non-protonated nitrogens in BiSA as well in SPOD-SPT can act as donors and acceptors in the proton-transfer reactions. In the protonation of the doping molecules, the neighbouring sulfonic groups in SPOD-SPT could also be involved. The nano-scale homogeneity observed by SEM and the high conductivity values measured with increasing concentration of BiSA until 9 mol %, support the assumed relation between the proton-conduction and the formation of a hydrogen bonding network practically without the need for liquid vehicular molecules at the intermediate temperature and low humidity conditions (Figure 6.9) [14]. However it must be mentioned that still some water is present in the membrane and can play a role in the proton transfer.

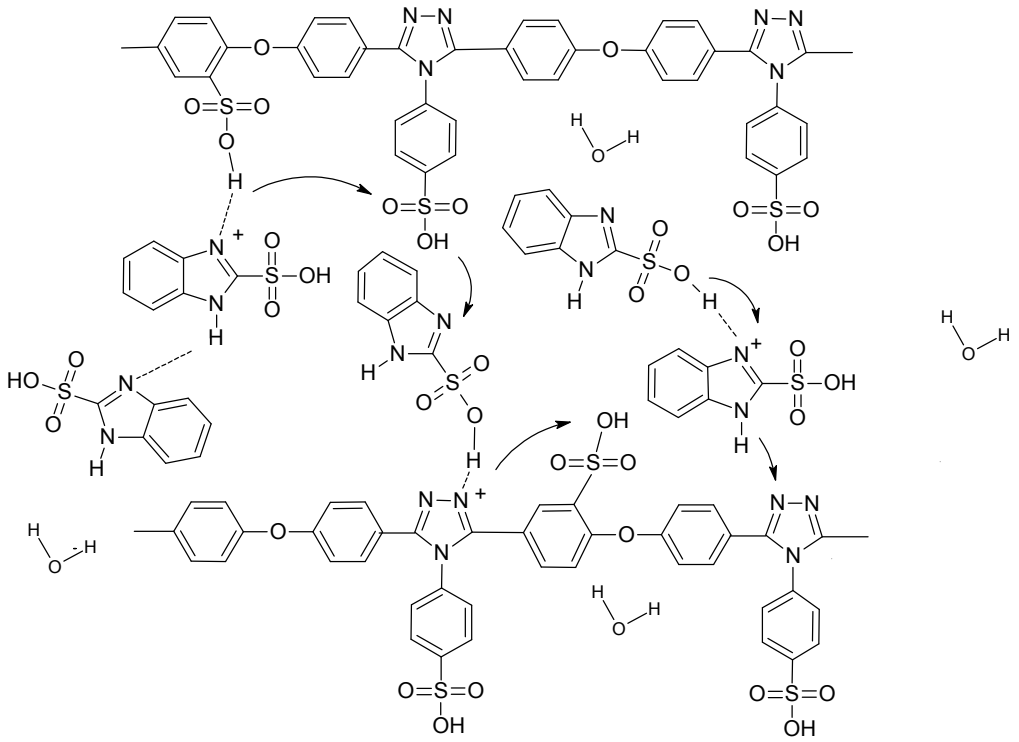

**Figure 6.9** Proposed proton-conducting mechanism in SPOD-SPT/BiSA membranes.

At doping ratios greater than 9 mol %, there is almost no improvement in the proton conductivity of the doped materials.

As it has been evidenced by SEM and FTIR, for a doping content of 22 mol %, a BiSA rich phase clearly separates from the polymer matrix and crystallization is at least partially induced. Therefore, with excess of BiSA the proton conduction is not only influenced by the hydrogen bonds involving the polymer matrix, but may occur also in a phase containing practically only BiSA. How fast the conduction is depends on the mobility of this phase. Below the BiSA melting temperature, the mobility is certainly too low for an effective transport in this phase. Figure 6.6 shows that just below 120 $^{o}$C a thermal transition starts in the membrane, which could be assigned to the melting of the BiSA rich phase. However, even at 120 $^{o}$C, micro-crystals might be still there, contributing for a low conductivity. Probably this effect is analogous to what has been considered by Schuster and Meyer [23]. The reduction of the proton conductivity of other systems with high content of doping agent (heterocycles) has been observed also by other authors before [5; 24-25].

## 6.5 Conclusions

Homogeneous membranes based on SPOD-SPT copolymer, bearing both acidic (-$SO_3H$ group) and basic sites (basic nitrogen) in the main chain were doped with 1H-benzimidazole-2-sulfonic acid, which also contains both type of sites, in order to improve the proton conductivity at high temperature and low relative humidity. The doped materials were studied with respect to their mechanical behavior and their proton conductivity. Doping ratios lower than 22 mol % are sufficient to get conductivities values in the same order of magnitude ($10^{-3}$ S·cm$^{-1}$) of systems reported with other polymers. These membranes also combine high thermal stability with the ability to form a hydrogen bonding network with a minimal doping content, facilitating the proton transfer between protonated (donors) and non-protonated (acceptors) nitrogen and sulfonic groups in BiSA and in the polymer.

## 6.6 Acknowledgments

The authors thank H. Böttcher and K. Prause for the DMTA and the SEM characterizations, respectively. The work of M. Boaventura was supported by FCT (Grant SFRH/BD/28187/2006). The present work was also partially supported by FCT project PTDC/EQU-EQU/70574/2006 and the Helmholtz Virtual Institute “Asymmetric Structures for Polymer Electrolyte Fuel Cell”.

## 6.7 References

[1] Bingol, B., Meyer, W.H., Wagner, M., Wegner, G., 2006. Synthesis, microstructure, and acidity of poly (vinylphosphonic acid). Macromol Rapid Comm 27, 1719-1724.

[2] Kaltbeitzel, A., Schauff, S., Steininger, H., Bingol, B., Brunklaus, G., Meyer, W.H., Spiess, H.W., 2007. Water sorption of poly(vinylphosphonic acid) and its influence on proton conductivity. Solid State Ionics 178, 469-474.

[3] Kreuer, K.D., Paddison, S.J., Spohr, E., Schuster, M., 2004. Transport in proton conductors for fuel-cell applications: Simulations, elementary reactions, and phenomenology. Chem Rev 104, 4637-4678.

[4] Schechter, A., Savinell, R.F., 2002. Imidazole and 1-methyl imidazole in phosphoric acid doped polybenzimidazole, electrolyte for fuel cells. Solid State Ionics 147, 181-187.

[5] Yamada, M., Honma, I., 2004. Alginic acid-imidazole composite material as anhydrous proton conducting membrane. Polymer 45, 8349-8354.

[6] Yamada, M., Honma, I., 2004. An anhydrous proton conductor based on Lactam-Lactim tautomerism of uracil. Chemphyschem 5, 724-728.

[7] He, R.H., Li, Q.F., Xiao, G., Bjerrum, N.J., 2003. Proton conductivity of phosphoric acid doped polybenzimidazole and its composites with inorganic proton conductors. J Membrane Sci 226, 169-184.

[8] He, R.H., Li, Q.F., Bach, A., Jensen, J.O., Bjerrum, N.J., 2006. Physicochemical properties of phosphoric acid doped polybenzimidazole membranes for fuel cells. J Membrane Sci 277, 38-45.

[9] Elliott, J.A., Paddison, S.J., 2007. Modelling of morphology and proton transport in PFSA membranes. Phys Chem Chem Phys 9, 2602-2618.

[10] Paddison, S.J., Elliott, J.A., 2006. On the consequences of side chain flexibility and backbone conformation on hydration and proton dissociation in perfluorosulfonic acid membranes. Phys Chem Chem Phys 8, 2193-2203.

[11] Kreuer, K.D., Fuchs, A., Ise, M., Spaeth, M., Maier, J., 1998. Imidazole and pyrazole-based proton conducting polymers and liquids. Electrochim Acta 43, 1281-1288.

[12] Zhou, Z., Li, S.W., Zhang, Y.L., Liu, M.L., Li, W., 2005. Promotion of proton conduction in polymer electrolyte membranes by 1H-1,2,3-triazole. J Am Chem Soc 127, 10824-10825.

[13] Kreuer, K.D., 1996. Proton conductivity: Materials and applications. Chem Mater 8, 610-641.

[14] Honma, I., Yamada, M., 2007. Bio-inspired membranes for advanced polymer electrolyte fuel cells. Anhydrous proton-conducting membrane via molecular self-assembly. B Chem Soc Jpn 80, 2110-2123.

[15] Roeder, J., Gomes, D., Ponce, M.L., Abetz, V., Nunes, S.P., 2007. Protonation of sulfonated poly(4,4 '-diphenylether-1,3,4-oxadiazole) membranes. Macromol Chem Physic 208, 467-473.

[16] Gomes, D., Roeder, J., Ponce, M.L., Nunes, S.P., 2007. Characterization of partially sulfonated polyoxadiazoles and oxadiazole-triazole copolymers. J Membrane Sci 295, 121-129.

[17] Gomes, D., Roeder, J., Ponce, M.L., Nunes, S.P., 2008. Single-step synthesis of sulfonated polyoxadiazoles and their use as proton conducting membranes. J Power Sources 175, 49-59.

[18] Ponce, M.L., Gomes, D., Nunes, S.P., 2008. One-pot synthesis of high molecular weight sulfonated poly(oxadiazole-triazole) copolymers for proton conductive membranes. J Membrane Sci 319, 14-22.

[19] Ponce, M.L., Gomes, D., Nunes, S.P., Abetz, V., 2007. in: 666.6, D.P.A. (Ed.), Germany.

[20] Acheson, R.M., 1976. An Introduction to the Chemistry of Heterocyclic Compounds. 3rd. John Wiley & Sons Inc,

[21] Vijayan, N., Babu, R.R., Gopalakrishnan, R., Ramasamy, P., Harrison, W.T.A., 2004. Growth and characterization of benzimidazole single crystals: a nonlinear optical material. J Cryst Growth 262, 490-498.

[22] Yamada, M., Honma, I., 2004. Anhydrous protonic conductivity of a self-assembled acid-base composite material. J Phys Chem B 108, 5522-5526.

[23] Schuster, M.E., Meyer, W.H., 2003. Anhydrous proton-conducting polymers. Annu Rev Mater Res 33, 233-261.

[24] Liu, Y.F., Yu, Q.C., Yuan, J., Ma, L.L., Wu, Y.H., 2006. Bronsted acid-base polymer electrolyte membrane based on sulfonated poly(phenylene oxide) and imidazole. Eur Polym J 42, 2199-2203.

[25] Yamada, M., Honma, I., 2005. Anhydrous proton conducting polymer electrolytes based on poly(vinylphosphonic acid)-heterocycle composite material. Polymer 46, 2986-2992.

# Chapter 7 Proton conductive membranes based on doped sulfonated polytriazole[6]

## 7.1 Abstract

This work reports the preparation and characterization of proton conducting sulfonated polytriazole membranes doped with three different agents: 1H-benzimidazole-2- sulfonic acid, benzimidazole and phosphoric acid. The modified membranes were characterised by scanning electron microscopy (SEM), infrared spectra, thermogravimetric analysis (TGA), dynamical mechanical thermal analysis (DMTA) and electrochemical impedance spectroscopy (EIS). The addition of doping agents resulted in a decrease of the glass transition temperature. For membranes doped with 85 wt. % phosphoric acid solution proton conductivity increased up to $2\times10^{-3}$ $S\cdot cm^{-1}$ at 120 °C and at 5.0 % relative humidity. The performance of the phosphoric acid doped membranes was evaluated in a fuel cell set-up at 120 °C and 2.5 % relative humidity.

[6] The content of this chapter is adapted from: Boaventura, M., Ponce, M.L., Brandao, L., Mendes, A., Nunes, S.P., 2010. Proton conductive membranes based on doped sulfonated polytriazole. Int J Hydrogen Energy 35, 12054-12064.

## 7.2 Introduction

The most widely used proton exchange membrane in polymer electrolyte fuel cells (PEMFC), Nafion®, exhibits high proton conductivity under humidified conditions. The need of water to solvate the acidic protons and support proton transport limits fuel cell operation to the boiling point of water and requires a rather complicated water management system. On the other hand, the water management in high temperature fuel cells is much simpler as well as the electrochemical kinetics is higher. Moreover, the cooling system and heat recovery are simplified and CO tolerance dramatically increases [1-2]. Anhydrous proton conductive polymers have received increased attention due to its application in high temperature PEMFC (120 °C - 200 °C). In these materials, the proton conduction is not dependent on the hydration level; rather it is assisted by other proton solvents. One approach intensively studied to produce anhydrous proton conductive polymers is blending neutral or basic polymers with strong oxo-acids like phosphoric to obtain for example phosphoric acid doped polybenzimidazole (PBI) [3-5]. Another approach is the use of nitrogen-containing aromatic heterocycles molecules - with boiling points higher than water - as proton carriers, either as doping agents or immobilized in the polymer backbone, originating polymers with intrinsic proton conductivity. Kreuer and co-workers emphasized the properties of nitrogen-containing aromatic heterocycles (like imidazole, benzimidazole and pyrazole) as viable water replacers and reported the first attempt for immobilizing imidazole [6-8]. These heterocycles molecules are amphoteric and present similar transport coefficients to those of water between 150 °C and 200 °C. Moreover, they exhibit hydrogen bond interactions and, to a certain extent, undergo self-dissociation [9]. When heterocycles are immobilized in a polymer backbone, extensive aggregates of heterocycle molecules may be formed by hydrogen bonding [7-8; 10-11]. In this case, the proton transfer properties rely on structure diffusion: the transport of protons is suggested to occur from protonated heterocycle molecule to non-protonated neighboring heterocycle molecule followed by reorganization of the hydrogen bond pattern [8; 11].

Schuster *et al.* [8; 12] studied the proton conductivity of imidazole terminated ethylene oxide oligomers materials; upon doping with small amounts of triflic acid, proton conductivity increased up to $2.6\times10^{-3}$ S·cm$^{-1}$ at 120 °C. This conductivity improvement is related to a higher proton concentration increase in the hydrogen bond network. Imidazole was also tethered in comb-like polysiloxanes and cyclic oligomers [13]. The highest proton conductivities were observed for the structures with the longest tethers ($1.5\times10^{-3}$ S·cm$^{-1}$ at 160 °C), which showed the lowest glass transition temperatures. Moreover, imidazole was added to PBI [14], fluorine - containing PBI [15] and polyimide (PI) [16], all equilibrated with phosphoric acid. Opposite effects were observed on proton conductivity of those systems. While in the first case the imidazole addition seemed to interrupt the proton transfer due to proton hopping along the phosphoric acid chains, in the remaining cases the heterocycle addition enhanced the proton conductivity of the electrolyte. The interactions between imidazole, polymer, and phosphoric acid promoted proton transfer. The proton conductivity of PI / $H_3PO_4$ / imidazole blends, at 120 °C, reached similar values of PI / $H_3PO_4$ membranes at 160 °C, up to $3.1\times10^{-3}$ S·cm$^{-1}$. Similarly, the addition of imidazole and its derivatives to sulfonated polyimides resulted in membranes with conductivity of $10^{-3}$ S·cm$^{-1}$, at 180 °C in anhydrous conditions, increasing with imidazole content and temperature [17]. Hamada and Homna [18] studied the addition of imidazole to alginic acid and reached conductivities as high as $2\times10^{-3}$ S·cm$^{-1}$ in anhydrous conditions at 130 °C, suggesting that conductive acid-base pairs were formed.

In other studies using benzimidazole (BI) as proton solvent, either intercalated with poly(vinylphosphonic acid) [19] or grafted onto polysulfone units [20], proton conductivity increased with BI content. For BI / poly(vinylphosphonic acid) membranes, a maximum conductivity of $10^{-3}$ S·cm$^{-1}$ was measured at 150 °C in anhydrous conditions. Person *et al.* [21-22] prepared comb-like copolymers with different lengths of BI - tethered side chains and BI concentrations. The conductivity was favored by high segmental mobility and by high BI contents. Interestingly, high benzimidazole concentrations suppressed the segmental mobility increasing the glass transition temperature value, resulting in low conductivities at low temperatures. However, at high temperatures, high heterocycle species concentration favored

proton conductivity. These two trends on polymers and copolymers containing benzimidazole were also investigated by Woudenberg *et al.* [23]. It was concluded that a balance between low glass transition temperature and charge carrier density must be obtained by the proper choice of both polymer backbone and heterocycle species.

The viability of poly(5-vinyltetrazole) as proton conductor was studied by Pu and co-workers [24-25]. These authors doped poly(5-vinyltetrazole) with phosphoric acid and observed an anhydrous proton conductivity of $3.05\times10^{-3}$ $S\cdot cm^{-1}$ at 110 °C. They also considered poly(5-vinyltetrazole-co-acrylonitrile) doped with phosphoric acid and observed that proton conductivity was favored by polymer low molecular weight, high tetrazole content and high acid doping level.

Recently, the use of triazole and its derivatives as proton transport facilitators was emphasized. 1H-1, 2, 4-triazole (Tri) was used as proton solvent in different acidic host matrices, acting as a plasticizer and having a positive effect on proton conductivity [26]. Tri was also immobilized in phosphoric acid doped poly(1-vinyl-1,2,4-triazole) [27] and poly(1-vinyl-1,2,4-triazole) / triflic acid [28]. Phosphoric acid doped poly(1-vinyl-1,2,4-triazole) reached a conductivity of $5\times10^{-3}$ $S\cdot cm^{-1}$, based on protonated and non - protonated triazoles and on N-H sites - phosphate ions. In a recent work with triazole and triazole derivatives, Subbaraman *et al.* [29] showed the importance of an ordered structure, ion exchange capacity and spacing between acid groups in proton conductivity of polymer composite membranes.

The effect of heterocycle basicity was studied using poly(ethylene glycol) methyl ether acrylate (PEGMEA) containing 1,2,3-triazole and BI [30]. A similar comparison was made between 1,2,3-triazole and 2-trifluoromethylbenzimidazole with heterocycle-grafted polysiloxanes [31]. In the first study [30], the 1,2,3-triazole containing polyacrylate (more basic heterocycle) showed higher proton conductivity and less sensitivity of conductivity to temperature. This can be attributed, partially, to the lower p*K*a and size of 1,2,3-triazole molecule and also due to its lower melting point when compared to those of BI, thus reducing the glass transition temperature of the polymer matrix. In the second study [31], it was concluded that p*K*a has little effect on proton conductivity, while heterocycle content within the polymer and

glass transition of polymer backbone have an important role, reinforcing the idea of the delicate balance between charge carrier density and polymer matrix mobility.

The fuel cell group at GKSS investigated proton conducting membranes of sulfonated poly(oxadiazoles - triazoles) and sulfonated polytriazoles with both acidic and basic groups in the polymer repeating unit [32-36]. In this work, membranes of sulfonated polytriazole polymer (S-DPE-PT), doped with phosphoric acid and small amphoteric molecules, 1H-benzimidazole-2- sulfonic acid (BiSA) and benzimidazole (BI) were prepared and characterized.

## 7.3 Experimental

### 7.3.1 Materials

All chemicals were used as received: hydrazine sulphate (>99%, Aldrich), 3-aminobenzenesulfonic acid (99%, Aldrich), 4,4'- diphenylether dicarboxylic acid (99%, Aldrich), poly(phosphoric acid) (115% as $H_3PO_4$, Aldrich), sodium hydroxide (99%, Vetec), rubidium chloride (99,8%, Aldrich), dimethyl sulfoxide, DMSO (Merck), orthophosphoric acid (crystalline, 99.99 %, Aldrich), orthophosphoric acid (solution, 85 wt. %, Aldrich), 1H-benzimidazole-2-sulfonic acid (BiSA, 98 %, Aldrich), benzimidazole (BI, 98 %, Aldrich).

### 7.3.2 Synthesis of sulfonated polytriazole (S-DPE-PT)

High molecular weight S-DPE-PT homopolymer, Figure 7.1, was synthesized according to improved conditions of the one-pot process previously reported [36]. The final polymer was soluble in common polar aprotic organic solvents like NMP and DMSO (Yield: 97 % - 99 %). 1H NMR ($d_6$-DMSO): $\delta$ = 8.58 ($H_{5,5'}$ , s), 8.45 ($H_{6,6'}$ , s), 8.3- 8.2 ($H_{2',2'',4',4''}$ , d), 8.2- 8.0 ($H_{2,4}$ , d), 8.1- 7.9 ($H_{7,7',8,8',9,9'}$ , m) 7.5–7.3 ($H_{1',1'',3',3''}$ , d), 7.25-7.15

($H_{1,3}$ ,d), 7.2- 7.05 ( $H_{10,10'}$ , m). $[x]_{0.24}[y]_{0.05}[o]_{0.3}[p]_{0.41}$ (388): Calc. N/C= 0.175, S/C= 0.10; Found N/C= 0.175, S/C = 0.10.

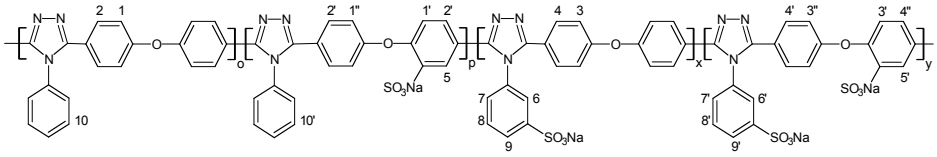

**Figure 7.1** Sulfonated polytriazole (S-DPE-PT) structure.

### 7.3.3 Membrane preparation

A solution containing 5 wt. % of S-DPE-PT in DMSO was stirred for 4 hours at 65 °C. Benzimidazole (BI) and 1H-benzimidazole-2-sulfonic acid (BiSA) were dissolved in dimethyl sulfoxide (DMSO) and mixed with the polymer solution. The homogeneous solutions were poured on a glass plate, previously hydrophobized, and dried at 65 °C during 24 hours for solvent evaporation. After casting, membranes were dried in a vacuum oven for 24 hours at 115 °C in order to remove residual solvent. The final thickness of the membranes was around 100 µm. The doping agent amount is expressed as the molar ratio (mol %) of additive per nitrogen sites in the polymer

Doped phosphoric acid membranes were obtained by two different ways: 1) immersing polytriazole membranes into an 85 wt. % phosphoric acid solution at 50 °C during 24 h and 48 h and 2) adding crystalline phosphoric acid previous to membrane casting. The doping agent amount is expressed as the molar ratio (mol %) of additive per nitrogen sites in the polymer for membranes doped with phosphoric acid concentrated solution. For membranes doped with crystalline phosphoric acid, the doping agent amount is expressed as molar ratio (mol %) of additive per mol of polymer. The membranes doped with crystalline phosphoric acid were used in fuel cell tests.

### 7.3.4 Membrane characterization

Infrared spectra were recorded in the range 4000 - 400 $cm^{-1}$ using a Bruker Equinox IFS 55 spectrophotometer and the morphology of the membranes was observed by scanning electron microscopy (SEM) type LEO 1550VP. The samples were previously coated with gold in a sputtering device.

Thermogravimetric analysis (TGA) was carried out in a Netzsch 209 TG, equipped with a TASC 414/3 thermal analysis controller. The polymers, under argon atmosphere, were heated from 0 to 700 °C at 10 °C·$min^{-1}$. Dynamic mechanical thermal analysis (DMTA) was used to determine glass transition temperature ($T_g$), storage modulus (E'), loss modulus (E'') and loss tangent (tan $\delta$). DMTA was performed using a TA instrument RSA 2 with a film tension mode at a frequency of 1 Hz and initial static force of 0.1 N. The temperature was varied from 25 °C to 500 °C at a heating rate of 2 °C·$min^{-1}$ and at a constant strain of 0.05 %, under dry air atmosphere.

The conductivity was measured by electrochemical impedance spectroscopy in the frequency range 10-$10^6$ Hz at signal amplitude $\leq$ 10 mV and derived from the high frequency intercept of the complex impedance with the real axis, using a two electrodes arrangement. Measurements were performed with a flow cell purged with wet nitrogen; relative humidity was controlled by bubbling nitrogen gas in water heated at a suitable temperature to obtain the desired humidity. The impedance measurements were carried out on membrane stacks containing up to five membranes (cumulative thickness of around 500 μm) using a Zahner IM6 electrochemical workstation.

### 7.3.5 Membrane Electrode Assembly (MEA) preparation and unit cell performance tests

Doped phosphoric acid polytriazole membranes with crystalline acid were sandwiched between two electrodes with an active area of 4 $cm^2$ directly in an

*Electrochem* single cell. A torque of 3.5 N·m was applied by using eight screws. The catalyst layer (*JM HISPEC* 1000, pure platinum, black) was applied to the gas diffusion layer (*Sigracet* 35D) using a dry spray technology [33, 34]. Both anode and cathode platinum loads were 1 $mg \cdot cm^{-2}$ and no electrolyte was added to the catalyst layer. After spray drying, the catalyst powder was pressed to the gas diffusion layer with heated plates at 160 °C and 5.5 bar for 2 minutes. The performance of phosphoric acid doped S-DPE-PT was compared to that of phosphoric acid doped PBI membrane, 100 μm thick and doped with 10 mol of phosphoric acid per mol of PBI (a commercial membrane provided by a partner).

The Electrochem single cell was placed in an in-house build fuel cell test station described in Chapter 2. The system was controlled using a LabView (National Instruments) application and electrochemical tests were performed using a Zahner IM6e electrochemical workstation coupled with a potentiostat PP-241. I-V curves were performed at 120 °C and 1 bar; hydrogen was fed at 1.7 $cm^3 \cdot s^{-1}$ and air at 5.0 $cm^3 \cdot s^{-1}$, both with 2.5 % relative humidity.

## 7.4 Results and Discussion

### 7.4.1 Scanning electron microscopy (SEM)

All prepared membranes were transparent and homogeneous. SEM was performed to confirm homogeneity of BiSA and BI doped membranes. For doping levels up to 20 mol % of BiSA and BI - Figure 7.2 (a) and (c), respectively - no change was observed in SEM images when compared to plain polymer membranes. However, homogeneity was lost for the membrane containing 30 mol % of doping agents BiSA and BI, Figure 7.2 (b) and (d) respectively, where doping molecule crystals are visible. Therefore, membranes with higher level of doping were not prepared.

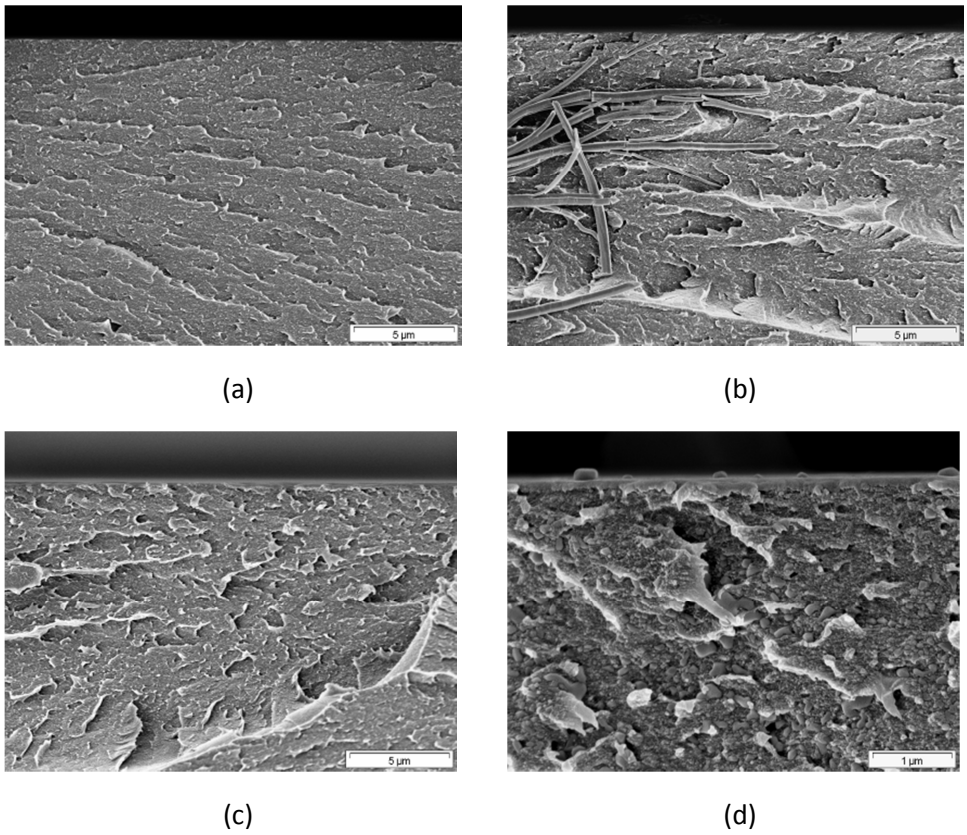


**Figure 7.2** Scanning Electron Microscopy (SEM) of membranes doped with BiSA at 20 mol % (a) and 30 mol % (b) and BI at 20 mol % (c) and 30 mol % (d).

### 7.4.2 Infrared spectra

Infrared spectra of plain and doped membranes, for two frequency ranges, can be seen in Figure 7.3 (3750 - 2350 $cm^{-1}$) to Figure 7.5 (1800 - 550 $cm^{-1}$).

In the high frequency region for plain, BiSA and BI doped membranes (Figure 7.3 (a) and (b), respectively), the characteristic peaks due to hydrogen bonded NH vibrations are present between 3300 - 2350 $cm^{-1}$. For the doped materials, the NH vibrations are shifted to a lower wave number and the peaks' intensity increase with the doping agent content, demonstrating that hydrogen bonding interactions between the BiSA and BI molecules may occur. The peak at 2590 $cm^{-1}$ may be related to the proton transfer between the doping agent molecules (BiSA and BI) and between the doping

agent and the nitrogen atoms in the heterocyclic rings of polymer. The peaks at 3145 $cm^{-1}$ and 3225 $cm^{-1}$ can be assigned to self - associated hydrogen-bonded N-H groups and non-associated N-H groups, respectively. For pure S-DPE-PT, the spectra show peaks at 3700 - 3200 $cm^{-1}$ that are related to the absorbed water and can be assigned to the OH stretch of the hydrogen-bonded groups.

For the S-DPE-PT membranes doped with phosphoric acid by immersion - Figure 7.4- a broad band appears between 3500 - 2500 $cm^{-1}$, which can be assigned to the hydrogen bonding network formation [27].

Figure 7.5 (a) shows the low frequency region, between 1800 - 550 $cm^{-1}$, for pure and BiSA doped membranes. For doped membranes, the shoulder at 1290 $cm^{-1}$ grows with the doping agent concentration, which can be assigned to CN stretching vibrations, and a peak appears at 800 $cm^{-1}$ that can be ascribed to the CS stretching. The peak at 1395 $cm^{-1}$ can be attributed to the $SO_2$ asymmetric stretching of the sulfonic group covalently bonded to the S-DPE-PT polymer. This peak shows an increasing intensity with the amount of doping. In its turn, the peak at 650 $cm^{-1}$ for the composite materials can be attributed to the $SO_2$ symmetric stretching of the sulfonic group covalently bonded to S-DPE-PT. The peaks at 1061 - 1067 $cm^{-1}$, with an increasing intensity alongside with the doping level, can be assigned to the $SO_3$ symmetric stretching of the sulfonic group in BiSA.

For the S-DPE-PT membranes doped with phosphoric acid by immersion, Figure 7.5 (b), a broad peak appears between 1050 - 900 $cm^{-1}$, which can be attributed to characteristic absorption of anions $HPO_4^{2-}$ and $H_2PO_4^-$ in the system S-DPE-PT/$H_3PO_4$ [37].

### 7.4.3 Thermogravimetric analysis (TGA)

Figure 7.6 (a) and (b) show the thermograms of pure and doped membranes with BiSA and BI, respectively, in the presence of dry argon.

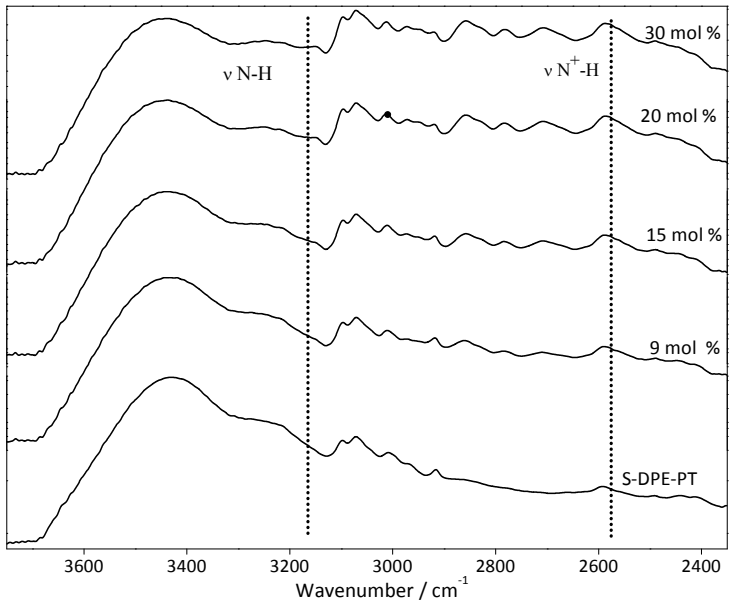


(a)

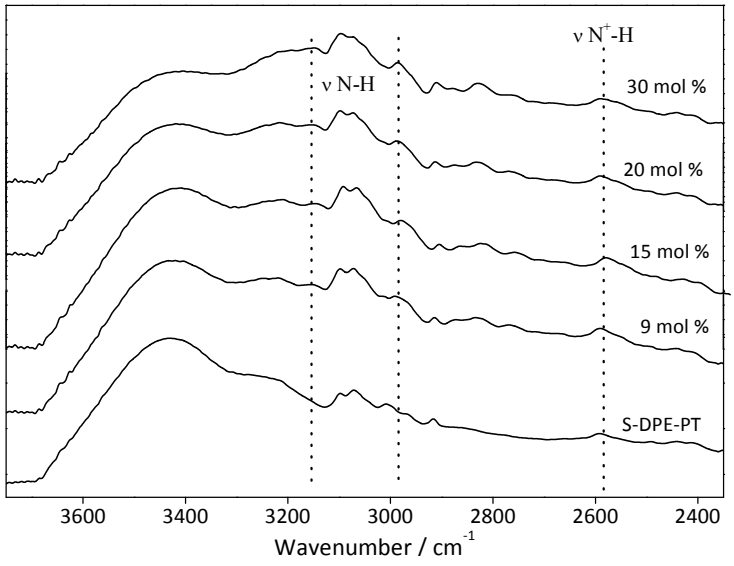


(b)

**Figure 7.3** FTIR spectra of pure S-DPE-PT and doped membranes in the region 3750 - 2350 cm $^{-1}$, for different doping levels for BiSA doped membranes (a) and BI doped membranes (b).

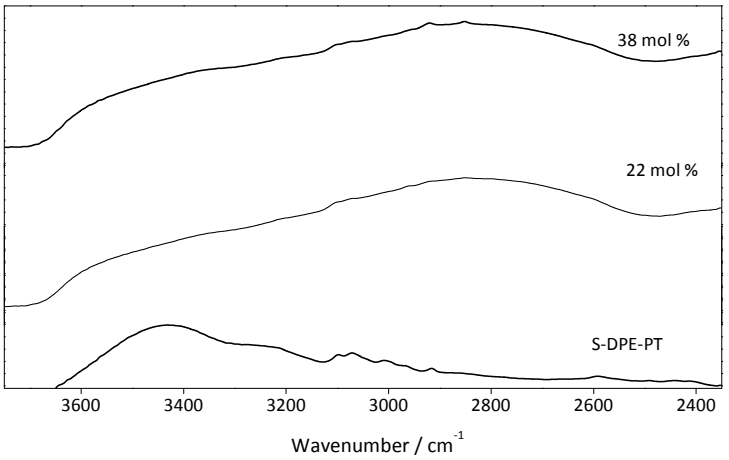


**Figure 7.4** FTIR spectra of pure S-DPE-PT and phosphoric acid doped membranes in the region 3750-2350 $cm^{-1}$.

The polymer membranes lost water up to 200 °C. Membranes doped with BiSA are less hydrophobic than the base membrane and the amount of water present increases with BiSA content. On the other hand, BI doped membranes are more hydrophobic and the amount of water decreased with the BI content. S-DPE-PT powder presents the lower water content, which indicates that some water may be trapped during preparation of the different membranes.

The weight loss after 200 °C can be assigned to solvent evaporation (DMSO boils at 196 °C). The loss of solvent is not observed for pure polymer in the powder form. At around 300 °C, an extra mass loss is observed for BiSA doped membranes, likely due to the loss of sulfonic acid groups (doping agent). All polymer membranes were chemically stable up to 450 °C. Above this temperature the weight loss was due mostly to polymer decomposition.

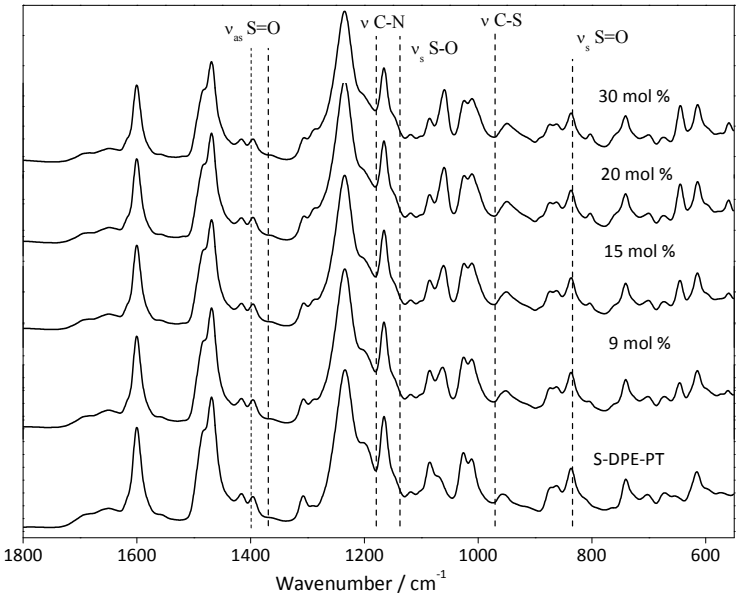


(a)

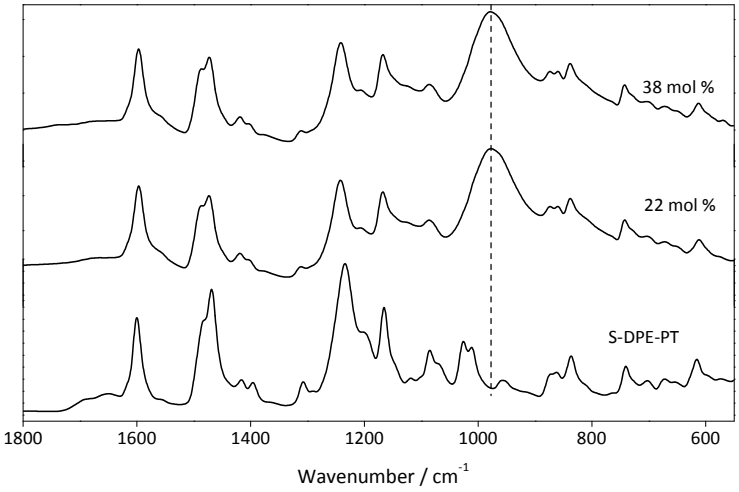


(b)

**Figure 7.5** FTIR spectra of pure S-DPE-PT and doped membranes in the region 1800 - 550 $cm^{-1}$ for different doping levels for BiSA doped membranes (a) and phosphoric acid doped membranes (b).

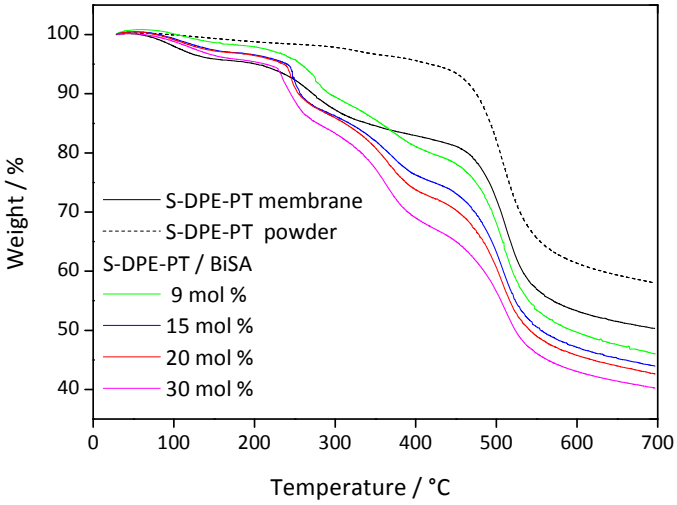


(a)

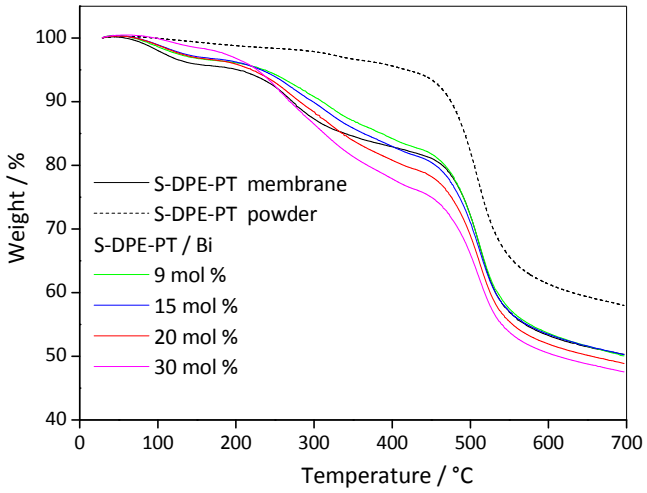


(b)

**Figure 7.6** Thermogravimetric analysis of pure S-DPE-PT, in powder (dotted line) and after membrane preparation (black line) and doped with BiSA (a) and BI (b), at different doping levels: 9 mol % (green line), 15 mol % (blue line), 20 mol % (red line) and 30 mol % (magenta line).

### 7.4.4 Dynamical mechanical thermal analysis (DMTA)

Differences in the morphology of the backbone as well as in the ionic domains strongly influence the mechanical properties of ionomers [38]. According to the DMTA technique (Figure 7.7 and Figure 7.8), the typical response of the mechanical damping (tan $\delta$) versus temperature for the pure S-DPE-PT membrane shows two mechanical relaxations, one at around 402 °C and another at around 450 °C. The first peak can be attributed to the devitrification of the ion-rich hard amorphous region beginning near 350 °C (glass transition temperature, $T_g$ = 402 °C).

When ion content is sufficiently high, regions with reduced mobility surrounding the aggregates form cluster regions or ion-rich phases that exhibit a glass transition temperature higher than that of matrix phase [39-41]. The presence of another small relaxation peak in the tan $\delta$ curves, above the $T_g$, can be assigned to the melting of the crystals [42] ($T_m$ = 450 °C) present in the hard amorphous phase; this has been observed from WAXS measurements [43]. Although the onset of devitrification of the ion-rich regions ($T_g$) precedes the crystal melting ($T_m$), the melting of the crystals at $T_m$ disrupts the continuity of the "hard" paths through the amorphous phase and produces a much larger modulus decrease.

The glass transition temperature of the host polymer decreases significantly to 285 °C for the membrane with 22 mol % of phosphoric acid, doped by immersion - Figure 7.7. The softening effect of phosphoric acid (plastization effect) was also observed for other polymer/acid blends [27; 44]. It was not possible to perform DMTA tests to the membranes doped with a higher doping level by immersion in the concentrated phosphoric acid solution, due to loss of mechanical resistance at temperatures higher than 120 °C, as discussed in more detail in Section 7.4.5.

For the BiSA and BI doped materials (Figure 7.8), the $T_g$ generally decreases with the doping agent concentration, which can be assigned to the plasticization of the chain backbone, including the ether segments. Since the inter chain distance increases with the intercalation of more mobile low molecular weight molecules, an additional relaxation was observed at around 300 °C ($T_\beta$) for doped membranes; increasing

levels of doping shifts $T_\beta$ to lower temperatures. The plasticizing effect of doped membranes is reinforced by lower values of E'.

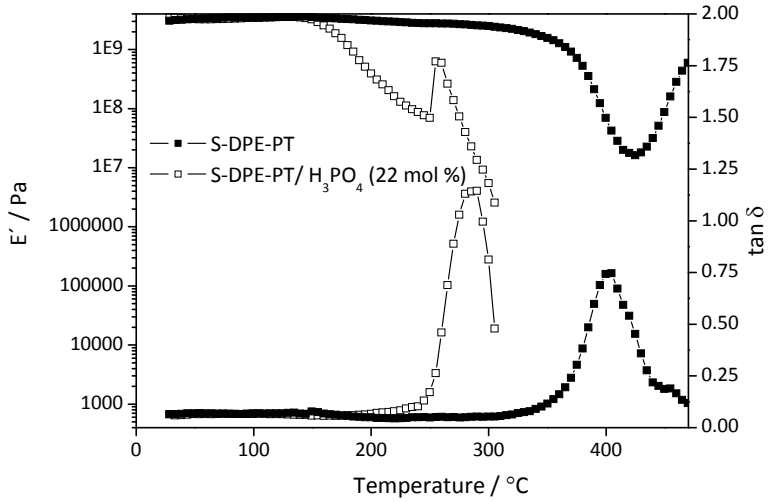


**Figure 7.7** E' and tan δ as a function of temperature for pure S-DPE-PT (■) and phosphoric acid doped polymer, at 22 mol % (□).

The intrinsic transitions of the doping agents are another general characteristic of dynamical mechanical relaxations in doped materials. Like imidazole molecule [45], one can assume that BiSA and BI may also form molecular assemblies that are responsible for the broad transitions between 120 °C and 300 °C, increasing with the doping level in the membranes, as it can be seen in the plots of tan δ and E' versus temperature (Figure 7.8). The broad transitions start at around 120 °C (benzimidazole sulfonic acid melting point is 120 °C and benzimidazole melting point is 171 °C), corresponding to a remarkable drop in storage modulus due to higher mobility - Figure 7.8. The storage module increases after this transition for both additives, suggesting that polymer matrix remains with rigidity below 300 °C, but decreases just afterwards, likely due to the weakening of the interactions between the additive and the polymer chain backbone.

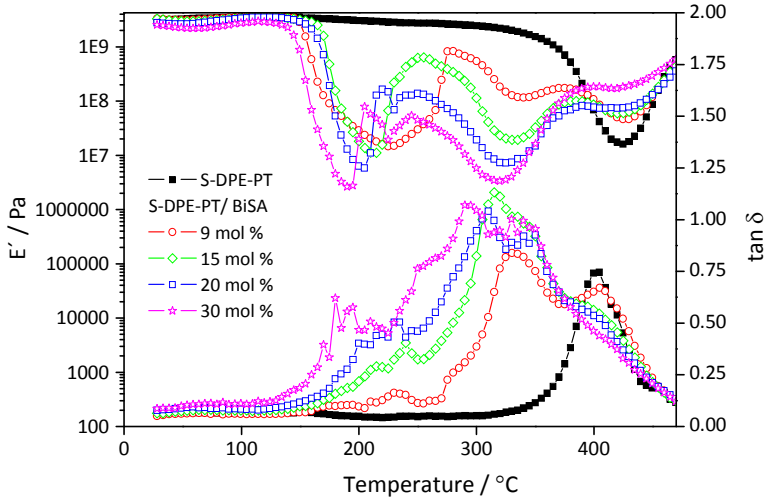


(a)

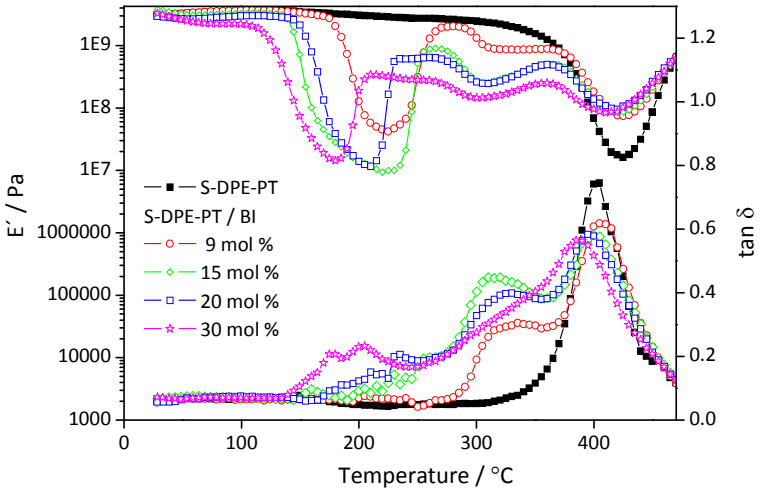


(b)

**Figure 7.8** E′ and tan δ as a function of temperature, for pure polymer membrane (■) and doped with BiSA (a) and BI (b), at different doping levels: 9 mol % (○), 15 mol % (◊), 20 mol % (□) and 30 mol % (☆).

The plastization effect of imidazole when this heterocycle was added to sulfonated polyimide was reported by Pu *et al.* [17]. Chuang *et al.* [15] observed the decrease of mechanical properties of doped PBI upon imidazole addition. It was observed that imidazole could act as non-reinforcement filler and that at high concentrations an induced phase can be formed.

### 7.4.5 Conductivity measurements

The membrane made of plain S-DPE-PT exhibits a relatively high ionic conductivity (Figure 7.9), around $5\times10^{-4}$ S·cm$^{-1}$ between 5.0 % and 25.0 % relative humidity (RH) and between 80 °C and 160 °C, despite the polymer matrix being in sodium form; sodium mobility is smaller than proton mobility [32; 34]. Conductivity is due to the presence of heterocycles in the polymer backbone (that undergo in some extent self-dissociation) and is also due to the presence of neighboring sulfonic groups. Conductivity of undoped sulfonated PBI was obtained between 80 °C and 160 °C, at 100 % RH [46] with values varying between $10^{-6}$ S·cm$^{-1}$ and $10^{-4}$ S·cm$^{-1}$.

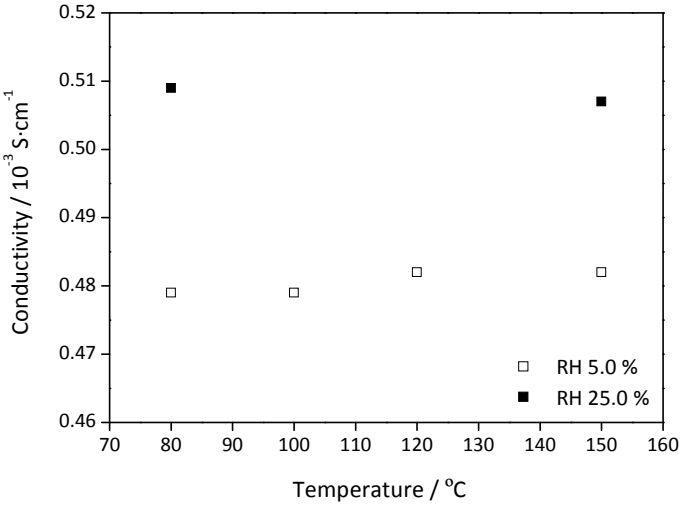


**Figure 7.9** Conductivity of S-DPE-PT polymer between 80 °C and 150 °C, at 5.0 % RH (□) and 25.0 % RH (■).

Unlike previously reported for heterocycle-based anhydrous proton conducting membranes, conductivity was not significantly influenced by temperature. A similar behavior was observed for sulfonated poly(oxadiazole-triazole) and sulfonated polyoxadiazole membranes [32; 34] and may be due to the high stiffness of the polymer between the studied temperatures, as observed in DMTA analysis.

The proton conductivity of the sulfonated polytriazole membranes (S-DPE-PT) doped with 22 and 38 mol % of phosphoric acid, after immersion on 85 wt. % phosphoric acid aqueous solution is shown in Figure 7.10. The measurements have been performed in the temperature range of 80 °C - 150 °C and at 5.0 % RH. After adding phosphoric acid into S-DPE-PT membrane, the proton concentration increased. The acid served as a proton source and aggregated to form dynamic hydrogen bonded chains. Hydrogen bonds can be established between the nitrogen sites of the polymer matrix, water molecules and phosphoric acid molecules, favoring conductivity. In the case of the membrane doped with 22 mol % of acid, the conductivity remained mostly constant above 100 °C, around $10^{-3}$ $S \cdot cm^{-1}$; a small conductivity increase was observed from 80 °C to 100 °C. In the case of the membrane doped with 38 mol % of acid, the conductivity reached a maximum at 120 °C, decreasing slightly above this temperature. The polymer matrix must be basic enough to complex with acid and also to retain the excess acid while keeping good mechanical properties. The presence of the ether moiety in the polymer backbone decreases the hydrolytic stability of polymer at high temperatures when doped with acid solutions and the polymer becomes brittle [47], explaining the small decrease in the conductivity values.

The conductivity increased up to $2 \times 10^{-3}$ $S \cdot cm^{-1}$ with phosphoric acid doping (38 mol %) at 120 °C and 5.0 % RH. This conductivity is close to the one obtained by Celik *et al.* [27] for phosphoric acid doped poly(1-vinyl-1, 2, 4-triazole), though for anhydrous conditions and at 130 °C.

Membranes doped with benzimidazole sulfonic acid (BiSA) and benzimidazole (BI), were characterized as proton conductors at 120 °C and 150 °C - Figure 7.11 (a) and (b). Small amphoteric BiSA molecules can increase the proton concentration and interact with the host polymer through proton hopping from $–SO_3H$ to N site, as

explained in Chapter 6. Besides, interactions among BiSA molecules are expected, since it possesses both proton donor and acceptor functions.

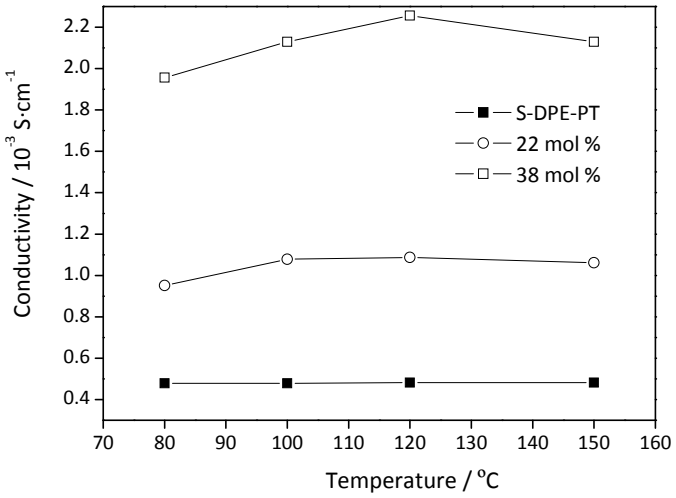


**Figure 7.10** Conductivity of S-DPE-PT polymer (■) and phosphoric acid doped polymers, at 22 mol % (○) and 38 mol % (□), between 80 °C and 150 °C and 5.0 % RH.

For 5.0 % relative humidity, there is a small increase in conductivity with the BiSA content for 120 °C and 150 °C (Figure 7.11); however, the conductivity increase is smaller than the one observed when phosphoric acid was added to the polymer (Figure 7.10). The difference between the p*K*a of both acids should have influenced this outcome: the stronger phosphoric acid, with a high degree of self-dissociation, interacts with the non-protonated nitrogen while the weaker benzimidazole sulfonic acid does not provide enough mobile protons to protonate the basic sites. One may also think that the small conductivity increase could be related to the increase of heterocycle concentration, since the transport in heterocycles molecules can occur from protonated molecules to non-protonated neighboring molecules; with a higher heterocycle concentration, new conducting pathways are added to the system resulting in a higher conductivity [35]. However, when the concentration of heterocycle without acid function (benzimidazole) was increased, it was observed a decrease of conductivity for 120 °C and 150 °C. The addition of benzimidazole to the

polymer matrix interrupts, in some extent, the charge transfer through the polymer matrix, meaning a reduction in the number of proton charge carriers. A similar behavior was observed when imidazole was added to phosphoric acid doped PBI [14].

At both temperatures, the increase of relative humidity to 25.0 % had no significant effect on the conductivity values. A slightly increase of conductivity was observed for plain polymer and low doping levels of BiSA, showing that the transport occurs within the hydrogen bonding structure with proton jumps between stationary donor and acceptor sites and it is not assisted by water. For 30 mol % doping level, the increase of RH from 5.0 % to 25.0 % led to a decrease of conductivity values. This result should be related to crystallization effects since the BiSA rich phase is, in some extent, separated from the polymer matrix (Figure 7.2).

The increase of temperature from 120 °C to 150 °C (above BiSA melting temperature) did not change the conductivity trend. A higher mobility of the doping agent was expected since BiSA was in liquid state at 150 °C. At this temperature, however, the polymer matrix presented a high stiffness - as indicated by DMTA analysis.

Pu at al. [17] showed that imidazole (Im) in imidazole doped sulfonated polyimide (sPI) (sPI/2 Im), under water vapor conditions, at 100 °C - 110 °C, was almost completely leached out. In order to observe the effect of BiSA leaching due to water vapor during the conductivity experiments, SEM images were performed, after conductivity tests (Figure 7.12), for doped membrane (30 mol %) at 150 °C and both relative humidities. At both relative humidities, it can be observed a rearrangement of BiSA micro crystals at the surface of the membranes, evidencing that it was in liquid state when in operation at 150 °C.

Also, a FTIR analysis was performed for membranes with lower doping of BiSA, 15 mol %, after proton conductivity measurements at 150 °C and 25.0 % RH and for membranes with 38 mol % of phosphoric acid doping, after proton conductivity measurements at 150 °C and 5.0 % RH (not shown). No changes were observed in spectra for both doping species; therefore, one can say that, for proton conductivity measurement conditions, there was no BiSA (and likely no Bi) and phosphoric acid leaching.

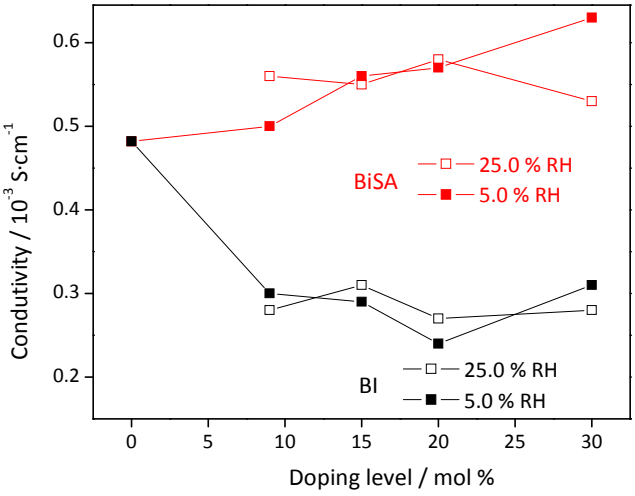


(a)

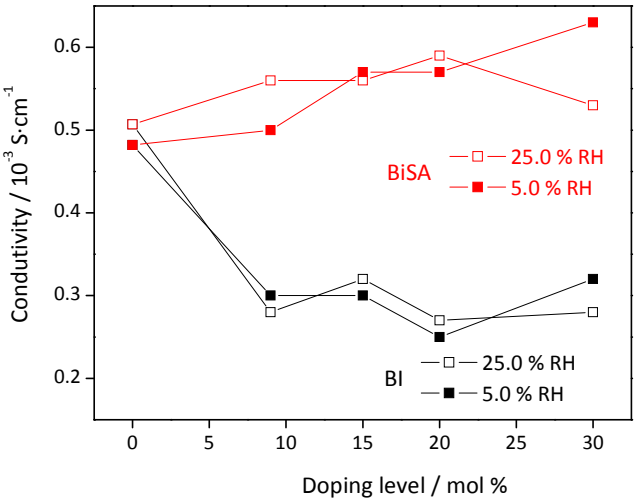


(b)

**Figure 7.11** Conductivity of S-DPE-PT polymer and doped membranes with BI (black points) and BiSA (red points) as a function of doping level at 5.0 % RH (full symbols) and 25.0 % RH (open symbols) at 120 °C (a) and 150 °C (b).

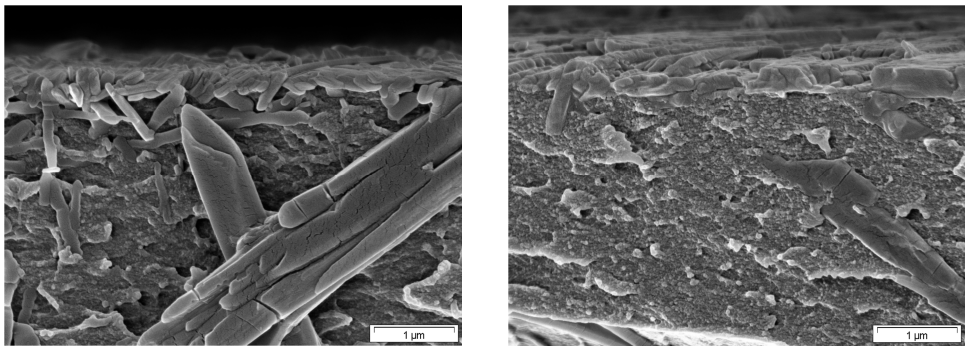


(a) (b)

**Figure 7.12** Scanning Electron Microscopy (SEM) of membranes doped with 30 mol % BiSA, after the conductivity measurements at 150 °C and 5.0 % RH (a), and 25.0 % RH (b).

### 7.4.6 MEA performance

The S-DPE-PT membrane with a doping level of 0.5 mol % (mol of crystalline $H_3PO_4$ per mol of S-DPE-PT) was tested in a fuel cell set-up, at 120 °C, 1 bar and 2.5 % RH. The use of crystalline phosphoric acid ensured that no water was trapped inside the membrane previous to the fuel cell test. It was used 2.5 % RH – lower than the relative humidity of conductivity measurements – in order to minimize possible phosphoric acid leaching during the fuel cell operation. On the other hand, the operation temperature, 120 °C, was chosen taking into account that the ether links are weak points on S-DPE-PT polymer and at temperatures higher than 150 °C some degradation is induced [48].

The I-V curves of phosphoric acid doped S-DPE-PT and phosphoric acid doped PBI membranes (doping of 10 mol of $H_3PO_4$ per mol of PBI) were compared using similar electrodes and for the same fuel cell operating conditions - Figure 7.13.

Figure 7.13 (a) shows the history for the MEA assembled with doped polytriazole polarization curves. During the first 7 hours of operation, a performance increase can be observed for the entire current density range; the open circuit voltage (OCV) increased from 0.73 V to 0.95 V and the resistance of electrodes and membrane decreased. The catalyst activity increase should be related to phosphoric acid

migration from the membrane to the catalyst layer, increasing the three-phase zone; this migration should increase with the relative humidity of the reactants. The membrane resistance also decreased with the humidification of the feeding reactants. Figure 7.13 (b) shows the history of I-V curves for the MEA assembled with the doped PBI membrane. Again, the performance increased over time due to phosphoric acid migration from the PBI membrane to the electrodes and membrane humidification. The very low initial performance for both MEAs can be explained with the absence of electrolyte at the electrodes, which would support the proton transport.

After 7 hours of operation, the performance of the acid doped S-DPE-PT MEA started to decrease (Figure 7.13 (a)). This trend was observed for all MEAs produced with phosphoric acid doped polytriazole membranes. The resistance increase of membrane and electrodes suggests a loss of phosphoric acid from the MEA. Without compromising the mechanical properties of the membrane, higher doping levels should be used in order to obtain more conductive membrane and electrodes. The PBI-based MEA showed increasing performance, until a stationary state was reached after few days of operation (Figure 7.13 (b)). Even though S-DPE-PT and PBI membranes were tested at similar conditions, PBI had a much higher phosphoric acid and water content than S-DPE-PT, due to the doping procedure of immersion in a concentrated acid solution.

The similar initial performance for both MEAs, using identical electrodes and fuel cell operating conditions, show that phosphoric acid doped polytriazole membrane can be used as proton conductor in fuel cells.

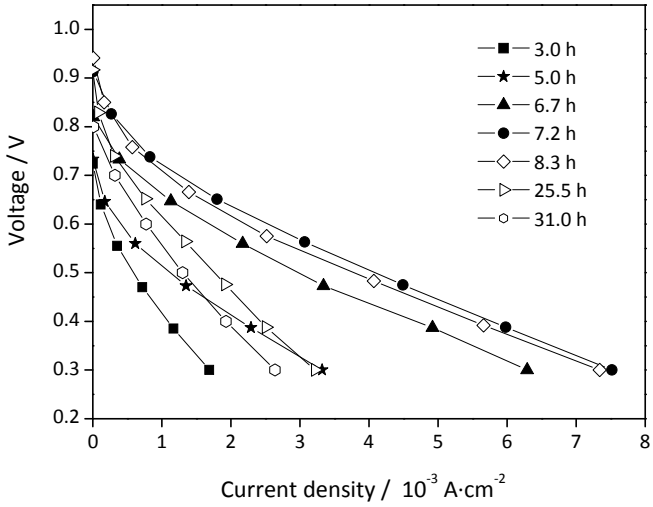


(a)

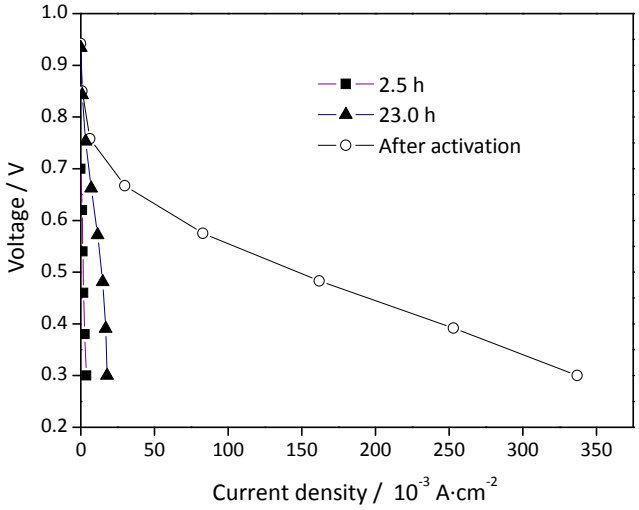


(b)

**Figure 7.13** I-V curves of phosphoric acid doped sulfonated polytriazole (a) and phosphoric acid doped PBI (b), at 1 bar, 120 °C and 2.5 % RH.

## 7.5 Conclusions

Sulfonated polytriazole (S-DPE-PT) membranes were synthesised and doped with 1H-benzimidazole-2- sulfonic acid (BiSA), benzimidazole (BI) and phosphoric acid in order to increase proton conductivity. Adding BI and BiSA did not significantly improve the conductivity of the corresponding doped membranes. On the other hand, adding phosphoric acid originated membranes with conductivity of $2\times10^{-3}$ $S\cdot cm^{-1}$ at 120 °C and 5.0 % relative humidity. The phosphoric acid doped S-DPE-PT membranes were tested in a fuel cell test bench at 120 °C and 2.5 % relative humidity. During the first 7 hours of operation it was observed a performance increase, decreasing afterwards, most probably due to phosphoric acid leaching. The phosphoric acid doped S-DPE-PT membrane showed promising performance for fuel cell application.

## 7.6 Acknowledgments

The work of M. Boaventura was supported by FCT (Grant SFRH/BD/28187/2006). The present work was also partially supported by FCT project PTDC/EQU-EQU/70574/2006.

The authors thank H. Böttcher and K. Prause for the DMTA and the SEM characterizations, respectively.

The authors also thank DLR (Institute of Technical Thermodynamics - German Aerospace Center) for receiving M. Boaventura and for the support on electrodes production.

## 7.7 References

[1] Jensen, J.O., Li, Q.F., Pan, C., Vestbo, A.P., Mortensen, K., Petersen, H.N., Sorensen, C.L., Clausen, T.N., Schramm, J., Bjerrum, N.J., 2007. High temperature PEMFC and the possible utilization of the excess heat for fuel processing. Int J Hydrogen Energy 32, 1567-1571.

[2] Zhang, J.L., Xie, Z., Zhang, J.J., Tanga, Y.H., Song, C.J., Navessin, T., Shi, Z.Q., Song, D.T., Wang, H.J., Wilkinson, D.P., Liu, Z.S., Holdcroft, S., 2006. High temperature PEM fuel cells. J Power Sources 160, 872-891.

[3] Asensio, J.A., Gomez-Romero, P., 2005. Recent developments on proton conducting poly(2,5-benzimidazole) (ABPBI) membranes for high temperature polymer electrolyte membrane fuel cells. Fuel Cells 5, 336-343.

[4] Li, Q., He, R., Jensen, J.O., Bjerrum, N.J., 2004. PBI-Based Polymer Membranes for High Temperature Fuel Cells - Preparation, Characterization and Fuel Cell Demonstration. Fuel Cells 4 147 - 159.

[5] Li, Q.F., Jensen, J.O., Savinell, R.F., Bjerrum, N.J., 2009. High temperature proton exchange membranes based on polybenzimidazoles for fuel cells. Prog Polym Sci 34, 449-477.

[6] Kreuer, K.D., Fuchs, A., Ise, M., Spaeth, M., Maier, J., 1998. Imidazole and pyrazole-based proton conducting polymers and liquids. Electrochim Acta 43, 1281-1288.

[7] Kreuer, K.D., 2001. On the development of proton conducting polymer membranes for hydrogen and methanol fuel cells. J Membrane Sci 185, 29-39.

[8] Schuster, M., Meyer, W.H., Wegner, G., Herz, H.G., Ise, M., Schuster, M., Kreuer, K.D., Maier, J., 2001. Proton mobility in oligomer-bound proton solvents: imidazole immobilization via flexible spacers. Solid State Ionics 145, 85-92.

[9] Schuster, M.E., Meyer, W.H., 2003. Anhydrous proton-conducting polymers. Annu Rev Mater Res 33, 233-261.

[10] Munch, W., Kreuer, K.D., Silvestri, W., Maier, J., Seifert, G., 2001. The diffusion mechanism of an excess proton in imidazole molecule chains: first results of an ab initio molecular dynamics study. Solid State Ionics 145, 437-443.

[11] Herz, H.G., Kreuer, K.D., Maier, J., Scharfenberger, G., Schuster, M.F.H., Meyer, W.H., 2003. New fully polymeric proton solvents with high proton mobility. Electrochim Acta 48, 2165-2171.

[12] Schuster, M.F.H., Meyer, W.H., Schuster, M., Kreuer, K.D., 2004. Toward a new type of anhydrous organic proton conductor based on immobilized imidazole. Chem Mater 16, 329-337.

[13] Scharfenberger, G., Meyer, W.H., Wegner, G., Schuster, M., Kreuer, K.D., Maier, J., 2006. Anhydrous polymeric proton conductors based on imidazole functionalized polysiloxane. Fuel Cells 6, 237-250.

[14] Schechter, A., Savinell, R.F., 2002. Imidazole and 1-methyl imidazole in phosphoric acid doped polybenzimidazole, electrolyte for fuel cells. Solid State Ionics 147, 181-187.

[15] Chuang, S.W., Hsu, S.L.C., Yang, M.L., 2008. Preparation and characterization of fluorine-containing polybenzimidazole/imidazole hybrid membranes for proton exchange membrane fuel cells. Eur Polym J 44, 2202-2206.

[16] Pu, H.T., Wang, D., 2006. Studies on proton conductivity of polyimide/H3PO4/imidazole blends. Electrochim Acta 51, 5612-5617.

[17] Pu, H.T., Qin, Y.J., Tang, L.M., Teng, X.R., Chang, Z.H., 2009. Studies on anhydrous proton conducting membranes based on imidazole derivatives and sulfonated polyimide. Electrochim Acta 54, 2603-2609.

[18] Yamada, M., Honma, I., 2004. Alginic acid-imidazole composite material as anhydrous proton conducting membrane. Polymer 45, 8349-8354.

[19] Sevil, F., Bozkurt, A., 2005. Proton conduction in PVPA - Benzimidazole hybrid electrolytes. Turk J Chem 29, 377-383.

[20] Persson, J.C., Josefsson, K., Jannasch, P., 2006. Polysulfones tethered with benzimidazole. Polymer 47, 991-998.

[21] Persson, J.C., Jannasch, P., 2006. Block copolymers containing intrinsically proton-conducting blocks tethered with benzimidazole units. Chem Mater 18, 3096-3102.

[22] Persson, J.C., Jannasch, P., 2006. Intrinsically proton-conducting comb-like copolymers with benzimidazole tethered to the side chains. Solid State Ionics 177, 653-658.

[23] Woudenberg, R.C., Yavuzeetin, O., Tuorninen, M.T., Coughlin, E.B., 2007. Intrinsically proton conducting polymers and copolymers containing benzimidazole moieties: Glass transition effects. Solid State Ionics 178, 1135-1141.

[24] Pu, H.T., Ye, S., 2006. Preparation and proton conductivity of acid-doped poly(5-vinyltetrazole-co-acrylonitrile). React Funct Polym 66, 856-862.

[25] Pu, H.T., Wu, J., Wan, D.C., Chang, Z.H., 2008. Synthesis and anhydrous proton conductivity of poly(5-vinyltetrazole) prepared by free radical polymerization. J Membrane Sci 322, 392-399.

[26] Gunday, S.T., Bozkurt, A., Aghatabay, N.M., Baykal, A.H., 2007. Benzimidazole tethered proton conducting organic electrolytes. Mater Chem Phys 105, 240-244.

[27] Celik, S.U., Aslan, A., Bozkurt, A., 2008. Phosphoric acid-doped poly(1-vinyl-1,2,4-triazole) as water-free proton conducting polymer electrolytes. Solid State Ionics 179, 683-688.

[28] Aslan, A., Celik, S.U., Sen, U., Haser, R., Bozkurt, A., 2009. Intrinsically proton-conducting poly(1-vinyl-1,2,4-triazole)/triflic acid blends. Electrochim Acta 54, 2957-2961.

[29] Subbaraman, R., Ghassemi, H., Zawodzinski, T., 2009. Triazole and triazole derivatives as proton transport facilitators in polymer electrolyte membrane fuel cells. Solid State Ionics 180, 1143-1150.

[30] Martwiset, S., Woudenberg, R.C., Granados-Focil, S., Yavuzcetin, O., Tuominen, M.T., Coughlin, E.B., 2007. Intrinsically conducting polymers and copolymers containing triazole moieties. Solid State Ionics 178, 1398-1403.

[31] Granados-Focil, S., Woudenberg, R.C., Yavuzcetin, O., Tuominen, M.T., Coughlin, E.B., 2007. Water-free proton-conducting polysiloxanes: A study on the effect of heterocycle structure. Macromolecules 40, 8708-8713.

[32] Gomes, D., Roeder, J., Ponce, M.L., Nunes, S.P., 2007. Characterization of partially sulfonated polyoxadiazoles and oxadiazole-triazole copolymers. J Membrane Sci 295, 121-129.

[33] Roeder, J., Gomes, D., Ponce, M.L., Abetz, V., Nunes, S.P., 2007. Protonation of sulfonated poly(4,4 '-diphenylether-1,3,4-oxadiazole) membranes. Macromol Chem Physic 208, 467-473.

[34] Gomes, D., Roeder, J., Ponce, M.L., Nunes, S.P., 2008. Single-step synthesis of sulfonated polyoxadiazoles and their use as proton conducting membranes. J Power Sources 175, 49-59.

[35] Ponce, M.L., Boaventura, M., Gomes, D., Mendes, A., Madeira, L.M., Nunes, S.P., 2008. Proton conducting membranes based on benzimidazole sulfonic acid doped sulfonated poly(oxadiazole-triazole) copolymer for low humidity operation. Fuel Cells 8, 209-216.

[36] Ponce, M.L., Gomes, D., Nunes, S.P., 2008. One-pot synthesis of high molecular weight sulfonated poly(oxadiazole-triazole) copolymers for proton conductive membranes. J Membrane Sci 319, 14-22.

[37] Bouchet, R., Siebert, E., 1999. Proton conduction in acid doped polybenzimidazole. Solid State Ionics 118, 287-299.

[38] Kundu, S., Simon, L.C., Fowler, M., Grot, S., 2005. Mechanical properties of Nafion (TM) electrolyte membranes under hydrated conditions. Polymer 46, 11707-11715.

[39] Jeon, H.S., Oh, S.H., Kim, J.S., Lee, Y., 2003. Effects of various carboxylated benzene salts on the mechanical properties and morphology of poly(styrene-co-methacrylate) ionomers. Polymer 44, 4179-4187.

[40] Kim, S.H., Kim, J.S., 2003. Effects of low matrix glass transition temperature on the cluster formation of ionomers having two ion pairs per ionic repeat unit. Macromolecules 36, 1870-1875.

[41] Ma, X., Sauer, J.A., Hara, M., 1997. Influence of plasticizers on poly(methyl methacrylate) ionomers. Polymer 38, 4425-4431.

[42] Wakabayashi, K., Register, R.A., 2006. Morphological origin of the multistep relaxation behavior in semicrystalline ethylene/methacrylic acid ionomers. Macromolecules 39, 1079-1086.

[43] Ponce, M.L., Vainio, U., Nunes, S.P., Morphology Study of Polytriazole Polymers by SAXS, WAXS and DMTA. In preparation,

[44] Celik, S.U., Bozkurt, A., 2008. Preparation and proton conductivity of acid-doped 5-aminotetrazole functional poly(glycidyl methacrylate). Eur Polym J 44, 213-218.

[45] Acheson, R.M., 1976. An Introduction to the Chemistry of Heterocyclic Compounds. 3rd. John Wiley & Sons Inc,

[46] Staiti, P., Lufrano, F., Arico, A.S., Passalacqua, E., Antonucci, V., 2001. Sulfonated polybenzimidazole membranes - preparation and physico-chemical characterization. J Membrane Sci 188, 71-78.

[47] Gomes, D., Nunes, S.P., 2008. Fluorinated polyoxadiazole for high-temperature polymer electrolyte membrane fuel cells. J Membrane Sci 321, 114-122.

[48] Ponce, M.L., Roeder, J., Gomes, D., Nunes, S.P., 2009. Stability of sulfonated polytriazole and polyoxadiazole membranes. Asia-Pac. J. Chem. Eng, in press: doi 10.1002/apj.1370.

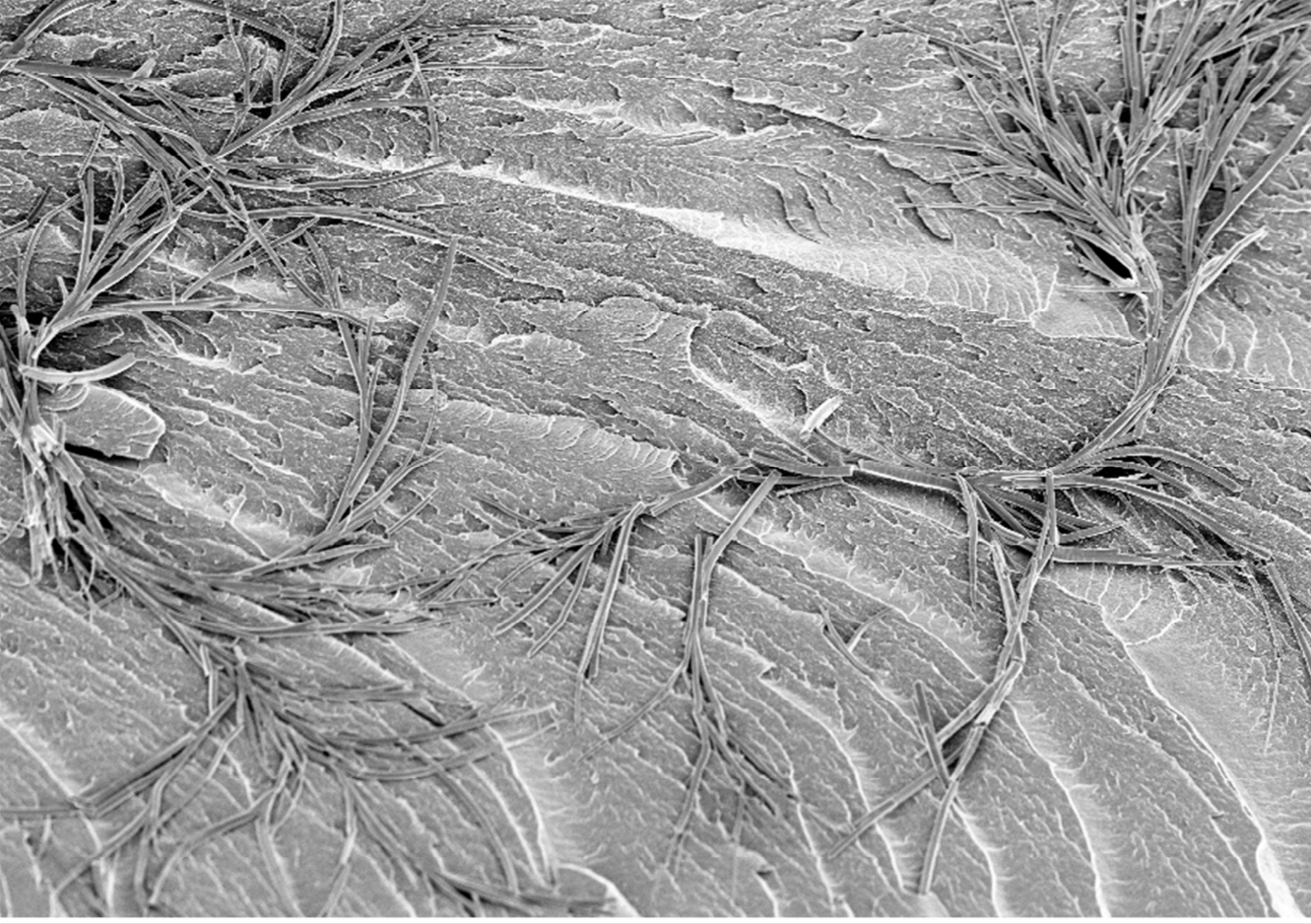

# Part IV Conclusions

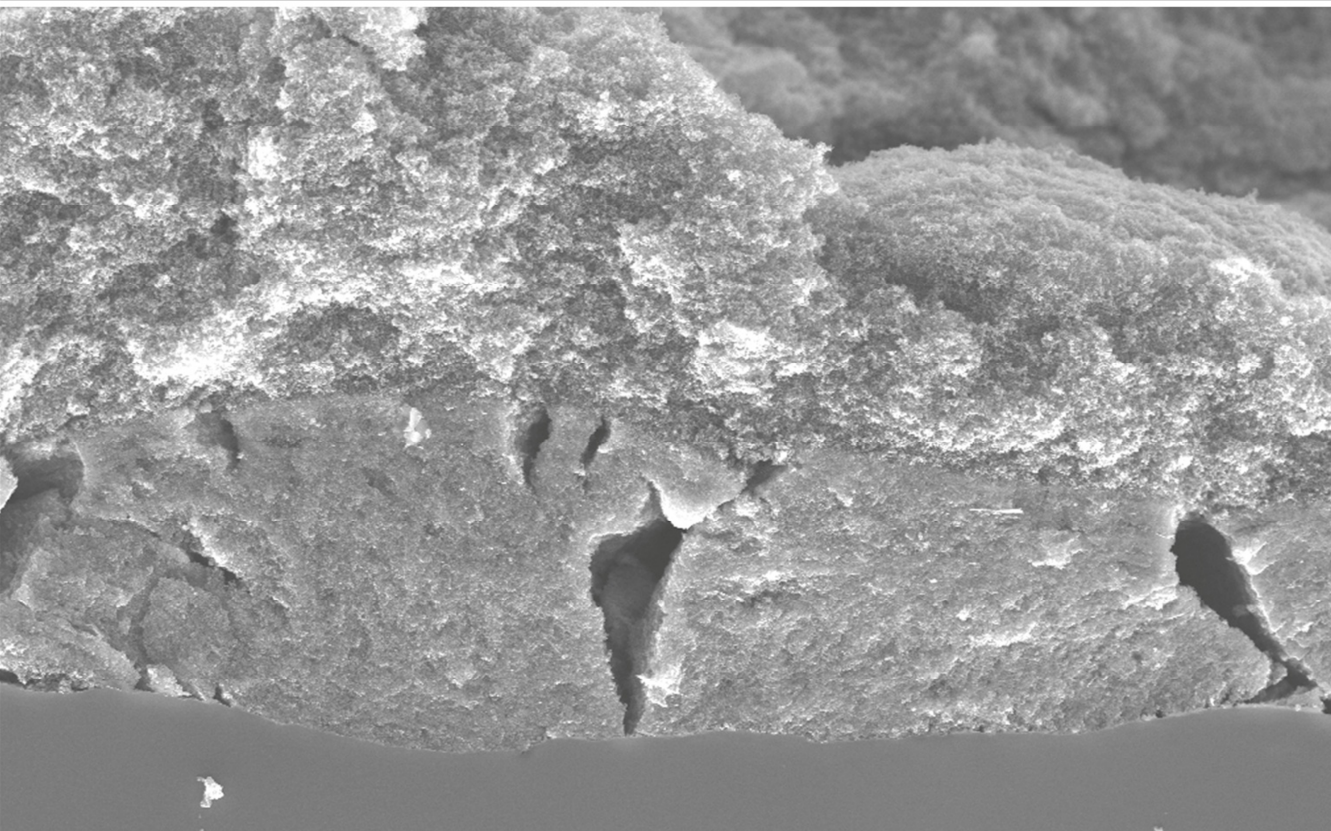

Top: S-DPE-PT membrane doped with 30 mol % of BiSA

Bottom: interface between PBI / $H_3PO_4$ membrane and catalytic

layer of Pt-SWNH-based electrode

# Chapter 8 Conclusions and future work

The activation process of two phosphoric acid doped polybenzimidazole-based MEAs (Celtec® - P1000 MEA and an in-house MEA) was studied at 160 °C. The activation process was studied based on I-V curves, electrochemical impedance spectroscopy and cyclic voltammetry analysis. The galvanostatic activation procedure enhanced the Celtec® - P1000 MEA performance increasing the catalyst activity and decreasing the ohmic resistance. A galvanostatic and potential cycling procedures were applied to an in-house prepared MEA; for the same activation time, the galvanostatic allowed a deeper activation than the potential cycling activation method. The in-house electrodes, prepared without any proton conducting polymer or phosphoric acid, showed an increased catalytic activity as a function of time due to migration of phosphoric acid from the membrane to the catalyst layer. Moreover, the MEA ohmic resistance decreased during the activation procedure and due to the PBI membrane humidification.

The behavior of in-house prepared MEA was assessed at different temperatures (120 °C - 160 °C) and relative humidities (1.0 % - 5.0 %). The water presence facilitated the migration of phosphoric acid to the electrodes and had an enhanced effect on ohmic resistance during the PEMFC operation. Nonetheless, water presence in these systems can also have a detrimental effect on the cathode resistance due to an increase of phosphoric acid leaching from the electrode. The highest performance was obtained for 160 °C and 2.5 % relative humidity.

The effect of stepping the CO amount at the anode gas feed, from 0.0 % to 1.5 % or 3.0 %, on the HT-PEMFC performance was studied using a Celtec® - P1000 MEA. The poisoning was assessed at 160 °C and 180 °C based on the transient behavior of the fuel cell voltage and current density distribution. The current density distribution at similar voltage and global current density were also compared for pure hydrogen and hydrogen containing CO. Furthermore, the I-V and power density curves and electrochemical impedance spectroscopy spectra were obtained.

Two different cell anodes were used to obtain the current density distribution, 1) a metal segmented flow field and 2) a non-segmented graphite flow field where it was applied a printed circuit board as segmented current collector.

The presence of CO caused a performance loss, which was more significant for higher CO concentrations and higher global current densities and for lower temperatures. The transient behavior of the voltage, for both cells used, showed that the poisoning effect of CO at the anode is very fast, within few minutes. The current density distributions obtained with metal segmented flow field showed that the use of hydrogen feed containing CO originated a spatial distribution of CO at the anode, which was more significant for higher CO concentrations and global current densities. On the other hand, no significant change on the current density distribution was observed with the graphite flow field.

A dynamic one-dimensional isothermal phenomenological model was developed for simulating the steady-state and transient behavior of two fuel cells operated at 160 °C, one equipped with an in-house assembled MEA and the other with Celtec® - P1000 MEA. The model accounts for two transient processes: the mass transport on the bipolar plates and gas diffusion layers and the double layers charge/discharge. A small voltage perturbation was imposed to the simulator, over a wide range of frequencies, and the Nyquist and Bode plots obtained. The steady-state response was predicted for both fuel cells systems and the Nyquist plots were qualitatively predicted. The observed differences were assigned to proton resistance and the gas diffusion limitations within the catalyst layer, which were not considered in the phenomenological model.

A performance comparison of electrodes prepared with electrocatalysts based on platinum supported in single-wall carbon nanohorns (SWNH) and supported in carbon black was obtained. The electrodes were assembled with a phosphoric acid doped polybenzimidazole membrane and characterized at 160 °C. Characterization techniques included I-V and power density curves, electrochemical impedance spectroscopy and cyclic voltammetry (CV). The chemical composition of PBI

membrane and catalyst layer after the electrochemical tests was analyzed by energy dispersive X-ray spectroscopy. Surprisingly, a similar power density peak was obtained for both MEAs. The higher hydrophobic character of the non-conventional carbon originated a MEA with higher ohmic resistance. Moreover, lower anode charge transfer resistance anode similar cathode charge transfer resistance were obtained for the single-wall carbon nanohorns-based MEA.

Sulfonated poly(oxadiazole-triazole) copolymer membranes were prepared and doped with amphoteric molecule, 1H-benzimidazole-2-sulfonic acid whereas sulfonated polytriazole membranes were prepared and doped with three different agents: 1H-benzimidazole-2- sulfonic acid, benzimidazole and phosphoric acid. The modified membranes were characterised by scanning electron microscopy (SEM), infrared spectra, thermogravimetric analysis (TGA), dynamical mechanical thermal analysis (DMTA) and electrochemical impedance spectroscopy. Sulfonated poly(oxadiazole-triazole) copolymer membranes presented good mechanical properties and a proton conductivity, up to $4\times10^{-3}$ $S\cdot cm^{-1}$, at 120 °C and low relative humidity. For sulfonated polytriazole membranes doped with 85 wt. % phosphoric acid solution, the proton conductivity increased up to $2\times10^{-3}$ $S\cdot cm^{-1}$ at 120 °C and 5.0 % relative humidity. The performance of the phosphoric acid doped sulfonated polytriazole was evaluated in a fuel cell set-up at 120 °C and 2.5 % relative humidity. The MEA was assembled using electrodes without any ion conductor polymer or phosphoric acid content. A similar procedure was applied for a phosphoric acid doped polybenzimidazole membrane, used as a reference. The phosphoric acid doped sulfonated polytriazole-based MEA increased its performance over the first 7 hours of operation and the performance was similar to those of phosphoric acid doped polybenzimidazole. The I-V curves performed afterwards for phosphoric acid doped sulfonated polytriazole showed a decrease in performance, due to phosphoric acid loss.

Taking into account the results presented in this thesis, suggestions of future work can be made.

It was showed that the PEMFC anode catalyst becomes less sensitive to CO and other contaminants poisoning as the temperature increases, especially above 150 °C, allowing the use of reformate gas on the fuel cell anode. Standard catalysts for steam reforming of methanol, such $Cu/ZnO/Al_2O_3$, exhibit relevant activity at temperatures above 240 °C. Our laboratory is developing a new catalyst for methanol steam reforming, with equivalent activities at 180 °C. Since methanol steam reforming is an endothermic reaction and the fuel cell operate exothermically, it is possible a synergetic integration of both reactors, that can operate at e.g. 180 °C.

The impact of changing the anode feed from pure hydrogen to a reformer gas (containing hydrogen, carbon monoxide, carbon dioxide and nitrogen) on the HT-PEMFC performance can be studied as well as the influence of carbon monoxide and carbon dioxide concentrations. Furthermore, a platinum alloy catalyst can be used instead of platinum as strategy to mitigate the effect of CO poisoning at the anode. One of the most promising alloys is the binary catalyst PtRu, usually used as anode catalyst in direct methanol fuel cells.

The development of a more complete one-dimensional model is recommended. Several improvements can be performed such: 1) take into account the mass transport in the thin film of phosphoric acid solution in the catalyst layer and proton transport within the catalyst layer, 2) inclusion of an energy balance and 3) application of Stefan-Maxwell equation to describe the electrodes mass transport.

To better assess the influence of carbon support morphology and hydrophobicity in the catalyst activity and reactants access to the catalyst sites, electrodes based on platinum supported in SWNH can be prepared including phosphoric acid doped polybenzimidazole (or other proton conductor) in the catalyst ink. The performance of these electrodes should be compared to those of electrodes prepared with carbon

black support. It is also suggested to perform dynamic tests (load cycles or shut-down cycles) in order to evaluate the aging of MEAs prepared with both carbon supports.